LOCAL CHARACTERISATION OF STRAIN IN SILICON NANOSTRUCTURES

A THESIS SUBMITTED TO THE FACULTY OF ENGINEERING FOR THE DEGREE
OF DOCTOR OF PHILOSOPHY

By

Fernando Ureña Begara

Newcastle University
School of Electrical and Electronic Engineering
Newcastle upon Tyne
United Kingdom

January 2014

Abstract

Strain engineering is used in the microelectronics industry for fabricating micro- and nano-electromechanical systems (MEMS and NEMS) and state-of-the-art metal-oxide-semiconductor field-effect transistors (MOSFETs). In these devices suspended silicon beams, films and nanowires are widely used. However, the mechanical, thermal and electrical properties of silicon change significantly at the nanoscale. Therefore, an accurate knowledge of the size effect on these properties, the role of the surface and an accurate characterisation of the stress and strain distribution in these devices is needed for a complete understanding of the device operation. Likewise, state-of-the-art MOSFETs incorporate strain into the channel to improve performance due to a carrier mobility enhancement compared with unstrained silicon channel transistors. However, the mobility enhancement especially at high vertical electric fields (where commercial MOSFETs operate), is still not well understood. The SiO_2/Si interface roughness exhibits, at the nanoscale, scaling behaviour with the scale of observation. However, to date, there is no experimental study of the SiO_2/Si interface roughness scaling behaviour with strain. This study is needed to better understand the surface roughness scattering-limited mobility of electrons and holes in strained devices.

Raman spectroscopy is a widely used technique to characterise strain. However, the conversion of Raman peak shifts to strain values requires a strain-shift coefficient. Traditionally, the reported strain-shift coefficients have been determined from experiments performed in bulk material. The applied stress has also been limited within the range 0 – 2 GPa. This range is reasonable for bulk silicon characterisation but is too narrow for silicon nanostructures and devices where higher stress values are often favourable for improving performance. Consequently, there is an outstanding need to find appropriate strain-shift coefficients for silicon nanowires and thin films under large values of stress.

In this thesis strain in silicon nanostructures is experimentally and theoretically investigated for strain values ranging from 0 to 3.6%. Strain has been characterised using scanning electron microscopy (SEM), Raman spectroscopy, and theoretically with analytical calculations and finite element simulations. The combination of these techniques and the large number of samples (up to 85) has allowed the accurate determination of the strain-shift coefficient for the technologically important (100) silicon surface and for stress values up to 4.5 GPa. The work also enables a better understanding of the changes in silicon properties with strain when device dimensions are reduced to the nanoscale. The size dependency of the Young’s modulus, fracture strain, thermal conductivity and the role of the surface in the size dependent physics are also investigated. It is found that some properties such as the fracture strain change with the dimensions of the sample whereas others such as the Young’s modulus and thermal conductivity do not change. Finally, the impact of uniaxial and biaxial strain on the surface roughness of silicon nanostructures and thin films has been analysed by atomic force microscopy (AFM). It is found that the silicon surface roughness changes in different manner with uniaxial and biaxial strain. The results show that the silicon surface roughness is self-affine with strain and that this behaviour has to be considered within the models used to describe the carrier mobility in MOSFETs at high vertical electric fields.

Acknowledgements

I would like to express my gratitude to my supervisors Dr. Sarah Olsen and Prof. Jean-Pierre Raskin for their support and advice throughout this project. It has been a great pleasure to work with them. Thank you.

Special thanks to Dr. Lidija Šiller at Newcastle University for her supervision during my first year.

This PhD was funded by the Engineering and Physical Sciences Research Council (EPSRC). The support from HORIBA Jobin Yvon Ltd. is also appreciated.

The structures used in this work were provided by the Université catholique de Louvain (UCL) in Belgium and by the Paul Scherrer Institute (PSI) in Switzerland. I would like to thank Dr. Umesh Bhaskar for the fabrication and SEM measurements of the samples processed at UCL and the measurements of the Young's modulus performed by dynamic resonance-based methods presented in the work. Also I would like to thank Dr. Renato Minamisawa for the fabrication of the samples processed at the PSI.

During this PhD, I have had the privilege to work with exceptional colleagues and friends in the Emerging Technologies and Materials (ETM) research group. In particular, I would like to thank Meaad al-Hadidi, Dr. Mariam Ahmed, Dr. Nor Farahidah Za'bah, Dr. Sergej Makovejev, Dr. Raman Kapoor, Andrew Lawson, Dr. Shahin Mojarad, Raied Al-Hamadany, Sami Ramadan, Dr. Amit Tiwari and Dr. Erhan Arac for sharing their knowledge and experience and for long friendly discussions. I would like to express my gratitude to Dr. Peter King for proofreading parts of the thesis.

My gratitude to Dr. Enrique Escobedo Cousin for his friendship and the innumerable and fruitful conversations during all this time. Many thanks for teaching me how to use the AFM and the Raman system.

I am thankful also to my friends in Catalonia and colleagues in the IES Pere Barnils for their long distance support.

Last but not least, my deepest gratitude to my parents and family for their support during all these years. This thesis is dedicated to you.

Publications

Several chapters of this thesis have already been published:

Journal papers

- **F. Ureña**, S. H. Olsen, and J.-P. Raskin, "Raman measurements of uniaxial strain in silicon nanostructures", *Journal of Applied Physics*, vol. 114, pp. 144507-1−144507-11, 2013 (Chapter 5)

- **F. Ureña**, S. H. Olsen, L. Šiller, U. Bhaskar, T. Pardoen, and J.-P. Raskin, "Strain in silicon nanowire beams", *Journal of Applied Physics*, vol. 112, pp. 114506-1−114506-12, 2012 (Chapter 4)

Conferences

- **F. Ureña**, S. H. Olsen, L. Šiller, U. Bhaskar, E. Escobedo-Cousin, and J.-P. Raskin, "Local Strain Characterization of MEMS-Based Silicon Beams by Raman Spectroscopy", *Electronic Materials Conference (EMC)*, June 2011, Santa Barbara, USA (Chapter 4)

Table of contents

List of figures

List of tables

List of symbols

$\boldsymbol{a_i}$	Lattice vector (i = 1, 2, 3)
$a_{i\leftrightarrow j}$	Direction cosine of the angle between the axes *i* and *j* (*i, j* = 1, 2, 3) (*i* and *j* belong to two sets of mutually orthogonal axes with the same origin)
b_i	Strain-shift coefficient of mode *i*
c	Speed of light
$\mathrm{C_{ij}}$	Fourth rank stiffness tensor in Voigt notation (i, j = 1, 2, 3, 4 ,5, 6)
C_{ijkl}	Fourth rank stiffness tensor in full tensor notation (*i, j, k, l* = 1, 2, 3)
D	Fractal dimension
$\boldsymbol{E}$	Electric field.
E_a	Actuator Young's modulus
$E_{<hkl>}$	Young's modulus in the directions <*hkl*>
$\boldsymbol{e_i}$	Unit vector of the polarised incident light
E_s	Sample Young's modulus
$\boldsymbol{e_s}$	Unit vector of the polarised scattered light
F_a	Force at the actuator
F_s	Force at the sample
$G_{\alpha\beta}$	Second rank force constants tensor in full tensor notation (α, β = 1, 2, 3)
$G^{\varepsilon}_{\alpha\beta\mu\nu}$	Fourth rank force constants derivative tensor (with respect to strain) in full tensor notation (α, β, μ, ν = 1, 2, 3)
h	Surface height
$\bar{h}$	Average surface height
[*hkl*]	Lattice direction defined by the normalised vector components *h, k, l*
(*hkl*)	Plane direction defined by the normalised vector components *h, k, l*
<*hkl*>	Group of equivalent directions to the normalised vector components *h, k, l*
$\{hkl\}$	Group of equivalent planes to the normalised vector components *h, k, l*
I_s	Intensity of the scattered light
$\boldsymbol{k}$	Wave vector
k	Wave number
$\boldsymbol{k_{Th}}$	Second rank thermal conductivity tensor.
l	Lag distance in autocorrelation functions
L_0	Initial length of the beam
L_{a0}	Actuator length with attached sample (before release)

L_{a0}^{free}	Actuator length without attached sample (before release)
L_c	Intersection point between the self-affine and the saturation regions
L_{s0}	Sample length (before release)
m^*	Conductivity effective mass
m_0	Free electron mass
m_l	Longitudinal conductivity effective mass
m_t	Transversal conductivity effective mass
$\boldsymbol{P}$	Electric moment.
p	Phonon deformation potential
q	Phonon deformation potential
q_e	Electronic charge
$\boldsymbol{Q_h}$	Heat flow rate.
$\boldsymbol{Q_j}$	Normal mode of vibration *j*.
$\boldsymbol{q_j}$	Phonon wave vector
$\boldsymbol{q_s}$	Wave vector in reciprocal space
q_s	Wave number in reciprocal space
r	Phonon deformation potential
$\boldsymbol{R_j}$	Second order Raman tensor for the normal mode of vibration *j*.
S_a	Actuator cross section
$\mathrm{S_{ij}}$	Fourth rank compliance tensor in Voigt notation (i, j = 1, 2, 3, 4, 5, 6)
S_{ijkl}	Fourth rank compliance tensor in full tensor notation (*i*, *j*, *k*, *l* = 1, 2, 3)
S_S	Sample cross section
T_i	Components of a first rank tensor in full tensor notation (*i* = 1, 2, 3)
T_{ij}	Components of a second rank tensor in full tensor notation (*i*, *j* = 1, 2, 3)
T_{ijk}	Components of a third rank tensor in full tensor notation (*i*, *j*, *k* = 1, 2, 3)
T_{ijkl}	Components of a fourth rank tensor in full tensor notation (*i*, *j*, *k*, *l* = 1, 2, 3)
u	Actuator contraction / sample elongation
u_{free}	Actuator free contraction
w	Interface width
α	Hurst exponent
α_{Si}	Thermal expansion coefficient of silicon
α_{Si3N4}	Thermal expansion coefficient of silicon nitride
Γ	Brillouin zone centre
$\varDelta_n$	*n*-fold conduction band degeneracy

Δ_{pv}	Maximum peak to valley height
$\Delta\omega$	Raman frequency difference (with and without the applied stress)
δ	Correction factor in SEM measurements
$\delta_{\alpha\beta}$	Kronecker delta
$\boldsymbol{\varepsilon}$	Second rank strain tensor
ε_0	Vacuum electrical permittivity
ε_a	Actuator longitudinal strain
ε_a^{mec}	Actuator mechanical strain
ε_a^{mis}	Actuator mismatch strain
$\boldsymbol{\zeta}$	Stress vector
λ	Wavelength
μ	Carrier mobility
μ_{SR}	Surface roughness scattering limited mobility
ξ	Correlation length
$\boldsymbol{\sigma}$	Second rank stress tensor
σ_a	Actuator normal stress
σ_s	Sample normal stress
τ	Momentum relaxation time
υ	Poisson’s ratio
$\boldsymbol{\chi}$	Susceptibility tensor.
ω	Angular frequency
$\mathrm{\omega_0}$	Raman shift in unstrained silicon
ω_i	Angular frequency of the incident light
ω_j	Angular frequency of phonon j.
ω_s	Angular frequency of the scattered light

Abbreviations

AFM	Atomic force microscopy
bcc	Body-centred cubic
CBED	Convergent beam electron diffraction
fcc	Face-centred cubic
FE	Finite element
FWHM	Full-width half-maximum
HH	Heavy hole
LH	Light hole
LO	Longitudinal optical
MEMS	Micro-electromechanical sytems
MOSFET	Metal-oxide-semiconductor field-effect transistor
NA	Numerical aperture
NEMS	Nano-electromechanical systems
PDP	Phonon deformation potential
PSD	Power spectral density
PSPD	Photo-sensitive photo detector
RMS	Root mean square
SEM	Scanning electron microscopy
SMT	Stress memorisation technique
SNR	Signal-to-noise ratio
SO	Split-off
SOI	Silicon-on-insulator
SPM	Scanning probe microscope
sSOI	Strained-silicon-on-insulator
SThM	Scanning thermal microscopy
STM	Scanning tunnelling microscopy
TEM	Transmission electron microscopy
TO	Transversal optical
UV	Ultra-violet
XRD	X-ray diffraction

Chapter 1. Introduction

Strain in semiconductors is an old research topic since, in 1950, Bardeen and Shockley [1] developed a deformation potential theory to account for the coupling between electrons and acoustic vibrations (phonons) in solids. In this theory, the local strain in the material (resulting from the acoustic vibrations) induces a proportional energy band shift. In 1954, the experimental measurements in silicon and germanium by Smith [2] at Bell Laboratories lead to the discovery of the piezoresistance effect (the change in resistance with applied stress). Since then, the piezoresistance effect has been widely used in micro- and nano-electromechanical systems (MEMS and NEMS) for fabricating and developing piezoresistive based sensors including pressure and force sensors, accelerometers and strain gauges [3-7]. With the advent of the metal-oxide-semiconductor field-effect transistor (MOSFET) in 1960 [8], there has been an aggressive and continuous scaling down of dimensions to increase performance and transistor density per chip [9]. However, the continuous shrinking of the MOSFET dimensions to the submicron and nanoscale level has resulted in issues such as velocity carrier saturation, leakage current, self-heating effects and dielectric breakdown compromising performance enhancements possible from scaling alone [10, 11]. Therefore, alternative solutions have been introduced. Among these, strained silicon MOSFET channels has proved to enhance device performance due to a mobility enhancement of holes and electrons when compared with unstrained silicon channel transistors [11-13]. The use of strain engineering in nanostructures and devices is described below.

1.1 Strain engineering

1.1.1 Strain in nanostructures

Strain engineering is used in MEMS and NEMS for fabricating and developing piezoresistive based sensors, e.g. pressure and force sensors [3]. Most MEMS- and NEMS-based sensors use thin films and nanowires. Pressure sensors, for instance, are based in a thin membrane or suspended nanowire which constitutes the detection mechanism [4, 14].

In these sensors, a bending force acting upon a membrane, or compressing or elongating a nanowire, is converted to an electrical signal by using the piezoresistive properties of silicon [15, 16]. The superior surface-to-volume ratio of these sub-micrometer dimension structures compared with their macro counterparts makes them highly sensitive to chemical and biological detection and consequently very attractive in fabricating and developing MEMS based sensors [17-19].

However, common problems associated with undesirable or excessive mechanical stresses are also a source of many reliability issues [20, 21]. Precise knowledge of mechanical properties such as Young's modulus, fracture strain and fracture stress are needed. Despite the mechanical, thermal and electrical properties of bulk silicon having been extensively studied [22], they change significantly at the nanoscale [23-25]. This is because the surface-to-volume ratio significantly increases and the surface atoms start to play a more important role in the physical properties of the material. In solids, during the process of creating a new surface, the free energy increases [26]. The charge distribution at the surface and in the bulk is different due to the absence of atoms above the free surface (Figure 1.1a) [27]. As a result, the surface atoms rearrange in order to minimise their positional energy (Figure 1.1b) [26].

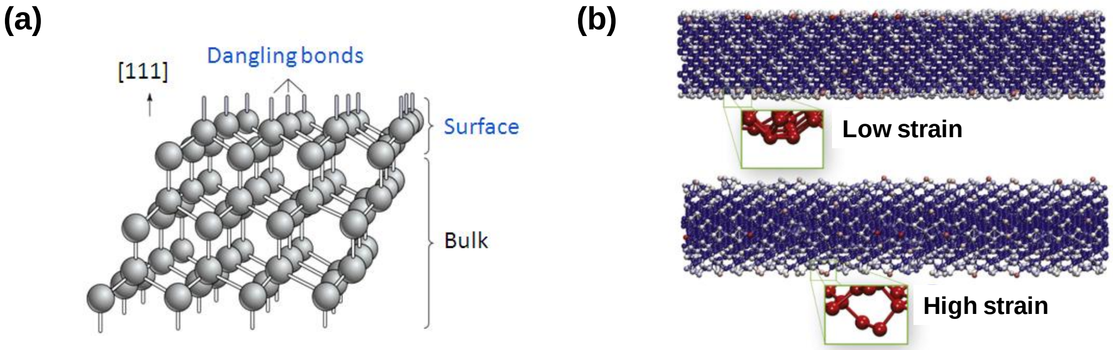

Figure 1.1 Surface reconstruction in silicon. (a) Surface dangling bonds observed from the silicon [111] direction. [28], (b) Molecular dynamics simulation of the surface reconstruction in a (100) silicon nanobeam by 2×1 symmetric dimers for low and high values of applied strain. At high values of strain, there is a buckling of the dimers. [29]

This surface reconstruction is considered to be the leading mechanism for the observed change in some physical properties in silicon at the nanoscale, for example elasticity and thermal conductivity [29, 30]. However, the discrepancies between theory and experiments are large. Thus, whereas some experiments have found a Young's modulus size dependency for dimensions ~300 nm [24], *ab initio* calculations only predict a size dependency in Young's modulus for dimensions below ~10 nm [31]. Moreover, some experiments have found a decrease in Young's modulus with size [24, 32] whereas other experiments have found no change [33, 34] or even an increase in Young's modulus with size [35]. The thermal conductivity variation with strain of silicon has also been largely studied analytically and experimentally [36-40]. However, to date, most of the experimental work has been performed in bulk silicon and no experimental data of the thermal conductivity variation in nanostructures with size and strain is available. Therefore, with devices well into the nanometre regime, a fundamental understanding and experimental investigation of the mechanical, electrical and thermal properties in silicon suspended beams and nanowires, is crucial.

1.1.2 Strain in MOSFETs

Strain is incorporated into the channel of the transistor globally (wafer based) or locally (process induced). Global or biaxial stress is generally introduced by epitaxial growing of silicon on top of a relaxed silicon germanium ($Si_{1-x}Ge_x$) substrate. As a result of a 4.2% lattice mismatch between silicon and germanium, the silicon epitaxial layer undergoes tensile strain (Figure 1.2).

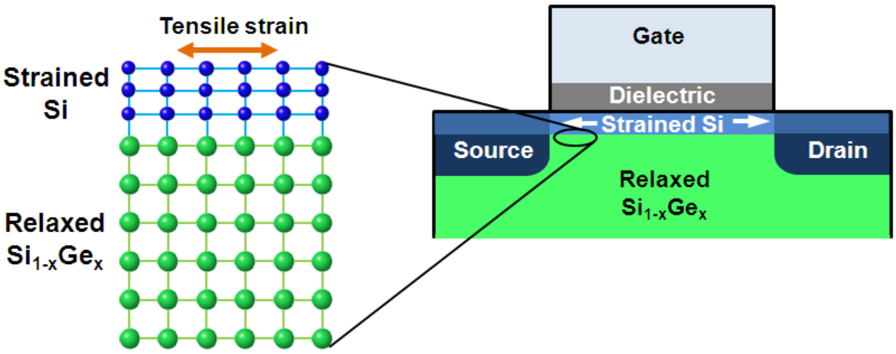

Figure 1.2 Global tensile strain is incorporated into the MOSFETs channel by the epitaxial growing of silicon on top of relaxed $Si_{1-x}Ge_x$.

The strained silicon layer can subsequently be transferred to an insulator substrate to combine performance and benefits of silicon-on-insulator (SOI) technology and high mobility [41]. However, at high vertical electric fields (perpendicular to the MOSFET channel) p-type MOSFETs show a modest or even degraded hole mobility with biaxial tensile strain [42, 43]. Also, process complexity, self-heating issues (due to a poor thermal conductivity of SiGe) and high costs have led the industry to adopt uniaxial process induced strain [44, 45]. The main obstacle to incorporate uniaxial strain into the MOSFET's channel arises from the difficulty of simultaneously improving n-type and p-type MOSFETs with the same stress (tensile or compressive). Whereas uniaxial tensile strain is advantageous for n-type MOSFETs, uniaxial compressive strain benefits p-type MOSFETs. Traditionally, devices are fabricated on a (100) substrate and oriented along the [110] direction. This is due to the low oxide-interface-charge density and high electron mobility of this geometry [46, 47]. However, for p-type MOSFETs this is not the most advantageous geometry and hybrid orientations with other substrates and device orientations have been reported [48]. Uniaxial process induced strain can be engineered into the MOSFET's channel by using different techniques including embedded SiGe and SiC source and drain regions, nitride capping layers and stress memorisation technique (SMT) [44, 49-51]. Often, some of these techniques are combined in the same device to enhance the strain induced in a MOSFET's channel [52]. In order to enhance the effect of compressive strain in the channel, a compressive nitride capping layer can be used in combination with embedded SiGe source and drain regions. Figure 1.3 shows the schematic of uniaxial process induced strain in n-type and p-type MOSFETs using capping nitride layers as stressors.

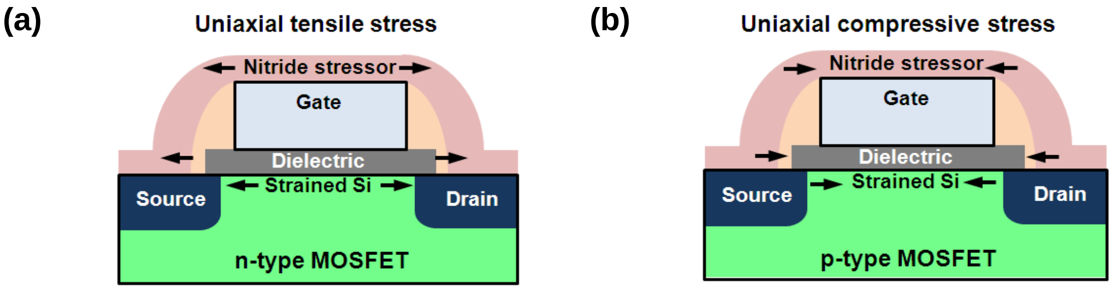

Figure 1.3 Uniaxial process induced strain using nitride capping layers as stressors. Stress is different for n-type and p-type MOSFETs. (a) Tensile strain induced into the channel of an n-type MOSFET. (b) Compressive strain induced into the channel of a p-type MOSFET.

For n-type MOSFETs, the nitride capping layer induces tensile strain whereas for p-type MOSFETs the deposition process is optimised such that it induces compressive strain. Figure 1.4 shows a transmission electron microscopy (TEM) picture of both an n-type and p-type MOSFET with a nitride capping layer (Figure 1.4a) and embedded SiGe source and drain regions (Figure 1.4b).

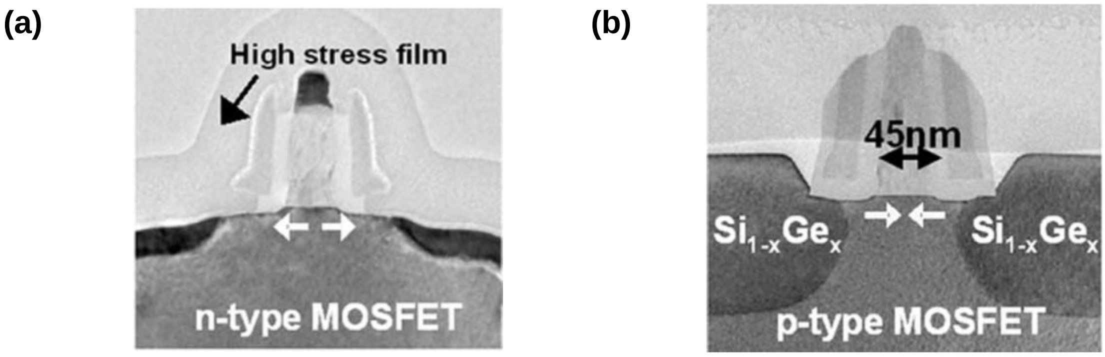

Figure 1.4 TEM images of (a) n-type MOSFET with uniaxial tensile induced strain using nitride capping stressors. (b) p-type MOSFET with uniaxial compressive induced strain using embedded $Si_{1-x}Ge_x$ source and drain regions. [42]

1.1.2.1 Impact of strain on the carrier mobility

Carrier mobility (electrons and holes) in Drude's model, is given by:

$$\mu = \frac{q_e \tau}{m^*}, \tag{1.1}$$

where q_e is the electronic charge, τ is the momentum relaxation time (average time for carriers to lose their original momentum due to a scattering event) and m^* is the carrier conductivity effective mass. From Equation 1.1, carrier mobility can be enhanced by reducing the scattering rate $1/\tau$ (number of times for a carrier to be scattered per unit time) or by reducing the carrier conductivity effective mass m^*. Different mechanisms contribute to alter the scattering rate including Coulomb scattering, phonon scattering and surface roughness scattering. Figure 1.5 shows the variation of the electron effective mobility with the vertical electric field in a MOSFET [53]. Each scattering mechanism predominates at a different electric field regime. Thus, whereas Coulomb scattering and phonon scattering predominate at low and medium electric fields, surface roughness scattering predominates at high electric fields. This is because at high vertical electric fields, electrons are highly attracted towards the surface (SiO_2/Si interface).

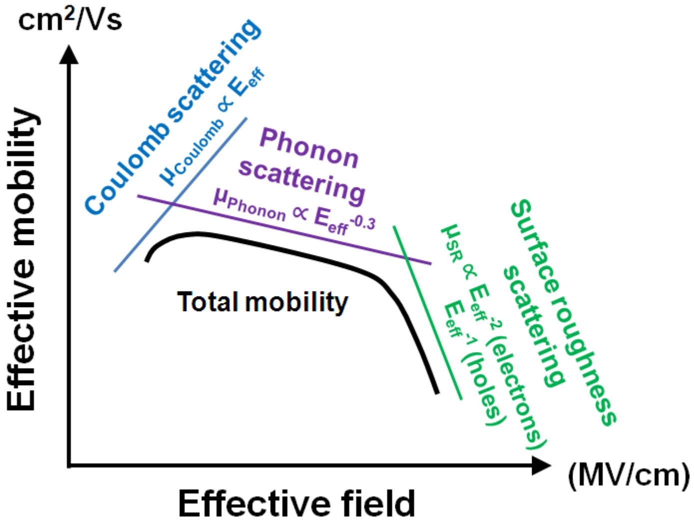

Figure 1.5 Effective mobility of electrons in a MOSFET inversion layer with the vertical electric field. Different scattering mechanisms predominate at low, medium and high electric fields. [12, 53]

Strain can enhance the mobility of electrons and holes by reducing both the scattering rate and the conductivity effective mass. This is accomplished by lowering the silicon crystal symmetry compared with bulk silicon [54]. Both uniaxial and biaxial strain alter the silicon band structure by splitting and/or warping the conduction and valence bands. Figure 1.6 shows the energy band structure of silicon in reciprocal space (***k*** space).

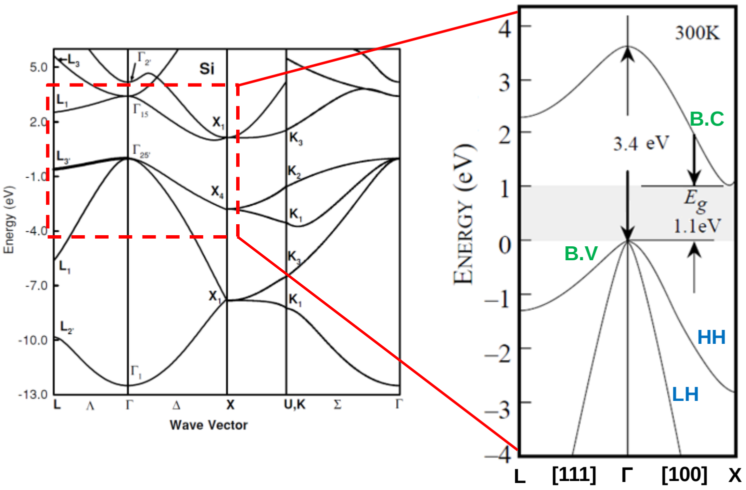

Figure 1.6 Band structure of silicon calculated using a semi-empirical (24-k·p) model. [55]

The silicon band structure exhibits a valence band maximum at the *Γ* point (***k*** = 0) and a conduction band minimum near the *X* point at ~0.85*X* along the <100> direction. The difference in energy between the conduction band minimum and the valence band maximum results in an indirect bandgap ~1.12 eV. There is also a direct bandgap at the *Γ* point ~3.4 eV [28].

The valence band maximum is composed by a heavy hole band (*HH*), a light hole (*LH*) band and a split-off (*SO*) band (Figure 1.7a). The split-off band is less important for hole transport since it is ~44 meV below the top of the valence band [11]. In unstrained silicon, the heavy hole band and the light hole band are degenerate at the *Γ* point. After applying biaxial tensile stress (Figure 1.7b) or uniaxial compressive stress (Figure 1.7c), the degeneracy is removed and the light and heavy hole bands split and warp. The splitting results in the light hole band being lifted and, as a consequence, preferentially occupied by the holes. This also reduces the intervalley scattering. The band warping results in a reduction of the conductivity effective mass of holes [56].

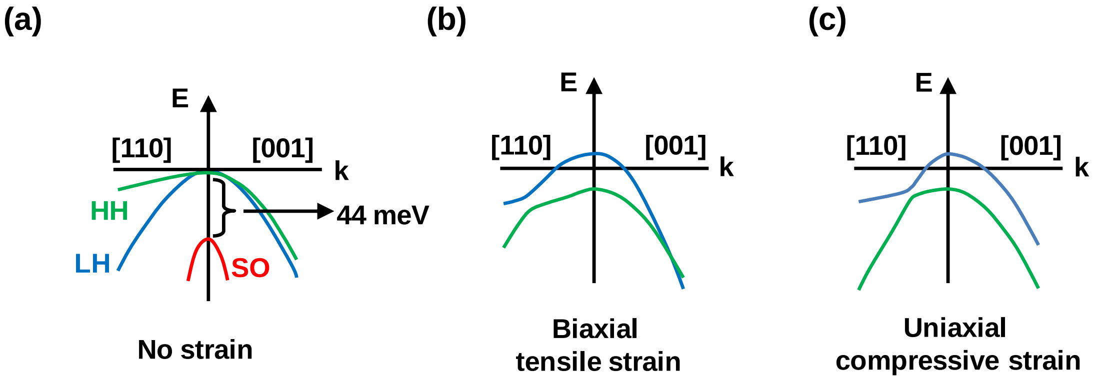

Figure 1.7 Valence band structures in silicon with (a) no strain, (b) biaxial tensile strain and (c) uniaxial compressive strain. [11, 54]

In bulk unstrained silicon, the conduction band minimum is composed of six degenerate valleys (Δ_6). These are surfaces of constant energy in three dimensions (ellipsoids in Figure 1.8). The conductivity effective mass m^* in Equation 1.1 is calculated from the harmonic average of the longitudinal m_l and transversal m_t effective masses contribution of each ellipsoid [57]:

$$m^* = \left[\frac{1}{3}\left(\frac{1}{m_l} + \frac{2}{m_t}\right)\right]^{-1} \tag{1.2}$$

In unstrained silicon, the longitudinal conductivity effective mass is $m_l = 0.98m_0$ and the transversal conductivity effective mass $m_t = 0.19m_0$ (here m_0 is the free electron mass). This results in a conductivity effective mass $m^* = 0.26m_0$ [57].

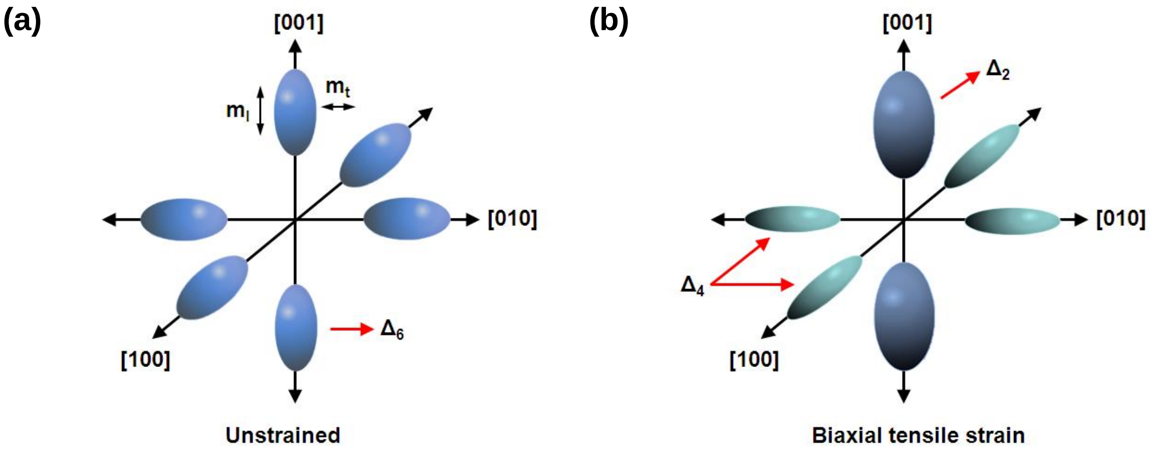

Figure 1.8 (a) Surfaces of constant energy (ellipsoids) in ***k*** space corresponding to the six minima conduction band valleys (Δ_6) in unstrained silicon. (b) After biaxial strain is applied, the six conduction band valleys split into four in-plane valleys (Δ_4) and two out-of-plane valleys (Δ_2).

After biaxial strain is applied, the degeneracy is removed and the six valleys split into 4 in-plane valleys (Δ_4) and two out-of-plane valleys (Δ_2) (Figure 1.8b). The energy of the out-of-plane valleys is lowered, and as a result, electrons prefer to populate the Δ_2 valleys. This has the benefit of reducing the inter-valley scattering. Also, for in-plane transport, electrons in the Δ_2 valleys experience a reduced conductivity mass $m_t = 0.19m_0$ compared with that of unstrained bulk silicon $m^* = 0.26m_0$ [12]. This reduction in the conductivity effective mass and intervalley scattering increases the in-plane electron mobility.

1.1.2.2 Electron mobility at the inversion layer

In n-type MOSFETs, application of a high vertical electric field (perpendicular to the channel) results in an electron inversion layer. In this situation, electrons are confined at the SiO_2/Si interface. This confinement results in the splitting of the degeneracy of the Δ_6

valleys. The smaller transversal conductivity effective mass $(m_t = 0.19m_0)$ of the Δ_4 valleys compared with that of the longitudinal conductivity effective mass $(m_l = 0.98m_0)$ of the Δ_2 valleys favours the Δ_4 occupancy. This raises the energy of the Δ_4 valleys compared with that of the Δ_2 valleys in a similar way as biaxial strain does [58]. Thus, any additional applied strain will only render minor or negligible energy shifts. Nevertheless, significant electron mobility enhancements in MOSFET devices at high electric field have been reported by using strained silicon channel transistors compared with unstrained channel transistors (Figure 1.9) [59-61]. Theoretical work suggests that mobility enhancement at the inversion layer may result from a reduction of the SiO_2/Si interface roughness scattering which is the main scattering mechanism at high electric fields (Figure 1.5) [58]. Nevertheless, experimental evidence is still needed.

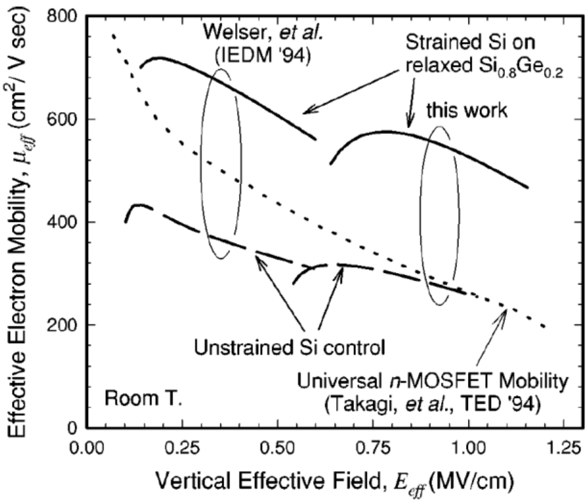

Figure 1.9 Electron mobility enhancement with the vertical effective field in strained silicon devices on relaxed $Si_{0.8}Ge_{0.2}$ compared with mobility in unstrained silicon devices. [61]

1.1.2.3 SiO_2/Si interface roughness

Rough surfaces originate from many fabrication processes including etching, film growth, and chemical mechanical polishing. The bulk (unstrained) SiO_2/Si interface roughness has been studied extensively theoretically and experimentally [62-66]. This is because the SiO_2/Si interface roughness is the main carrier scattering mechanism in the MOSFET inversion layer. In addition, it has been shown that many thin film surfaces, including the SiO_2/Si interface, exhibit scaling behaviour with the scale of observation (self-affinity) [67-69]. The concept of self-affinity is closely related to the mathematical description of fractal surfaces developed by Mandelbrot in the 1980s [70]. Before these studies, a surface profile was assumed to be a continuous and everywhere differentiable curve. Figure 1.10 shows the difference between the classical and fractal definition of a surface profile. In the classical definition of a surface profile, the continuous magnification of a region within the profile will eventually look flat. This is in contrast to the concept of a fractal surface, defined as a single-valued and nowhere-differentiable curve. However, despite the significant effort dedicated to study the SiO_2/Si interface roughness, to date there is no experimental investigation of the scaling behaviour of the strained SiO_2/Si interface roughness. Without proper understanding and measurement of strained silicon surface roughness, device performance cannot be explained.

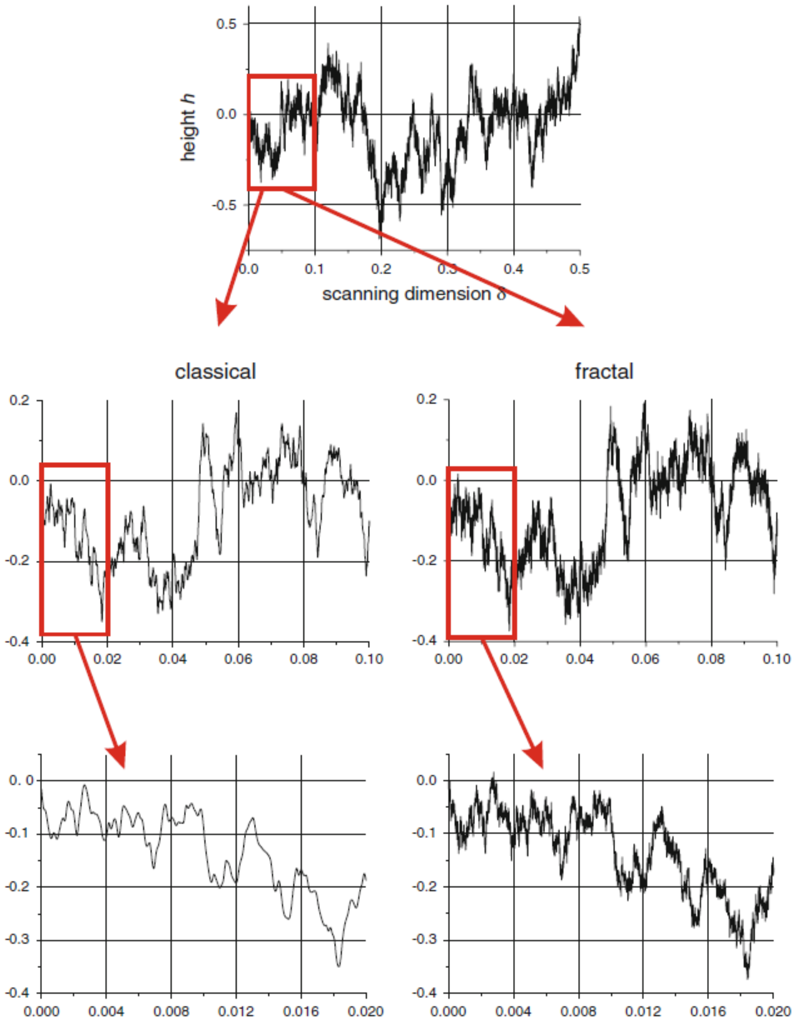

Figure 1.10 Classical and fractal definitions used to describe a random surface profile. [71]

1.2 Characterisation techniques

1.2.1 Surface roughness characterisation

Common techniques used to characterise the roughness of a surface include surface profilometry, scanning tunnelling microscopy (STM) and atomic force microscopy (AFM). Surface profilometry is a non-destructive technique which uses a sharp tip in contact with the surface of the sample. It measures the deflection of the tip as it moves along the height profile of the sample. The deflection is recorded and converted to an electrical signal. It can measure areas as large as 300 mm although the lateral resolution is limited to $\sim 0.05 - 0.15$ μm [68]. STM is a type of scanning probe microscope (SPM) which offers atomic resolution. It was developed by Binnig *et al.* in 1981 [72]. It uses a very sharp conductive tip which scans the surface of a conductive sample at a very close distance (~ 1nm). The application of a bias voltage between the sample and the tip results in a tunnelling current which varies depending on the tip-sample spacing. The tunnelling current is recorded and used to form a 3D image of the surface topography. However, in order to have a current to flow from the tip to the sample, samples must be conductive. Based on the STM, Binnig *et al.* developed the AFM in 1986 [73]. The AFM operates by measuring the deflection of the tip of a cantilever due to the attractive and repulsive atomic forces between the tip and the sample. It renders atomic resolution and both conductive and non-conductive samples may be used. In this work AFM is used to characterise the surface topography of the samples.

1.2.2 Strain characterisation

In order to study the surface of a strained material, it is necessary to know the magnitude and type (tensile or compressive) of strain in the material under investigation. A large range of techniques are used to investigate strain in silicon structures. Some common techniques are X-ray diffraction (XRD) [74], transmission electron microscopy (TEM) and convergent beam electron diffraction (CBED) [75-77]. However, not all of those are suitable for nanoscale analysis. XRD is a non-destructive technique which requires limited effort in sample preparation and can directly measure strain from a crystalline lattice, but its spatial resolution is limited to several micrometers and requires large sample areas.

TEM and CBED provide high resolution measurements but require time-consuming, destructive sample preparation. Raman spectroscopy is a widely used technique to characterise strain. It is non-destructive, requires little or no sample preparation and has a good spatial resolution (below 1 μm). Strain is determined by measuring the inelastic scattering of light resulting from a laser beam focused onto a sample. However, to date, the strain-shift coefficient used to convert Raman shifts to strain has not been validated for structures at the nanometre scale. This prevents accurate evaluation of strain at the nanoscale.

The strain-shift coefficient depends on multiple factors including phonon deformation potentials (PDPs). PDPs have been reported for silicon which differ by 30% [78-80]. This leads to varying strain-shift coefficients. Using the wrong strain-shift coefficient affects the strain determined. The discrepancies in the reported PDPs were previously ascribed to surface stress relaxation and the opacity of the material to the laser radiation [80, 81]. Previous experiments to determine PDPs and strain-shift coefficients in silicon have been limited to bulk material and stress only in the range 0 – 2 GPa. However, state-of-the art devices use nanowires and thin films under large values of stress. Therefore with the aforementioned changes of the silicon properties at the nanoscale (section 1.1.1), it is necessary to accurately determine the strain-shift coefficient in silicon nanowires and thin films under large values of stress. This is a major aim of this work.

1.3 On-chip tensile testing technique

In order to study the impact of strain on the material properties at the micro- and nano-scale, several types of devices based in MEMS and NEMS have been proposed [33, 82-84]. However, these testing devices often have complex designs which complicate the stress-strain analysis. Also, sample manipulation, gripping and misalignment issues are frequently encountered. As a consequence, the range of strain, geometries and number of samples investigated is greatly reduced.

In this work, a novel on-chip technique which allows multiple structures with different geometries and strain values to be characterised from a single batch with no sample preparation and manipulation is presented. Strain values ranging from 0 to 3.6% equivalent to an applied stress of ~6 GPa in silicon have been investigated. Strain is measured by visual and direct inspection of the elongation of the samples using SEM. This has been made possible by implementing a pair of cursors at the ends of each sample. Raman spectroscopy and SEM are used to characterise strain and the measurements are compared with analytical calculations. The combination of these techniques and the large number of samples (up to 85) has allowed the accurate determination of the strain-shift coefficient along the <110> direction for the technologically important (100) silicon surface. The impact of the surface-to-volume ratio on the mechanical properties of silicon is studied by analysing the Young's modulus and fracture strain. Surface effects are analysed with Raman spectroscopy by using a UV laser characterised by a low penetration depth and comparing results with a visible laser which penetrates the entire thickness of the silicon samples. In addition, the discrepancy between the Raman shifts measured using the UV and visible lasers is used to investigate the thermal conductivity in strained silicon for different geometries. Finally, the accurate determination of strain in the nanostructures has allowed the study of the evolution of the silicon surface roughness with uniaxial strain. The results have been compared with the analysis of the silicon surface roughness evolution with biaxial strain in SOI samples.

1.4 Thesis outline

The thesis is organised as follows. Chapter 2 describes the crystal structure of silicon and presents the theory of elasticity. The mathematical analysis for tensor transformations is also presented. The chapter ends with a description of the mechanical and thermal properties in silicon.

Chapter 3 describes the principles of AFM and Raman spectroscopy and details the instrumentation set-up used in this project.

In Chapter 4, a detailed analysis of the principles of the on-chip tensile testing structures and the results of finite element simulations are presented. The geometry of the samples and the fabrication process are also described. Results of strain extracted using Raman shifts and SEM images of the structures are presented alongside with a discussion of the accuracy of the analysis. The experimental data is compared with the analytical calculations and finite element simulations. The range of elasticity in silicon is evaluated alongside other experimental and theoretical work. The chapter also investigates the dependency of Young’s modulus and fracture strain with sample geometry. The role of the surface in the size dependent physics is analysed and the impact of strain on the thermal conductivity of silicon is discussed.

Chapter 5 deduces the longitudinal and transversal optical strain-shift coefficients in silicon. The theory and background for determining strain-shift coefficients and their relation with PDPs is given. A thorough discussion of the factors affecting these values and a comparison with other reported strain-shift coefficients are presented.

Chapter 6 uses the values of strain in the nanostructures to accurately evaluate the evolution of surface roughness with strain. Both biaxial and uniaxial samples are studied. The theory of self-affine surfaces and the parameters required to characterise the roughness of a self-affine surface are discussed. The geometries, fabrication details of the wires and thin films and the AFM multiple scan technique are also described. The results of the AFM surface roughness measurements in the strained wires and thin films are detailed. An analysis of the validity of the functional models used to fit the experimental data of a surface roughness profile is given. A discussion of the parameters dependency with strain is also presented.

Chapter 7 summarises the main conclusions of the work. Future investigations are described arising from the results of the research carried out.

Chapter 2. Background

2.1 Introduction

This thesis investigates the impact of strain on silicon nanostructures. In this chapter, the crystal structure of silicon in real and reciprocal space (section 2.2) and the theory of elasticity (section 2.3) are briefly reviewed. The theory of elasticity, i.e. the deformation (or strain) produced by a mechanical stress is formulated in tensorial notation more appropriate to describe the properties of anisotropic materials such as silicon. In these materials, the physical properties may vary depending upon the crystal direction in which they are measured. Tensors are a convenient mathematical tool to describe the physical properties of a material regardless of the direction of measurement of the physical property. The physical quantities which define a specific physical property, such as strain and stress define the elasticity, are also fully described by tensors. In section 2.3.1, a brief description of the concept of tensors and the notations used in this thesis will be presented. The strain and stress tensors will be introduced in sections 2.3.2 and 2.3.3. The relation between the strain and stress in the elastic regime (Hooke's law) and the different parameters extracted from a stress-strain curve in a tensile test will be presented in sections 2.3.4 and 2.3.5.The chapter will finish with a description of the mechanical and thermal properties of silicon studied in this work, i.e. fracture strain, Young's modulus, and thermal conductivity (sections 2.3.6, 2.3.7 and 2.4).

2.2 The silicon crystal structure

2.2.1 Crystal lattices

The crystal structure of a material is formed by the periodic arrangement of atoms. This arrangement is created by repeating a basis, formed by one or more atoms, within a lattice (Figure 2.1).

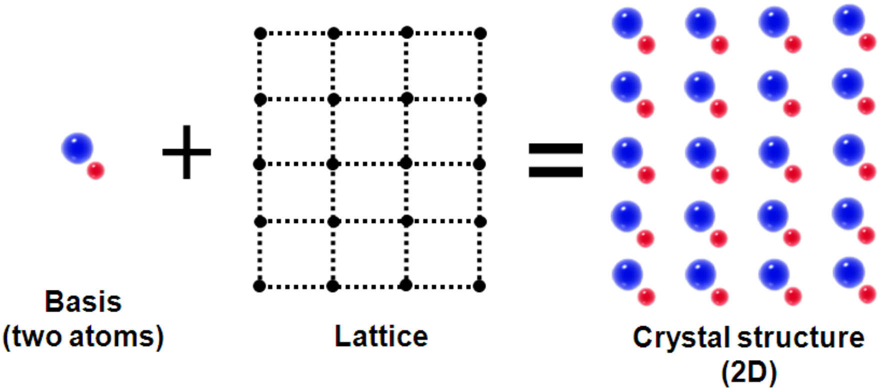

Figure 2.1 The periodic repetition of the basis within a lattice results in the final crystal structure. In this case, the basis is formed by two atoms of different species and the lattice is a two dimensional lattice.

In three dimensions, the crystal structure is obtained after the periodic repetition of a unit cell. Unit cells can be primitive or non-primitive. A non-primitive unit cell, also called conventional unit cell, is larger than a primitive unit cell. A primitive unit cell is that of minimum volume and is not unique. Many semiconductors including silicon and germanium crystallise in the diamond structure which belongs to the cubic system. Figure 2.2 shows the conventional unit cell of a face-centred cubic crystal and its primitive unit cell.

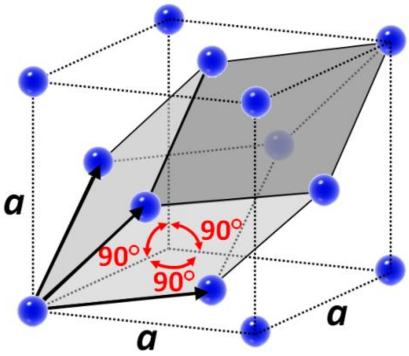

Figure 2.2 The conventional face-centred cubic crystal structure and the primitive unit cell (shaded). A set of primitive vectors is also shown (arrows).

2.2.2 The zincblende / diamond structure

The zincblende and diamond structures are face centred cubic crystal structures with two atoms per basis and tetrahedral bonding. These structures can also be seen as two interpenetrating face centred cubic lattices with one atom per basis each, with one of the lattices displaced one quarter from the cube diagonal (Figure 2.3a). In the diamond structure however, the two atoms are from the same species and are indistinguishable in the final structure (Figure 2.3b). The lattice constant in silicon is a_{Si} = 5.43 Å and the distance between neighbour atoms (bond length) is $\frac{a_{Si}\sqrt{3}}{4} = 2.35$ Å.

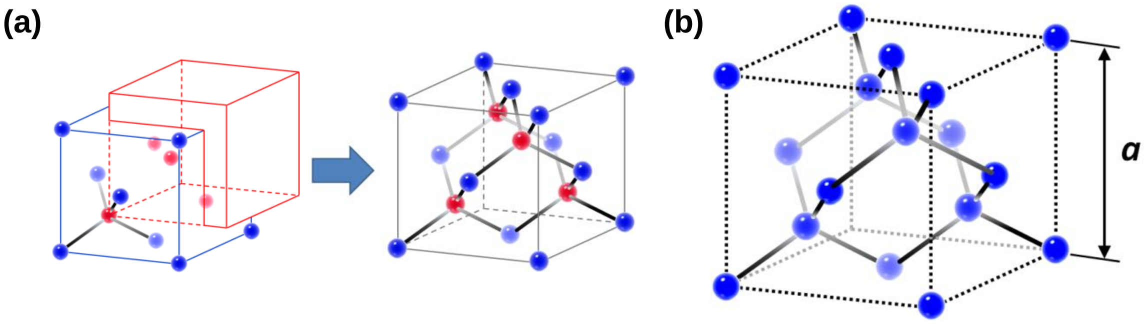

Figure 2.3 (a) The zincblende and diamond structures are formed by two interpenetrated face-centred cubic structures. This, results in two atoms per basis (each red-blue pair) tetrahedrally bonded. In the diamond structure (b) all the atoms are from the same species and thus indistinguishable.

2.2.3 Crystal planes and Miller indices

In crystallography, Miller indices are used to describe directions and planes. Miller indices describing a crystallographic direction are represented with three integers [*hkl*] enclosed in square brackets. For the cubic system, the three integers *h*, *k* and *l* are the normalised vector components of the direction resolved along the main crystallographic axes. A small bar above the component is used to represent negative values. Figure 2.4a shows some important directions for the cubic system.

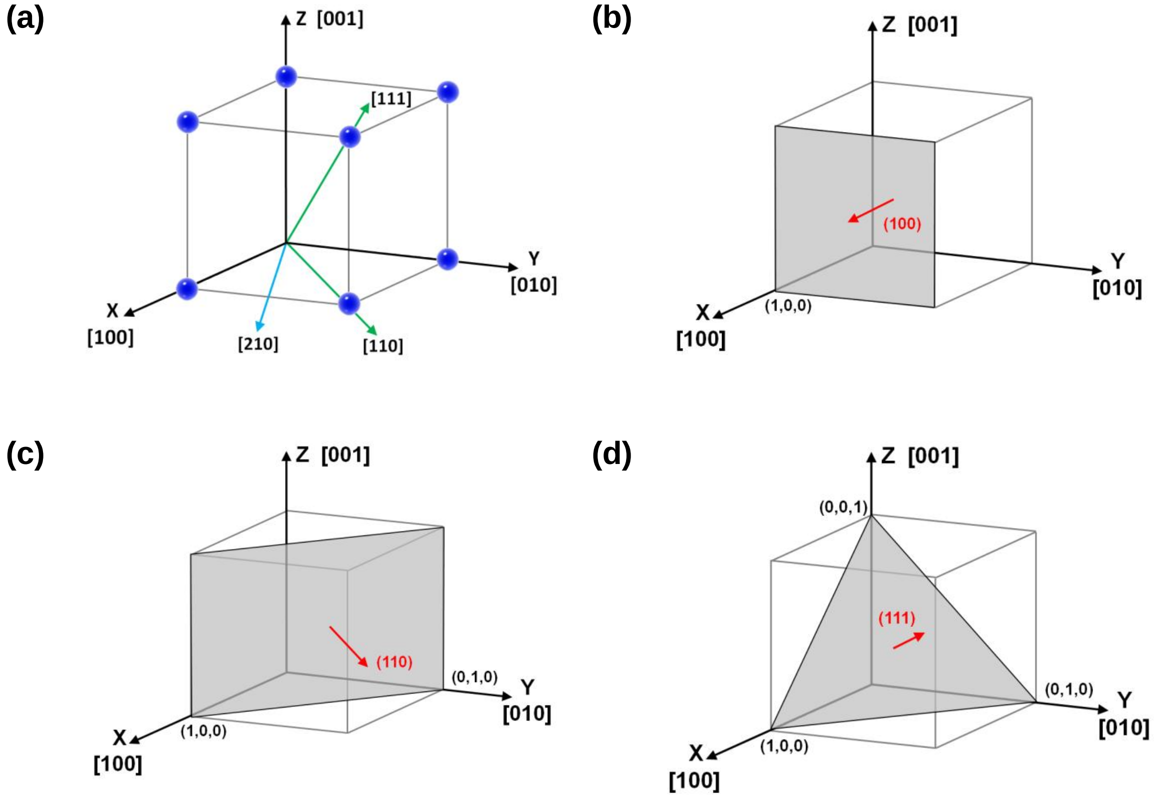

Figure 2.4 (a) Important crystallographic directions for the cubic system. (b) (100) plane (c) (110) plane (d) (111) plane

For planes, the three integers *h*, *k* and *l* relate to the components of a vector normal to the plane and are enclosed in parentheses.

Figure 2.4b-d shows the main crystallographic planes (100), (110) and (111). In addition, groups of equivalent directions such as [100], [010] and [001] are expressed using angle brackets e.g. <100> and groups of equivalent planes such as (100), (010) and (001) are expressed using curly brackets e.g. {100}.

2.2.4 The reciprocal lattice

The reciprocal lattice is defined as the set of wave vectors in ***k***-space**,** which results in plane waves with the same periodicity as a given periodic arrangement of atoms in real space.

The reciprocal lattice of a face-centred cubic crystal structure is a body-centred cubic (*bcc*). The *bcc* however, is not a primitive unit cell. The truncated dodecahedron depicted in Figure 2.5 is a special primitive cell which in reciprocal space is called the Brillouin zone. The Brillouin zone has all the symmetries of the crystal structure. High symmetry points and lines inside the Brillouin zone are conventionally denoted with Greek letters. Points at the surface are represented with Roman letters. The centre of the Brillouin zone is always denoted with the Greek letter Γ.

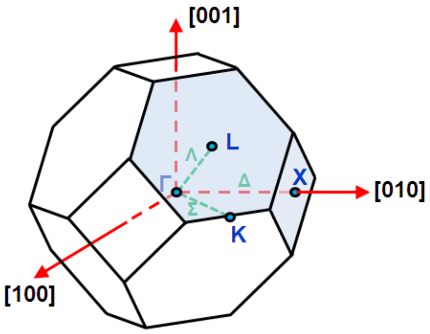

Figure 2.5 The truncated dodecahedron in reciprocal space is known as the Brillouin zone. The centre of the Brillouin zone is represented by the Greek letter gamma (*Γ*). Other important symmetry points and directions are (*X, K, L*) and (*Δ, Σ, Λ*) respectively.

2.3 Elasticity theory

Elasticity is the property of a solid body to recover its original shape upon the removal of the forces originating the deformation. The forces acting on a solid body can be classified as body forces and surface forces. Body forces are those which act on a volume of the body e.g. gravity. In contrast, surface forces are forces which act over the surface of the body e.g. pressure. Since body and surface forces are proportional to the volume and area respectively on which they act, body forces will be significantly smaller compared with surface forces for an infinitesimal volume.

Crystals are generally anisotropic with respect to their properties. The value of a specific property may differ depending upon the direction of measurement. In order to study the physical and mechanical properties of a crystal, tensor analysis is a very convenient mathematical tool.

2.3.1 The concept of a tensor

A tensor is a physical quantity whose components transform according to some specific transformation laws [85]. Tensors are classified according to their rank. Zero rank tensors are called scalars and have magnitude but no direction. First order rank tensors are called vectors and have magnitude and one direction. Second order rank tensors are called dyads and have magnitude and two directions. In general, an *nth* order tensor will have a magnitude and *n* directions. The components of a tensor are conveniently represented by matrices. However, in order for the components of a matrix to represent a tensor, they must transform according to the transformation laws of tensors. The transformation laws of tensors specify how the tensor components which are expressed in a set of orthogonal axes transform to another set of orthogonal axes (with the same origin). Tensors of zero order (scalars) however, are independent of the set of orthogonal axes being chosen. The transformation laws for tensors of first, second, third and fourth ranks are given in Equations 2.1 - 2.4. The coefficients $a_{i\leftrightarrow j}$ in Equations 2.1 - 2.4 are the direction cosines of the angles between the axis *i* in the new set of axes, and the axis *j* in the current axes. The value of each subscript relates to one of the three orthogonal axes (i, j = 1, 2, 3). T'_i, T'_{ij}, T'_{ijk} and T'_{ijkl} are the components of the tensor in the new axes and T_j, T_{kl}, T_{lmn} and T_{mnop} are the components of the tensor in the current axes.

First order: $$T'_i = \sum_{j=1}^{3} a_{i\leftrightarrow j} T_j \quad (i = 1,2,3) \tag{2.1}$$

Second order: $$T'_{ij} = \sum_{k=1}^{3}\sum_{l=1}^{3} a_{i\leftrightarrow k} a_{j\leftrightarrow l} T_{kl} \quad (i,j = 1,2,3) \tag{2.2}$$

Third order: $$T'_{ijk} = \sum_{l=1}^{3}\sum_{m=1}^{3}\sum_{n=1}^{3} a_{i\leftrightarrow l} a_{j\leftrightarrow m} a_{k\leftrightarrow n} T_{lmn} \quad (i,j,k = 1,2,3) \tag{2.3}$$

Fourth order: $$T'_{ijkl} = \sum_{m=1}^{3}\sum_{n=1}^{3}\sum_{o=1}^{3}\sum_{p=1}^{3} a_{i\leftrightarrow m} a_{j\leftrightarrow n} a_{k\leftrightarrow o} a_{l\leftrightarrow p} T_{mnop} \quad (i,j,k,l = 1,2,3) \tag{2.4}$$

The tensors components in Equations 2.1 - 2.4 are expressed in full tensor notation. In this thesis, full tensor notation (in italic) will be used when the components of the tensor need to be explicit. A simplified notation, particularly suitable for symmetric tensors, known as Voigt notation (not in italic), will be also introduced in section 2.3.4.

2.3.2 The stress tensor

Figure 2.6 depicts a body in static equilibrium under the action of external forces. The body undergoes a deformation due to the reaction of the internal forces to the external forces.

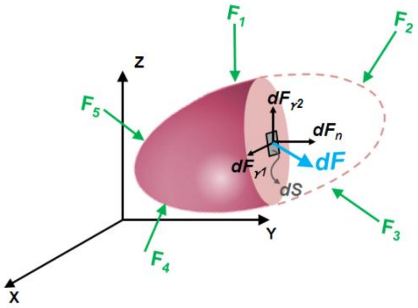

Figure 2.6 Body in static equilibrium under the action of external forces. As a result of the internal forces reacting to the external forces, the infinitesimal area *dS* will undergo stress.

Considering an infinitesimal area dS and a net force $d\boldsymbol{F}$ acting upon it, the stress $\boldsymbol{\zeta}$ undergone by the area dS, is defined as:

$$\boldsymbol{\zeta} = \frac{d\boldsymbol{F}}{dS} \tag{2.5}$$

The stress vector $\boldsymbol{\zeta}$ undergone by the area dS, can be split into three components, a normal component due to the force ($d\boldsymbol{F}_{\boldsymbol{n}}$) acting perpendicular to the area, and two shear components due to the forces ($d\boldsymbol{F}_{\gamma 1}$, $d\boldsymbol{F}_{\gamma 2}$) acting tangential to the area. The stress defined in Equation 2.5, depends on the plane of the area dS. For any arbitrary plane defined by its normal vector $\boldsymbol{n}_{\boldsymbol{j}}$ passing through a point of the body, Cauchy's stress theorem [86], states that the stress can be completely described in terms of three stress vectors acting on mutually orthogonal planes. Figure 2.7 shows the components of the stress vectors acting on the faces of an infinitesimal cube of the body.

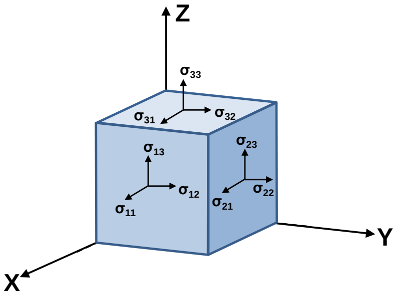

Figure 2.7 Stress components in an infinitesimal cube within a body. The stress components σ_{11}, σ_{22}, σ_{33} are the normal components and the components σ_{12}, σ_{13}, σ_{21}, σ_{23}, σ_{31}, σ_{32} are the shear (tangential) components.

The nine stress components can be expressed in matrix notation as:

$$[\sigma_{ij}] = \begin{bmatrix} \sigma_{11} & \sigma_{12} & \sigma_{13} \\ \sigma_{21} & \sigma_{22} & \sigma_{23} \\ \sigma_{31} & \sigma_{32} & \sigma_{33} \end{bmatrix}, \qquad (2.6)$$

where the components σ_{11}, σ_{22}, σ_{33} are the normal components of the stress and the components σ_{12}, σ_{13}, σ_{21}, σ_{23}, σ_{31}, σ_{32} are the shear or tangential components. From the assumption of the body in static equilibrium, it can be seen that the stress shear components are:

$$\begin{aligned} \sigma_{12} &= \sigma_{21} \\ \sigma_{13} &= \sigma_{31} \\ \sigma_{23} &= \sigma_{32} \end{aligned} \qquad (2.7)$$

The stress components given in Equation 2.6, relate the components of the stress vector $\boldsymbol{\zeta}$ (acting on the area dS) with the components of the vector $\boldsymbol{n}$ (normal to the plane of the area dS) as:

$$\zeta_i = \sum_{j=1}^{3} \sigma_{ij} n_j \quad (i = 1, 2, 3) \qquad (2.8)$$

The components of σ_{ij} transform like a second rank tensor [85] and tensor transformation rules (Equation 2.2) may be applied to express the stress in any particular set of orthogonal axes. Thus, $\boldsymbol{\sigma}$ is called the stress tensor. An important property of the stress tensor is that it is symmetric with respect to the diagonal elements (Equation 2.7), i.e. $\sigma_{ij} = \sigma_{ji}$.

2.3.3 The strain tensor

Most engineering materials, including steel, aluminium and silicon, undergo small deformations. In order to study the deformation in these materials, the infinitesimal strain theory is particularly suitable. In the infinitesimal strain theory (opposed to the finite strain theory), only small deformations are considered. This simplification requires changes in length to be small compared with the body dimensions. In this section, only small deformations are considered.

When a body undergoes a deformation, the internal and external points of the body rearrange and displace to new positions. Figure 2.8 shows two arbitrary points P and Q in a body in an undeformed state (solid line). After undergoing a deformation (dashed line), the points displace to the positions P’ and Q’. The displacement undergone by the points P and Q is expressed by the displacement vectors $\boldsymbol{u_p}(u_{px}, u_{py})$ and $\boldsymbol{u_q}(u_{qx}, u_{qy})$. In general, the deformed state of a body can be expressed as a function of the displacement undergone by all the points of the body with respect to the undeformed state. This constitutes the displacement vector field $\boldsymbol{u}(u_x, u_y, u_z)$. The displacement of points P and Q to the positions P’ and Q’ could also originate from a pure body translation or rotation (or combination of both displacements) with no deformation. Therefore, knowledge of the relative displacements between points rather than individual displacements is required in order to study the deformation of a body. The total deformation of the body may be studied as changes in lengths (distance of separation between two points) and angles (rotation of the segments connecting two points).

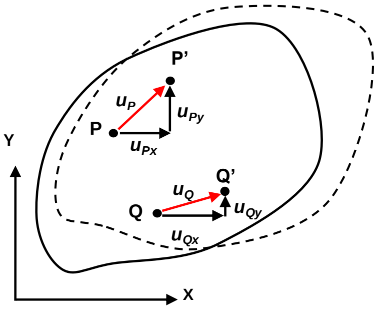

Figure 2.8 A body in an undeformed state (solid line) and deformed state (dashed line). Two arbitrary points P and Q in the undeformed state move to new positions P’ and Q’ after undergoing a deformation. The displacement experienced by the points P and Q is expressed by the vector displacements $\boldsymbol{u_p}$ and $\boldsymbol{u_q}$.

Figure 2.9 shows a small element with dimensions dx, dy before (solid lines) and after (dashed lines) undergoing a small deformation. After deformation, the lengths and angles of the element experience a change in magnitude compared with those in the undeformed state.

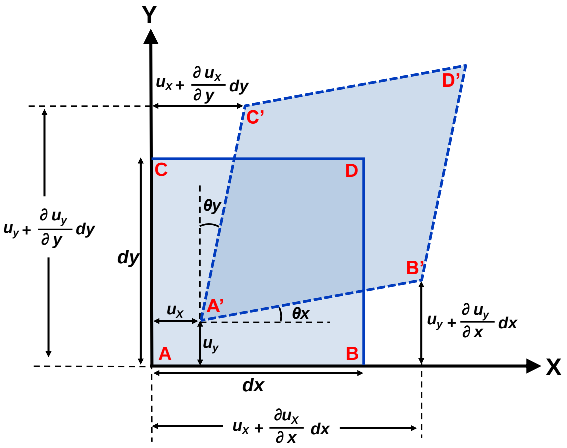

Figure 2.9 Deformation undergone by a small rectangular element (solid line) with lengths dx × dy. The lengths and angles of the element undergo a change in magnitude after deformation (dashed line).

The changes in lengths are described by the longitudinal (or normal) strain and the changes in angles by the shear strain.

The normal strain undergone by two points of a body in a particular direction is defined as the change in distance between the two points per unit length (with respect to the original distance). Thus, from Figure 2.9, the normal strain undergone by the two adjacent points A and B along the *x* direction is:

$$\varepsilon_x = \frac{\left(u_x + \frac{\partial u_x}{\partial x} dx - u_x\right)}{dx} = \frac{\partial u_x}{\partial x} \tag{2.9}$$

Here, the partial derivatives arise from the first order Taylor expansion (second and higher products are neglected) of the small displacement $u(u_x+dx)$, undergone by point B.

Similar expressions are obtained for the normal strain undergone along the y and z directions. Thus for a three dimensional small element, the normal strain along the x, y and z coordinates is defined as:

$$\varepsilon_x = \frac{\partial u_x}{\partial x}, \quad \varepsilon_y = \frac{\partial u_y}{\partial y}, \quad \varepsilon_z = \frac{\partial u_z}{\partial z} \tag{2.10}$$

The shear strain is defined as the change in radians undergone by a rectangular angle between two linear elements (in the undeformed state). With reference to Figure 2.9 the change in angle experienced by the rectangular angle $\widehat{CAB}$ is:

$$\gamma_{xy} = \gamma_{yx} \approx \frac{\left(u_y + \frac{\partial u_y}{\partial x}dx - u_y\right)}{dx} + \frac{\left(u_x + \frac{\partial u_x}{\partial y}dy - u_x\right)}{dy} = \frac{\partial u_y}{\partial x} + \frac{\partial u_x}{\partial y}, \tag{2.11}$$

where the approximations $\theta_x \approx \tan(\theta_x)$ and $\theta_y \approx \tan(\theta_y)$ have been used for small angle deformations. Similar expressions are obtained for the shear strains $\gamma_{xz} = \gamma_{zx}$ and $\gamma = \gamma_{zy}$. Thus for a three dimensional small element, the shear strain in the planes xy, xz and yz is defined as:

$$\begin{gathered}
\gamma_{xy} = \gamma_{yx} = \frac{\partial u_x}{\partial y} + \frac{\partial u_y}{\partial x} \\
\gamma_{xz} = \gamma_{zx} = \frac{\partial u_x}{\partial z} + \frac{\partial u_z}{\partial x} \\
\gamma_{yz} = \gamma_{zy} = \frac{\partial u_y}{\partial z} + \frac{\partial u_z}{\partial y}
\end{gathered} \tag{2.12}$$

The nine strain components (Equations 2.10 and 2.12) can be expressed in matrix notation as:

$$[e_{ij}] = \begin{bmatrix} \varepsilon_x & \gamma_{xy} & \gamma_{xz} \\ \gamma_{yx} & \varepsilon_y & \gamma_{yz} \\ \gamma_{zx} & \gamma_{zy} & \varepsilon_z \end{bmatrix} \tag{2.13}$$

The components of $[e_{ij}]$ however, do not transform like a second rank tensor [85](Equation 2.2). In order to transform as a second rank tensor, the shear strain components are modified as:

$$\varepsilon_{xy} = \varepsilon_{yx} = \frac{1}{2}\gamma_{xy}, \qquad \varepsilon_{xz} = \varepsilon_{zx} = \frac{1}{2}\gamma_{xz}, \qquad \varepsilon_{yz} = \varepsilon_{zy} = \frac{1}{2}\gamma_{yz} \tag{2.14}$$

This results in the strain tensor:

$$\varepsilon_{ij} = \begin{bmatrix} \varepsilon_{11} & \varepsilon_{12} & \varepsilon_{13} \\ \varepsilon_{21} & \varepsilon_{22} & \varepsilon_{23} \\ \varepsilon_{31} & \varepsilon_{32} & \varepsilon_{33} \end{bmatrix} \qquad i, j = 1, 2, 3 \tag{2.15}$$

where the subscripts x, y and z in Equations 2.13 and 2.14 have been replaced by the numerical subscripts 1, 2 and 3 respectively in Equation 2.15. Similar to the stress tensor, the strain tensor is also symmetric with respect to the diagonal elements. i.e. $\varepsilon_{ij} = \varepsilon_{ji}$

2.3.4 Hooke's law

Hooke's law states that within the elastic regime of a material, the strain is proportional to the applied stress. In full tensor notation, Hooke's law may be written as:

$$\varepsilon_{ij} = \sum_{k=1}^{3} \sum_{l=1}^{3} S_{ijkl} \sigma_{kl} \qquad i, j = 1, 2, 3 \tag{2.16}$$

Here, S_{ijkl} are the components of a fourth rank tensor called the compliance coefficient tensor. As Equation 2.16 indicates, every strain component is a linear combination of the nine components of the stress tensor.

Alternatively, Hooke's law can be written as:

$$\sigma_{ij} = \sum_{k=1}^{3} \sum_{l=1}^{3} C_{ijkl} \varepsilon_{kl} \qquad i, j = 1, 2, 3 \tag{2.17}$$

where C_{ijkl} are the components of a fourth rank tensor called the stiffness coefficient tensor.

Both tensors S_{ijkl} and C_{ijkl} have 81 coefficients. Due to the large number of coefficients involved in the compliance and stiffness tensors, a more concise notation is often used. This notation, known as Voigt notation [85], benefits of the symmetry of some tensors to reduce each pair of suffixes to one according to the convention:

$$11 \rightarrow 1, \quad 22 \rightarrow 2, \quad 33 \rightarrow 3, \quad 23, 32 \rightarrow 4, \quad 31, 13 \rightarrow 5, \quad 12, 21 \rightarrow 6$$

Due to the symmetry of the stress and strain tensors, the number of coefficients of S_{ijkl} and C_{ijkl} reduce to 36 independent coefficients. Also, if crystal symmetries are considered, the numbers of independent coefficients may reduce even further. Thus, in case of silicon, the high symmetry of the cubic system reduces the number of components of S_{ijkl} and C_{ijkl} to only 3 independent components. Using Voigt notation, Hooke's law (for cubic crystals) reads as:

$$\begin{bmatrix} \varepsilon_1 \\ \varepsilon_2 \\ \varepsilon_3 \\ \varepsilon_4 \\ \varepsilon_5 \\ \varepsilon_6 \end{bmatrix} = \begin{bmatrix} S_{11} & S_{12} & S_{12} & 0 & 0 & 0 \\ S_{12} & S_{11} & S_{12} & 0 & 0 & 0 \\ S_{12} & S_{12} & S_{11} & 0 & 0 & 0 \\ 0 & 0 & 0 & S_{44} & 0 & 0 \\ 0 & 0 & 0 & 0 & S_{44} & 0 \\ 0 & 0 & 0 & 0 & 0 & S_{44} \end{bmatrix} \begin{bmatrix} \sigma_1 \\ \sigma_2 \\ \sigma_3 \\ \sigma_4 \\ \sigma_5 \\ \sigma_6 \end{bmatrix} \tag{2.18}$$

The correspondence between the coefficients S_{ij} expressed in Voigt notation and the coefficients S_{ijkl} expressed in full tensor notation is [85]:

$$\begin{aligned} S_{11} &= S_{1111} = S_{2222} = S_{3333} \\ S_{12} &= S_{2233} = S_{3322} = S_{1133} = S_{3311} = S_{1122} = S_{2211} \\ S_{44} &= 4S_{2323} = 4S_{3131} = 4S_{1212} \end{aligned} \tag{2.19}$$

Table 2.1 lists the stiffness and compliance coefficients in silicon from [87] and [88].

2.3.5 Stress-strain curve

In order to investigate the strain deformation of a material with different levels of stress, tension tests are often performed. In these tests, a specimen is loaded under tensile stress and the sample elongation is measured. Stress is gradually increased up to the fracture of the sample. Figure 2.10 shows a typical stress-strain diagram for a ductile and a brittle material.

Table 2.1 Silicon stiffness and compliance coefficients

Stiffness coefficients [87] (Pa)	$C_{11} = 165.6 \times 10^9$ $C_{12} = 63.94 \times 10^9$ $C_{44} = 79.51 \times 10^9$
Compliance coefficients [88] (Pa^{-1})	$S_{11} = 7.67 \times 10^{-12}$ $S_{12} = -2.14 \times 10^{-12}$ $S_{44} = 12.6 \times 10^{-12}$

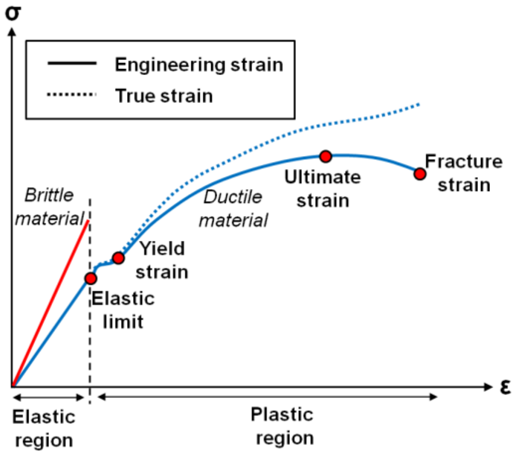

Figure 2.10 Stress-strain diagram of a brittle and a ductile material. Brittle materials show a linear proportion between stress and strain up to the fracture. Ductile materials possess a plastic region. For stress values above the elastic limit, the materials experience permanent deformations.

Brittle materials show a linear relationship between stress and strain for all values of applied stress and they exhibit no plastic deformation. In contrast, plastic materials exhibit plasticity before fracture occurs. In these materials permanent deformation occurs after the applied stress exceeds the elastic limit, i.e. after the stress causing the deformation is released, the material no longer recovers its original shape. In the plastic region however, deformation is large and the small deformation assumption used for the normal strain definition (engineering strain) given in section 2.3.3 is not longer valid. In this region, the logarithmic definition of strain (true strain) is better suited. The logarithmic strain is determined by integrating the changes in length from the initial length up to the final length:

$$\varepsilon = \int_{L_0}^{L_F} \frac{dl}{l} = ln\left(\frac{L_F}{L_0}\right) = ln\left(\frac{L_0 + \Delta L}{L_0}\right) \tag{2.20}$$

2.3.6 Yield strain, ultimate strain and fracture strain

As shown in Figure 2.10, the yield strain is the point at which the material starts to undergo a permanent deformation. Due to the difficulty of a precise determination of the yield point, it is often quoted as the stress value at which a permanent 0.2% of strain deformation is obtained [89].

The ultimate strain point relates to the strain value at which the maximum engineering stress is obtained. From that point, the actual cross-section of the material under test starts to decrease and lower stress values are required in order to further deform the material. As shown in Figure 2.10, the engineering definition of stress significantly differs from that of the true stress at high values of strain. This is because the engineering definition of stress uses the original cross-section to determine the stress whereas the true stress definition uses the actual cross-section [89]. At low values of strain, the engineering stress and the true stress are almost equivalent.

The fracture strain relates to the maximum value of strain obtained in a tensile test before fracture occurs. In brittle materials however, this point occurs with no noticeable change in the stress-strain ratio.

2.3.7 Young's modulus and Poisson's ratio

Young's modulus is defined as the ratio between the normal stress component acting along a particular direction and the longitudinal strain determined along the same direction. From the stress-strain diagram, it corresponds to the slope of the stress-strain curve in the elastic regime. In anisotropic materials such as silicon, the Young's modulus differs for each crystal direction. For cubic crystals, the Young's modulus for a particular direction <*hkl*> is given by [85]:

$$E_{<hkl>} = \frac{1}{\mathrm{S}_{11} - 2\left(\mathrm{S}_{11} - \mathrm{S}_{12} - \frac{1}{2}\mathrm{S}_{44}\right)\left(g^2_{hkl\leftrightarrow x} g^2_{hkl\leftrightarrow y} + g^2_{hkl\leftrightarrow x} g^2_{hkl\leftrightarrow z} + g^2_{hkl\leftrightarrow y} g^2_{hkl\leftrightarrow z}\right)} \tag{2.21}$$

Here, $g_{hkl\leftrightarrow x}$, $g_{hkl\leftrightarrow y}$ and $g_{hkl\leftrightarrow z}$ are the direction cosines, i.e. cosines of the angle between the longitudinal direction <*hkl*> where the stress is being applied and the directions $x = [100]$, $y = [010]$ and $z = [001]$ respectively. S_{11}, S_{12} and S_{44} are the compliance coefficients in silicon as defined in Equation 2.19. Equation 2.22 gives simplified expressions for the Young's modulus in silicon along the <100>, <110> and <111> directions and the values obtained using the compliance coefficients given in Table 2.1.

$$E_{<100>} = \frac{1}{S_{11}} \approx 130\ GPa$$

$$E_{<110>} = \frac{2}{S_{11} + S_{12} + \frac{1}{2}S_{44}} \approx 169\ GPa \tag{2.22}$$

$$E_{<111>} = \frac{3}{S_{11} + 2S_{12} + S_{44}} \approx 188\ GPa$$

When a material is stressed along a specific direction, it also shrinks or expands across the other two perpendicular directions. Thus, a tensile normal stress applied along the *x* direction, will induce a contraction in the *y* and *z* directions. The ratio between the transversal strain and the longitudinal strain is called Poisson's ratio:

$$\upsilon = -\frac{\varepsilon_t}{\varepsilon_l}, \tag{2.23}$$

where ε_t is the transversal strain and ε_l is the longitudinal strain.

2.4 Thermal conductivity

Thermal conductivity is defined as the ability of a material to conduct heat between two points separated by a gradient of temperature. Heat transfer occurs in the direction of the largest fall of temperature. In a crystal however, the heat transfer will not necessarily flow parallel to the temperature gradient. Therefore, the relation between the temperature gradient $\nabla\mathbf{T}$ and the heat flow rate $\boldsymbol{Q_h}$ will be in general a second rank tensor expressed as [90]:

$$\boldsymbol{Q_h} = \boldsymbol{k_{Th}}\nabla\mathbf{T}\ , \tag{2.24}$$

where $\boldsymbol{k_{Th}}$ is the thermal conductivity second rank tensor in units of $Wm^{-1}K^{-1}$.

In the same way as the compliance and stiffness tensors in crystals with cubic symmetry reduce to only three independent components (section 2.3.4) the second rank thermal conductivity tensor in these crystals reduces to only one component. Therefore, in crystals such as silicon and germanium, the thermal conductivity is represented by a scalar.

Two main mechanisms contribute to the conduction of heat: lattice vibrations (phonons) and electrical carriers (electrons and holes) [90]. In insulators and many undoped semiconductors including silicon, the total thermal conductivity is mainly ascribed to lattice vibrations. In case of undoped bulk silicon, the thermal conductivity at room temperature is ~150 $Wm^{-1}K^{-1}$ [36]. This is comparable with the thermal conductivity of many metals. Figure 2.11 shows the thermal conductivity of silicon determined experimentally in the range 3 – 1580 K.

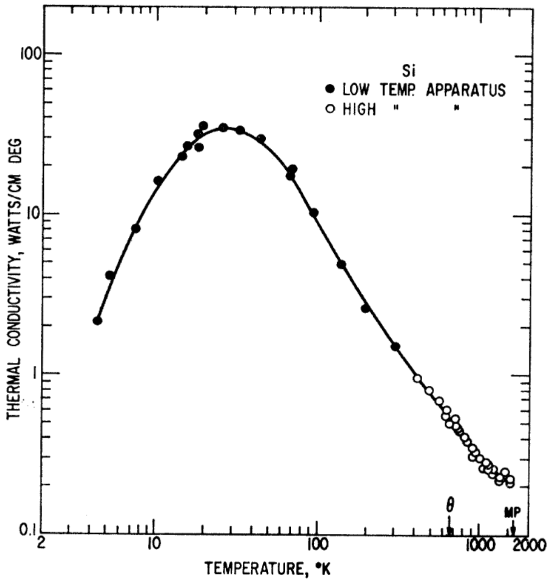

Figure 2.11 Thermal conductivity in silicon with temperature in the range 3 – 1580 K. [36]

The thermal conductivity in semiconductors depends on multiple factors including temperature, doping, defects, and geometry. Figure 2.12 shows the dependency of the thermal conductivity in silicon for various types of bulk and nanostructures.

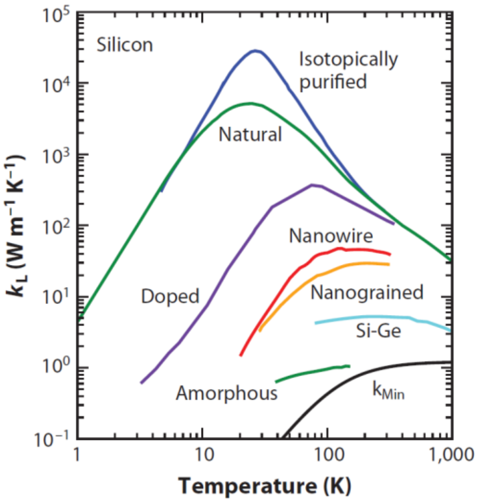

Figure 2.12 Thermal conductivity in silicon from various bulk and nanostructures. [37]

Theoretical studies have also shown that the thermal conductivity of silicon significantly changes with strain. Figure 2.13 shows the results of molecular dynamics simulations in strained bulk silicon and nanowires [38]. The results show that the thermal conductivity of silicon in both bulk and nanowires decreases as the applied strain changes from compressive to tensile. Nevertheless, there is a lack of experimental data especially for nanostructures and high values of strain. This is important for devices using strain and SOI substrates where thermal effects are more severe [91, 92].

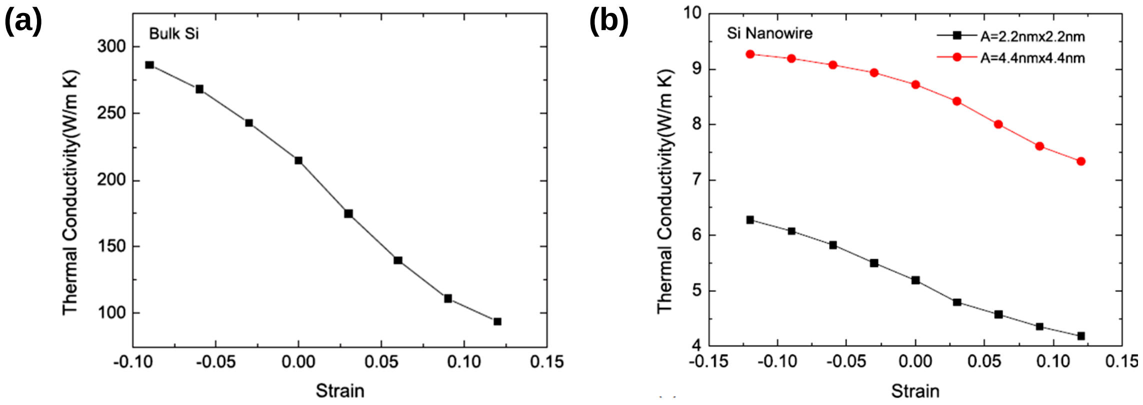

Figure 2.13 Thermal conductivity in bulk silicon (a) and in silicon nanowires (b) with strain determined by molecular dynamic simulations. [38]

2.5 Summary

In this chapter, the crystal structure of silicon (section 2.2) has been reviewed. The chapter has started with a brief description of the silicon crystal structure in real space. The Miller index notation, used to describe the different directions and planes in crystals such as silicon, and the silicon crystal structure in reciprocal space (Brillouin zone) have also been described in sections 2.2.3 and 2.2.4. A good knowledge of the real and the reciprocal silicon crystal structures and the Miller index notation is important for a better understanding of the Raman spectroscopy and the different modes of vibration in silicon (chapters 3-5).

The chapter has also introduced the theory of elasticity (section 2.3). The theory of elasticity has been formulated in tensorial notation more appropriate to describe the properties of anisotropic materials, including those of silicon. A brief description of the concept of tensors and the notations used in this thesis has been given in section 2.3.1. The strain and stress tensors have been introduced in sections 2.3.2 and 2.3.3. A good knowledge of the components and the tensor nature of the strain and stress tensors are desirable for a better understanding of the effect of strain on the optical phonon frequencies of silicon and the impact of stress and strain on the roughness of the silicon surface. Both topics will be investigated in chapters 5 and 6. The relation between strain and stress in the elastic regime (Hooke’s law) has been presented in section 2.3.4 and the different parameters extracted from a stress-strain curve in a tensile test in section 2.3.5. Two important parameters extracted from the stress-strain curve are the Young’s modulus and the fracture strain. These two parameters have been described in sections 2.3.6 and 2.3.7 and they will be investigated in chapter 4. The chapter has finished with a description of the thermal conductivity (section 2.4). The size-effect on the Young’s modulus, fracture strain and thermal conductivity in silicon nanostructures will be investigated in chapter 4.

Chapter 3. Local characterisation techniques

3.1 Introduction

Traditionally, the properties of a material have been studied using macroscopic techniques. The information provided by such techniques corresponds to the value of the property averaged over the entire material. Therefore, the value obtained by such techniques is more representative of the bulk of the material. However, the properties of a material such as the elasticity and thermal conductivity may change at the nanoscale. Characterisation of the properties at the nanoscale is important to understand and optimise the operation of nanoscale devices such as state-of-the-art transistors. In order to obtain information of the material properties at the nanoscale, local characterisation techniques need to be used. In this work, Raman spectroscopy and atomic force microscopy (AFM) are used to locally characterise strain and the roughness of the surface respectively in silicon nanostructures. Both techniques are non-destructive and require little or no sample preparation. The information provided by these techniques is used to evaluate the impact of strain on the surface roughness of silicon nanostructures. Both techniques are described in detail below.

3.2 Raman spectroscopy

Raman spectroscopy has progressed remarkably in the last few decades. Raman spectroscopy is now used to characterise the chemical composition and structure of a sample, the quality of a crystal and the stress and strain levels in a material among other parameters. The advance in laser technology since the laser invention in 1960 [93], the development and fabrication of high selective filters to suppress the Rayleigh scattering and the improvements in the resolution and efficiency of gratings and detectors, has permitted a rapid development in Raman instrumentation.

In a typical Raman experiment, a beam of monochromatic light, usually from a laser source, is projected onto a sample and interacts with the lattice vibrations (phonons in a crystal). As a result of this interaction, some photons are scattered. Most of the scattered photons are elastically scattered (Rayleigh scattering) and therefore have the same frequency of that of the incident beam. However, a few photons, about one out of 10^7, are inelastically scattered (Raman effect). The inelastic scattering (Raman scattering) results as a consequence of an energy transfer between the incident photons and the phonons. Two common photon-phonon interactions are possible. In a typical Stokes-scattering process, the incident photon transfers part of its energy to the lattice. This energy transfer leads to the creation of a phonon and the emission of a photon with lower energy. In a second process called anti-Stokes, the incident photon interacts with a phonon in a vibrational excited state. In this case, the phonon is annihilated and a photon with higher energy than that of the incident photon is released. The probability for the anti-Stokes scattering process to occur is however lower than that of the Stokes scattering process since phonons in the excited state are required for the Anti-stokes process to occur. Figure 3.1 shows a schematic of the Rayleigh and Stokes and anti-Stokes scattering processes.

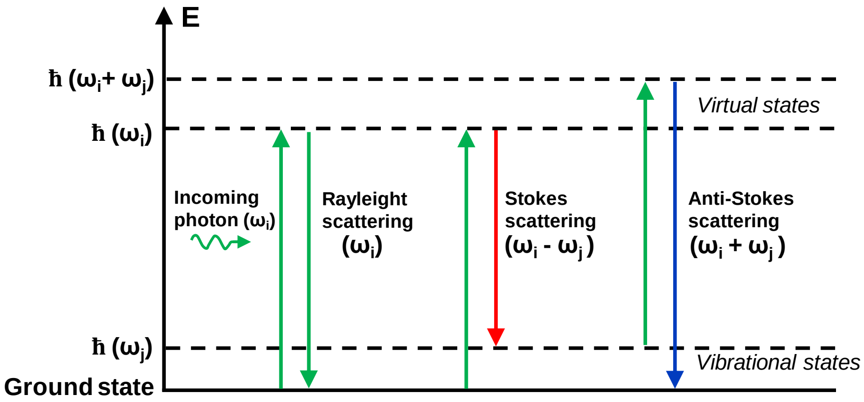

Figure 3.1 Elastic scattering (Rayleigh scattering) and inelastic scattering (Raman scattering).

3.2.1 Classical explanation of the Raman effect

In classical electromagnetism theory, the electric field $\boldsymbol{E}$ associated with a monochromatic incident light such that of a laser induces an electric moment $\boldsymbol{P}$ proportional to the susceptibility χ of the material:

$$\boldsymbol{P} = \varepsilon_0 \chi \boldsymbol{E} \tag{3.1}$$

Here, ε_0 is the vacuum electrical permittivity. If the material is anisotropic, the susceptibility $\boldsymbol{\chi}$ will be in general a second rank tensor since the induced electric moment needs not to be parallel to the electric field.

The electric field associated to the incident electromagnetic radiation can be described by a plane wave function:

$$\boldsymbol{E} = E_0 \exp[\mathrm{i}(\boldsymbol{k_i x} - \omega_i t)]\,, \tag{3.2}$$

where $\boldsymbol{k_i}$ is the wave vector of the electric field at position $\boldsymbol{x}$, ω_i is the angular frequency and E_0 is the electric field amplitude.

Combining Equations 3.1 and 3.2, the electric moment is expressed as:

$$\boldsymbol{P} = \varepsilon_0 \boldsymbol{\chi} E_0 \exp[\mathrm{i}(\boldsymbol{k_i x} - \omega_i t)] \tag{3.3}$$

Likewise, the crystal vibrations can be described in terms of the vibration of entire planes of atoms with wave function:

$$\boldsymbol{Q_j} = A_j \exp\left[\pm \mathrm{i}\left(\boldsymbol{q_j x} - \omega_j t\right)\right] \tag{3.4}$$

Here, $\boldsymbol{Q_j}$ is the normal mode of the vibration j, with wave vector $\boldsymbol{q_j}$, angular frequency ω_j, and amplitude A_j at position $\boldsymbol{x}$. The susceptibility of the material may change with the position of the atoms within the material. Assuming small changes in the amplitude of the lattice vibrations (compared with the lattice constant), the susceptibility $\boldsymbol{\chi}$ can be expanded in Taylor series with respect to the normal mode $\boldsymbol{Q_j}$, as:

$$\boldsymbol{\chi} = \chi_0 + \left(\frac{\partial \boldsymbol{\chi}}{\partial \boldsymbol{Q_j}}\right)_0 \boldsymbol{Q_j} + \left(\frac{\partial \boldsymbol{\chi}}{\partial \boldsymbol{Q_j}\, \partial \boldsymbol{Q_k}}\right)_0 \boldsymbol{Q_j Q_k} + \cdots \tag{3.5}$$

Substituting Equations 3.5 into Equation 3.3, the electric moment can be expressed (to second order terms) as:

$$\boldsymbol{P} = \varepsilon_0 \chi_0 E_0 \exp[\pm \mathrm{i}(\boldsymbol{k_i x} - \omega_i t)] + \varepsilon_0 E_0 \left(\frac{\partial \boldsymbol{\chi}}{\partial \boldsymbol{Q_j}}\right)_0 A_j \exp\left[-i\left(\omega_i \pm \omega_j\right)t\right] \exp\left[i\left(\boldsymbol{k_i} \pm \boldsymbol{q_j}\right)\boldsymbol{x}\right] \tag{3.6}$$

The first term of Equation 3.6 does not involve any phonon interaction. It relates to the Rayleigh scattering radiation with the same frequency as that of the incident light ω_i. The second term relates to the first order Raman scattering. In the first order Raman scattering, monochromatic light with frequency ω_i interacts with a phonon with frequency ω_j. This, results in light scattered with frequency $\omega_s = \omega_i \pm \omega_j$. The frequency $\omega_i - \omega_j$ corresponds to the Stokes radiation whereas the frequency $\omega_i + \omega_j$ is the anti-Stokes radiation. The third and higher terms involve the participation of two or more phonons and relate to the second and higher orders Raman scattering. Figure 3.2 shows a typical Raman spectrum in bulk silicon acquired with an extended window to show the Rayleigh scattering and the first (Stokes and anti-Stokes peaks) and second order Raman scattering.

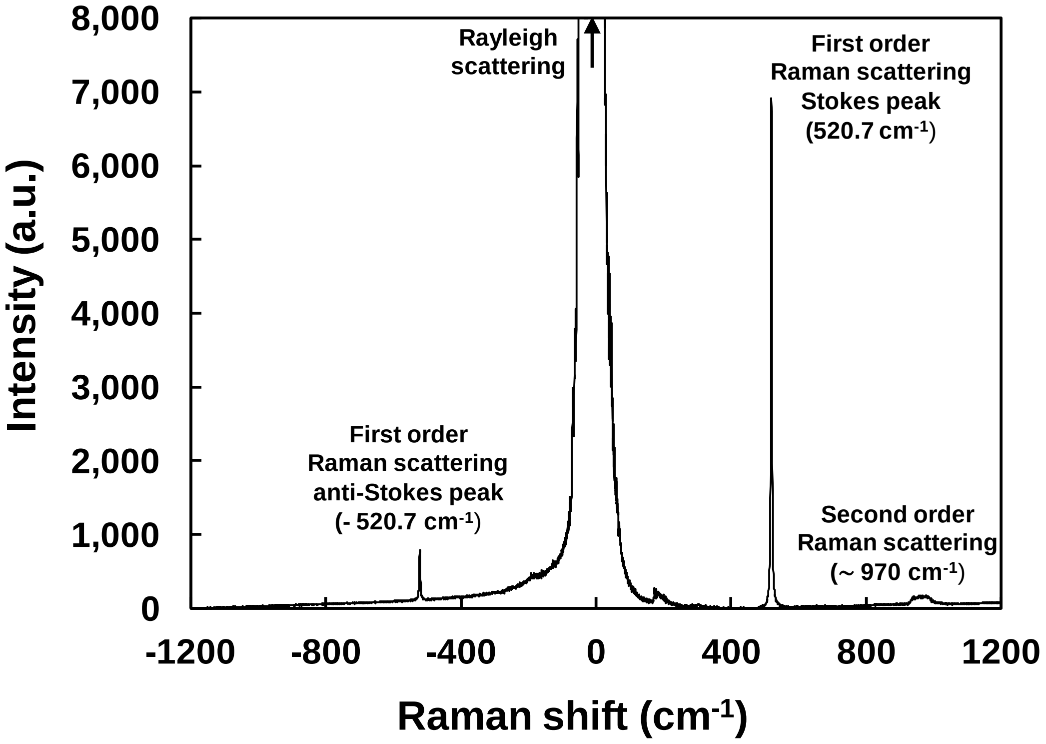

Figure 3.2 Raman spectrum in bulk silicon showing the first and second order Raman scattering and the more intense Rayleigh scattering.

3.2.2 Phonon dispersion curves

In the first order Raman scattering, wave vector conservation in a photon-phonon interaction yields [94]:

$$\boldsymbol{k_s} = \boldsymbol{k_i} \pm \boldsymbol{q_j} \qquad (3.7)$$

Incident photons from a laser source have large wavelengths (~300 – 600 nm) compared with the lattice constant of silicon (a_{Si} = 5.43 Å). This implies that the wave vector $\boldsymbol{k_i}$ is small compared with the length of the first Brillouin zone $\left({}^{2\pi}/_{a_{Si}}\right)$. Therefore, the first order Raman scattering is limited to phonons with wave vectors $\boldsymbol{q_j} \approx 0$ i.e. near the Brillouin zone centre. Figure 3.3 shows the phonon dispersion curves in silicon.

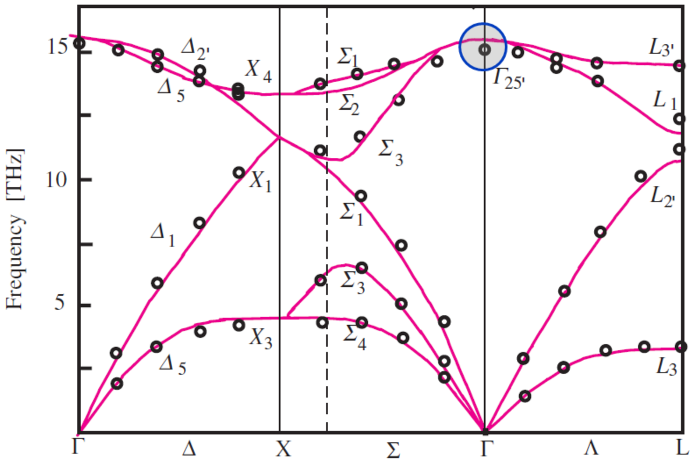

Figure 3.3 Phonon dispersion curves in silicon. The centre of the Brillouin zone for the optical phonons is the $\Gamma_{25'}$ point. [94]

First order Raman scattering using visible radiation is limited to photon-phonon interactions near the point Γ'_{25}. Lattice vibrations at this point involve the two atoms per basis (Figure 2.3a) to move 180° out of phase. These lattice vibrations are called optical phonons as opposite to the acoustic phonons where the two atoms per basis move in phase. Phonons are also classified according to their displacement directions. Those that move parallel to their wave vector are called longitudinal phonons, whereas those that move perpendicular to their wave vector are transversal phonons [94]. In unstrained silicon, at room temperature, the Γ'_{25} point is triply degenerate and both the longitudinal (LO) and the two transversal optical (TO) phonons have the same frequency $\omega_{j0} \sim 520\ \mathrm{cm}^{-1}$ [95] (Figure 3.4).

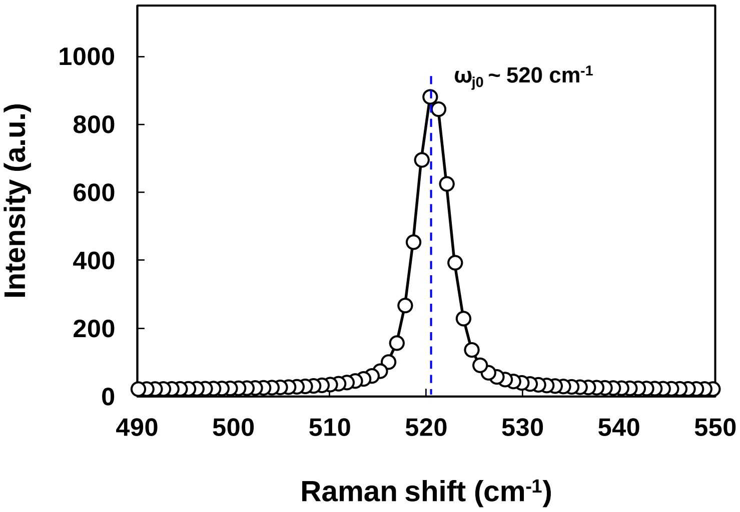

Figure 3.4 Raman spectrum in bulk silicon of the longitudinal optical peak. At room temperature, the longitudinal optical peak is centred at ~520 cm^{-1}.

The phonon frequency ω_j (Equation 3.6), which is the difference between the incident and the scattered frequencies, is called the Raman shift. In spectroscopy, Raman shifts are typically reported as wave numbers in units of cm^{-1}. The correspondence between wave numbers (k) and wavelengths (λ) is:

$$k = \frac{1}{\lambda}, \tag{3.8}$$

and the correspondence between the wavelength λ and the angular frequency ω is:

$$\omega = 2\pi \frac{c}{\lambda}, \tag{3.9}$$

where c is the speed of light. The Raman shift depends on the material composition and is also sensitive to factors such as strain and temperature. In silicon, the triply degenerate frequency of the longitudinal and transversal optical phonons at the Brillouin zone centre shifts from its bulk value when uniaxial or biaxial stress is applied to the sample [95]. Strain can be determined from a linear relation between the phonon frequency shift and strain. This will be discussed in detail in chapter 5 alongside with the experimental determination of strain-shift coefficients for silicon nanostructures. When stress is applied, the peak shifts towards a lower Raman frequency for tensile stress and a higher Raman frequency for compressive stress. In both cases the difference in peak position for unstressed and stressed samples relates to the applied stress (Figure 3.5) [95].

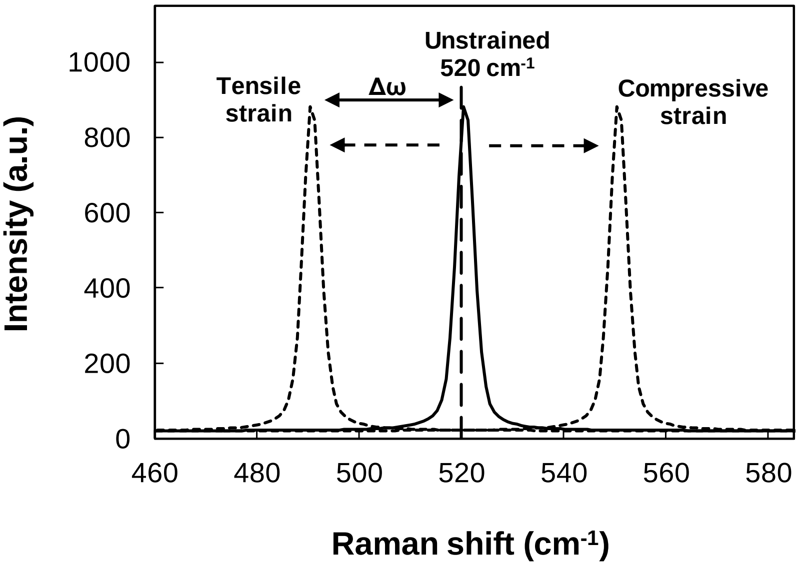

Figure 3.5 Raman shift dependency with strain in silicon. In the absence of stress, silicon exhibits a major peak centred at ~520 cm^{-1}. Tensile strain causes the peak position to shift towards lower frequency values whereas compressive strain will shift the peak position towards higher frequency values.

3.2.3 Polarisation selection rules

As shown in Equation 3.6, in order to have first order Raman scattering, the term $\left(\frac{\partial \chi}{\partial Q_j}\right)_0 \neq 0$ i.e. the susceptibility of the material must change with the normal mode of vibration $\boldsymbol{Q_j}$. Since the susceptibility in anisotropic materials is in general expressed by a tensor, the components of $\left(\frac{\partial \chi}{\partial Q_j}\right)_0$ are often described in terms of a second order tensor called the Raman tensor $\boldsymbol{R_j}$. The components of $\boldsymbol{R_j}$ were derived by Loudon [96] from symmetry considerations, for each crystal class. In case of silicon, the Raman tensors corresponding to the normal modes of vibration along the directions *x* = [100], *y* = [010] and *z* = [001] reduce to one independent component commonly denoted by *d*:

$$\boldsymbol{R_X} = \begin{bmatrix} 0 & 0 & 0 \\ 0 & 0 & d \\ 0 & d & 0 \end{bmatrix}$$

$$\boldsymbol{R_Y} = \begin{bmatrix} 0 & 0 & d \\ 0 & 0 & 0 \\ d & 0 & 0 \end{bmatrix} \tag{3.10}$$

$$\boldsymbol{R_Z} = \begin{bmatrix} 0 & d & 0 \\ d & 0 & 0 \\ 0 & 0 & 0 \end{bmatrix}$$

The intensity of the first order Raman scattered radiation is proportional to the square of the induced electric moment (second term in Equation 3.6) hence to the Raman tensor [94], and depends also on the incident and scattered light polarisation as:

$$I_s \propto \left|\boldsymbol{e_i} \boldsymbol{R_j} \boldsymbol{e_s}\right|^2 \tag{3.11}$$

Here, $\boldsymbol{e_i}$ and $\boldsymbol{e_s}$ are the unit vectors for the polarisation of the incident and scattered light. The intensity of the scattered radiation vanishes for specific polarisations of the incident and scattered radiation. Therefore, only certain modes will be observed depending on the incident and scattering polarisation (polarisation selection rules). Table 3.1 lists the allowed Raman modes for backscattering from a (001) and (110) surfaces (backscattering refers to the specific configuration where the incident and scattered radiation are directed along the same axis). Thus, for backscattering from a (001) surface, only the third Raman mode ($\boldsymbol{R_z}$) can be observed regardless of the polarisation of the incident and scattered radiations.

Table 3.1 Polarisation selection rules for backscattering from a (001) and (110) surface

Backscattering Surface	**Polarisation**		**Allowed Raman modes**
	e$_i$	**e$_s$**	
(001)	(100)	(100)	-
	(100)	(010)	R_z
	$(1\bar{1}0)$	$(1\bar{1}0)$	R_z
	(110)	$(1\bar{1}0)$	-
(110)	$(1\bar{1}0)$	(001)	R_x, R_y
	$(1\bar{1}0)$	$(1\bar{1}0)$	R_z
	(001)	(001)	-

3.2.4 The Raman system

The Raman system used in this work is a LabRAM HR 800. Figure 3.6 shows a picture of the system. The HR800 is an integrated Raman system with the microscope coupled confocally to an 800 mm focal length spectrograph. Externally, it has two laser units, an argon ion laser from Spectra-Physics operating at the wavelength of 364 nm (UV radiation) and a tunable argon-ion laser from Melles-Griot operating at three visible wavelengths: 514, 488 and 458 nm.

Figure 3.6 The Raman unit used in this work, a LabRAM HR 800. [97]

3.2.4.1 Optics description

Figure 3.7 shows the schematic of the optical path in the LabRAM HR 800. At the laser entrance there is a clean-up filter. The clean-up filter is a band pass filter with a cut-off frequency centred at the laser frequency. The purpose of the clean-up filter is to eliminate some lower level transitions, plasma, and “glows” that may appear at the output of the laser source. After the clean-up filter, a neutral density filter (filter-wheel) attenuates the laser intensity incident onto the sample to some predefined value. Reduction of the laser intensity incident onto the sample is often necessary to avoid excessive sample heating. In the LabRAM HR 800 the attenuation value is selected by the software. The possible options are 100%, 50%, 25%, 10%, 1%, 0.1% and 0.01%. These percentages though, refer to the laser signal incident onto the sample. After the clean-up filter the laser signal reaches the sample and retraces (backscattering) towards a notch filter. The purpose of the notch filter is to reject the scattered Rayleigh radiation coming from the sample. Since the visible laser can be adjusted at three different frequencies, both the clean-up filter and the notch filter have to be selected accordingly.

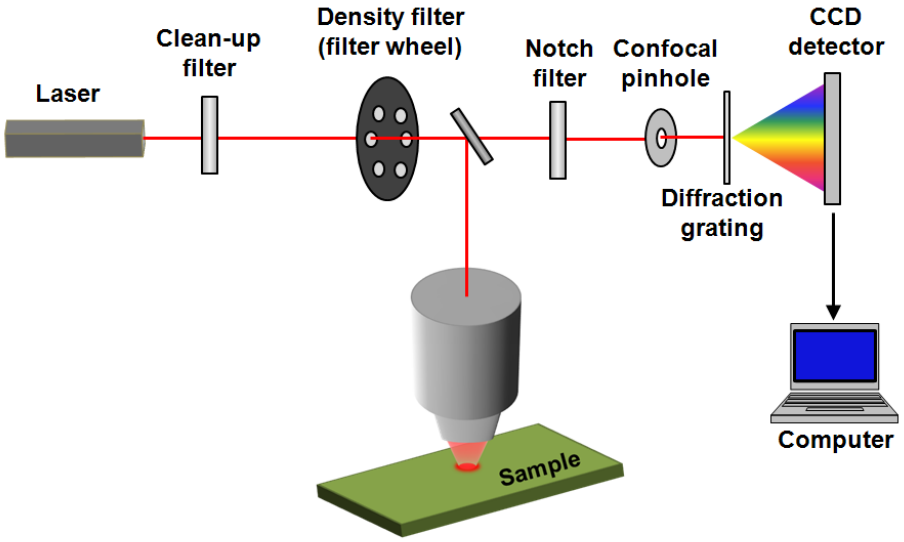

Figure 3.7 Schematic of the laser path and the different optics used in the Raman system.

After the notch filter, the laser signal passes through a confocal pinhole. The confocal hole is used to adjust the spatial resolution and analysis volume of the measurement. The spatial resolution is usually defined by the laser spot size focused onto the sample and depends on the wavelength of the laser and the numerical aperture of the microscope objective (*NA*). The theoretical minimum diameter of the focused laser spot is given by [98]:

$$\emptyset = \frac{0.88\,\lambda}{NA} \tag{3.12}$$

For a high numerical aperture lens *NA*= 0.9 and a laser wavelength $\lambda = 458\ nm$, this results in a theoretical minimum diameter for the laser spot ~ 0.5 µm. Experimentally the laser spot size is always larger than the theoretical value obtained with Equation 3.12 mainly due to the inability to have a perfect focus onto the sample.

Figure 3.8 shows a schematic of the principle of a confocal system. By controlling the width of the confocal hole, the volume of the scattered signal that will reach the spectrometer i.e. signal that will be analysed, may be regulated.

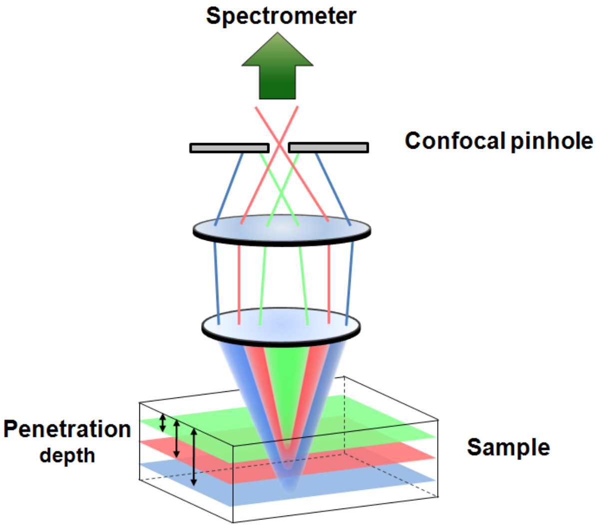

Figure 3.8 Confocal principle. By controlling the width of the confocal hole, the volume of the scattered signal that will be analysed (reaching the spectrometer) may be regulated.

The main part of the spectrometer is a diffraction grating (Figure 3.9) which splits and disperses the incoming light towards a CCD (charge-coupled device) detector. The resolution of the diffraction grating depends on the groove density (gr/mm). In the Raman equipment used in this work, two gratings with groove density of 2400 and 3000 gr/mm were available.

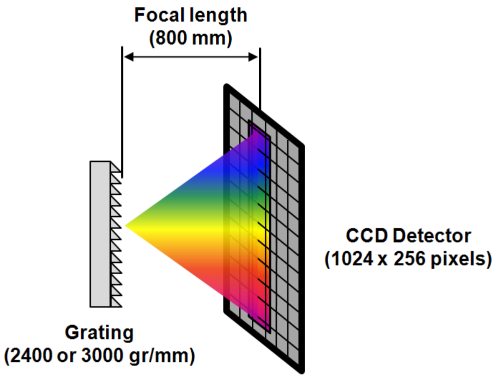

Figure 3.9 Diffraction grating. The diffraction grating splits and disperses the incoming light towards the CCD detector.

The separation distance between the grating and the CCD (focal length) affects the spectral resolution (Figure 3.9). Large focal lengths decrease the spectrum density reaching the CCD detector which results in an increase of the spectral resolution. Several factors including the laser wavelength, the focal length, the grating groove density, and the CCD resolution (number of pixels) affect the spectral resolution of the instrument. For an 1800 gr/mm grating, 800 mm focal length and 633 nm wavelength laser the spectral resolution in the LabRAM HR is ~0.35 cm^{-1}/pixel.

3.3 Atomic force microscopy

Atomic force microscopy (AFM) is a technique used for the analysis of surfaces down to the nanometer scale. The invention of the AFM in 1986 by Binnig *et al.* [73] was preceded by the development of the scanning tunnelling microscope (STM) in 1981 [72] which was awarded the Nobel Prize in physics in 1986. Both microscopes are currently widely used in many research fields since, in general, are sample non-destructive and require little or no sample preparation.

The AFM system used in this work is the XE-150 model from Park Systems. The XE-150 model incorporates a XY motorised sample stage optimised for large samples (150 mm × 150 mm). In order to minimise the external acoustic noise, the system is operated inside an acoustic isolation enclosure.

3.3.1 AFM principle

In atomic force microscopy, a sharp tip mounted at the end of a cantilever scans the surface of a sample in a raster pattern. Figure 3.10 shows a schematic representation of the AFM operating principle. In a first step, the tip is brought in contact or in close contact with the surface of the sample. Depending on the distance between the tip and the sample, attractive or repulsive atomic forces will force the cantilever to deflect. The deflection of the cantilever is measured by a laser beam which is directed on to the back side of the cantilever and is reflected towards a position sensitive photo-detector (PSPD). The photo-detector is composed of four photodiodes arranged in four quadrants A–D. The (A+C) − (B+D) signal provides the information for the vertical direction. The (A+B) − (C+D) signal yields the lateral information, which is generally related to changes in the surface friction and is used in lateral force microscopy. The information of the PSPD is sent to an electronic controller, which by means of a feedback loop modulates the voltage applied to the Z-scanner. The Z-scanner consists of a high-force piezoelectric element which allows precise control of the vertical movement. The Z-scanner in the XE-150 unit is totally decoupled from the X-Y scanner. This contrasts with the single piezo-tube scanner used in conventional AFMs which controls the movement of the tip in the three orthogonal directions at the same time. In these AFMs, since the piezo-tube cannot move in one direction independently of the other two, cross-talk and non-linearity responses are often encountered.

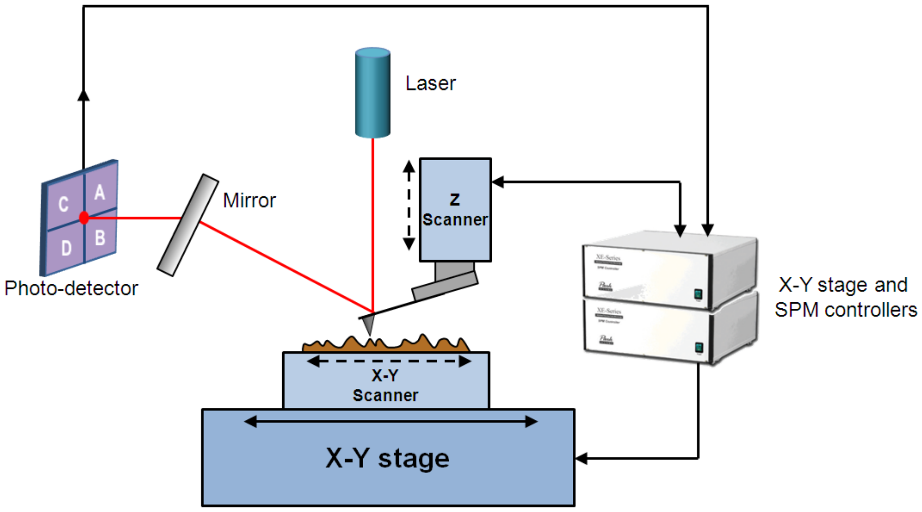

Figure 3.10 Schematic of the AFM operating principle.

3.3.2 AFM modes

As mentioned in section 3.3.1, the AFM operates by measuring the interacting forces between the atoms at the tip and the atoms at the sample (Figure 3.11). When the AFM tip is far from the sample, the attractive forces between ion cores and valence electrons predominate (van der Waals forces). In contrast, at very short distances the repulsive forces between ion cores at the end of the probe tip, and those at the surface of the sample dominate. These two forces are the basis of the different modes of operation of the AFM (Figure 3.11).

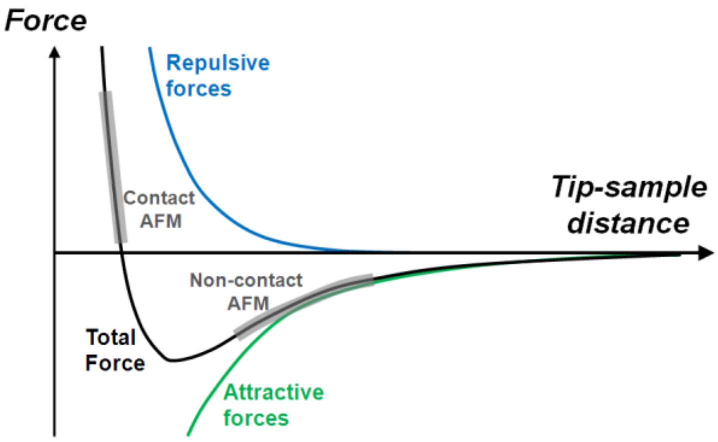

Figure 3.11 Diagram of the atomic interacting forces between the AFM tip and the surface of the sample. At short distances, the repulsive forces predominate whereas at long distances the attractive forces predominate.

3.3.2.1 Contact mode

In contact mode, the AFM tip is in soft contact with the surface of the sample. The inter-atomic forces between the atoms at the tip of the sample and those at the surface are repulsive (1~10 nN). The cantilevers used in contact mode need to have a spring-constant sufficiently small to react to these atomic forces. In contact mode, the electronic controller keeps a constant force between the tip and the sample by monitoring the cantilever deflection and sending the appropriate error-signal to the Z-scanner. The contact mode is commonly used with hard surfaces which do not get deformed by the AFM probe tip.

3.3.2.2 Non-contact mode

The non-contact mode uses the attractive long range van der Waals forces to measure the topography of the sample. In non-contact mode, the electronic controller keeps a constant height between the tip and the sample while scanning across the sample. This is done by monitoring the attractive force between the tip and the surface of the sample (deflection of the cantilever) and sending the appropriate error signal to the Z-scanner. However, since the force between the tip and the surface of the sample is very small, it is extremely difficult to directly measure the deflection of the cantilever. Therefore, in non-contact mode, the cantilever is made to vibrate at its natural resonant frequency (typically between 100 – 400 kHz) and the error signal is determined as a function of the change in phase and amplitude of the vibration. When the tip is close to the surface of the sample, the attractive forces cause the phase and amplitude of the vibration to change. The main advantage of non-contact mode is that the force between the tip and the sample is very weak thereby minimising the sample damage and tip degradation.

In this work, non-contact mode has been used for the AFM measurements due to the fragile nature of the structures (thin free-standing silicon beams undergoing large values of tensile strain) and to minimise tip degradation. Tip degradation is important in order to get accurate and repeatable measures of the surface roughness. This will be further discussed in section 3.3.3.1.

3.3.3 AFM common artefacts

AFM images often exhibit features which are not present in the real sample and are artefacts of the measurement itself. One such artefact is the thermal drift. Thermal drift is caused by the thermal expansion or contraction of the AFM mechanical parts such as the piezoelectric elements of the X-Y scanner. Images affected by thermal drift often exhibit distorted and drifted features (Figure 3.12a). Thermal drift is commonly encountered during the first scans and reduces after the system warms-up. Thus, it is important to always perform some initial scans to reduce (or eliminate) this effect. In this work, all the images were taken after the AFM had been performing some initial scans (warming-up) for ~ 1 hour.

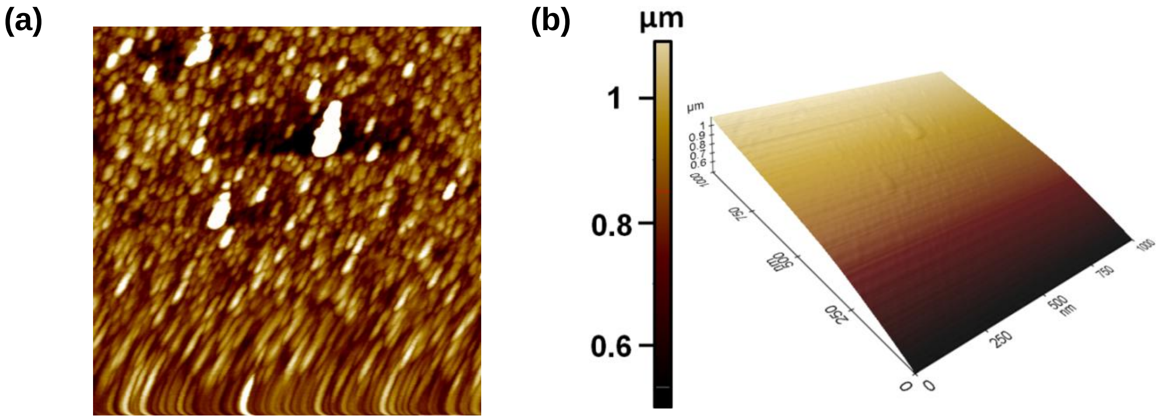

Figure 3.12 AFM common artefacts. (a) Thermal drift. (b) Z out-of plane motion (3D view).

Another common artefact is the Z out-of-plane motion due to the X-Y scanner stage movement. In this case, the image results with a slope or curvature in the Z direction. This artefact also reduces after an initial warming-up period. Nevertheless, the slope or curvature in the Z direction may also be caused by the tilt of the sample relative to the X-Y plane (Figure 3.12b). Therefore, the AFM images generally require a flattening process to suppress the slope or curvature effect. The flattening process is performed by estimating the slope or curvature introduced in the image with a polynomial regression fitting algorithm. In this algorithm, the fitted curve is subtracted from the surface profile. High order regression polynomial however, may alter severely the surface profile compared with the original surface profile. For the samples analysed in this work, only zero and first order flattening were required.

3.3.3.1 AFM tip

An AFM image is ultimately the result of the convolution between the shape of the tip and the profile of the sample [99, 100]. Many artefacts result from the shape and actual condition of the tip. Since the shape of the tip degrades with each scan, it is important to maximise and preserve its sharpness. Non-contact mode minimises the tip degradation and increases surface roughness repeatability. However, since the AFM working principle is based in the interacting forces between the tip and the surface of the sample, there will be always tip degradation. Other factors such as scanning time, profile of the sample and tip and sample materials, may compromise the integrity of the tip. In this work, the tip integrity was regularly tested using as a reference a sample with a regular pattern of nanowires (Figure 3.13) fabricated at the Paul Scherrer Institute (PSI) in Switzerland.

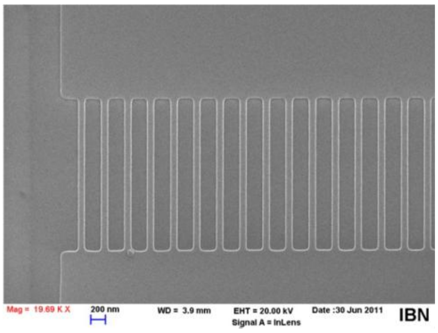

Figure 3.13 SEM image of the array of nanowires used for testing the AFM tip integrity. (*Samples fabricated by Renato Minamisawa at the Paul Scherrer Institute (PSI) in Switzerland).*

Figure 3.14 shows a sequence of AFM images corresponding to the pattern of nanowires shown in the SEM image of Figure 3.13 with a new tip, a slightly degraded tip and a highly degraded tip.

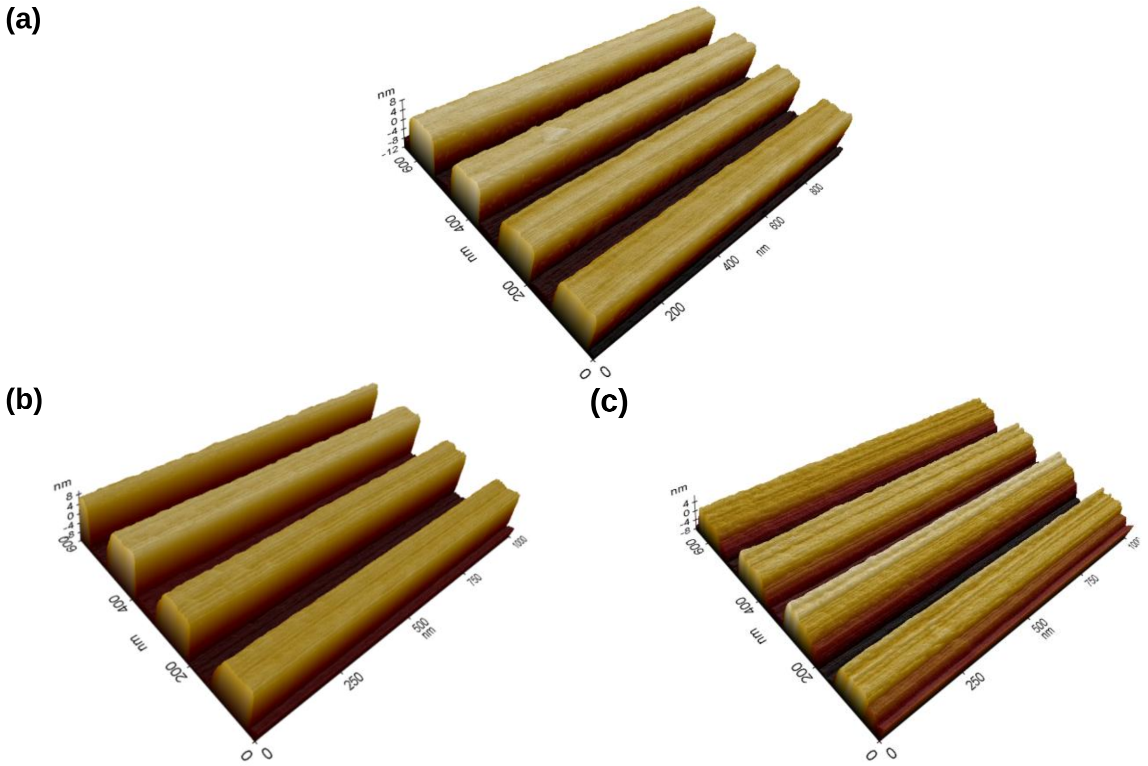

Figure 3.14 AFM images taken with (a) a new tip, (b) a slightly degraded tip and (c) a highly degraded tip of an array of nanowires with dimensions: width = 100 nm and thickness = 15nm.

In Figure 3.14b, the left edges of the nanowires start to exhibit a slight alteration (rounded effect) as compared with the nanowires in Figure 3.14a. In Figure 3.14c the right edges are highly altered. The vertical scale in Figure 3.14c shows also a decrease in magnitude of the thickness of the nanowires compared with that of Figure 3.14a.

3.4 Summary

In this chapter the two main techniques utilised to analyse the samples used in this work, Raman spectroscopy and AFM, have been presented.

The chapter has started with a classical explanation of the Raman effect along with a description of the optical modes of vibration in silicon and the Raman polarisation selection rules. It has been shown that in unstrained silicon, the longitudinal and transversal optical modes are triply degenerate. From the Raman polarisation selection rules it has been shown that in backscattering geometry from a (001) surface, in silicon, only the longitudinal optical mode is allowed. The Raman frequency for this mode is ~520 cm^{-1}. The Raman system and the optics used in this work have also been described. The technique will be used in chapter 4 to characterise strain in the silicon nanostructures and in chapter 5 to accurately determine the uniaxial strain-shift coefficient in silicon nanostructures for the <110> direction.

The AFM system used in the work has been presented in section 3.3. The AFM working principle and the two main modes of operation, contact and non-contact mode, have also been described. The non-contact mode will be used in chapter 6 to characterise the evolution of the surface roughness of the samples with strain. The non-contact mode is preferred over the contact mode due to the especial fragile nature of the samples and also to minimise the AFM tip degradation. The chapter has finished with a brief explanation of common artefacts found in AFM alongside with a description of the effect of the shape of the tip on the AFM image.

Chapter 4. Strain characterisation and size effects on the material properties in silicon nanostructures.

4.1 Introduction

Numerous testing methods have been previously used to perform mechanical tests in silicon free-standing beams replicating nanowires. Buckling and bending are common dedicated methods. In general, they use an atomic force microscope (AFM) tip to deform a cantilever or nanowire and thereafter measure the exerted force [35, 101, 102]. Other techniques use singular mechanisms to supply the needed deformation force, for example by inserting a material between cantilevers or by using a polymer spun over the base of an array of nanowires pillars to create a contraction force which deforms the nanowires [103, 104]. In these techniques it can be difficult to precisely control the exerted force. Often a probe for the specimen manipulation is required [33]. Methods based on buckling and bending are also frequently complicated by the non-linear analysis associated with the specimen deformation. Further challenges arise from the difficulty in obtaining large and uniform ranges of strain with precision, especially in long free-standing beams which are required for generating high values of strain. In silicon high strain values are necessary to maximise the potential of the MEMS and NEMS devices.

Tensile testing machines provide a very direct stress-strain measurement and the capability of probing high values of stress. However, the tensile testing stages developed often have complex designs which can complicate the stress-strain analysis [105-107]. Problems derived from external loading such as sample manipulation, gripping issues and misalignment are also encountered [82-84]. Furthermore, most tensile testing machines require an electrical based actuator to pull the sample specimen, which generally involves an additional power supply and high precision.

In this work an on-chip tensile testing technique for measuring the mechanical properties of micro- and nanometre-thick films while avoiding the issues described, is exploited to measure strain. The fabrication method allows multiple geometries (and thus strain values) to be processed simultaneously on the same wafer while being studied independently. The induced strain is varied and controlled by using different beam geometries of a large number of structures fabricated on the same chip.

Raman spectroscopy and scanning electron microscopy (SEM) are used to characterise strain in silicon nanostructures and the measured results are compared with analytical calculations and finite element simulations. Strain values ranging from 0 to 3.6%, equivalent to an applied stress of ~6 GPa, have been investigated in silicon. The impact of the surface-to-volume ratio on the mechanical properties of silicon is studied by analysing the Young’s modulus and fracture strain of the silicon samples. Surface effects are analysed with Raman spectroscopy by using a UV laser characterised by a low penetration depth and comparing results with a visible laser which senses the whole thickness of the silicon samples. The discrepancy between the Raman shifts measured using the UV and visible lasers is used to investigate the thermal conductivity in strained silicon.

4.2 On-chip tensile testing structures

4.2.1 Sample fabrication

The on-chip tensile samples used in this work were fabricated at the Université catholique de Louvain (UCL) in Belgium. The samples consist of arrays of silicon beams having beam widths of 1, 2, 4, 6, 8 and 10 μm. The beams are under tensile stress along the [110] direction. Each array is composed of thirty beams with lengths varying between 3 and 1,300 μm and a constant thickness of ~200 nm. The induced stress is provided by a silicon-nitride beam (actuator) attached to the silicon sample. The actuator widths are 10 and 15 μm and the thickness is ~400 nm. The length of the actuator is varied between 175 and 1,988 μm. The total length of the actuator and sample is kept constant and four different configurations with lengths of 500, 1,000, 1,500 and 2,000 μm were fabricated (Figure 4.1). Thus, the total number of samples is 6 × 30 × 2 × 4 = 1440. Strain values ranging from 0 to 3.6%, equivalent to an applied stress of ~6 GPa, have been investigated in silicon.

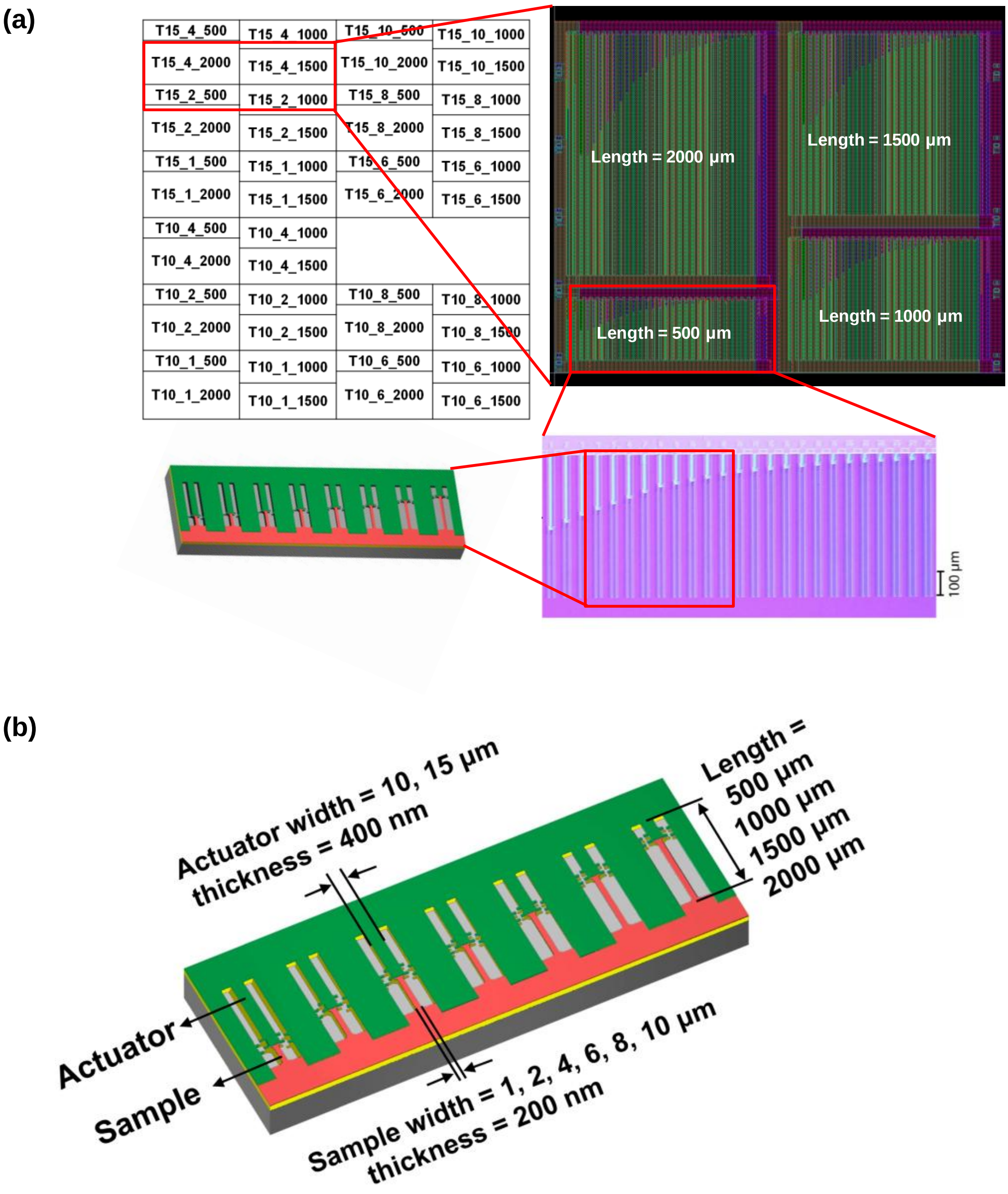

Figure 4.1 Structures analysed in this work. (a) The samples are coded with three numbers (top-left image). The first number indicates the width of the actuator. The second number is the width of the sample. The third number corresponds to the total length of the sample and actuator. (b) Each array of structures consists of 30 samples with lengths ranging from 3 to 1,300 μm. Six different sample widths and two actuator widths were also used. The thickness of the samples and actuators are 200 and 400 nm, respectively. The total length i.e. sample and actuator, is also varied between 500 and 2,000 μm. (Samples fabricated at the Université catholique de Louvain (UCL) in Belgium).

The complete fabrication process is shown in Figure 4.2. It starts with a standard (100) SOI wafer with a 400 nm-thick top silicon film (step 1, Figure 4.2). An oxide layer is thermally grown above the silicon film (step 2, Figure 4.2) and thereafter the oxide layer is used as a mask for patterning the silicon into beams (step 3, Figure 4.2). After sample patterning using plasma etching (step 4, Figure 4.2), a second oxide layer is thermally grown (step 5, Figure 4.2) and a window opened (step 6, Figure 4.2) where the actuator contacts the sample. A 400 nm-thick silicon nitride layer is then deposited by low pressure chemical vapour deposition at high temperature (800 °C) (step 7, Figure 4.2) and patterned for making the actuator (step 8, Figure 4.2). Finally, the sample (Si) and actuator (Si_3N_4) are released by etching the silicon dioxide sacrificial layer with hydrofluoric acid (HF) (step 9, Figure 4.2). A critical point drying process completes this step for avoiding stiction with the substrate. As a result of the silicon nitride high deposition temperature and the difference in thermal expansion coefficients between silicon nitride ($\alpha_{Si3N4} \sim 5 \times 10^{-6}\,K^{-1}$) and silicon ($\alpha_{Si} \sim 2 \times 10^{-6}\,K^{-1}$) [108, 109], the silicon nitride undergoes internal stress relaxation after the final HF release. This induces a tensile stress in the silicon sample. Figure 4.3 shows a microscope image of the structures after the final release process.

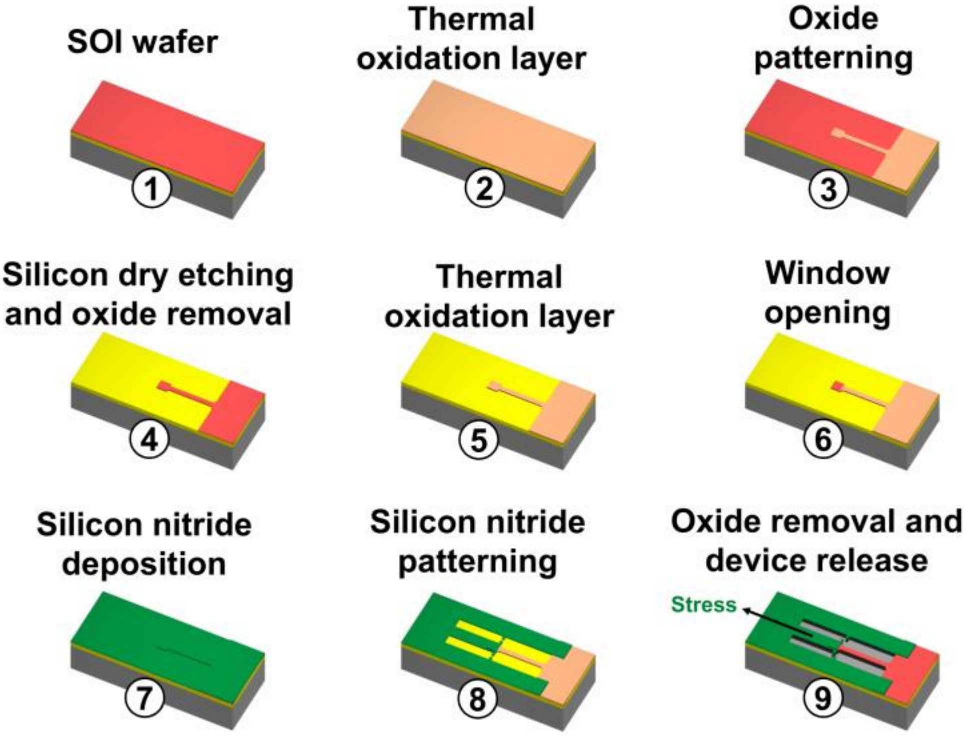

Figure 4.2 The fabrication process flow for the MEMS-based silicon beams. An induced stress due to the contraction of the actuator appears in the silicon sample beam after the final release process.

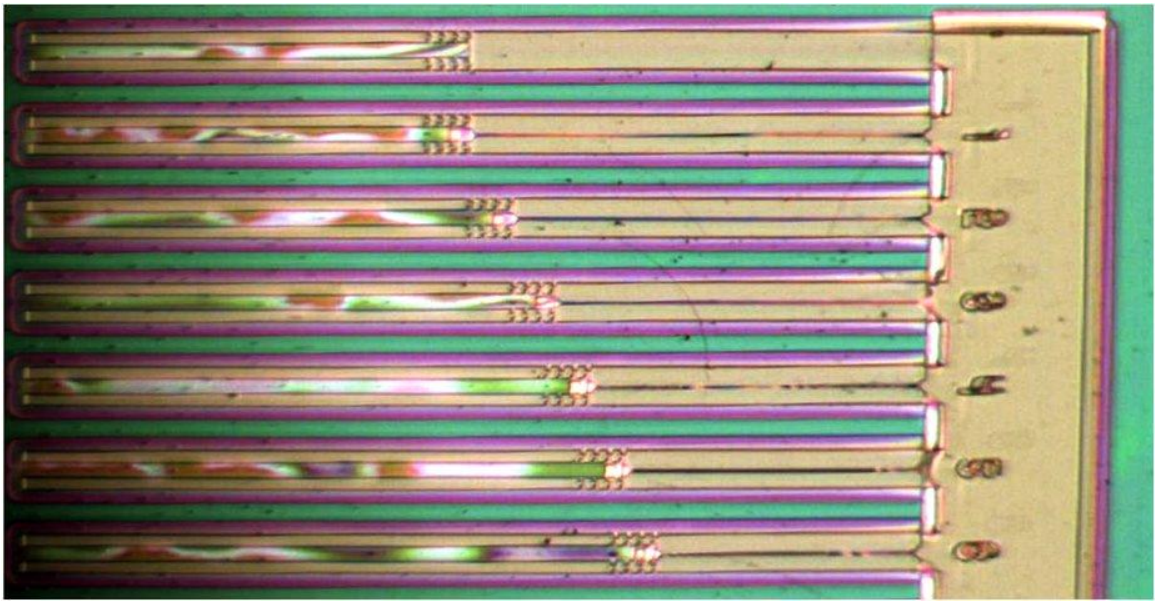

Figure 4.3 Microscope image of the structures. The top structure corresponds to a free actuator used to determine the silicon nitride mismatch strain after the release of the samples.

In order to correct for misalignments and lithography errors, the samples and actuators dimensions were measured by SEM after processing. SEM measurements were carried out at the lab facilities of the Université catholique de Louvain (UCL) in Belgium. The accuracy for the SEM measurements is estimated to be 50 nm [108]. A pair of cursors was fabricated alongside the silicon beams (Figure 4.4a) to measure the sample elongation by direct visual inspection using SEM and giving indication of the strain induced. One cursor is positioned at the actuator side (mobile cursor) and the other is positioned at the substrate sidewalls (fixed cursor). The displacement between the mobile and fixed cursors (sample elongation) (inset in Figure 4.4a) is then converted to strain (section 4.4). In order to minimise the error in the strain determination, additional pairs of cursors per sample (four in the present structures) were fabricated and the resulting displacements averaged (Figure 4.4b).

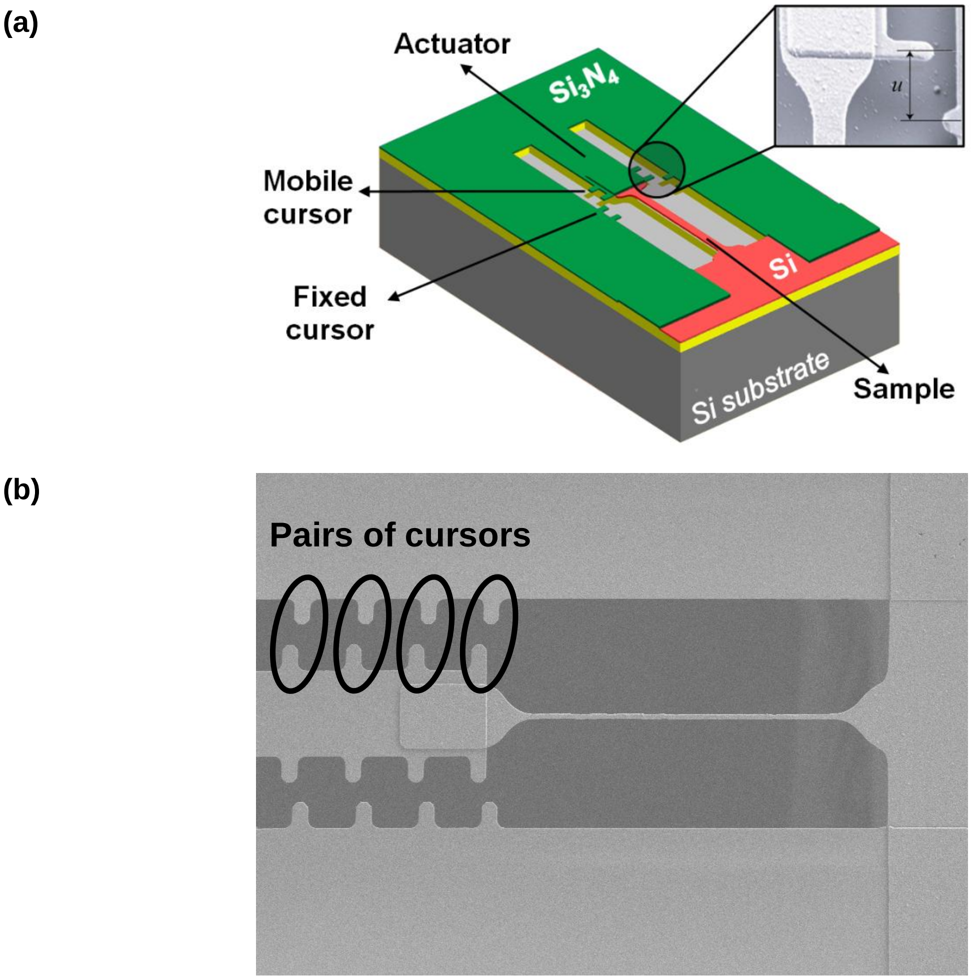

Figure 4.4 (a) Mobile and fixed cursors attached to the actuator and silicon nitride sidewalls allow accurate SEM measurements of the displacement u (inset); (b) SEM micrograph of a sample showing four pairs of cursors. Multiple cursors are used to minimise error in strain estimated by SEM measurements.

4.2.2 Principles of an elementary on-chip tensile testing structure

The strain and stress induced in the beam can be theoretically deduced from force equilibrium conditions between the actuator and sample beam. Figure 4.5 compares the structure deformations and force equilibrium involved before and after the sacrificial oxide removal during device fabrication. Figure 4.5a shows the expected deformation which will be experienced by the actuator with no attached sample after the sacrificial oxide etching. Following release, the actuator is free to contract by an amount u_{free} due to its internal stress relaxation. In contrast, the loaded actuator in Figure 4.5b can only contract by an amount u smaller than u_{free}. Figure 4.5b shows also that the displacement u can be considered either as the actuator contraction or the sample elongation.

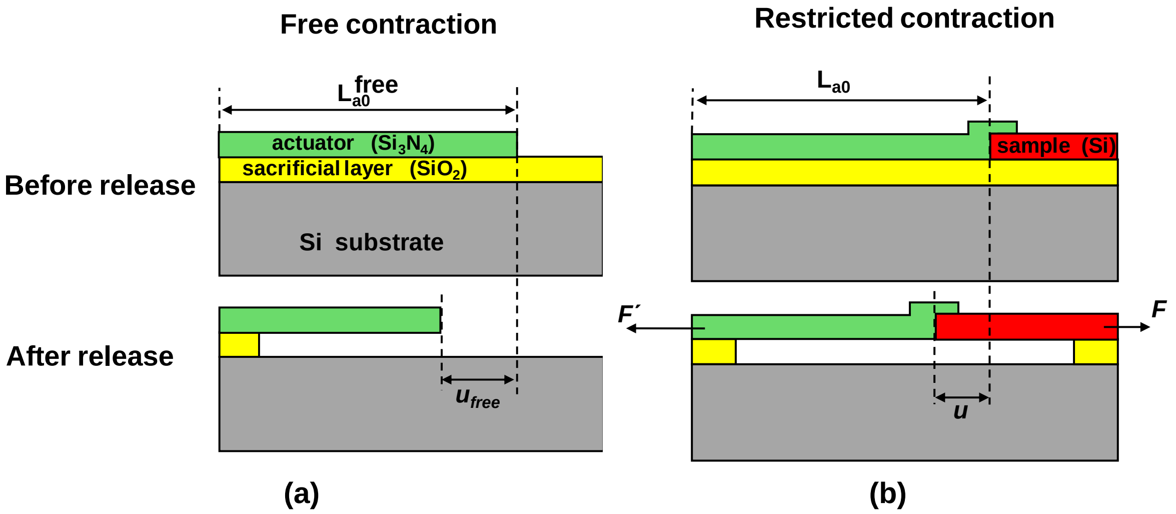

Figure 4.5 Schematic showing how the actuator contracts. (a) Actuator is free to contract i.e. with no attached sample; (b) Actuator is restricted by an attached sample. The actuator deformation u with the attached load is smaller than that of the free actuator u_{free}. Due to the actuator contraction after release, a tensile stress (*F-F'*) is induced along the silicon sample.

From Hooke's law, the stress in the actuator σ_a is:

$$\sigma_a = E_a \varepsilon_a \,, \tag{4.1}$$

where E_a is the Young's modulus of the actuator and ε_a is the actuator strain. The actuator strain is the net difference between the mismatch strain ε_a^{mis} due to the deposition process (silicon nitride contracts due to the difference between the deposition and room temperatures) and the mechanical strain ε_a^{mec} imposed by the attached sample. From Equation 4.1 and assuming the actuator has a cross section S_a, the load condition for the actuator is expressed by:

$$F_a = \sigma_a S_a = E_a\, S_a \varepsilon_a = E_a\, S_a\left(\varepsilon_a^{mis} - \varepsilon_a^{mec}\right) = E_a\, S_a\left(\frac{u_{free}}{L_{a0}^{free}} - \frac{u}{L_{a0}}\right), \tag{4.2}$$

where L_{a0} and L_{a0}^{free} represent the actuator length with and without the attached sample beam, before release. The actuator mismatch strain is obtained by measuring the contraction of a free actuator before and after release via SEM inspection (Figure 4.3). In this work, $\varepsilon_a^{mis} = 0.0032$. Following the same approach as for the actuator, the load condition for the sample beam is expressed by:

$$F_s = E_s\, S_s \left(\frac{u}{L_{s0}}\right), \tag{4.3}$$

where E_s, S_s and L_{s0} represent the Young's modulus, cross section and initial length, before release of the silicon beam. Mismatch strain is not considered since the silicon sample is produced from blanket SOI [110] (no thermal gradient is involved). Combining Equations 4.2 and 4.3 to enforce equilibrium ($F_a = F_s$) the displacement u is estimated as:

$$u = \frac{\varepsilon_a^{mis}}{r\frac{1}{L_{s0}} + \frac{1}{L_{a0}}}, \tag{4.4}$$

where r has been defined as $r = \frac{E_s S_s}{E_a S_a}$.

The displacement u (or sample elongation) is converted to strain using the logarithmic strain (true strain) more appropriate to describe large deformation behaviour [85]:

$$\varepsilon = ln\left(\frac{L_{s0} + u}{L_{s0}}\right) \tag{4.5}$$

Assuming silicon in the elastic regime and uniaxial stress along the [110] direction, strain can be converted to stress using Hooke's law (Equation 4.1) and the Young's modulus of bulk silicon for the <110> direction ($E_{<110>}$ = 169 GPa [111])).

4.3 Finite element simulations of strain

Finite element simulations of the strain distribution along the samples were performed using Ansys Workbench 13.0 software [112]. The silicon anisotropy was modelled using the elastic constants (stiffness coefficients) in silicon for the <100> direction: $C_{11} = 165.6 \times 10^9$ Pa, $C_{12} = 63.9 \times 10^9$ Pa and $C_{44} = 79.5 \times 10^9$ Pa [87]. The silicon nitride actuator was simulated using an isotropic model with a Young's modulus of 235 ± 10 GPa (as obtained by nanoindentation measurements [108]) and a thermal expansion coefficient ($\alpha_{Si3N4} \sim 5 \times 10^{-6}\,\mathrm{K}^{-1}$) [109]. The initial temperature in the actuator was set at 800 °C and thereafter linearly decreased to 22 °C to simulate the contraction undergone by the actuator. The sample temperature was kept constant at 22 °C. The sample and actuator were designed with ’dog-bone’ shape ends and the dimensions were the same as those experimentally measured by SEM (Figure 4.6). The sample axes X and Y were rotated by 45° with respect to the global axes, corresponding to the <110> direction.

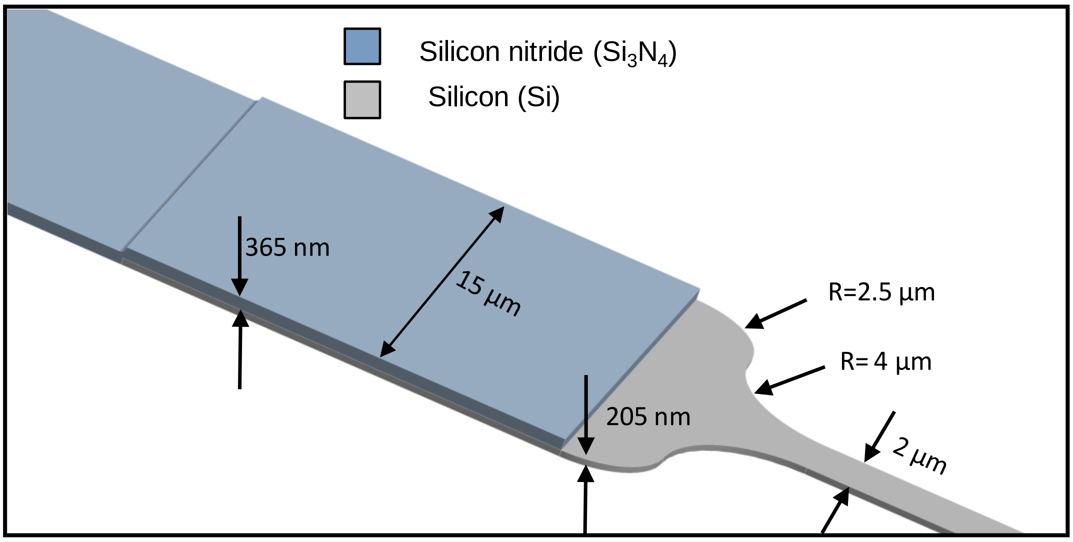

Figure 4.6 Detail of the actuator and sample dimensions used in Ansys to model a 180 µm-long and 2 µm-wide sample.

Figure 4.7 shows the modelled strain distribution in a 180 µm-long and 2 µm-wide sample. The strain is uniform along the sample beam (ε = 2.2%). At the ‘dog-bone’ ends however, there is a gradient of strain (inset in Figure 4.7). The strain along the ‘dog-bone’ end is shown to rapidly decay (up to 86%) within ~6 µm (‘dog-bone’ end length). However, since the sample and actuator lengths used in Equations 4.4 and 4.5 refer to the dimensions without the ‘dog-bone’ ends, the gradient of strain at the ends of the sample is not considered for the analytical calculations. Therefore, using Equation 4.4 for the same sample modelled in Figure 4.7, a cursor displacement of 3.9 µm is obtained which relates to 2.14% strain. This is very close to the modelled value of 2.2% strain. Figure 4.8 shows the variation in strain for three beam widths (1, 2 and 4 µm) with length L_{s0} (before release). There is a general $1/L_{s0}$ dependency in the measured values of strain, as expected from Equation 4.5. At short lengths, u and L_{s0} values become similar in magnitude and the resultant strain significantly increases. The increase is more pronounced for the 1 µm-wide samples than for the 2 and 4 µm-wide samples. This is because for a given length and thickness the 1 μm-wide beams have a higher applied stress due to the inverse relationship between stress and cross-section ($\sigma = F/S$).

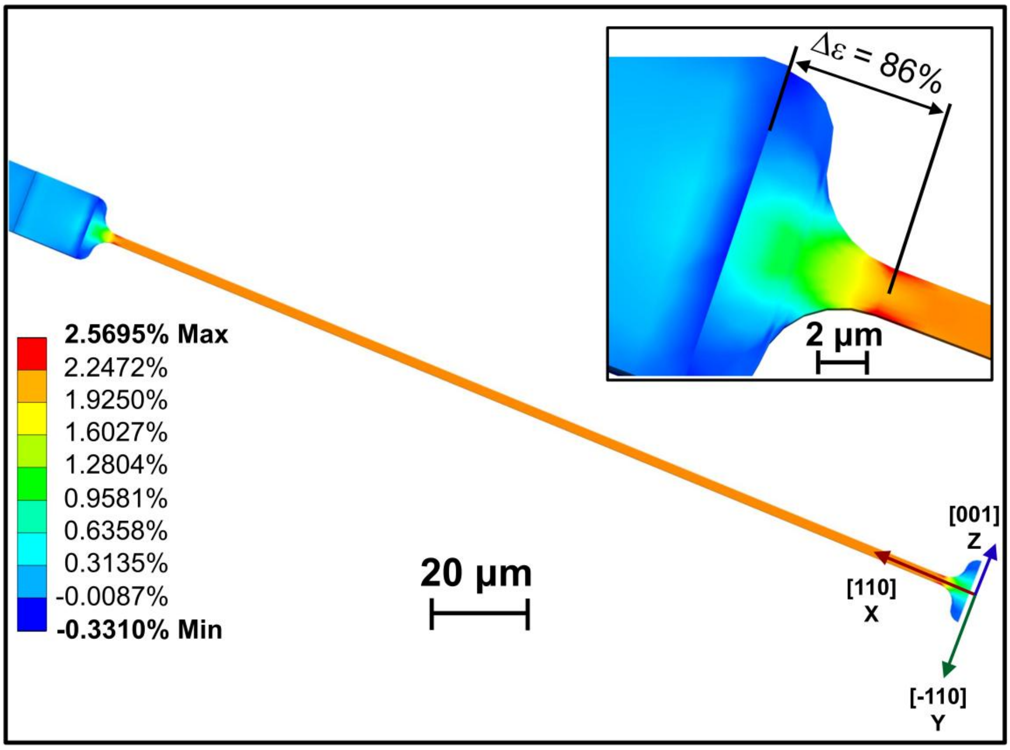

Figure 4.7 Ansys model of a 180 μm-long and 2 μm-wide sample showing the strain distribution along the longitudinal axis X. Sample axes X and Y were rotated by 45° to be aligned with the <110> direction and fixed boundary conditions were imposed at both ends of the structure. The strain distribution along the sample is uniform with a rapid decay (up to 86%) within the first 6 μm at the 'dog-bone' ends (inset).

For all the beam geometries, the maximum difference between the simulated and calculated values of strain is 0.08% (Figure 4.8). The maximum error in strain determined with both techniques is ~0.02% which is very small and therefore not presented in the figures. This error is mainly due to the variation in the actuator Young's modulus determination i.e. 235 ± 10 GPa [108] used with the calculations and finite element simulations.

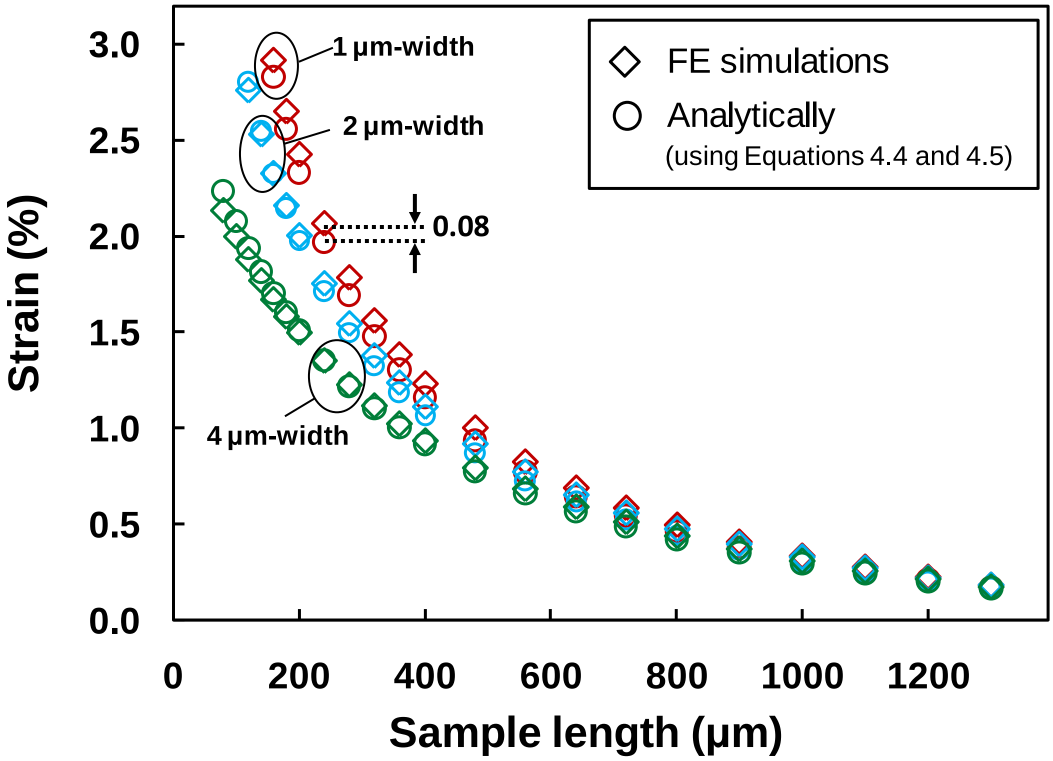

Figure 4.8 FE simulations and analytical calculations of the strain with the length of the samples. The maximum difference ~0.08% strain.

4.4 SEM measurements

SEM measurements were carried out, as discussed in section 4.2.1, to determine strain by direct inspection of the displacement *u* of the attached cursors. The cursor displacement is compared with the estimated values extracted from the analytical calculations using Equation 4.4 and assuming E_s = 169 GPa [113] and E_a = 235 GPa [108]. Figure 4.9 shows the comparison with theoretical calculations (section 4.2.2) for the samples with beam lengths in the range 80 to 1,300 µm. There is a good agreement between SEM and the analytical calculations using Equation 4.4. The maximum error in cursor displacements measured by SEM is ~0.5 µm and the root mean square error is ~0.38 µm. For the 1 µm wide samples, the maximum observed difference between cursor displacement determined by SEM and using Equation 4.4 is 0.14 µm. For the 4 µm wide and 80 µm long samples (shortest samples) however, the maximum observed difference is 0.33 µm. The reason for the increase in differences between cursor displacement values measured by SEM and determined by Equation 4.4 for the 4 µm wide and 80 µm long samples compared with the

1 µm wide samples is related to the gradient of strain at the sample ends shown in section 4.3. Since the cursors used to measure the sample elongation by SEM are located at the beginning of the actuator (Figure 4.4), the measured displacement *u* will be affected by the strain gradient at the 'dog-bone' ends. Also, the ratio between the length of the 'dog-bone' ends and the length of the sample increases with decreasing sample length. Consequently, the differences between the cursor displacements values determined from the SEM measurements and from the analytical calculations will also increase with decreasing sample length. Thus, the strain gradient at the 'dog-bone' ends has to be considered with the strain calculations by SEM.

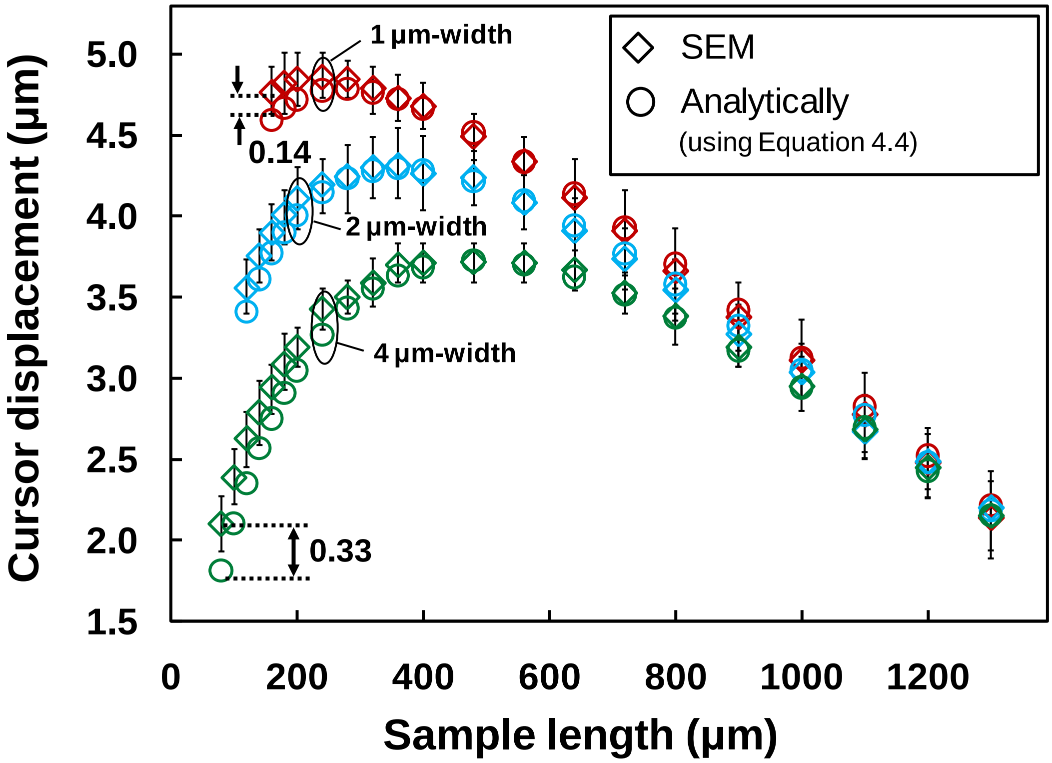

Figure 4.9 SEM measurements and analytical calculations of the cursor displacement *u*. For the 4 µm wide samples, the maximum observed difference is 0.33 µm equivalent to ~0.4% strain. For the narrowest samples the maximum difference is 0.14 µm equivalent to ~0.08% strain.

In order to convert displacement values from SEM cursor measurements to strain, Equation 4.5 has to be modified with a correction factor δ to account for the length of the strain gradient at the 'dog-bone' ends as:

$$\varepsilon = ln\left(\frac{L_{s0} + \delta + u}{L_{s0} + \delta}\right) \tag{4.6}$$

The correction factor δ can be estimated from the finite element simulations and Raman shift measurements (section 4.5). Nevertheless, in order to minimise the impact of the correction factor in the SEM measurements only samples longer than 170 µm were analysed by SEM. Figure 4.10 compares the variation in strain determined by SEM and analytically using Equations 4.4 and 4.5 for three beam widths (1, 2 and 4 µm). For samples longer than 170 µm (dasehd line), the maximum error in strain determined by SEM is ~0.2% and the difference in strain determined with and without the correction factor is estimated to be less than ~0.1%. Values up to 2.7% strain, equivalent to 4.5 GPa, were obtained despite omitting the use of short samples.

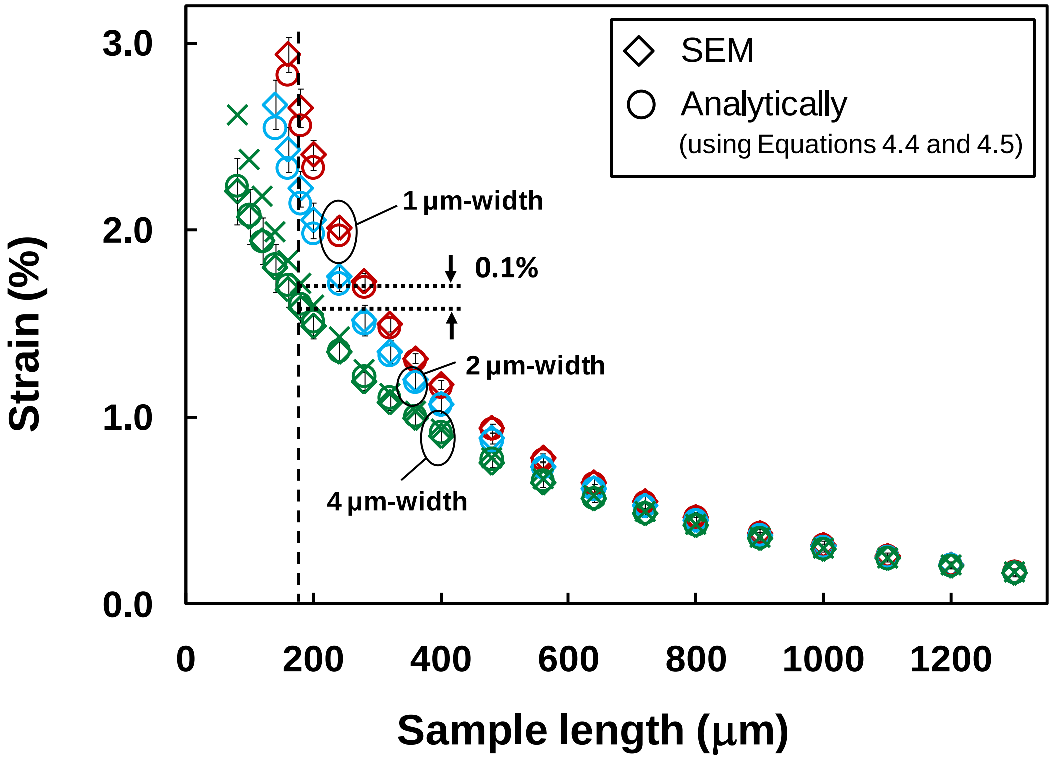

Figure 4.10 The strain variation with sample length obtained from direct SEM measurements of cursor displacement and from analytical calculations using Equations 4.4 and 4.5. Crosses are the strain determination from SEM measurements without applying a correction factor for the gradient of strain at the 'dog-bone' ends. For samples shorter than 170 µm (dashed line), the discrepancies between the strain extracted experimentally (by SEM) and that extracted analytically using Equations 4.4 and 4.5 are larger than 0.1%.

4.5 Raman measurements

4.5.1 Measurement set-up

The Raman measurements were performed in backscattering configuration (used for opaque materials) with a high numerical aperture lens (*NA* = 0.9). A visible laser with wavelength $\lambda = 458$ nm and penetration depth ~300 nm [114] was used to characterise strain in the bulk of the silicon samples and a UV laser with wavelength $\lambda = 364$ nm and penetration depth ~15 nm [114] was used to analyse strain near the surface. The incident laser light of both radiations was polarised in the plane of the sample (along the vertical optical axis). No analyser was used for the scattered radiation.

The frequency of the LO peak in the silicon substrate of the samples was used as a reference (unstrained frequency) for the strain calculations. After calibration, the unstrained frequency was found at $\omega_0 = 520.7$ cm^{-1} (Figure 4.11). This is in agreement with the experimental values of the LO peak in relaxed silicon reported in literature [95].

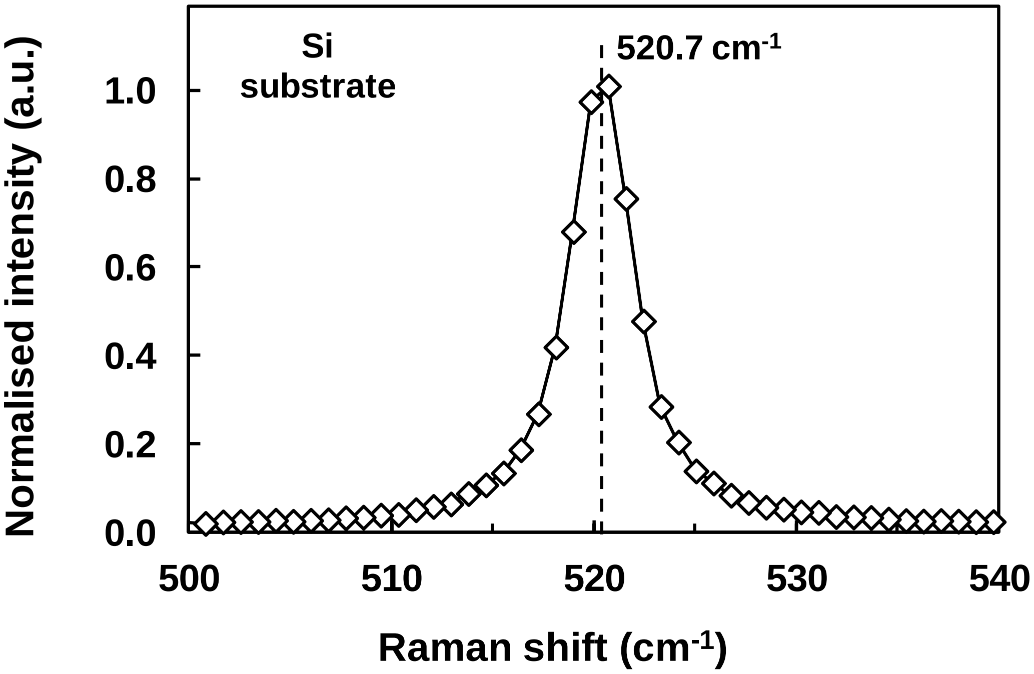

Figure 4.11 The frequency of the LO peak in the silicon substrate (unstrained) of the samples was used as a reference for the strain calculations. After calibration, the unstrained frequency was found at $\omega_0 = 520.7$ cm^{-1}.

For each sample the laser was focused at three locations near the centre of the beam length, with each measurement separated by ~1 μm (Figure 4.12). Each measurement consisted of 3 accumulations and an integration time of 10 seconds per accumulation in order to optimise measurement accuracy. The Raman information presented for each sample corresponds to the median of the three measurements.

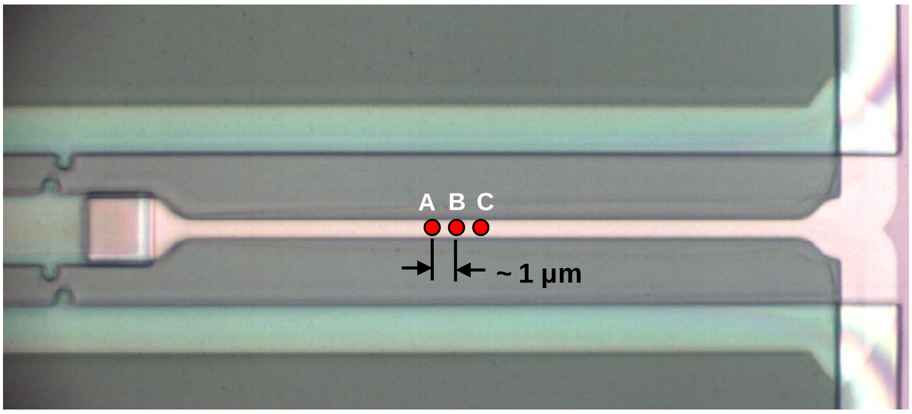

Figure 4.12 Raman measurements were performed in three locations (A, B and C) at the centre of the beam length and separated by ~1μm.

4.5.2 Peak deconvolution

Each peak on the Raman spectrum was deconvolved using a Gaussian-Lorentzian function to determine the peak position (Raman frequency) and thus strain. The deconvolution process is less accurate for peaks located near the silicon substrate peak (520.7 cm^{-1}) as the high intensity of the substrate peak can mask the other peaks (Figure 4.13a). The maximum difference in peak deconvolution between the three measurements at each location was found to be ~0.33 cm^{-1}, corresponding to the samples with the smallest strain (peak position ~520.7 cm^{-1}). For the samples with higher stress levels, the peak position is clearly resolved and the error in peak position is smaller (~0.05 cm^{-1}, which corresponds to ~26 MPa stress) (Figure 4.13b). The error bars for the measurements are very small and are therefore not presented in the figures below.

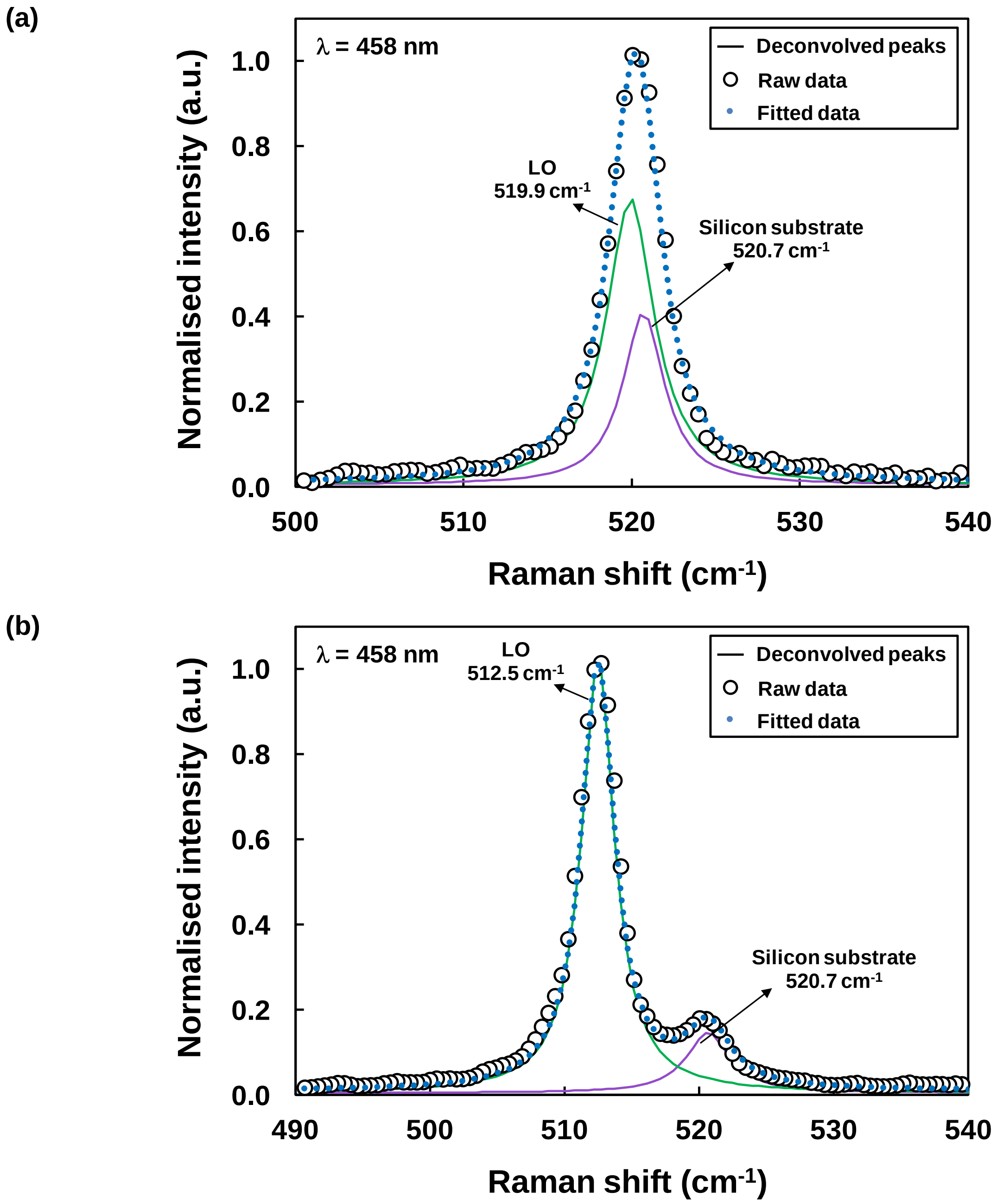

Figure 4.13 Raman spectrum from a low strained sample (a) and a high strained sample (b). Peak deconvolution in high strained samples is accurately resolved.

4.5.3 Laser heating

Raman measurements can be affected by sample heating from the irradiating laser since it may alter the local strain distribution [115, 116]. Using low laser power circumvents heating effects, however higher laser powers increase the Raman spectra peak intensity and aids accurate identification of peak position. To determine the maximum laser power that could be delivered to the sample before data interpretation becomes erroneous through heating effects, preliminary tests were undertaken. The effects of sample heating were considered for the 1 and 4 µm-wide samples by using different power attenuation filters. By changing the filters the power delivered to the sample is varied from 1 – 100%. The resulting Raman peak shift is shown in Figure 4.14.

(a)

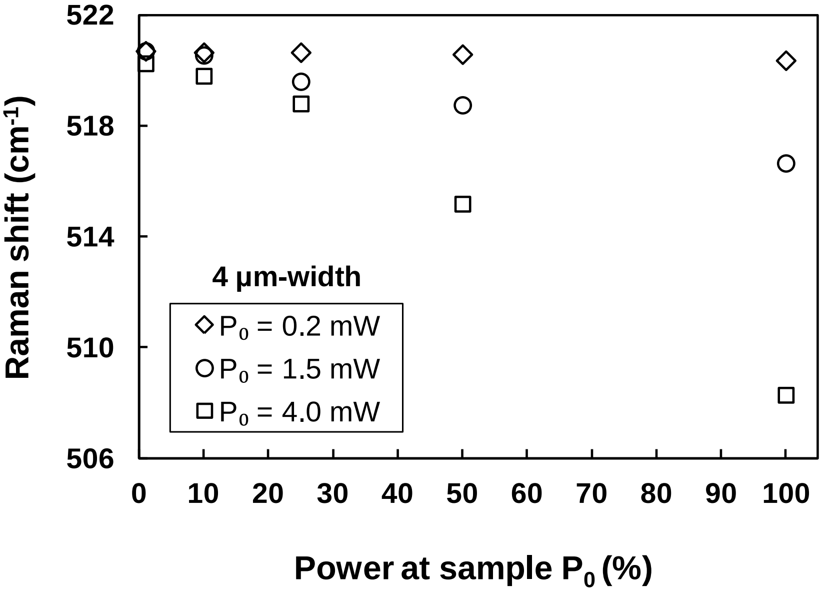

(b)

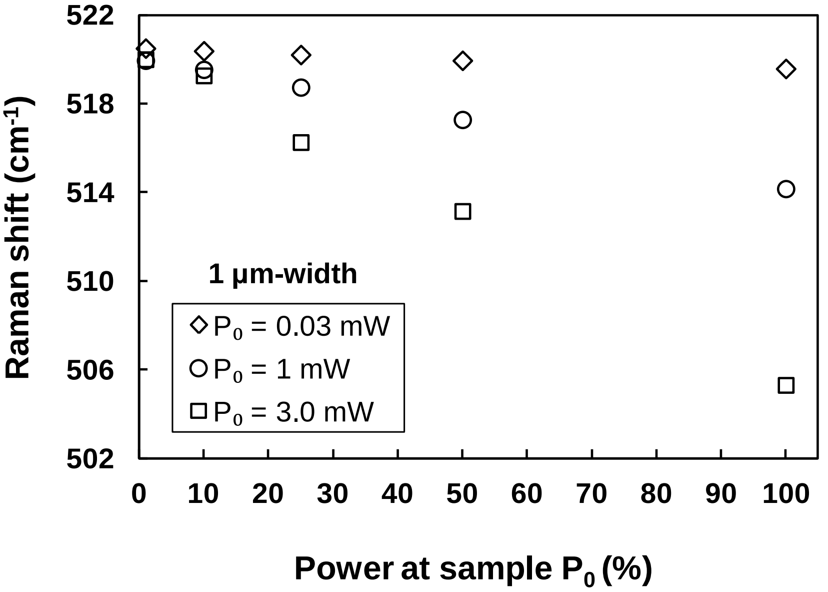

Figure 4.14 Raman power tests on a (a) 4 µm- and (b) 1 µm-wide samples using a visible laser (λ = 458 nm). For 4 µm-wide samples, powers at sample (P_0) higher than 0.2 mW can introduce shifts in the Raman peak position due to laser sample heating rather than strain. For 1 µm-wide samples P_0 must be reduced below 0.03 mW.

For the visible radiation, there is no Raman peak shift observed for delivered laser powers below 30 and 200 µW for the 1 µm- and 4 µm-wide samples respectively, due to a bigger heat evacuation cross-section (Figure 4.14). In order to avoid any heating, the delivered power was kept under 30 µW for all the samples. For the UV radiation, the maximum delivered power could not be measured directly. In order to accurately identify peak positions, a minimum attenuation filter of 10% on the UV laser was necessary. Compared with the visible radiation, an additional Raman peak shift due to sample heating is observed. This is 0.05 cm^{-1} for the 4 µm-wide samples and 0.17 cm^{-1} for the 1 µm-wide samples.

4.5.4 Raman analysis

The evolution of the Raman frequency peak with the sample length for the visible radiation (λ = 458 nm) in the 4 µm-wide samples is depicted in Figure 4.15. There is a progressive down-shift towards lower frequencies at shorter sample lengths. This corresponds to an increase in the applied tensile stress due to longer actuator lengths and agrees with the trends in strain observed by analytical and SEM cursor displacement methods (Figure 4.4).

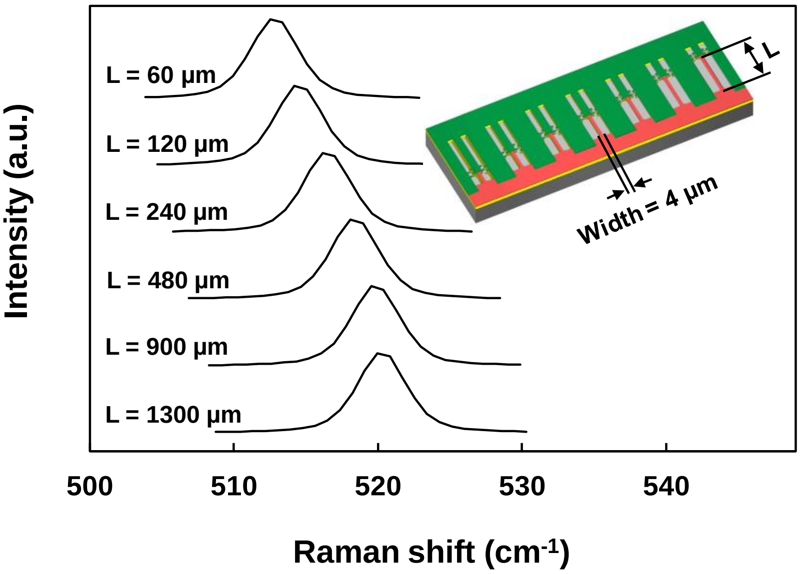

Figure 4.15 Raman spectra for varying sample lengths. There is a progressive downshift of the Raman peak position at shorter sample lengths (longer actuator lengths) due to the proportional increase in applied stress with the actuator length.

Figure 4.16 shows the variation in Raman shift with the beam length for the 1 μm-, 2 μm- and 4 μm-wide samples and lengths ranging from 80 – 1,300 μm.

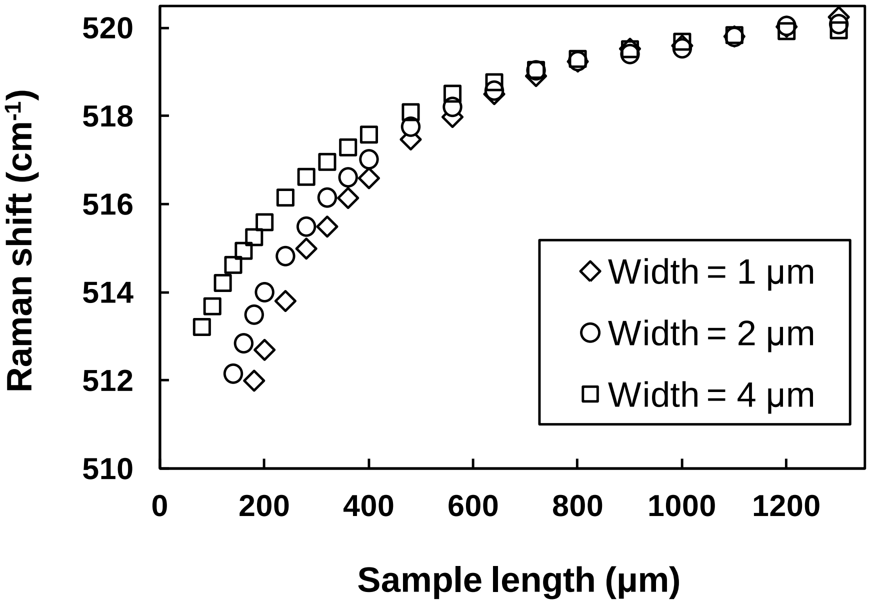

Figure 4.16 Variation in Raman peak position for the samples with lengths ranging from 60 to 1,300 μm.

In order to convert Raman shifts to strain, several equations can be found in the literature, which depend on multiple factors, including the type and direction of the applied stress. For uniaxial stress along the [110] direction, some commonly used equations to convert the Raman shift to strain are:

$$\Delta\omega = -337\,\varepsilon \qquad \text{(Anastassakis \textit{et al.} 1970 [78])} \qquad (4.7)$$

$$\Delta\omega = -339\,\varepsilon \qquad \text{(Chandrasekhar \textit{et al.} 1978 [79])} \qquad (4.8)$$

$$\Delta\omega = -389\,\varepsilon \qquad \text{(Anastassakis \textit{et al.} 1990 [80])} \qquad (4.9)$$

Here, $\Delta\omega$ represents the difference between the frequencies with and without applied stress (ω_0 = 520.7 cm^{-1}). There is no proper explanation however, for the discrepancies between the different coefficients appearing in equations 4.7 – 4.9. Figure 4.17 compares experimental values of strain (determined by SEM and Raman spectroscopy using Equations 4.7 – 4.9 and strain determined analytically and with finite element simulations for the 1, 2 and 4 μm-wide samples.

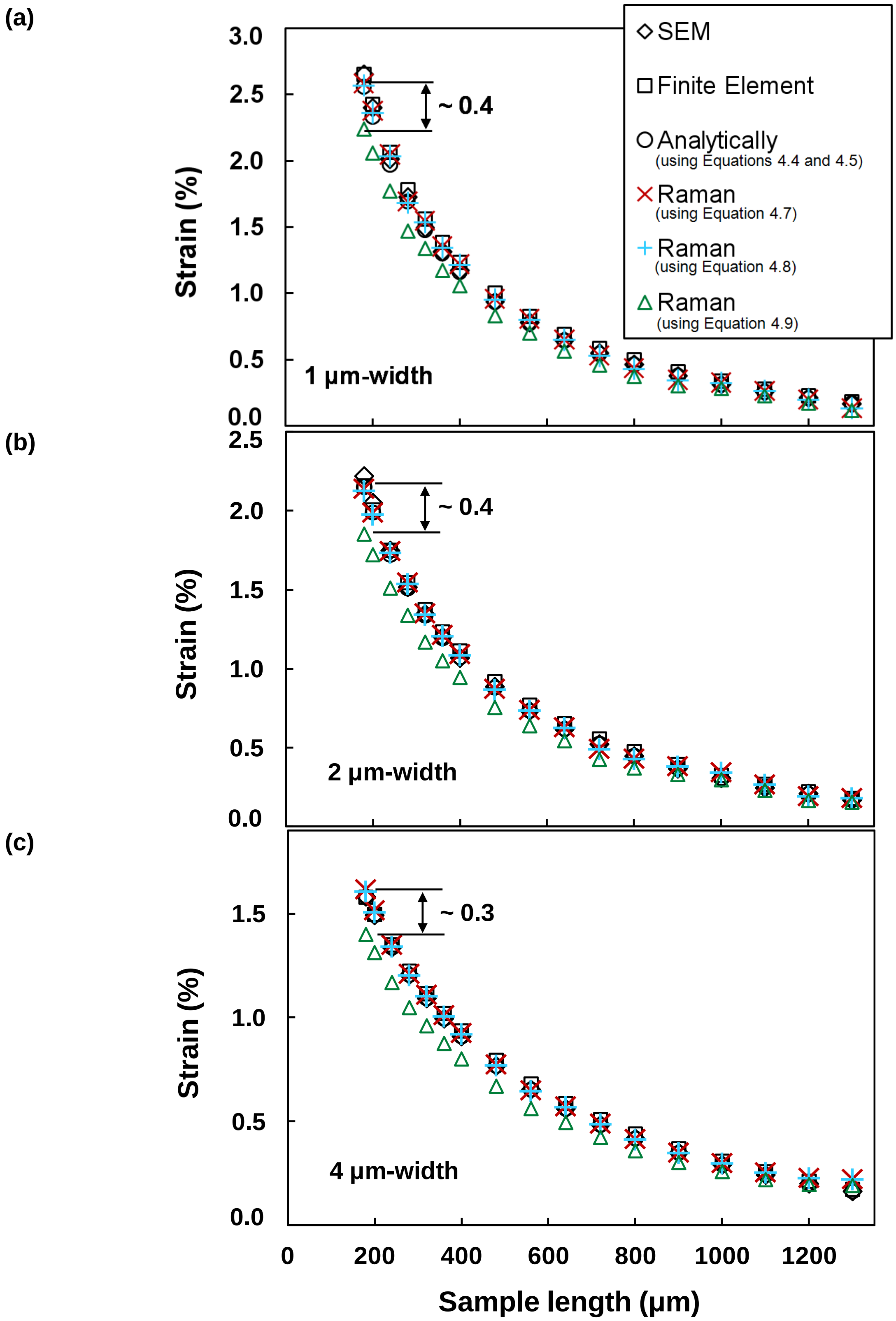

Figure 4.17 SEM, Finite element simulations, analytical calculations (using Equations 4.4 and 4.5) and Raman measurements (using Equations 4.7 - 4.9) show an excellent agreement in strain values for all geometries. (a) 1 µm- (b) 2 µm - and (c) 4 µm - wide samples.

Strain values using equations 4.7 and 4.8 yields an excellent agreement with the SEM cursor displacement measurements of strain and with finite element simulations and analytical calculations using Equations 4.4 and 4.5. There are minor differences between strain determined using equations 4.7 and 4.8. The average discrepancy (using equations 4.7 and 4.8) for the range of lengths is found to be ~0.05% strain (equivalent to 80 MPa stress) between all the techniques. This small error validates the accuracy in conversion from Raman shifts (wave-numbers) to strain. Using Equation 4.9 for the strain determination however, discrepancies up to 0.4% in strain are found compared with the other techniques. This corresponds to ~13% discrepancy in strain determination. Compared with Equation 4.8, strain determined using Equation 4.7 gives a slightly better agreement with the other techniques for the samples with highest values of strain i.e. 1 μm-wide samples. Thus, Equation 4.7 will be used for the conversion of Raman shifts to strain within the rest of this chapter.

Despite the significant discrepancies in strain determination as a result of using the wrong equation to convert Raman shifts to strain, Equations 4.7 – 4.9 are frequently used in the literature to convert Raman shifts to strain with no proper justification. Thus, a thorough study of the origin of the discrepancies between the different coefficients in Equations 4.7 – 4.9 is of paramount importance. This will be covered in detail in chapter 5.

The good agreement obtained between analytical calculations, FE simulations and experiments to determine strain confirms the technique is suitable for accurate analysis of strain in suspended silicon beams, thin films and nanowires in the range 0 – 3% (equivalent to a mechanical stress of 5 GPa). This range of values is similar to that used in other experimental work in bulk silicon [117, 118]. Kozhusko *et al.* [117], using nonlinear surface acoustic wave pulses, measured the critical fracture strength of single crystal silicon and obtained values in the range 5 – 7 GPa. Ando *et al.* [118] measured the fracture strain in single crystal silicon samples 50 μm-long, 50 μm-wide and 5 μm-thick along the [110] direction and found an average fracture strain of 3.4%. The ideal tensile strength has also been calculated for a perfect crystal [119, 120]. A range of values from 15 – 22 GPa was obtained depending on the stress orientation. However, unlike perfect crystals, real materials contain defects such as impurities, dislocations and vacancies which reduce the tensile strength. Thus, the ideal tensile strength must be considered as an upper limit for a real material.

4.5.5 Strain distribution

Strain distribution is particularly important in silicon nanowires where small changes in strain can significantly modify the silicon band gap and electron effective mass m^* [121, 122]. Any such changes cause a change in carrier mobility, which affects performance in nanowire based devices. In order to investigate the strain distribution along the silicon sample, Raman measurements were carried out in three different locations along the sample length; at each end and in the centre. This is in contrast to the previous Raman analysis where each measurement was performed at three locations near the centre of the beam length. Figure 4.18 shows the Raman spectra for the 4 μm-wide samples. Since no significant differences are observed, it is concluded that strain is homogeneously distributed along the sample length.

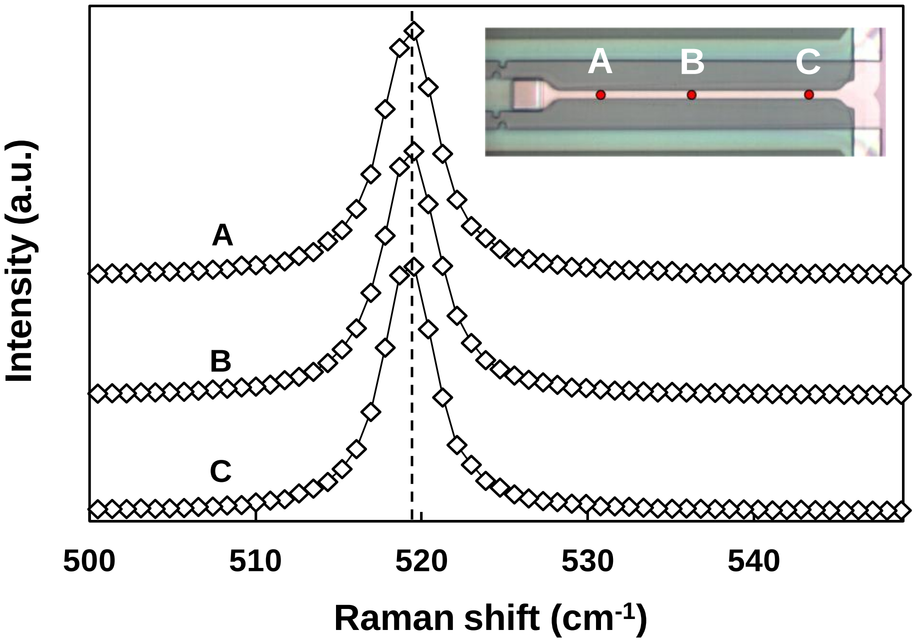

Figure 4.18 Raman spectra corresponding to a 4 μm-wide sample in three different locations (A, B and C) along the sample length. No difference in peak position was found between the three locations indicating a homogenous strain distribution.

In order to test for the normality of the experimental data from the SEM and Raman measurements, standard deviations and normality tests with a 95% confidence interval were carried out for the SEM measurements from the four measured cursor displacements Δu (Figure 4.19a) and Raman frequency shifts $\Delta\omega$ (Figure 4.19b). For both types of strain measurement, p-values > 0.05 are obtained which validates the null hypothesis i.e. a normal distribution. This reduces also the probability of the data being altered by systematic errors e.g. instrument errors. The small standard deviations, $stdev_{\Delta u}$ = 0.09603 μm and $stdev_{\Delta\omega}$= 0.06345 cm^{-1}, confirm good uniformity in both SEM and Raman measurements.

(a)

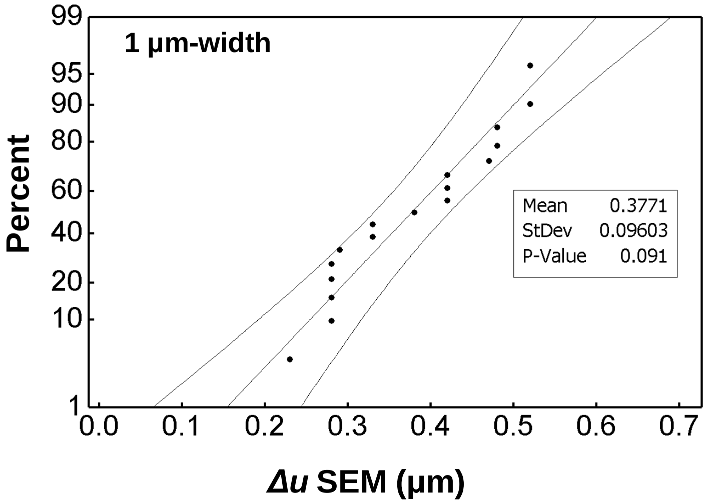

(b)

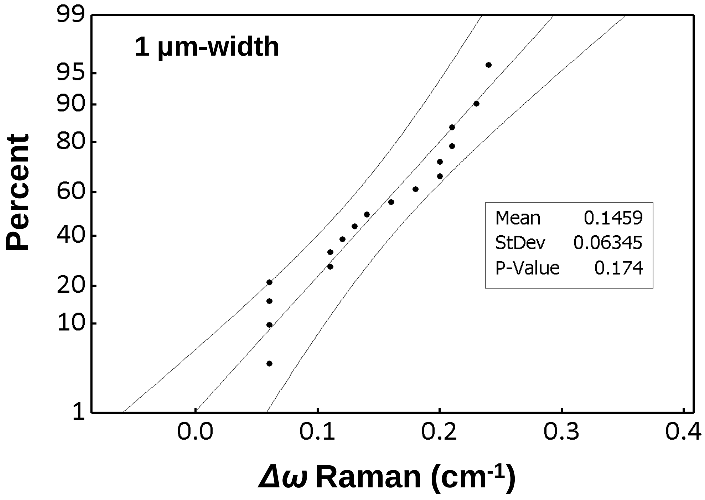

Figure 4.19 Normality tests and p-values of (a) SEM discrepancies of the four cursors measurements per sample, (b) Raman discrepancies in frequency shifts for the three measurement locations per sample. P-values > 0.05 validated the normal distribution of the SEM and Raman shifts measurements.

The strain distribution was also investigated at the sample ends. Figure 4.20 shows a Raman-scan taken at seven different positions along the ‘dog-bone’ end in a 180 μm-long and 2 μm-wide sample.

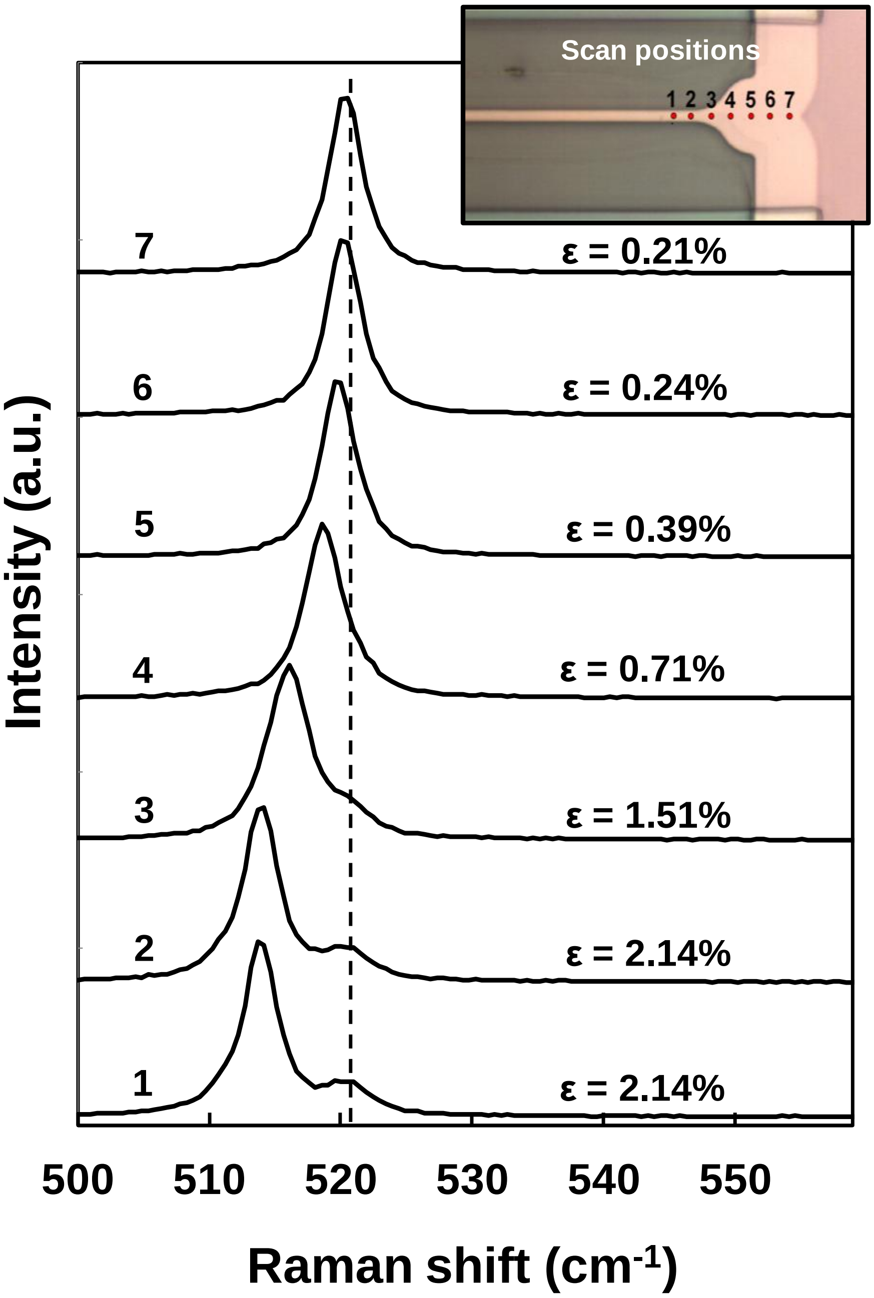

Figure 4.20 Raman-scan in a 180 μm-long and 2 μm-wide sample. The Raman shift (hence strain) is constant at positions 1 and 2 alongside the sample beam and the small peak corresponding to the silicon substrate centred at 520.7 cm^{-1} is still visible. At the ‘dog-bone’ end, the Raman shift rapidly moves towards the unstrained frequency (positions 3, 4 and 5). Outside the ‘dog-bone’ end (positions 6 and 7), the Raman shift practically coincides with that of the silicon substrate.

The strain values determined are in close agreement with those obtained with the finite element simulations (section 4.3) for a sample with the same geometry. At positions 1 and 2 (Figure 4.20), the values of strain are constant ($\varepsilon = 2.14\%$) and equal to those obtained in the centre of the sample. The small peak ~520.7 cm^{-1} corresponds to the silicon substrate. At positions 3 and 4 (beginning of the 'dog-bone' shape), the strain experiences a rapid decay. At the end of the 'dog-bone' shape, position 5, the strain is $\varepsilon = 0.39\%$ which represents ~82% of decay with respect to the value of strain at positions 1 and 2. This is in correspondence with the value obtained with finite element simulations at the same position ~86% (Figure 4.7). Finally, at positions 6 and 7, the strain has already decayed at ~90% (Raman shift ~520.7 cm^{-1}). Figure 4.21 shows the strain distribution with the scan positions shown in Figure 4.20, along the 'dog-bone' end of the sample.

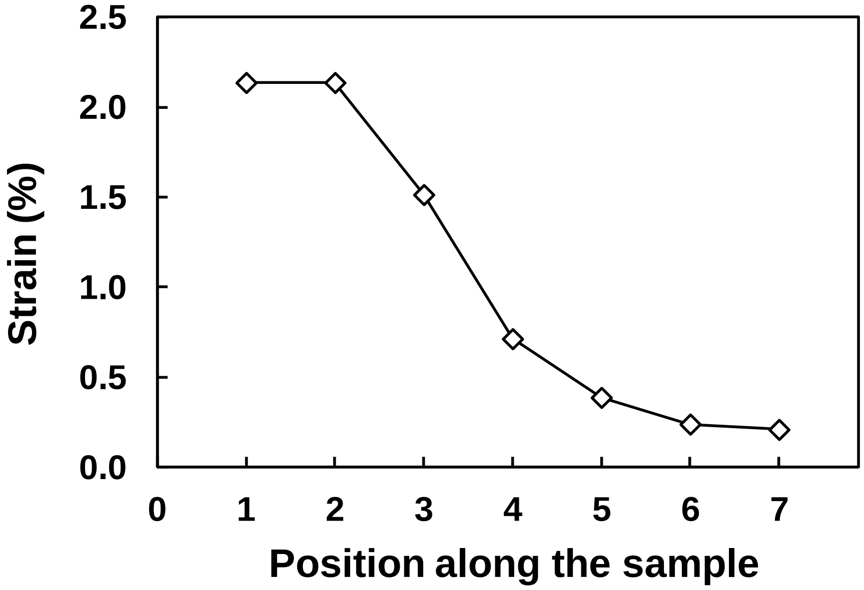

Figure 4.21 Strain distribution along the 'dog-bone' end in a 180 μm-long and 2 μm-wide sample.

4.6 Size effects on silicon properties

The mechanical properties of silicon such as the Young's modulus and fracture strain have been previously reported and found to be size dependent [24, 25, 83, 123]. From the previous SEM and Raman measurements of strain, the dependence of Young's modulus and fracture strain on beam size have also been analysed to verify the size dependency.

4.6.1 Young’s modulus

To analyse the size dependency of the Young’s modulus, five arrays of silicon samples with widths between 1 and 4 μm were studied.

In order to calculate the Young’s modulus, the applied stress is determined using Equation 4.2 which can be written as:

$$\sigma_s = E_a \frac{S_a}{S_s}\left(\frac{u_{free}}{L_{a0}^{free}} - \frac{u}{L_{a0}}\right) \tag{4.10}$$

The Young’s modulus of the sample can be subsequently extracted from the slope of the stress-strain curve by applying a weighted least-square (chi-squared) linear fit. In a weighted least-square fit, the experimental data is fitted considering the differences in the magnitude of the uncertainties (error bars) of the measurements. Equation 4.10 does not require use of Young’s modulus in silicon. This is in contrast of Equations 4.7 – 4.9 to determine strain from Raman shifts. The coefficient in these equations does depend on the Young’s modulus. Thus, strain and stress values determined by Raman cannot be used to extract the Young’s modulus. Therefore only SEM measurements of the cursor displacements will be used to experimentally determine the Young’s modulus. Figure 4.22 shows the stress-strain curve and the fitted line (dashed line) used to determine the Young’s modulus (slope of fitted line) of three samples with widths of 1, 2 and 4 μm. The uncertainties in the slope and intercept of the fitted lines are indicated by the dotted lines. The goodness-of-fit is assesed by computing the reduced chi-squared ($\tilde{\chi}^2$) and R-squared (R^2) figure-of-merits. In a reduced chi-squared test, the model used to fit the experimental data is validated by assessing the value of $\tilde{\chi}^2$. If $\tilde{\chi}^2$is of order of one or less, then there is no reason to question the model. Values of $\tilde{\chi}^2 \gg 1$ generally indicate that the model used to fit the experimental data is not valid. Values of $\tilde{\chi}^2 \ll 1$, do not question the model although they generally indicate that the error bars have been overestimated. The R-squared figure-of-merit is used to estimate the quality of the fitting. A value of $R^2 = 1$ corresponds to a model that perfectly fits the experimental data. Table 4.1 summarises all the results.

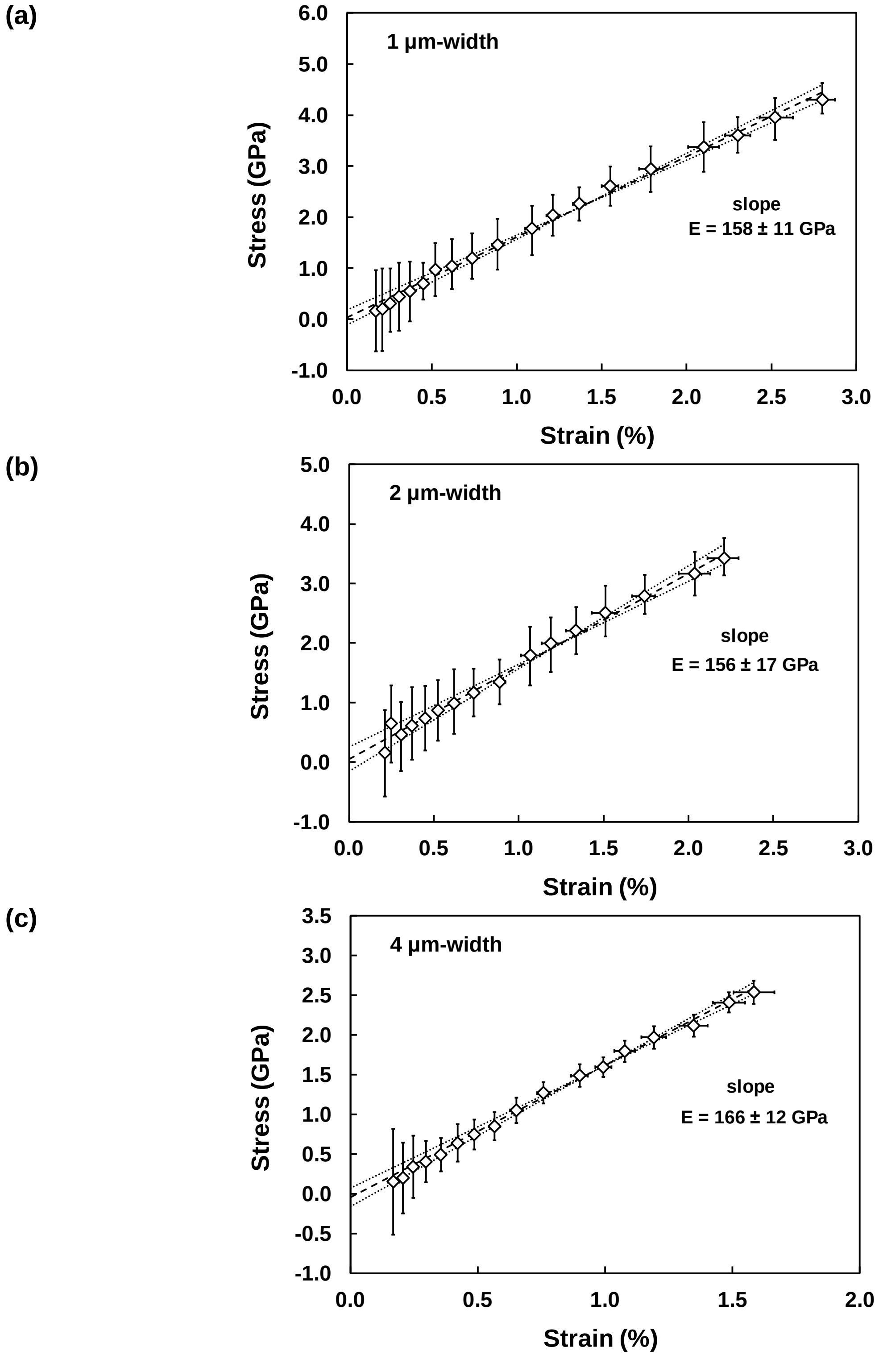

Figure 4.22 The stress-strain curve determined from SEM measurements for the (a) 1 µm- (b) 2 µm- and (c) 4 µm-wide samples. The fitted line (dashed line) is determined from a chi-squared fitting with uncertainties (error bars) in both coordinates. The goodness-of-fit is estimated by the reduced chi-squared and the *R*-squared figure-of-merits (Table 4.1). The uncertainty in the fitted parameters (slope and interception) is indicated by the dotted lines.

Table 4.1. Experimental Young's modulus extracted by SEM measurements.

Sample	**A**	**B**	**C**	**D**	**E**
Width (μm)	4	2	2	1	1
Young's modulus (GPa)	166 ± 12	156 ± 17	168 ± 15	158 ± 11	144 ± 28
Goodness-of-fit					
Reduced chi-squared ($\tilde{\chi}^2$)	0.061	0.050	0.012	0.054	0.018
***R*-squared** (R^2)	0.9961	0.9905	0.9981	0.9360	0.9857
Weighted average (GPa)	161 ± 6				

The main error in the Young's modulus determination, originates from the large variations in stress values (vertical error bars in Figure 4.22). As shown in Equation 4.10, the cursor displacement is multiplied by the factor E_a = 235 GPa. Thus, any small change in cursor displacements will originate a large variation in stress determination. As a consequence of the large uncertainty in stress determination, values of the reduced chi-squared in the range $0.012 < \tilde{\chi}^2 < 0.061$ are obtained. The goodness-of-fit given by the values of *R*-squared ≈ 1 ($0.936 < R^2 < 0.996$) and the values of $\tilde{\chi}^2 < 1$ confirm the quality of the fittings and validate the model.

The Young's modulus extracted from the five samples varies between 144 ± 28 GPa and 168 ± 15 GPa (Table 4.1). This corresponds to a weighted average of 161 ± 6 GPa. This value is (within the accuracy of the measurements) the same of bulk silicon i.e. 169 GPa. The large error in stress measurements determined by the cursor displacements of the samples recommends however, the use of additional techniques to confirm the Young's modulus determined from the samples in this work.

The Young's modulus of 200 nm-thick silicon free-standing beams was previously determined using dynamic resonance-based measurements [124]. An average value of ~160 GPa was found, which is within 5% of the bulk value. This result is the same of that of the present findings obtained by SEM. Discrepancies in Young's modulus evaluated using different techniques have previously been reported. Jin *et al.* [125] compared different techniques to extract the Young's modulus including resonance, electrostatic pull-in instability, SEM and TEM. They observed a general decrease in Young's modulus with decreasing nanobeam thickness, although the onset of the reduction in Young's modulus occurred at higher thicknesses for the resonance and pull-in methods compared with SEM and TEM. A decreasing trend in Young's modulus with decreasing thickness has also previously been reported [32]. Other groups, however, have found no Young's modulus size-dependency, [33, 34, 126] and in some cases a Young's modulus increase with decreasing thickness has been reported [35]. Table 4.2 compares the measurements in this work with these data. *Ab initio* calculations predict a size dependency in Young's modulus for dimensions below 10 nm [127, 128]. Several effects including surface stress [129, 130], native oxide [131-133], loading conditions [134] and material defects [25, 135] are believed to affect the Young's modulus and mechanical properties in general. Nevertheless, none of them can individually explain all the differences observed between various experiments and theory. Sadeghian *et al.* [25] used molecular dynamics simulations to study the size-dependent elasticity of silicon nanocantilevers and concluded that the differences between experiments and theory could be reduced if surface effects, native oxide layers and fabrication-induced defects were included in the simulation. Thus, from the results and all the above comments, it is clear that more experimental investigation is required in order to understand the size effect in the Young's modulus with structures thinner than 200 nm. This will be discussed in section 7.3

Table 4.2. Comparison of Young's modulus extracted using different methods.

Work	**Method**	**Loading**	**Orientation**	**Young's modulus (GPa)**
Li *et al.*[a] [24]	Resonance	Bending	110	142
Gordon *et al.*[b] [35]	AFM force modulation and tapping	Bending	111	100, 140, 185
Sadeghian *et al.*[c] [32]	Electrostatic pull-in instability	Bending	110	161
Sohn *et al.*[d] [34]	AFM indentation	-	111	70 − 240
This work	Static SEM cursor displacement	Tensile	110	161 ± 6
	Dynamic resonant methods	Tensile	110	160

[a] Young's modulus is extracted by cubic interpolation from the supplied data for a thickness of 200 nm.

[b] Selected results for vapour-liquid-solid grown nanowires with diameters of 700, 480 and 450 nm, respectively.

[c] Young's modulus is extracted by cubic interpolation from the supplied data for a thickness of 200 nm.

[d] Chemically grown nanowires with diameters between 80- 600 nm.

4.6.2 Fracture strain

In order to study the effect of structure dimensions on fracture strain, forty arrays of thirty samples, each with different geometries, were studied. Fracture strain was analysed by visual inspection of the last unbroken sample within each array (Figure 4.23). For the 1 µm-wide nanowires, 3.6% strain corresponding to ~6 GPa (assuming $E_{<110>}$ = 169 GPa) stress was obtained. This value is in good agreement with previous experiments in silicon nanowires with similar dimensions along the [110] direction [83].

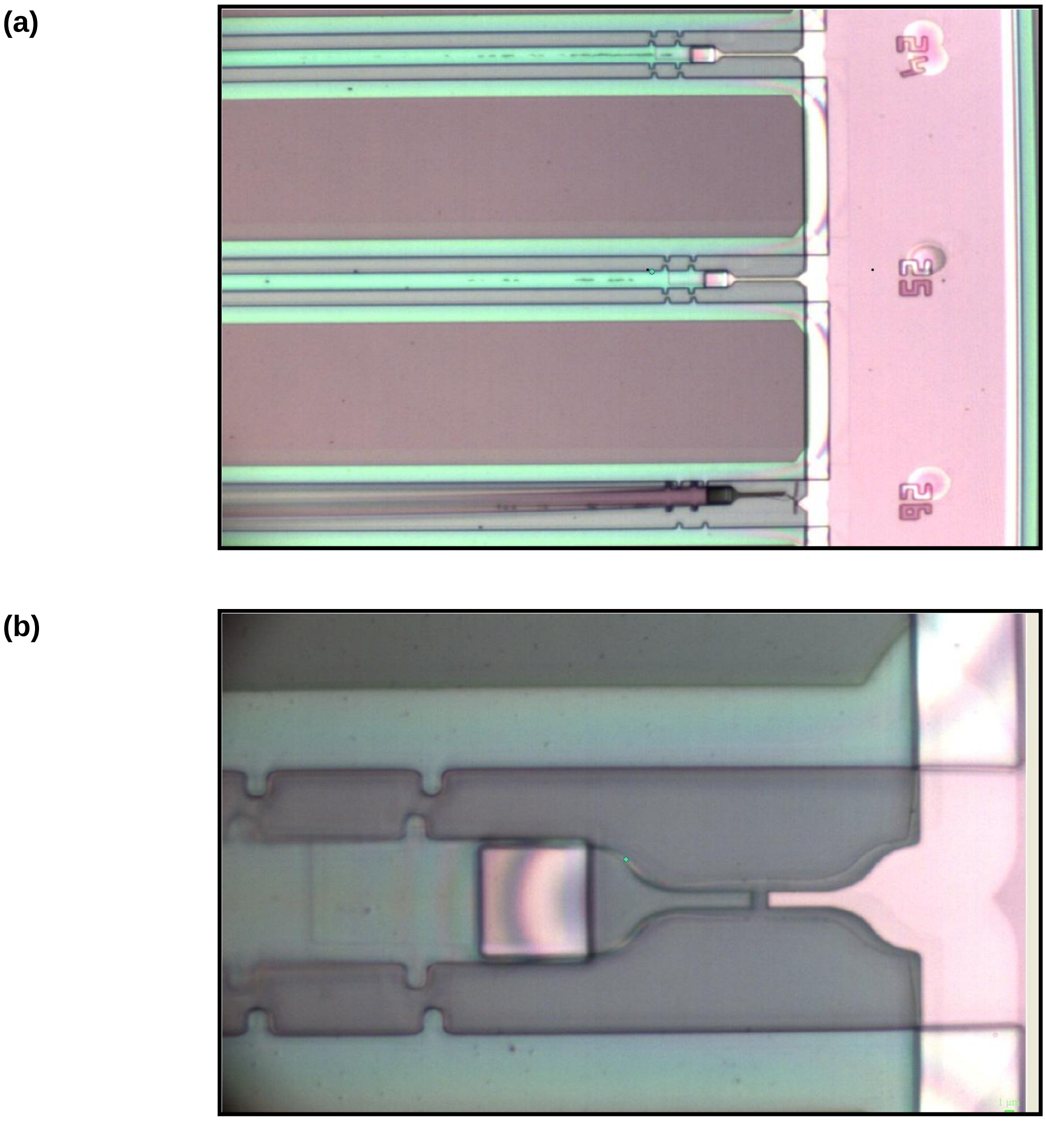

Figure 4.23 Fracture strain was determined by visual inspection of the last unbroken sample (number 25 in this picture); (a) Fracture at the 'dog-bone' end of the sample. (b) Fracture at the centre of the sample (magnified).

Figure 4.24 shows the dependence of fracture strain on the surface-to-volume ratio, calculated from the sample geometry. The data show that fracture strain increases with increasing surface-to-volume ratio although this tendency seems to stabilise at the highest surface-to-volume ratios. An analysis of samples with smaller dimensions would confirm that the general increasing trend is also preserved at high surface-to-volume ratios.

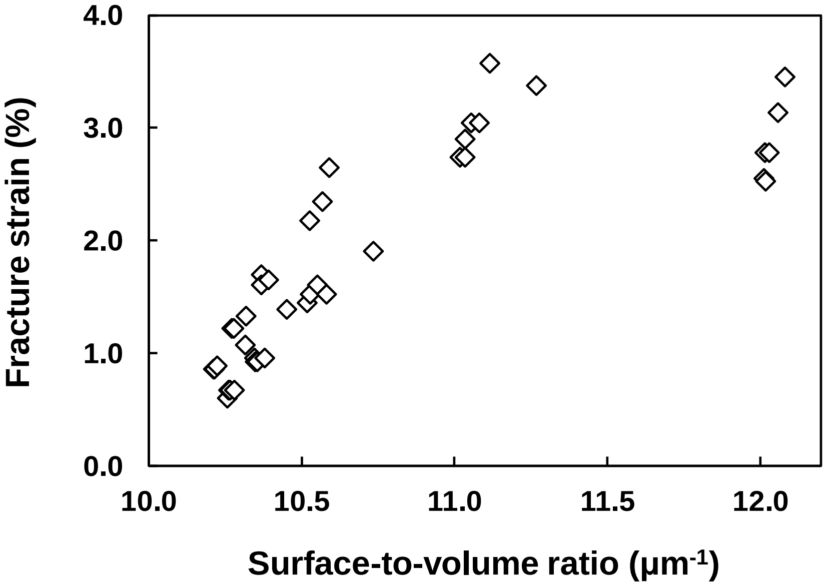

Figure 4.24 The dependence of fracture strain on the surface-to-volume ratio. The increase in fracture strain with increasing surface-to-volume ratio appears to flatten at the highest ratios.

Figure 4.25 shows the same relationship for samples having the same actuator widths but different sample widths. There is a 2% increase in fracture strain (from around 1% to 3%) as the sample width is reduced from 10 μm to 1 μm. These results agree with other recent studies of the fracture strain in silicon [83, 134].

Steighner *et al.* [83] investigated the size-dependence of silicon nanowire strength under tensile stress. Nanowires with diameters ranging from 268 to 840 nm and with different orientations were studied and fracture strain was found to decrease with increasing diameter. The magnitude of the change was further dependent on crystal orientation. Tang *et al.* [134] studied the fracture mechanisms of silicon nanowires grown along the [111] direction with diameters ranging from 9 to 42 nm. Under tension, the silicon nanowires deformed elastically before exhibiting an abrupt brittle fracture, and again there was an increase in tensile strength with decreasing diameter. However, under bending they observed that the silicon nanowires deformed plastically [134].

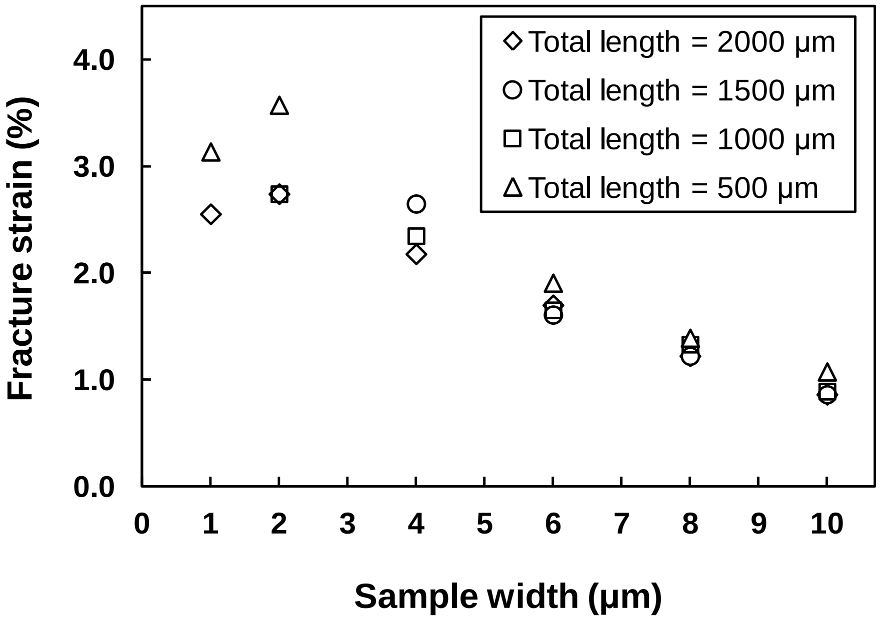

Figure 4.25 The dependence of fracture strain on the sample width. There is an increase in fracture strain with decreasing sample width.

Fracture mechanisms in crystals are complex and have been studied both experimentally and theoretically [83, 117, 134, 136-138]. The fracture process is frequently initiated at a flaw or at a surface defect [136, 138]. Since defects are usually randomly distributed [83], there is a decreased probability of defects in smaller structures [83, 134]. This could explain the increase in fracture strain with decreasing size. However, other factors such as inhomogeneous defect distributions are also believed to affect the fracture strain of brittle materials such as polycrystalline silicon [139].

Previous work on polycrystalline silicon, based on Weibull analysis, predicts the fracture originates on the edges, corners and surface of the specimens [140, 141]. Weibull failure analysis is usually employed to study the fracture of brittle materials based on the weakest link hypothesis (worst flaw) [142]. The validity of the Weibull analysis, however, has been questioned at the micrometer scale [142, 143]. There is little information on the impact of the defects distribution in silicon nanowires under tensile stress but it is possible that this may also play a role in the variation in fracture strain observed here. In the samples studied in this work, fracture was observed to be initiated at different positions along the sample (Figure 4.23).

In 1920, Griffith proposed a theory to explain the differences between the theoretical and the experimental fracture stresss (smaller than the theoretical) in brittle materials [144]. In this theory, the smaller value of the experimental fracture stress compared to the theoretical stress, is explained based on a population of micro-cracks contained within the material. The largest defect in the strained material is the one which originates the failure of the material. According to this theory, the fracture strain ε_f can be expressed as a function of the length a of a pre-existing defect (crack-length) [144]:

$$\varepsilon_f = \sqrt{\frac{\mathcal{G}_\mathrm{c}}{\pi E a}} \tag{4.11}$$

Here, $\mathcal{G}_\mathrm{c}$ is the critical energy per unit area required to extend the surface of a pre-existing crack (which eventually will lead to the failure of the material), and E the Young's modulus of the material. In silicon, $\mathcal{G}_\mathrm{c} \sim 25\ \mathrm{J/m^2}$. Figure 4.26 shows the crack-length values which relate to the fracture strain of the samples shown in Figure 4.25 determined from Equation 4.11.

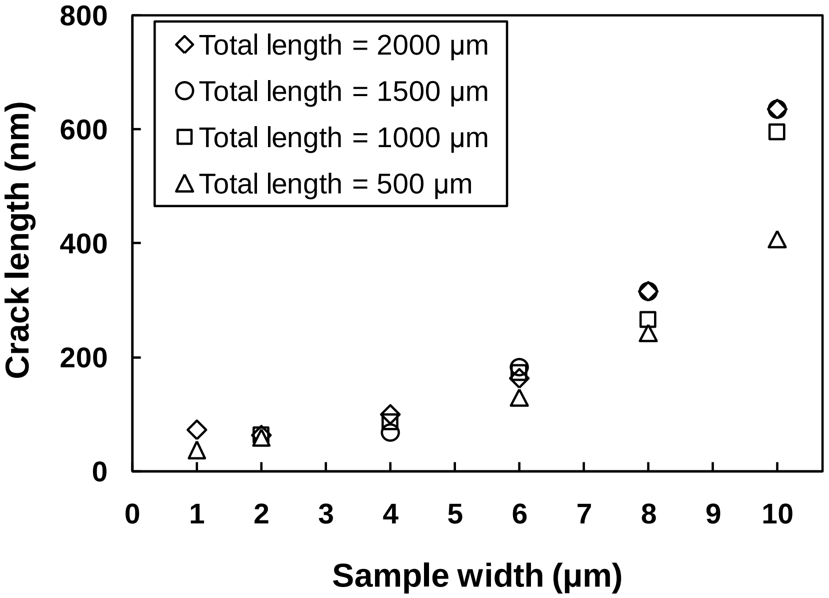

Figure 4.26 Crack length (defect size) determined using Equation 4.11 with the fracture strain of the samples shown in Figure 4.25 for each sample width.

As shown in Figure 4.26, there is a decrease in crack-length with decreasing sample width. However, from Equation 4.11, the fracture strain increases with decreasing crack-length. Thus, the increase in fracture strain observed in Figures 4.24 and 4.25 is most likely related to a decrease of the crack-length with decreasing sample size.

4.6.3 Surface effects

Surface effects such as surface stress, contamination and native oxide can affect the mechanical properties of the material [129, 133, 145]. The surface stress is the reversible work per unit area required to stretch a surface elastically [146]. It originates from the reconstruction, relaxation and molecular adsorption of atoms on the surface [129, 131, 145]. Sadeghian *et al.* [129] studied the effect of changes in the stiffness of silicon cantilevers on their resonance frequency in air and vacuum due to surface stress. They observed that when the cantilever dimensions approach the nanometric regime, the change in resonance frequency due to surface stress becomes significant. Zang *et al.* [145] studied the effect of molecular adsorption on the bending of nanocantilevers and observed that their behavior significantly differs compared with microscopic and macroscopic thick cantilevers. The work shows that the classical Stoney's equation used to calculate the bending curvature required modification when the thickness of cantilevers is reduced to a few nanometers.

Native oxide can also affect the mechanical properties of silicon nanowires. The smaller Young's modulus of SiO_2 (~73 GPa [35, 147]) compared with silicon and the thickness of the native oxide layer itself (2 – 5 nm [131]) are contributing factors to the observed changes to the Young's modulus in nanowires [131, 132].

In order to study the impact of surface effects in the structures, the Raman spectra obtained using the visible and UV lasers have been compared. This has been possible due to the differences in penetration depth in silicon from both laser radiations. The visible laser primarily probes the bulk whereas the UV laser provides information nearest to the surface. Figure 4.27 shows the strain for the 1, 2 and 4 μm-wide samples and lengths in the range 60 – 1,300 μm. Only minor discrepancies in strain between the two radiations are found across the entire range of strains (~0 to 2.7%). These are 0.05%, 0.12% and 0.17%, for the 4, 2 and 1 μm-wide samples respectively. There is a slight increase in discrepancies however with decreasing sample width. Both lasers have penetration depths significantly larger than the thickness of the native oxide layer and both lasers are optically transparent in silicon dioxide. Therefore, additional factors other than surface effects alone must contribute to the discrepancies in strain determined using the two lasers. For example, additional heating from the UV laser heating may play a role. This is discussed in section 4.6.4.

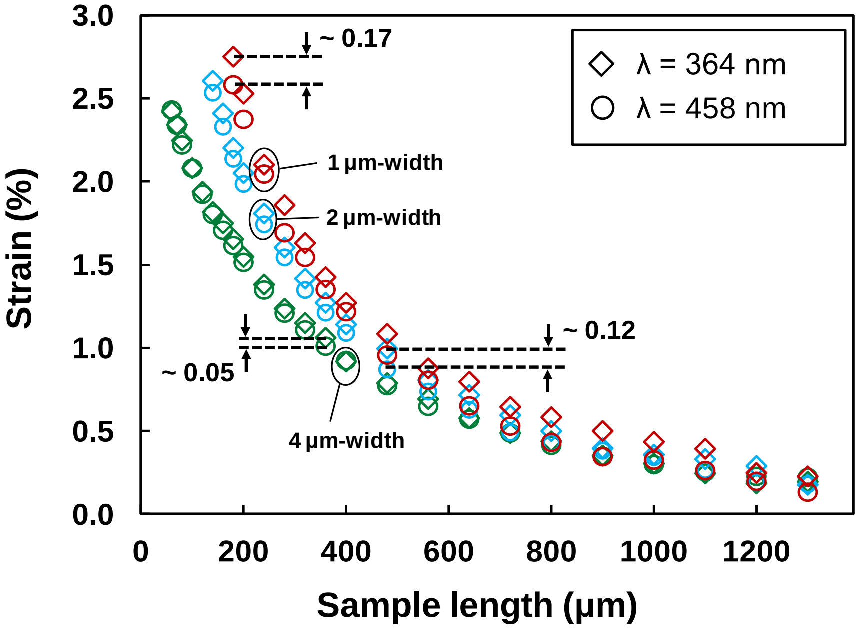

Figure 4.27 The strain determined by Raman measurements using UV and visible radiations. There is good agreement in strain values across the entire range of strains and geometries. Since the UV radiation probes only ~15 nm while the visible radiation probes the whole sample thickness (200 nm), the data suggest that strain is homogenous throughout the structures.

4.6.4 Thermal conductivity

Previous work on the thermal conductivity of solids and liquids, including some covalent semiconductors under pressure [148], concluded that thermal conductivity increases in semiconductors with increasing compressive strain, aside from a small decrease observed in silicon under uniaxial stress. Similar results were found through molecular-dynamics simulations in diamond films [149] and more recently in silicon nanowires and thin films [38]. In general these studies agree on two factors; firstly that stress-induced defects, which increase phonon scattering, dominate thermal conductivity, and secondly, that the overall thermal conductivity continually decreases as the applied strain changes from compressive to tensile. Gan *et al.* [150] investigated the thermal conductivity change with strain in heavily-doped silicon cantilevers with dimensions of 225 × 42 × 5 μm^3 and found that the thermal conductivity increases from 110 to 140 Wm^{-1}K^{-1} when the compressive strain increases from 0.1 to 0.3%. Other factors such as surface stress [40], geometry [38] and defects [39] are also shown to affect the thermal conductivity of nanostructures. However to date, most of the experimental studies of the thermal conductivity variation with strain have been conducted in bulk silicon and no experimental data of the thermal conductivity variation in nanostructures with size and large values of strain is available.

In order to investigate changes in thermal conductivity with strain, the discrepancy in the UV-visible Raman shift of the nanostructures has been used as a measure of heat evacuation. Figure 4.28 shows the variation in UV-visible measurements with strain determined by SEM. For the data acquisition, the UV and visible laser powers are kept constant. Therefore, any significant change in UV-visible discrepancy could indicate a change in heat evacuation related to the thermal conductivity.

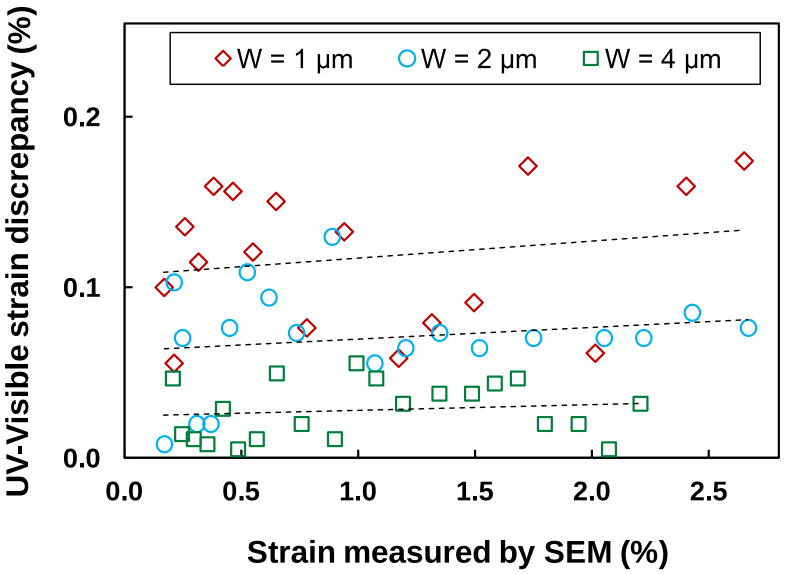

Figure 4.28 The variation in strain discrepancy (between UV and visible Raman measurements) with induced strain (measured with SEM). No clear trend in discrepancies with strain (highlighted by the dotted lines) is observed within the error of the data. The significant scatter in data suggests that other factors such as laser heating have to be considered.

No clear trend in discrepancies with strain is observed (highlighted by the dotted lines) within the error of the data (the scatter in data is too large to ascribe any change in discrepancies to thermal conductivity or surface effects). Consequently, it is believed that other factors such as a less effective heat evacuation in samples with smaller dimensions are likely to dominate the results [151].

4.7 Summary and conclusions

Strain has been characterised in arrays of free-standing silicon beams using Raman spectroscopy, SEM measurements, finite element simulations and analytical calculations. The beams were fabricated with a wide range of geometries under uniaxial tensile stress along the [110] direction. The induced strain was varied and controlled by the beam geometry and fabrication process which enabled a large number of structures to be fabricated on the same chip. The beam geometries (1440 in total) comprised six different widths of 1, 2, 4, 6, 8 and 10 μm with lengths varying between 3 and 1,300 μm and a constant thickness of 200 nm. SEM and Raman data were converted to strain values and compared with the analytical calculations and finite element simulations.

Several equations commonly encountered in the literature for the conversion of Raman shifts to strain, (Equations 4.7 – 4.9), were investigated. An excellent agreement in strain determination was found between Raman (using Equations 4.7 and 4.8), SEM, analytical calculations (using Equations 4.4 and 4.5) and finite element simulations. The small average discrepancies in strain between experiments (~0.05% using Raman and ~0.04% using SEM) and analytical calculations, confirm that accurate conversion of Raman measurements to strain is possible in the range 0 to 3% strain. The good agreement between characterisation techniques also gives validity to the on-chip test structures as a method to produce accurate strain levels in beams over a large range of sample lengths. It was determined however, that discrepancies up to 13% in strain determination could be obtained as a consequence of using the wrong equation to convert Raman shifts to strain. The origin of the discrepancies between the different equations to convert Raman shifts to strain (Equations 4.7 – 4.9) however, is not well understood and it will be investigated in the next chapter.

The dependency of Young’s modulus and fracture strain on beam size has also been studied. Static SEM measurements showed that the Young’s modulus of the 200 nm-thick samples (161 ± 6 GPa) corresponds to that of bulk silicon (169 GPa) within the accuracy of the experiments. This result was shown to be the same as that obtained previously with dynamic resonance methods for the same thickness (160 GPa). The analysis indicated that the Young’s modulus, and its determination, is highly dependent on the measurement technique and also on internal and external factors including surface stress, native oxide and loading conditions.

The fracture strain was investigated by visual inspection of the last unbroken sample within forty arrays of thirty samples and values up to 3.6% were identified. The fracture strain was shown to increase with decreasing beam width and increasing surface-to-volume ratio. The variation in fracture strain with surface-to-volume ratio is considered to arise from a lower probability of defects in smaller structures and the likelihood that fracture originates in material flaws or surface defects. Homogeneity of the defect distribution may also affect the fracture strain. Within the framework of Griffith theory, the increase in fracture strain was shown to be most likely related to a decrease in the defect size (crack-length) for smaller widths.

UV and visible lasers having penetration depths of 15 nm and 300 nm in silicon, respectively, were used to study the role of the surface on the size dependent material properties. Small discrepancies in Raman shift between the two lasers were attributed to a small increase in sample heating using the UV laser. The variation of thermal conductivity with tensile strain was thus investigated using the discrepancy between Raman measurements as a measure of heat evacuation. Within the range of strain studied (0 – 3%), and limited by the scatter in the data, no clear trend in thermal conductivity with strain was found.

Chapter 5. Precise determination of the strain-shift coefficient of silicon nanostructures

5.1 Introduction

In chapter 4, strain was theoretically determined in the beam structures by analytical calculations and with finite element simulations, and experimentally by SEM and Raman spectroscopy. In order to determine strain with Raman spectroscopy, it was shown that several equations commonly encountered in the literature, could be used to convert the Raman shifts to strain. However, it was determined that discrepancies up to 13% in strain determination could be obtained as a consequence of using the wrong equation to convert Raman shifts to strain. The origin of the discrepancies between the different equations to convert Raman shifts to strain is not well understood. Motivated by the excellent agreement in strain determination in the nanostructures with all the techniques described in chapter 4, it is possible now to determine the correct Raman-shift strain relationship for the nanostructures. A thorough analysis on the origin of the discrepancies between the different equations will be also conducted.

A large range of strain-shift coefficients in silicon have been reported in literature. They take into account the type of applied stress, sample and substrate orientation, and optical phonon mode, longitudinal (LO) or transversal (TO) [81, 152, 153]. The strain-shift coefficient also depends upon material constants including the phonon deformation potentials (PDPs) and the elastic compliance coefficients. PDPs relate the different strain components with the phonon frequencies and the elastic compliance coefficients relate the different strain components with stress. The bulk silicon elastic compliance coefficients are well known and agreed upon [87, 88, 111]. However, the phonon deformation potentials for silicon reported in literature differ by up to 30% [80]. Table 5.1 at the end of this section summarises the main experiments and PDPs found in the literature and their corresponding strain-shift coefficients for uniaxial stress along the [110] direction on a (001) plane. The [110] direction and the (001) plane are a common alignment direction and plane in most electronic structures including silicon nanowire-based transistors and MEMS devices [11, 154]. Using the wrong value of PDPs affects the strain determined by Raman measurements. Therefore, it is important to use the correct PDPs and understand why the reported values differ.

The discrepancies in PDP values have generally been ascribed to the impact of the sample surface stress relaxation and opacity of the material to the laser radiation [80, 81, 95]. Other explanations include sample temperature [155] and the impact of the substrate lattice constant where strain was induced by heteroepitaxial growth [81]. The first experiments to determine the phonon deformation potentials in bulk silicon were performed in 1970 by Anastassakis *et al*. [78] and were followed up in 1978 by Chandrasekhar *et al*. [79]. Both experiments were carried out at room temperature and using lasers with energies above the silicon band gap. However, since silicon is opaque under these conditions, both experiments were performed in backscattering configuration (commonly used for opaque materials) and the results were believed to be affected by stress relaxation near the surface. Thus, experiments were repeated in 1990 by Anastassakis *et al*. [80] using an infrared radiation in 90° scattering configuration and cooling the sample down to 110 K. At this temperature, silicon is transparent to the utilised radiation and the phonon deformation potentials obtained were considered to be intrinsically related to bulk silicon. These results have been recently confirmed by Miyatake *et al*. [156]. They studied the surface stress field in a sample using two different methods: ball-on-ring and micro-indentation. In this way they accounted for any possible surface stress which could affect the Raman measurements while using a visible radiation at room temperature. The sample thickness was ~0.3 – 0.4 mm which is of the same magnitude (~1 mm) as that used in the earlier experiments [78-80] for bulk silicon characterisation.

The biaxial strain-shift coefficient of silicon in strained $Si_{1-x}Ge_x$ epilayers pseudomorphically grown on silicon [81] and $Si/Si_{1-x}Ge_x$ heterostructures [153] was also determined for different germanium compositions. In both experiments, radiations above the silicon band gap were used as excitation sources and values for the silicon strain-shift coefficient were obtained which were close to those determined using the PDPs from the 1970 [78] and 1978 [79] experiments. In both [81] and [153], it was determined that stress relaxation near the surface was not a determinant factor behind the differences in strain-shift coefficient obtained using the PDPs from 1990 [80] and those of 1970 [78] and 1978 [79].

More recently, Peng *et al.* [152] investigated the impact of the Raman shift on different silicon substrate orientations. A 488 nm wavelength laser was used on samples with strain values ranging from 0 – 0.1%. The uniaxial strain-shift coefficient obtained for the LO mode along the [110] direction on a (001) substrate orientation (*b* = -336) was similar to that determined using the PDPs of 1970 [78] (*b* = -337) and 1978 [79] (*b* = -339). They also used an analytical expression to determine the best combination of PDPs to fit the experimental data. Table 5.1 gives the PDPs which best fit the experimental data on all substrate orientations and the calculated uniaxial strain-shift coefficients for each optical mode. The strain-shift coefficient corresponding to the LO mode (*b* = -336) is in close agreement with that obtained using the PDPs of the 1970 [78] and 1978 [79] experiments. However, the calculated strain-shift coefficient for the transversal optical mode TO1 (*b* = -511) significantly differs from that determined using the 1970 [78] PDPs (*b* = -384). Instead, the strain-shift coefficient for the TO1 mode is in better agreement with that obtained using the 1990 [80] PDPs (*b* = -486). Furthermore, it appears that the strain-shift coefficient for the TO2 mode undergoes a change in sign and differs from all other experimental PDPs reported to date. Nevertheless, there is no experimental confirmation of the strain-shift coefficients for the TO modes in backscattering from silicon from a (001) surface. This is because under ideal backscattering configuration on a silicon (001) surface the Raman selection rules dictate that only the LO mode is observed. However, experimental observation of the TO modes under backscattering geometry has been recently reported [157]. Characterisation of the TO strain-shift coefficients under backscattering geometry on a (001) surface is important to understand the discrepancies between the reported PDPs, but to date this data is missing. Moreover, despite the recent confirmation [156] of the 1990 [80] PDP values for bulk silicon, there is still no proper understanding why experimental data [81, 152, 153] agrees better with the strain-shift coefficients determined using the PDPs of 1970 [78] and 1978 [79] than 1990 [80].

From all the literature, it can be concluded that numerous factors including the surface stress relaxation, laser radiation and PDPs used for the conversion may all impact the strain-shift coefficient. Consequently, selecting the appropriate strain-shift coefficient for a particular experiment is challenging. In some work, the final selection of PDPs is based simply in the best fit with an analytical model [103, 155]. In other cases, there is no justification given for the selection [158, 159].

It is also evident that all research has been focused on identifying accurate strain-shift coefficients and PDPs for bulk silicon. This is because the PDPs are strongly related to the symmetry of the crystal structure [160]. Therefore the experiments have been performed in materials with thicknesses of hundreds or even thousands of micrometers. The applied stress has also been limited within the range 0 – 2 GPa (Table 5.1). This range is reasonable for bulk silicon characterisation but is too narrow for silicon nanostructures where higher stress values are often favourable [134]. The superior surface-to-volume ratio in nanostructures compared with bulk means that surface or interface effects may define the overall behaviour [161, 162]. Using PDPs or strain-shift coefficients intended for bulk material characterisation of nanometer-scale structures may lead to erroneous conclusions. Consequently, there is an outstanding need to validate the strain-shift coefficient in silicon nanowires and thin films under large values of stress.

In this chapter, the strain-shift coefficient in silicon free-standing beams in backscattering geometry from a (001) surface and uniaxial stress applied along the [110] direction is accurately determined. Stress has been investigated throughout 0 – 4.5 GPa. Characterisation of the transversal optical mode TO1 in backscattering geometry has also been possible by using a high numerical aperture lens [157]. Visible and ultra-violet (UV) radiations have been used to account for the impact of surface stress. The small discrepancies in strain values between the experimental and theoretical techniques described in the previous chapter and with the two laser radiations from Raman measurements have permitted an accurate determination of the strain-shift coefficients.

Table 5.1 Bulk silicon PDPs reported in literature including laser wavelength, temperature, sample thickness, stress and calculated strain-shift coefficients for uniaxial stress along the [110] direction on a (001) surface, as determined from Equations 5.5 – 5.7. Additional details for the experiments can be found in the corresponding references.

Work	**PDPs**	**Laser wavelength**	**Temperature**	**Thickness**	**Stress**	**Strain-shift Coefficient**[b]		
						LO	**TO1**	**TO2**
Anastassakis *et al.* (1970) [78]	$p = -1.2 \times 10^{28}\ s^{-2}$ $q = -1.8 \times 10^{28}\ s^{-2}$ $r = -0.63 \times 10^{28}\ s^{-2}$	632.8 nm	Room temperature	1 mm	Compressive ~0 – 1.15 GPa	-337	-384	-22
Chandrasekhar *et al.* (1978) [79]	$p = -1.43 \times 10^{28}\ s^{-2}$ $q = -1.89 \times 10^{28}\ s^{-2}$ $r = -0.59 \times 10^{28}\ s^{-2}$	647.1 nm	Room temperature	1.3 mm	Compressive ~0 – 1.8 GPa	-339	-405	-66
Anastassakis *et al.* (1990) [80]	$p = -1.85\ \omega_0^2$ $q = -2.31\ \omega_0^2$ $r = -0.71\ \omega_0^2$	1064 nm	110 K	1 – 1.5 mm	Tensile ~0 – 1.2 GPa	-389	-486	-93
Peng *et al.*[a] (2009) [152]	$p = -1.56\ \omega_0^2$ $q = -1.98\ \omega_0^2$ $r = -0.96\ \omega_0^2$	488 nm	Room temperature	-	-	-336	-511	21
This work	-	458 nm 364 nm	Room temperature	200 nm	Tensile ~0 – 4.5 GPa	-343	-485	-

[a] PDPs were determined analytically from the best combination to fit the experimental data on the (001), (110) and (111) substrate orientations.

[b] Strain-shift coefficients from works in 1970, 1978, 1990 and 2009 are calculated using the corresponding PDPs and equations 5.5 – 5.7 in text. Strain-shift coefficients from this work are determined experimentally.

5.2 Effects of strain on the optical phonon frequencies of silicon

The first lattice theory showing the strain effects on the Raman modes in crystals of the diamond structure was developed by Ganesan *et al.* in 1970 [160]. It was shown that the frequencies ω in the presence of strain of the three optical phonons at the $\boldsymbol{k} \approx 0$ zone centre are associated with a second rank force constants tensor $\boldsymbol{G_{\alpha\beta}}$ given by the equation

$$\sum_{\beta} G_{\alpha\beta}\eta_{\beta} = \omega^2\eta_{\alpha}, \quad \alpha, \beta = 1,2,3, \tag{5.1}$$

where $\boldsymbol{\eta_{\alpha}}$ are the eigenvectors of the three optical phonons. The coefficients of the $\boldsymbol{G_{\alpha\beta}}$ tensor can be expanded in powers of strain to terms linear as

$$\boldsymbol{G_{\alpha\beta}} = G_{\alpha\beta}^{0} + \sum_{\mu\nu} \frac{\partial G_{\alpha\beta}}{\partial \varepsilon_{\mu\nu}} \varepsilon_{\mu\nu} = G_{\alpha\beta}^{0} + \sum_{\mu\nu} G_{\alpha\beta\mu\nu}^{\varepsilon}\, \varepsilon_{\mu\nu}, \quad G_{\alpha\beta}^{0} = \omega_0^2 \delta_{\alpha\beta}, \quad \mu, \nu = 1,2,3, \tag{5.2}$$

where $\boldsymbol{G_{\alpha\beta}^{0}}$ is a diagonal second rank tensor whose components are force constants in the absence of strain, $\boldsymbol{\varepsilon_{\mu\nu}}$ is the second rank strain tensor, ω_0 is the frequency in the absence of strain, $\delta_{\alpha\beta}$ is the Kronecker delta and $\boldsymbol{G_{\alpha\beta\mu\nu}^{\varepsilon}}$ is a fourth rank tensor whose components represent the changes in force constants due to applied strain.

From thermodynamic and symmetry considerations for a cubic crystal, the 81 components of the fourth rank tensor $\boldsymbol{G_{\alpha\beta\mu\nu}^{\varepsilon}}$ reduce to only three independent components p, q and r, called phonon deformation potentials.

$$\begin{aligned} G_{1111}^{\varepsilon} &= G_{2222}^{\varepsilon} = G_{3333}^{\varepsilon} = p \\ G_{1122}^{\varepsilon} &= G_{2233}^{\varepsilon} = G_{1133}^{\varepsilon} = q \\ G_{1212}^{\varepsilon} &= G_{2323}^{\varepsilon} = G_{1313}^{\varepsilon} = r \end{aligned} \tag{5.3}$$

All the other components of the $\boldsymbol{G_{\alpha\beta\mu\nu}^{\varepsilon}}$ tensor are zero. Combination of Equations 5.1, 5.2 and 5.3 yields the secular equation:

$$\begin{vmatrix} p\varepsilon_{11} + q(\varepsilon_{22} + \varepsilon_{33}) - \lambda & 2r\varepsilon_{12} & 2r\varepsilon_{13} \\ 2r\varepsilon_{12} & p\varepsilon_{22} + q(\varepsilon_{33} + \varepsilon_{11}) - \lambda & 2r\varepsilon_{23} \\ 2r\varepsilon_{13} & 2r\varepsilon_{23} & p\varepsilon_{33} + q(\varepsilon_{11} + \varepsilon_{22}) - \lambda \end{vmatrix} = 0\,, \tag{5.4}$$

with eigenvalues $\lambda_i = \omega_i^2 - \omega_0^2$.

Since the strain tensor has six components, solutions for the secular equation can be very complex. Nevertheless, for uniaxial or biaxial stresses, Equation 5.4 can be readily diagonalised. All the strain components and PDPs in Equation 5.4 are expressed in the crystal coordinate system i.e. [100], [010] and [001]. Thus, solutions in a different coordinate system will first require rotating the strain or stress tensor from the sample system to the crystal coordinate system (or alternatively, the secular equation to be expressed in the new coordinate system). Figure 5.1 depicts the sample coordinate system used in this work.

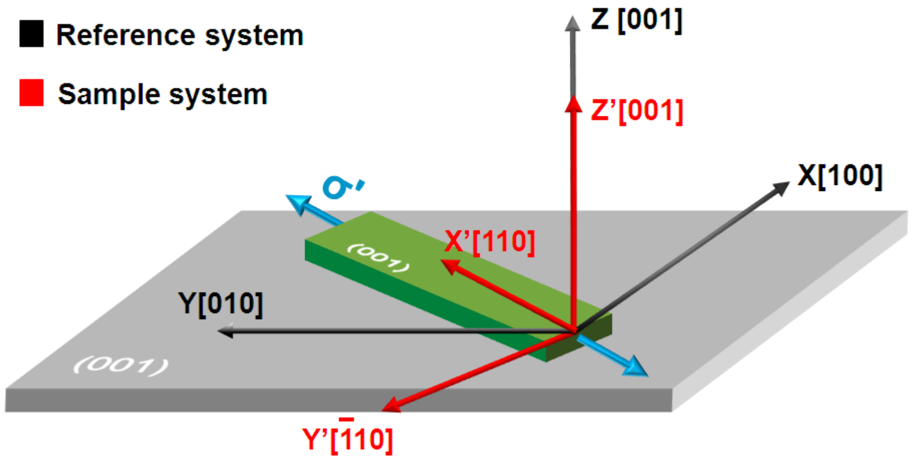

Figure 5.1 Reference and sample coordinate system used in this work. Samples are oriented along the [110] direction on a (001) surface.

For backscattering from a (001) surface and uniaxial stress σ' (prime denotes sample system) along the [110] direction, the solution of the secular equation results in [103]:

$$\begin{aligned}
\Delta\omega_1 &= \frac{[p(S_{11}+S_{12})+q(S_{11}+3S_{12})+rS_{44}]}{4\omega_0}\sigma' \\
\Delta\omega_2 &= \frac{[p(S_{11}+S_{12})+q(S_{11}+3S_{12})-rS_{44}]}{4\omega_0}\sigma' \\
\Delta\omega_3 &= \frac{[pS_{12}+q(S_{11}+S_{12})]}{2\omega_0}\sigma'
\end{aligned} \tag{5.5}$$

Here, S_{11}, S_{12} and S_{44} are the three independent components of the fourth rank compliance tensor, which relates strain and stress in the crystal coordinate system. $\Delta\omega_i$ is the frequency difference of the normal vibrational mode i between the frequencies measured with and without the applied stress, i.e. $\Delta\omega_i = \omega_i - \omega_0$. Depending on the incident and analysed polarisations, only certain vibrational modes may be observed [95]. Using the Raman polarisation rules, it is easy to show that in backscattering geometry from a (001) surface only the third mode can be observed. This corresponds to the longitudinal optical LO phonon. The two transversal optical TO phonons are forbidden.

Using Hooke's law, the strain components in the sample coordinate system used in this work (Figure 5.1) are [154]:

$$\begin{aligned} \varepsilon'_{11} &= \left[\frac{1}{2}(S_{11} + S_{12}) + \frac{1}{4}S_{44}\right]\sigma' \\ \varepsilon'_{22} &= \left[\frac{1}{2}(S_{11} + S_{12}) - \frac{1}{4}S_{44}\right]\sigma' \\ \varepsilon'_{33} &= S_{12}\sigma' \\ \varepsilon'_{23} &= \varepsilon'_{13} = \varepsilon'_{12} = 0 \end{aligned} \tag{5.6}$$

Combining Equations 5.5 and 5.6 results in a set of linear equations:

$$\Delta\omega_i = b_i \varepsilon'_{ii} \tag{5.7}$$

Here, b_i is the strain-shift coefficient which relates the observed Raman shift with the different strain components. Thus, numerous factors such as sample geometry, polarisation of the incident and analysed light and type of stress can generate different strain-shift coefficients. It also becomes clear from Equations 5.5 and 5.6 that the strain-shift coefficient depends on the PDPs and compliance coefficients.

5.3 Strain-shift coefficient determination

The strain-shift coefficient depends on the Raman mode being characterised. From Equation 5.5, uniaxial stress along the [110] direction results in three singlets with Raman frequency ω_i. In backscattering geometry from a (001) surface the Raman shift $\Delta\omega_3$ relates to the longitudinal optical mode LO, $\Delta\omega_1$ relates to the transversal optical mode TO1, and $\Delta\omega_2$ relates to the transversal optical mode TO2.

5.3.1 Longitudinal optical mode

The strain-shift coefficient is deduced from the values of strain (obtained from analytical calculations, finite element simulations and SEM measurements) and the Raman shifts (obtained from Raman measurements using a visible and UV radiation) determined in the previous chapter. Figure 5.2 shows the variation in Raman shift with the strain, obtained by SEM using Equation 4.5 for the 1, 2 and 4 µm-wide samples and measurements using the visible and UV radiations.

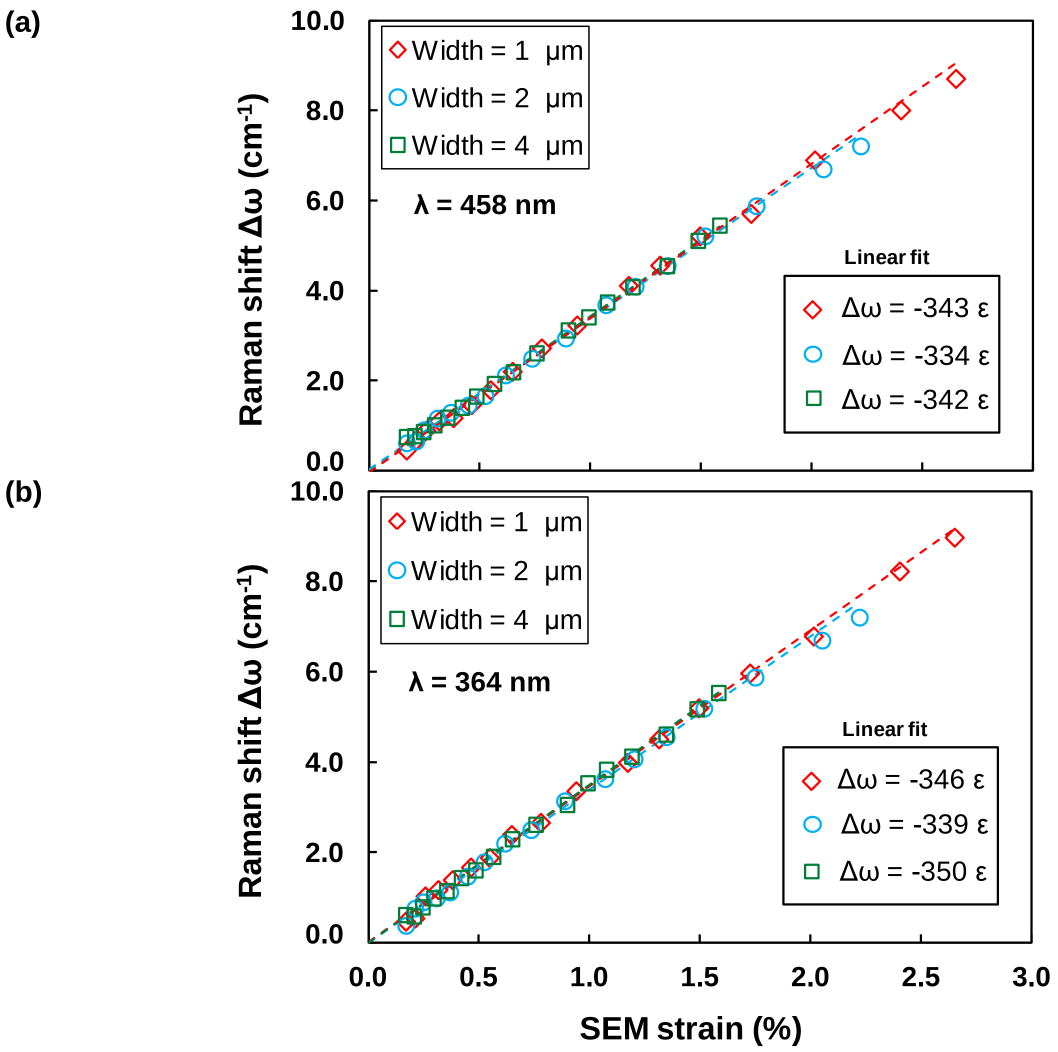

Figure 5.2 Strain-shift coefficients determined in this work. Strain values were determined by SEM. Raman shifts were obtained with (a) the visible radiation and (b) the UV radiation. Reduced chi-squared values in the range $1.30 < \tilde{\chi}^2 < 1.94$ for the visible radiation and $1.33 < \tilde{\chi}^2 < 2.20$ for the UV radiation with uncertainties ~± 2 cm^{-1} in the strain-shift coefficients (slope of the fit) were obtained.

There is a linear relation between the Raman shift and strain in the range 0 – 2.7%. The strain-shift coefficient is directly calculated from the slope of the strain-shift curve using a chi-squared linear fit. The goodness-of-fit was tested by the reduced chi-squared figure-of-merit and values in the range $0.65 < \tilde{\chi}^2 < 2.25$ were obtained for all the fits. The strain-shifts coefficients calculated from this data vary between -334 ± 2 cm^{-1} and -350 ± 2 cm^{-1} for all the geometries. The negative strain-shift coefficients relate to a down-shift in Raman frequency with tensile strain.

The strain-shift coefficient was also determined by analytical calculations (using Equations 4.4 and 4.5) of strain (Figure 5.3) and finite element simulations (Figure 5.4) of strain using the Raman shifts of the UV and visible radiations for all the geometries. The maximum difference in Raman shift between the two radiations for a given value of strain is ~0.2 cm^{-1}, corresponding to ~0.06% strain using the calculated strain-shift coefficients.

Table 5.2 summarises the strain-shift coefficients and the goodness-of-fit (reduced chi-squared) obtained with the visible and UV radiations for all the sample geometries and the three techniques used to calculate strain. Each value in Table 5.2 relates to the weighted average strain-shift coefficients obtained for the 1, 2 and 4 μm-wide samples. This results in a strain-shift coefficient $b_3 = -343 \pm 1$ cm^{-1}.

Table 5.2 Longitudinal strain-shift coefficients and goodness-of-fit obtained in this work.

Strain determination	**Radiation**	
	Visible (λ = 458 nm)	**UV (λ = 364 nm)**
Analytically using Equation 4.5	-340 ± 2 ($0.65 < \tilde{\chi}^2 < 2.21$)	-346 ± 2 ($1.48 < \tilde{\chi}^2 < 1.74$)
Finite element simulation	-342 ± 2 ($1.95 < \tilde{\chi}^2 < 2.15$)	-341 ± 2 ($2.03 < \tilde{\chi}^2 < 2.25$)
SEM images of cursor displacements	-340 ± 2 ($1.30 < \tilde{\chi}^2 < 1.94$)	-348 ± 2 ($1.33 < \tilde{\chi}^2 < 2.20$)
Weighted average	-340 ± 1	-346 ± 1
	-343 ± 1	

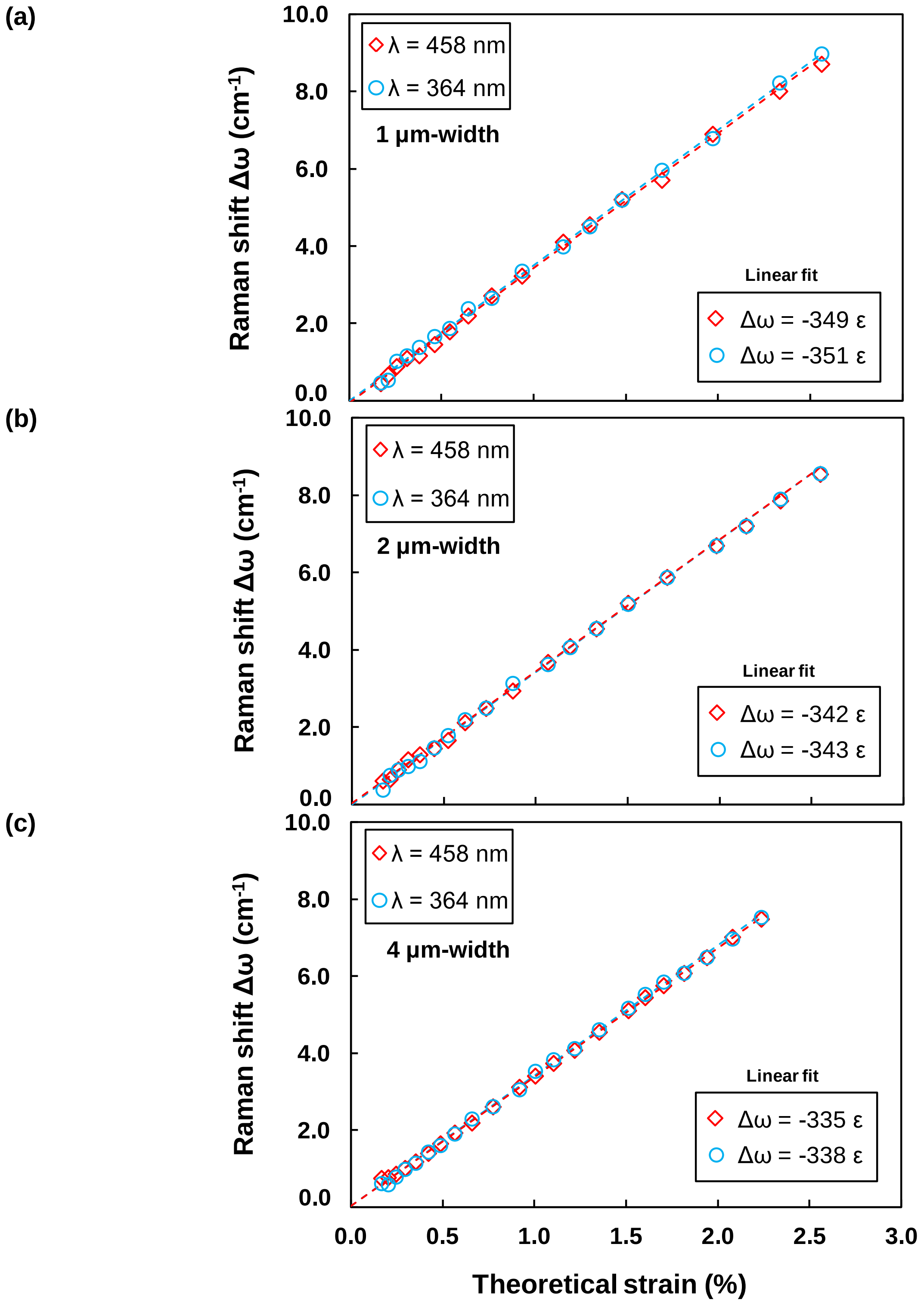

Figure 5.3 Strain-shift coefficients determined in this work. Strain values were determined analytically using Equation 4.5. (a) 4µm- (b) 2µm- and (c) 1µm- wide samples. Reduced chi-squared values in the range $0.65 < \tilde{\chi}^2 < 2.21$ for the visible radiation and $1.48 < \tilde{\chi}^2 < 1.74$ for the UV radiation with uncertainties ~± 2 cm^{-1} in the strain-shift coefficients (slope of the fit) were obtained.

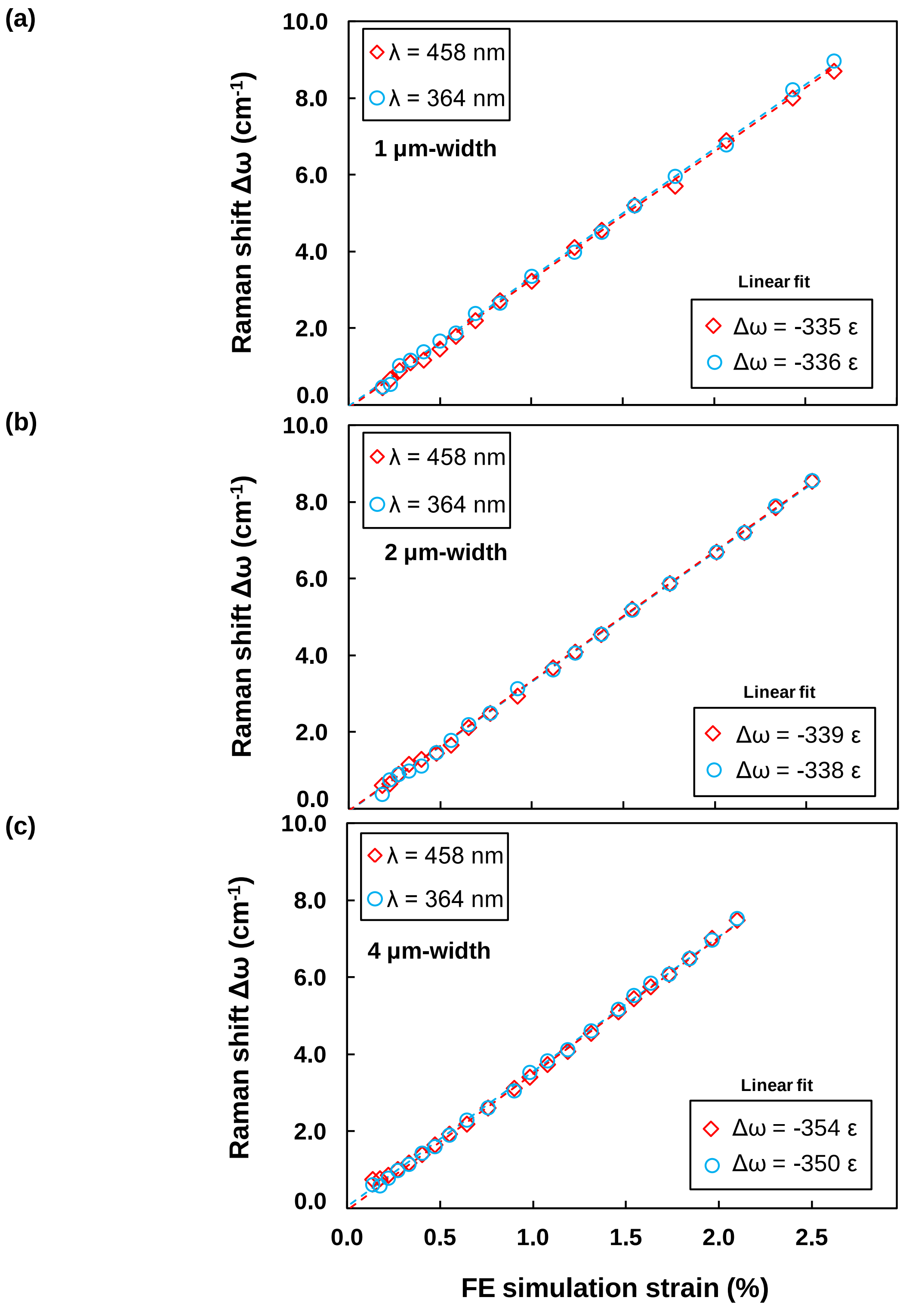

Figure 5.4 Strain-shift coefficients determined in this work. Strain values were determined by finite element simulations (a) 4µm- (b) 2µm- and (c) 1µm- wide samples. Reduced chi-squared values in the range $1.95 < \tilde{\chi}^2 < 2.15$ for the visible radiation and $2.03 < \tilde{\chi}^2 < 2.25$ for the UV radiation with uncertainties ~± 2 cm^{-1} in the strain-shift coefficients (slope of the fit) were obtained

The strain-shift coefficient in bulk silicon along the [110] direction can also be determined from PDPs in literature using Equations 5.5 - 5.7. Table 5.1 gives the three main experimentally extracted PDPs in silicon reported to date and their corresponding strain-shift coefficients [78-80]. Figures 5.5 - 5.6 compare the strain determined in this work using the visible radiation with strain determined using the strain-shift coefficients listed in Table 5.1 for a 1, 2 and 4 μm-wide samples. The strain in abscissas was determined by the SEM technique. Figures 5.5 - 5.6 show that the values of strain (hence the average strain-shift coefficient) determined in this work are in very close agreement with those calculated using the PDPs determined in 1970 [78] and 1978 [79]. However, they significantly differ from those obtained using the PDPs determined in 1990 [80] and the discrepancy steadily increases with increasing applied strain. Using the PDPs of 1990 [80] and assuming that the true strain is obtained with the PDPs of 1970 [78], the relative error in strain for a given Raman shift is ~13%. Using the PDPs of 1970 [78] and assuming the true strain is obtained with the PDPs of 1990 [80], the relative error in strain is ~15%.

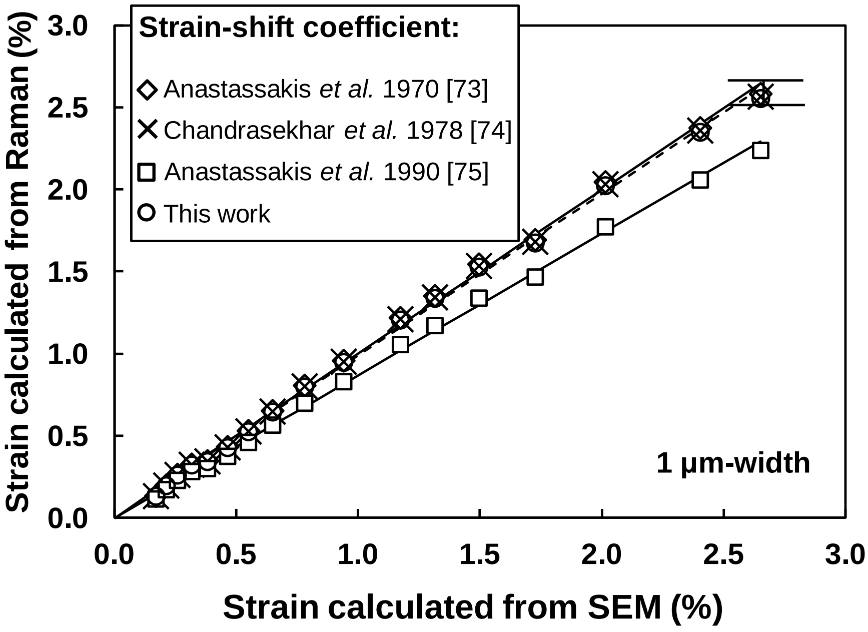

Figure 5.5 Strain determined from Raman measurements (using the strain-shift coefficient obtained from the PDPs of references [78-80], and this work) compared with strain determined by SEM for a 1 μm-wide sample. Solid lines are the linear fit of data determined using the PDPs. The dashed line is the linear fit of data using the average coefficient determined in this work. The error bar is the variation in strain obtained from the maximum and minimum strain-shift coefficient determined in this work.

(a)

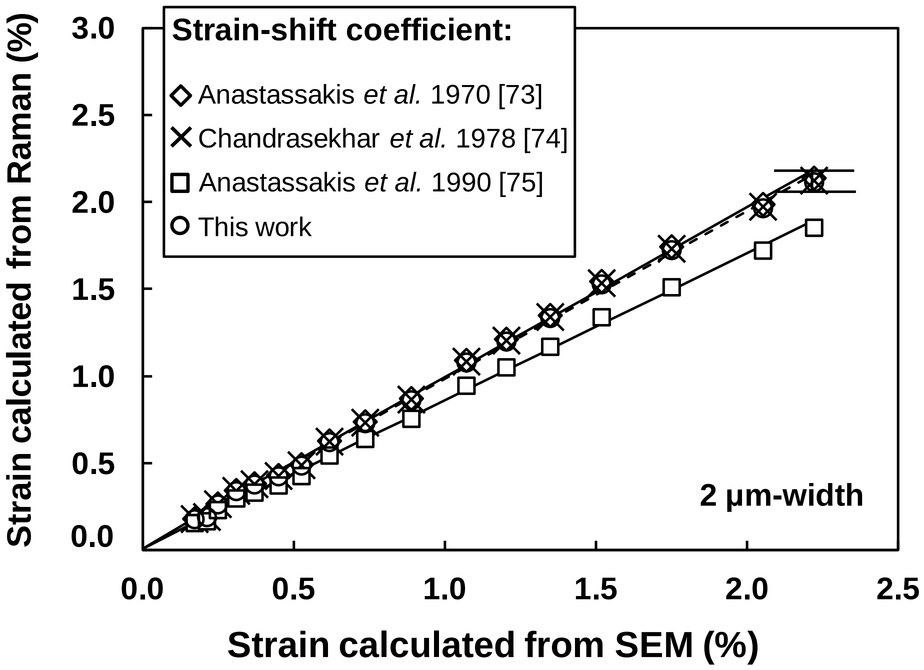

(b)

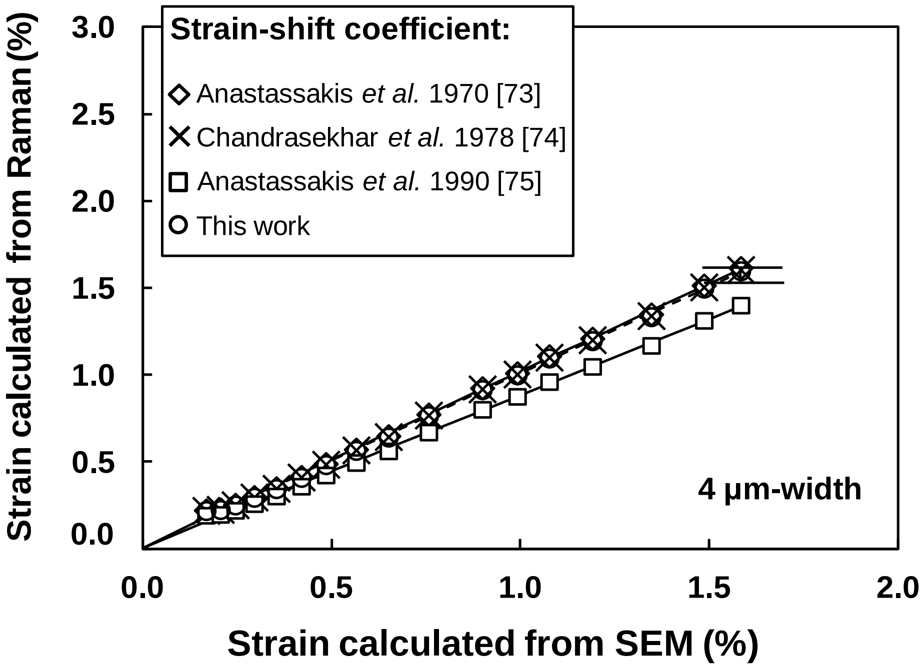

Figure 5.6 Strain determined from Raman measurements (using the strain-shift coefficient obtained from the PDPs of references [78-80], and this work) compared with strain determined by SEM for (a) 2 µm- and (b) 4 µm-wide sample. Solid lines are the linear fit of data determined using the PDPs. Dashed line is the linear fit of data using the average coefficient determined in this work. The error bar is the variation in strain obtained from the maximum and minimum strain-shift coefficient determined in this work.

Despite the differences in penetration depth from the visible and UV radiations used in this work, (~300 nm and ~15 nm respectively) the strain-shift coefficients are very similar $b_{VIS} = -340$ and $b_{UV} = -346$. Both b_{VIS} and b_{UV} are also very similar to those obtained using the PDPs resulting from the 1970 [78] and 1978 [79] experiments (Table 5.1). These experiments utilised wavelengths of 632.8 nm [78] and 647.1 nm [79] having a penetration depth in silicon greater than 1 μm. These results suggest that the effect of stress relaxation near the surface, which has previously been ascribed [80] as the main cause in PDPs discrepancy between [78], [79] and [80], either does not affect or equally affects the strain-shift coefficients for laser radiations within the range 364 – 647 nm. These findings are in spite of the significant differences between the thicknesses of the samples used in the earlier experiments (~1 mm [78, 79]) and those used in this work (~200 nm). Thus, other factors including the sample orientation and Raman configuration have to be considered in order to explain the discrepancy in PDPs. These hypotheses are tested in section 5.3.2.

5.3.2 Transversal optical mode

In ideal backscattering configuration from a (001) surface, the Raman selection rules dictate that only the longitudinal optical mode is allowed. In this configuration, the incident laser light is polarised along the vertical Z axis perpendicular to the X-Y plane of the sample, and transversal phonons cannot be excited. A high numerical aperture lens, however, causes the incident rays to have a component in the X-Y plane which can excite the TO phonons (Figure 5.7). In this way, forbidden optical TO modes have been observed [157, 163]. Nevertheless, the TO phonons have lower intensity than the LO phonons and remain difficult to observe in the Raman spectrum. Equation 5.5 shows that in the absence of stress, the three optical modes have the same Raman frequency i.e. they are triply degenerate. When stress is applied, the degeneracy is removed and the three peaks split to new frequencies. However, under low stress values, the frequencies are only slightly separated. Consequently, the TO peaks are masked behind the more intense LO peak and remain difficult to resolve. Even high values of stress may be insufficient to accurately resolve the position of the TO peaks.

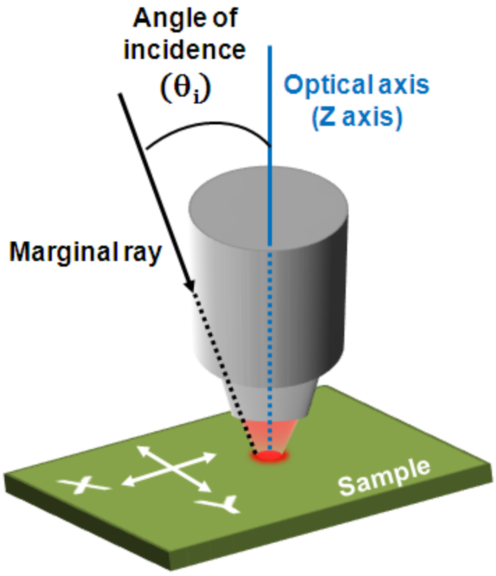

Figure 5.7 Schematic of the laser incident ray components in the plane of the sample due to the high numerical aperture lens. The X-Y in-plane components are responsible for the excitation of the transversal phonons.

Figure 5.8a shows the Raman spectrum of a 2 µm wide sample with a high value of strain (~3%). The laser was focused near the centre of the beam using visible radiation. The TO1 peak begins to appear downshifted as a shoulder behind the LO peak but it is still difficult to resolve. The TO2 peak which occurs midway between the LO and the unstrained silicon substrate peak is hardly visible and cannot be resolved. Focusing the laser at the sample edges however, causes rays with a larger incident angle to also hit the sample sides. This excites fewer LO phonons. Since the TO1 peak is downshifted with respect to the LO peak, the TO1 peak is enhanced compared with the LO peak on the Raman spectrum, as shown in Figure 5.8b. This enables the TO1 peak position to be unambiguously resolved. The TO2 peak occurs close to the silicon substrate peak. Since the silicon substrate peak is also enhanced by focusing the laser near the sample edges, the TO2 peak remains masked and cannot be accurately resolved using this method. Thus, only the LO and TO1 peaks are considered.

Also, shown in Figure 5.8, the Raman frequency of the LO and TO1 peaks is shifted ~0.3 cm^{-1} depending on whether the laser is focused at the sample centre or edges. The position where the laser is focused onto the sample may also affect the frequency of the Raman peaks. In order to characterise the variation in frequency of the Raman peaks with the position of the laser on the sample, a complete line scan was performed across a 4 μm wide sample.

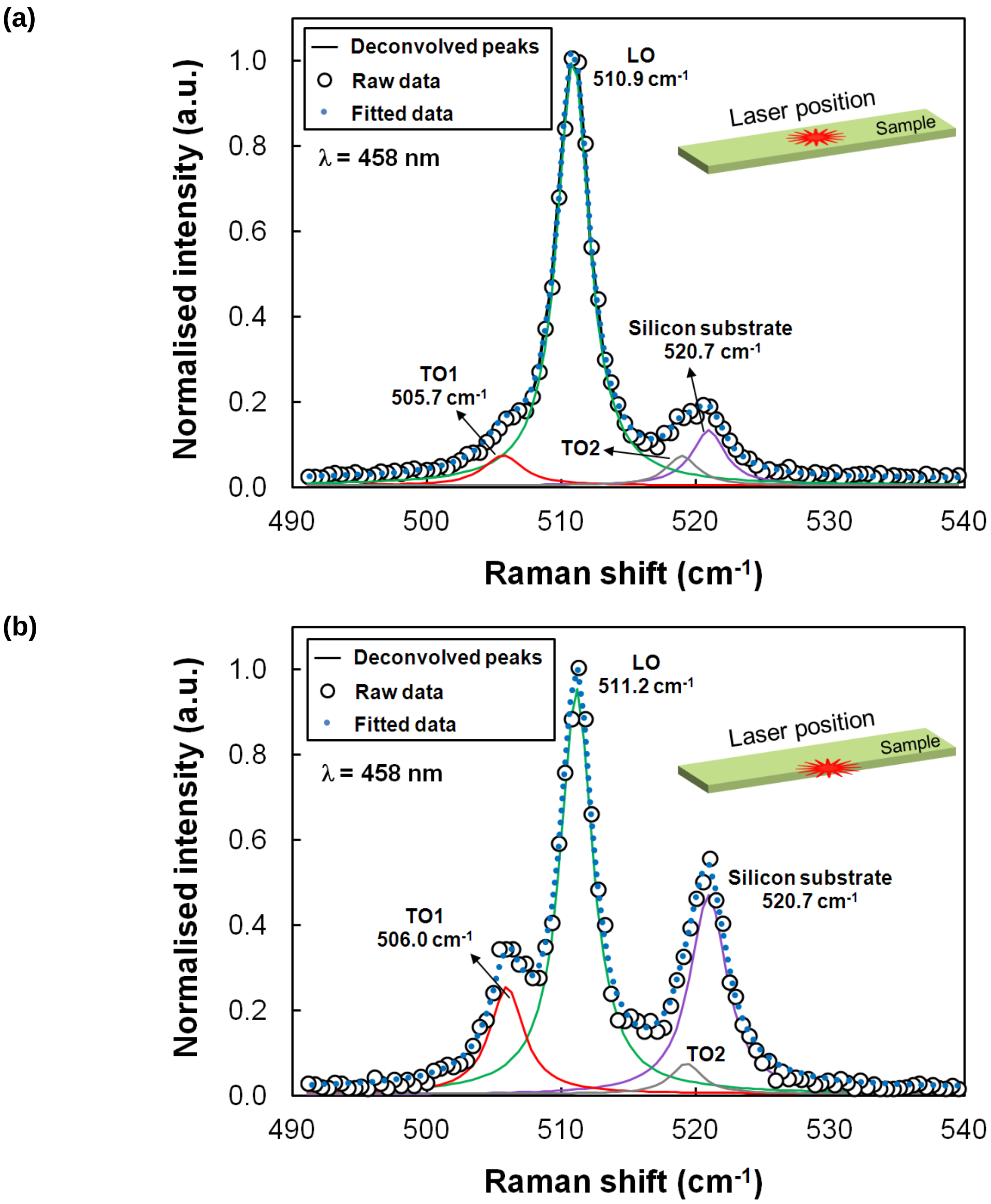

Figure 5.8 Raman spectra of a 3% strained sample (2 μm-wide) with (a) laser focused near the centre of the beam. Only the longitudinal phonon can be accurately deconvolved (solid lines); (b) laser focused at the edges of the sample. The lateral sides of the sample are also exposed and fewer LO phonons are excited. This results in an enhancement of the TO1 peak compared with the LO peak. The TO2 peak cannot be accurately resolved since it is hidden behind the more intense peak of the silicon substrate.

Figure 5.9 shows the Raman shift with respect to the unstrained silicon frequency and the normalised intensity for both the LO and TO1 peaks across the sample.

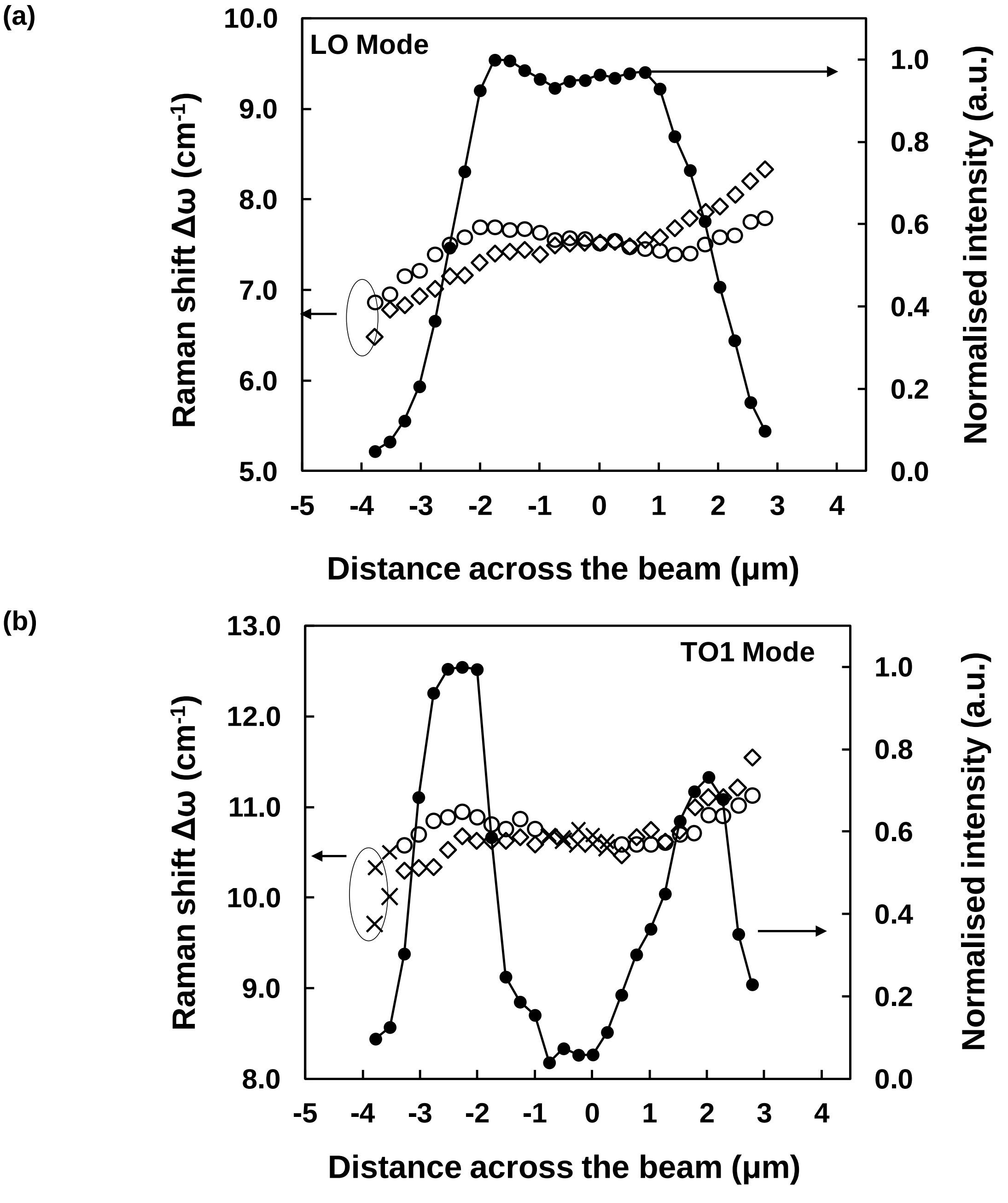

Figure 5.9 Line scan across a 4 µm wide sample: (a) The LO peak position can be most accurately resolved at the centre of the sample since the Raman shift is stable and the intensity is highest in this region; (b) The TO1 peak intensity is maximum near the sample edges and minimum near the sample centre (peak deconvolution is less accurate (black crosses)). In both modes, the Raman shift changes when the laser is focused far from the sample centre. After rotating the sample 180° the same trend (open symbols) for both the LO and TO1 peaks was obtained.

A significant shift in the Raman frequency occurs ~2 – 3 μm from the centre of the sample beam. The Raman frequency is highly dependent on the incident light polarisation on the (110) and (111) planes [152]. Figure 5.1 shows the lateral sides of the sample correspond to the (-110) plane. Thus, the observed shift in the Raman frequency towards the sample edges is most likely due to the change in polarisation of the incident rays at the sample sides. This explains the apparent asymmetry observed in the Raman shift at each edge of the sample (Figure 5.9). The Raman frequency shifts towards higher values near the left edge and towards lower values near the right edge. This is observed in both the LO and TO1 modes. Figure 5.9 further shows that after rotating the sample 180° the same trend is obtained in both modes (open symbols). This confirms that the observed asymmetry is due to the change in polarisation of the incident rays at the sample sides. Near the sample centre, the Raman shift is fairly constant in both modes and the LO peak intensity is maximum.

To evaluate the impact of the light incident on the sample sides on the LO peak position, it is necessary to know the laser spot size. The theoretical minimum diameter of the focused laser spot size is given by [98]:

$$\emptyset = \frac{0.88\,\lambda}{NA} \tag{5.8}$$

However, the experimental laser spot size is always larger than the theoretical spot size. This is mainly due to the inability to have a perfect focus of the laser onto the sample. Using a conventional 100X lens, NA = 0.95 and a laser wavelength λ = 458 nm the diameter of the laser spot size is found to be ~0.9 μm [98] which is about twice the theoretical value obtained using Equation 5.8. The experimental laser spot diameter is less than the smallest sample width (1 μm). This verifies that when the laser beam is focused near the centre of the beam, most of the light will be incident on the top (001) plane and the LO peak intensity is maximum, as observed.

The TO1 peak intensity is maximum near the edges and minimum at the centre of the beam (Figure 5.9b). Consequently, the TO1 measurements at the centre of the beam are less accurate. Measurements near the edges are affected by the dependence of Raman frequency on the incident light polarisation with the lateral (-110) faces and the non-uniaxial stress components at the lateral faces. Thus, it is not possible to determine the strain-shift coefficient using the method described in section 5.3.1. Instead, the ratio between the LO and TO1 peaks is used to estimate the strain-shift coefficient for the TO1 mode. Assuming that strain does not change regardless of the strain-shift relation used:

$$\frac{\Delta\omega_1}{\Delta\omega_3} = \frac{b_1}{b_3} \tag{5.9}$$

Previously $b_3 = -339$ was used for the visible radiation. Only values with sufficient intensity to be accurately resolved and samples with strain values higher than 2.5% were considered. After performing a linear squares fitting, the TO1 strain-shift coefficient at the centre of the beam (position 0 in Figure 5.9b) is $b_1 = -476$. The average strain-shift coefficient is $b_1 = -485$. The standard deviation *stdev* = 22.4 is large due to the major differences in Raman shifts at positions far from the centre of the beam. Unlike the LO strain-shift coefficient determined in section 5.3.1, the TO1 strain-shift coefficient is in excellent agreement with those obtained using the PDPs of Anastassakis *et al*. in 1990 [80] (Table 5.1). The same agreement between the LO strain-shift coefficient determined with the 1970 [78] and 1978 [79] PDPs and the TO1 strain-shift coefficient determined with the 1990 [80] set of PDPs is found in [152]. Using the modelled PDPs [152], the strain-shift coefficient for the LO mode (b_3 = -336) agrees better with the 1970 [78] and 1978 [79] PDPs whereas that for the TO1 mode (b_1 = -511) agrees better with the 1990 [80] PDPs. In order to explain this, several arguments in addition to the impact of the laser radiation already discussed in section 5.3.1 have been considered.

Firstly, from Equation 5.3, it is clear that the PDPs are strongly related to the symmetry of the crystal structure. This symmetry, however, is significantly different at the material surface compared with material bulk. This is because the atoms at the surface rearrange in order to minimise their positional energy compared with those within the bulk [26]. This surface reconstruction is considered to be the leading mechanism for the observed changes in some physical properties in silicon at the nanoscale, such as the elasticity and thermal conductivity [29, 30]. Thus, it is likely there will be a greater impact of the surface in the strain-shift coefficient for structures at the nanoscale. Nevertheless, to date, there is little experimental information about the impact of the surface of thin films and nanowires on the strain-shift coefficient. In section 4.6.1, the impact of the surface on the Young's modulus of the structures (thickness ~200 nm) was determined. It was concluded that the Young's modulus was the same as that of bulk silicon. Since the Young's modulus is related to strain, it is reasonable to conclude that the surface reconstruction is not the main factor for the discrepancies in the strain-shift coefficients found in this work.

Secondly, the fabrication process may alter the crystal symmetries of the nanostructures. Chemicals used during etching or deposition, or high temperatures from annealing processes may modify the silicon structure, rendering inappropriate strain-shift coefficients. Contamination, high doping and crystal defects are all known to cause a broadening or asymmetry of the Raman silicon peak [164]. In perfect crystalline silicon, the full-width half-maximum (FWHM) is estimated to be ~3 cm^{-1} and can be fitted with a Lorentzian function [164, 165]. In this work, the FWHM of the Raman peaks is ~3.2 ± 0.1 cm^{-1} for both the visible and UV radiations and no asymmetry was observed (Figure 4.11). Therefore, it is unlikely that the agreement between the LO and TO1 strain-shift coefficients determined with different sets of PDPs, is related to changes in the silicon structure during the fabrication process.

Thirdly, it has been suggested that the elastic properties of silicon may change with the temperature [155]. Since Raman measurements in the 1990 [80] experiment were taken at 110K whereas earlier experiments [78, 79] were performed at room temperature this might have resulted in different PDP values [155]. However, the recent experiments of Miyatake *et al*. [156] (to validate the 1990 [80] PDPs) and some other experiments [103, 152, 153] involving the determination of the strain-shift coefficient were also performed at room temperature. Despite the similarity in penetration depth of the lasers utilised and temperature in these experiments [103, 152, 153, 156], the agreement with one or another set of PDPs is completely different. In the present work, all the experiments have been performed at room temperature and yet a contradictory agreement is found: the LO strain-shift coefficient agrees better with the PDPs determined in 1970 [78] and 1978 [79] whereas the TO1 strain-shift coefficient agrees better with the PDPs determined in 1990 [80]. Thus, the impact of the sample temperature in the Raman experiments [78-80] is not likely to be the correct explanation for the discrepancies between the different sets of PDPs.

A further consideration to understand the PDPs discrepancies which to date has received little attention is the impact of scattering geometries and sample surface orientation. The two sets of PDPs reported in 1970 [78] and 1978 [79] were obtained using backscattering geometry while that reported in 1990 [80] was carried out in 90° scattering configuration. All the experiments used samples with laser radiation incident on the (110) and (111) planes. However, the Raman frequency is highly dependent on the incident light polarisation on the (110) and (111) planes.

Based on: (i) the excellent agreement found in this work between the LO strain-shift coefficient and that determined using the 1970 [78] and 1978 [79] PDPs, and the excellent agreement of the TO1 strain-shift coefficient and that determined using the 1990 [80] PDPs; (ii) both sets of PDPs of 1970 [78] and 1978 [79] yield an almost identical LO strain-shift coefficient although they significantly differ regarding the TO modes; and (iii) all the previous PDPs experiments [78-80] were performed using laser radiation incident on the (110) and (111) planes which results in the Raman frequency being highly dependent on the incident light polarisation, it is believed that the discrepancies between the different sets of PDPs and strain-shift coefficients are strongly dependent on the scattering geometry and sample surface orientation used for the Raman experiments.

Consequently, the work indicates that the 1990 [80] PDPs are more accurate than the PDPs of 1970 [78] and 1978 [79] to characterise the TO1 mode of silicon nanostructures in backscattering geometry from a (001) surface. Conversely, the PDPs of 1970 [78] and 1978 [79] are more accurate than the PDPs of 1990 [80] to characterise the LO mode in backscattering geometry from a (001) surface in silicon nanostructures.

5.4 Summary and conclusions

The LO strain-shift coefficient in silicon nanostructures under uniaxial tensile stress (0 – 4.5 GPa) along the [110] direction in backscattering geometry from a (001) surface has been accurately determined. Based on the Raman shift measurements from two laser radiations (364 and 458 nm) and strain values validated by three different techniques, a value for the LO strain-shift coefficient b = -343 has been determined. This is in close agreement with that obtained using the PDPs of Anastassakis *et al.* in 1970 [78] and

Chandrasekhar *et al*. in 1978 [79]. These results indicate that the effects of stress relaxation near the surface either do not affect or equally affect the strain-shift coefficient for laser radiations within the range 364 – 647 nm. Thus the strain-shift coefficient determined in this work, along with the PDPs in [78] and [79], are the most suitable to determine strain in silicon nanostructures using the shift of the LO peak with either visible or UV Raman spectroscopy in backscattering geometry from a (001) surface.

The TO1 strain-shift coefficient in backscattering geometry from a (001) surface has also been characterised. The TO phonons, which are usually invisible in the Raman spectrum in this configuration, have been excited and further split by means of a high numerical aperture lens (NA = 0.9) and high values of applied strain (~3%). By assessing the Raman shift ratio between the longitudinal and transversal peaks, and the position of the laser on the sample, has further allowed us to resolve the TO1 peak position. The results confirm that the Raman frequency is highly dependent on the incident light polarisation on the (110) plane. In contrast with the LO strain-shift coefficient, the TO1 value has a closer agreement with the strain-shift coefficient obtained using the 1990 PDPs [80]. After eliminating factors including temperature and potential changes in crystal structure during the sample fabrication, it has been concluded that the strong dependence of the Raman frequency on the incident light polarisation on the (110) and (111) planes and the different scattering geometries may explain the significant discrepancies between the different sets of PDPs reported to date [78-80]. The work indicates that the PDPs from 1990 [80] are more accurate to characterise the TO1 mode in silicon nanostructures in backscattering from a (001) plane than the PDPs of 1970 [78] and 1978 [79].

Chapter 6. Effects of strain on the surface roughness of silicon nanostructures

6.1 Introduction

The beam structures have enabled precise determination of strain in nanostructures with a wide range of strain values (chapters 4 and 5). With this knowledge of strain in the structures it is now possible to determine the effect of strain on surface roughness. This topic has long been debated in literature [59, 65, 66, 166]. In metal-oxide-semiconductor field-effect transistors (MOSFETs), strained silicon channels enhance the mobility of holes and electrons compared with unstrained channels [44, 167]. Theoretically, the effect of strain is lowering the symmetry of the crystal by lifting and splitting the degeneracy of the conduction and valence band maxima and minima (thereby reducing inter-valley scattering) and reducing the effective mass in the transport direction, which increases carrier mobility (section 1.1.2.1). However, while these effects explain the strain-induced mobility enhancements at low vertical electric fields, they do not explain the increase in mobility observed consistently at high vertical electric fields, where devices operate and where surface roughness-limiting mechanisms dominate (section 1.1.2.2) [59-61]. Theoretical work suggests that reduced roughness scattering at high electric field regimes may result from the smoother surface of strained silicon [58]. This has never been proven experimentally under reliable conditions or understood. This is a big omission since strained silicon is now used in MOSFET devices and will be incorporated in future devices including FinFETs and SOI and nanowire-based devices [11].

6.1.1 Roughness-mobility analysis

In order to study the surface roughness scattering limited mobility of electrons and holes with strain, several statistical functions have been used to analyse the surface profile in real space and in reciprocal space [65, 66, 168]. The mathematical definitions of these statistical functions will be given in section 6.2. Traditionally, the experimental data determined from these functions has been fitted using either a Gaussian or an exponential functional model with two parameters, the root mean square (RMS) roughness and the correlation length [62, 65, 169]. The RMS roughness has been used to model the variations of the surface profile in the vertical directions whereas the correlation length has been used to model the variations of the surface profile in the horizontal direction. However, it has been suggested that neither the Gaussian nor the exponential model can describe the electron and hole mobility using the same parameters for the RMS roughness and correlation length [43]. In order to describe the mobility of both electrons and holes, alternative expressions have been proposed both in real and reciprocal space [170, 171]. These alternative expressions included an additional exponential parameter n which for specific values reduces to the Gaussian and exponential models. No physical meaning has been given however, to this exponential parameter. Isihara *et al*. [170] studied the silicon interface with pure oxide (SiO_2) and with oxynitride oxides ($SiON_x$). They found that different values of the exponential parameter n were needed to successfully describe the roughness of both interfaces [170]. To date, however, there is no proper study of the relation between the surface exponent parameter n with strain (uniaxial and biaxial). Moreover, the relation between the surface exponent parameter n and the different surface models, including the Gaussian and exponential forms is not well understood. This study is needed for a complete understanding of the differences in mobility enhancement for electrons and holes with uniaxial and biaxial strain at high electric fields.

6.1.2 Roughness characterisation methods

Experimentally, the surface roughness of the SiO_2/Si interface has been characterised using different techniques including profilometry, scanning tunnelling microscopy (STM), transmission electron microscopy (TEM) (section 1.2.1) [62, 65, 168, 172]. Atomic force microscopy (AFM) is another common technique used to characterise the roughness of a surface. It is non-destructive, renders atomic resolution and can be used with conductive and non-conductive samples. In this work AFM has been used to characterise the roughness of the silicon structures.

From Pirovano's work [168], it was determined that in order to explain the dependency of electrons and holes mobility at high electric fields with strain, correlations length values higher than ~1.5 nm would fail to fit the experimental mobility data. It was also concluded that AFM measurements were not able to detect the surface short wavelength undulations due to the finite AFM tip diameter (~10 nm) [168]. That is, the tip diameter cuts off the high frequency components of the surface roughness i.e. those most likely to affect the surface roughness mobility. Therefore, it is clear that nanoscale analysis is necessary in order to filter the surface long wavelength undulations and concentrate on the high frequency components of the surface roughness.

6.1.3 Self-affinity of the SiO_2/Si interface

The SiO_2/Si interface has been shown to exhibit self-affinity [69]. Self-affinity is a characteristic related to fractal objects [70] which look the same (or statistically the same) after applying a different rescaling of the lengths (Figure 1.10). In a self-affine surface, the rescaling of the lengths is connected with the fractal dimension through the Hurst exponent [67, 68]. The Hurst exponent relates to the jaggedness of the surface. In order to completely describe the roughness of a self-affine surface, three parameters are needed: the RMS roughness, the correlation length and the Hurst exponent [67, 68]. For a self-affine surface, Sinha *et al*. [173] proposed a functional form to fit the data extracted from the statistical analysis which included these three parameters. The functional form proposed to fit the experimental data obtained from the statistical analysis of a self-affine surface is the same or nearly the same as that used within the mobility models [170, 171]. Despite the strong relation between the functional form proposed by Sinha *et al*. [173] for the self-affine analysis of a rough surface and that used within the mobility models [170, 171], to date the self-affine behaviour of the SiO_2/Si interface has not been considered within the mobility studies. Furthermore, there is no proper study of the self-affinity of the silicon surface with uniaxial and biaxial strain.

In this chapter the impact of strain on the surface roughness of silicon thin films and wires is investigated by AFM. Strain levels ranging from 0 – 2.3 % have been characterised. The impact of strain on the surface roughness at the nanoscale has been investigated by using a super-sharp AFM tip and filtering the surface undulation wavelengths down to 50, 30 and 20 nm. The self-affinity of the silicon surface with strain has been analysed by using the technique of multiple scan analysis [174-176]. This technique allows the study of the self-affine behaviour of a surface by analysing multiple areas of different size of the same sample. The technique has allowed us to accurately extract and study the RMS roughness, correlation length and Hurst exponent dependency with strain and with the undulation wavelength regime (filter cut-off wavelength used for filtering the surface undulations).

6.2 Self-affine theory

The SiO_2/Si interface can be well described as a self-affine surface [69, 177]. A surface is said to be self-affine if after performing an anisotropic dilation and rescaling of the different lengths, the surface looks the same (or statistically the same) [68, 178]. This type of scaling is characteristic of fractal objects [70]. The height-profile of a self-affine surface is described by the singled-value function [68]:

$$h(x) \simeq \epsilon^{-\alpha} h(\epsilon x) \tag{6.1}$$

Here, h is the height value of the surface at a position x along the x-axis, ϵ is the scaling factor along the x direction and α the Hurst exponent $(0 \leq \alpha \leq 1)$. For a real and self-affine surface however, the scaling behaviour will hold only within a certain range of lengths, i.e. the height values cannot keep increasing or decreasing indefinitely. The Hurst exponent and the fractal dimension D of a fractal surface are related by [69]

$$D = 3 - \alpha \tag{6.2}$$

The fractal dimension D is a non-integer number which measures the capacity of a fractal object to fill the space in which it is embedded [174].

In order to completely characterise the morphology of a self-affine surface, three independent parameters are necessary [68]: the interface width or standard deviation of the surface heights, the correlation length and the Hurst exponent. The interface width w is defined as:

$$w = \sqrt{\langle [h(\boldsymbol{r}) - \bar{h}]^2 \rangle}\,, \tag{6.3}$$

where $h(\boldsymbol{r})$ is the surface height at the position $\boldsymbol{r}$ and $\bar{h}$ is the average height over all $\boldsymbol{r}$. It is common practice for a digitised image to shift all the sampled heights in order to have a zero-mean height. For a zero-mean height, the standard deviation of the height profile hence the interface width, is the same as the RMS of the height profile values. In this work, all the surface profiles are redefined to be zero-mean height and the term RMS roughness will be used to describe the surface height profile.

The correlation length ξ is usually defined from the autocorrelation function $R(l)$:

$$R(l) = \frac{1}{w^2}\langle h(\boldsymbol{r})h(\boldsymbol{r}+l)\rangle \tag{6.4}$$

Here, l is the lag distance at which the autocorrelation function is estimated. The correlation length is defined as the distance l at which $R(l)$ decays at *1/e* of its initial value $R(0)$. Essentially, the correlation length is a parameter which estimates the onset of the lateral distance at which the surface height values are still correlated. Surface height values separated by lateral distances above the correlation length are uncorrelated.

Another correlation function commonly used to characterise random surfaces is the height-height correlation function, defined as:

$$H(l) = \langle \big(h(\boldsymbol{r}+l) - h(\boldsymbol{r})\big)^2 \rangle \tag{6.5}$$

The height-height correlation function is related to the autocorrelation functions as

$$H(l) = 2w^2[1 - R(l)] \tag{6.6}$$

Several analytical functions have been proposed to model the experimental data obtained from real rough surfaces using Equations 6.4 and 6.5 including the Gaussian and exponential forms [62, 65]. These functions, however, do not account for the self-affine behaviour. For a real self-affine and isotropic surface, i.e. a surface statistically invariant under a rotation transformation, an equivalent analytical expression for the height-height correlation function was proposed by Sinha *et al.* [173]:

$$H(l) = 2w^2\left[1 - e^{-\left(\frac{l}{\xi}\right)^{2\alpha}}\right] \sim \begin{cases} 2w^2, & l \gg \xi, \quad saturation\ region \\ \propto\ l^{2\alpha}, & l \ll \xi, \quad self - affine\ region \end{cases} \tag{6.7}$$

Here, the Gaussian and exponential functions are represented by the particular cases of $\alpha = 1$ and $\alpha = 0.5$, respectively. Alternatively, the Hurst exponent α can be understood as the jaggedness of the surface [67, 68, 173] which is a measure of the high-frequency and low-amplitude components of the surface profile [174]. Values closer to 1 relate to smooth surfaces whereas values closer to 0 relate to more jagged surfaces. Unfortunately, there is no exact physical definition relating the Hurst exponent with the jaggedness or smoothness of a surface, or with the frequency components of a surface profile. Figure 6.1 shows two height-profiles with the same RMS roughness and correlation length values although different Hurst exponent.

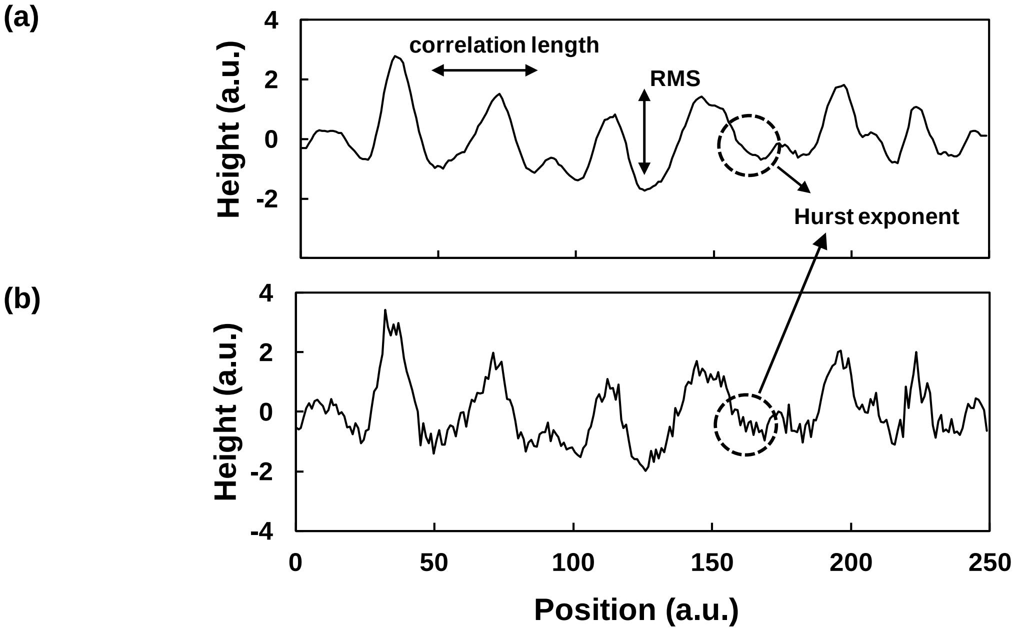

Figure 6.1 Height-profile of two rough surfaces (a) and (b). Both height-profiles have the same RMS roughness and correlation length although different Hurst exponent. Profile (b) is more jagged than profile (a). This indicates that the Hurst exponent of profile (b) is smaller than that of profile (a)

The height-profile of Figure 6.1b is more jagged (smaller Hurst exponent), than that of Figure 6.1a. Equation 6.7 also reflects the fact that a real surface will only exhibit self-affine behaviour within a short range $l \ll \xi$ and will saturate at a constant value for $l \gg \xi$. From the relation between the height-height correlation function and the autocorrelation function (Equation 6.6), it is easy to see that the functional form of the autocorrelation function proposed by Sinha *et al.* [173] for a self-affine surface is:

$$R(l) = e^{-\left(\frac{l}{\xi}\right)^{2\alpha}} \tag{6.8}$$

The height-height correlation function has been traditionally used to extract the roughness parameters from a digitised surface image such as that of an AFM image [65, 179, 180]. However, as pointed out by several researchers [174, 176, 181], due to the scale dependence of Equations 6.4 and 6.5 with a self-affine surface, extracting the roughness parameters from a single scan may result in erroneous values. An alternative procedure based on multiple scans was proposed by Vicsek *et al.* [175]. In this approach, the roughness parameters are extracted from measurements of the RMS of the height profile values of areas with different lateral lengths. For a real self-affine surface, the interface width scale dependence can be fitted using the expression [174, 176]:

$$w(L) = w_0\sqrt{1 - e^{-\left(\frac{L}{\xi}\right)^{2\alpha}}} \sim \begin{cases} w_0, & L \gg \xi, \quad saturation\,region \\ \propto L^{\alpha}, & L \ll \xi, \quad self-affine\,region \end{cases} \tag{6.9}$$

Here, L is the scan-length (lateral size of the scanned area) and w_0 the true interface width of the scanned surface. For a self-affine surface and lateral scan-lengths large enough, a semi-log plot of $w(L)$ with the lateral length L will show two regions (Figure 6.10). The self-affine region (at low values of L) is scale dependent with L^{α}. The saturation region (at high values of L) is scale independent with a constant value $w(L) = w_0$. Equation 6.9 will be used in section 6.4.2.3 to fit the experimental data and determine the roughness parameters.

6.3 Methodology

Five uniaxially strained samples and two biaxially strained samples were investigated. The uniaxially strained samples consisted of five silicon free-standing beams of 2 μm width and strain levels of 0.2%, 0.6%, 1.3%, 2.0% and 2.3% fabricated in an SOI wafer (section 4.2.1). The strain levels were verified by SEM and Raman spectroscopy and compared with analytical calculations and finite element simulations (section 4.2). The samples with biaxial strain were fabricated at the Paul Scherrer Institute (PSI) in

Switzerland. They consisted of a 14 nm-thick biaxial tensile strained silicon layer on top of a 145 nm buried oxide layer (sSOI). Two strain levels were investigated, 0.8% and 1.3%. Unstrained SOI samples with equal layer thickness as the sSOI samples were also investigated alongside the sSOI samples for comparison purposes (Figure 6.2). The strain levels were verified by Raman spectroscopy.

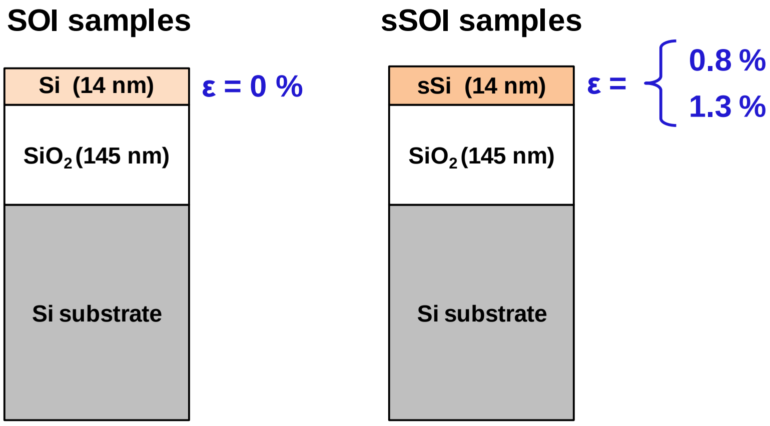

Figure 6.2 SOI and sSOI samples used in this work. The thickness of the silicon and silicon dioxide layers in the SOI samples is the same as the thickness of the strained silicon and silicon dioxide of the sSOI samples. Two strained layers were investigated, 0.8% and 1.3% and the results of the roughness analysis were compared with those of the unstrained samples (SOI).

Before the analysis, the SOI and sSOI samples were cleaned with a 2:1 solution of H_2SO_4:H_2O_2 for 10 minutes and HF 1% for 15 seconds. The short time and low concentration of this solution is known to minimise the impact on the silicon surface whereas removes the native oxide and organic residues [182].

Surface roughness was characterised by AFM using an XE-150 model from Park Systems (section 3.3). A super-sharp silicon tip with a typical radius ~2 nm was used. Three areas of 250 × 250 nm^2 separated ~10 µm apart were analysed for each sample. Only zero and first order regression polynomial fitting were required for the flattening process (section 3.3.3). The image resolution was 512 × 512 pixels. This set-up results in a scan step of ~0.5 nm / pixel.

All the measurements were performed in non-contact mode within an acoustic isolation enclosure and an on anti-vibration table to minimise noise background. The baseline noise (noise floor) was measured before and at the end of the measurements (Figure 6.3).

In a baseline noise measurement the scan size is set at 0 × 0 nm^2 while the tip-sample working distance and the scan-rate are set at the same values as those for a topography measurement. The response signal for this one-point scan measurement is the noise floor of the instrument. The RMS values of the noise background were ~ 0.2 – 0.3 Å.

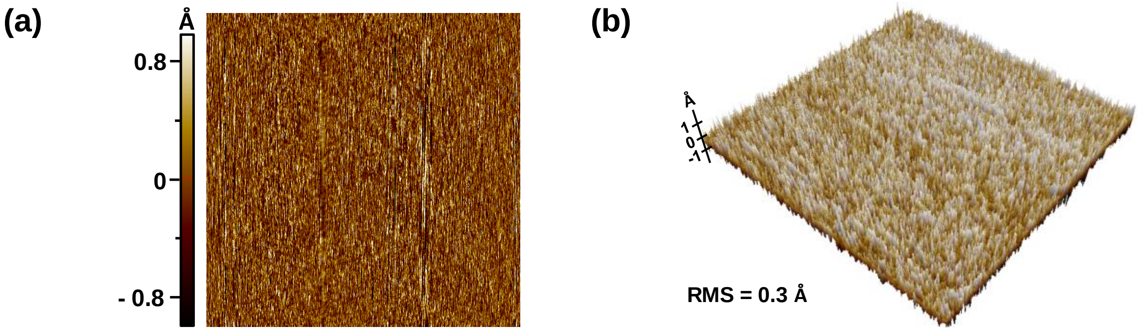

Figure 6.3 AFM image (0 × 0 nm^2) of the noise background. RMS values of the noise background ~ 0.2 – 0.3 Å were obtained. (a) Top view. (b) 3D view.

6.3.1 AFM images analysis: Multiscan technique.

Matlab 7.10 (R2010a) was used for the analysis of the AFM images. As mentioned in the previous section, three areas of 250 × 250 nm^2 were analysed for each sample. The RMS roughness dependency with scan-length was characterised by progressively scaling each scanned area (250 × 250 nm^2) to a minimum scan-length of ~10 nm (Figure 6.4a). This, results in 12 square areas with scan-lengths scaled with a factor ~1.3 (Figure 6.4c).

To increase accuracy and account for roughness variations with the sample orientation, the scan areas were scaled from five different directions. One scaling was performed from the centre towards the corners of the image (Figure 6.4a). The other remaining four scaling were performed from each corner of the image towards the diagonally opposite corner (Figure 6.4b). Thus, 3 × 5 × 12 = 180 areas for each sample were analysed. The RMS value of the height profile for each scan-length was determined from the average of all equal size areas, i.e. 3 × 5 = 15 areas.

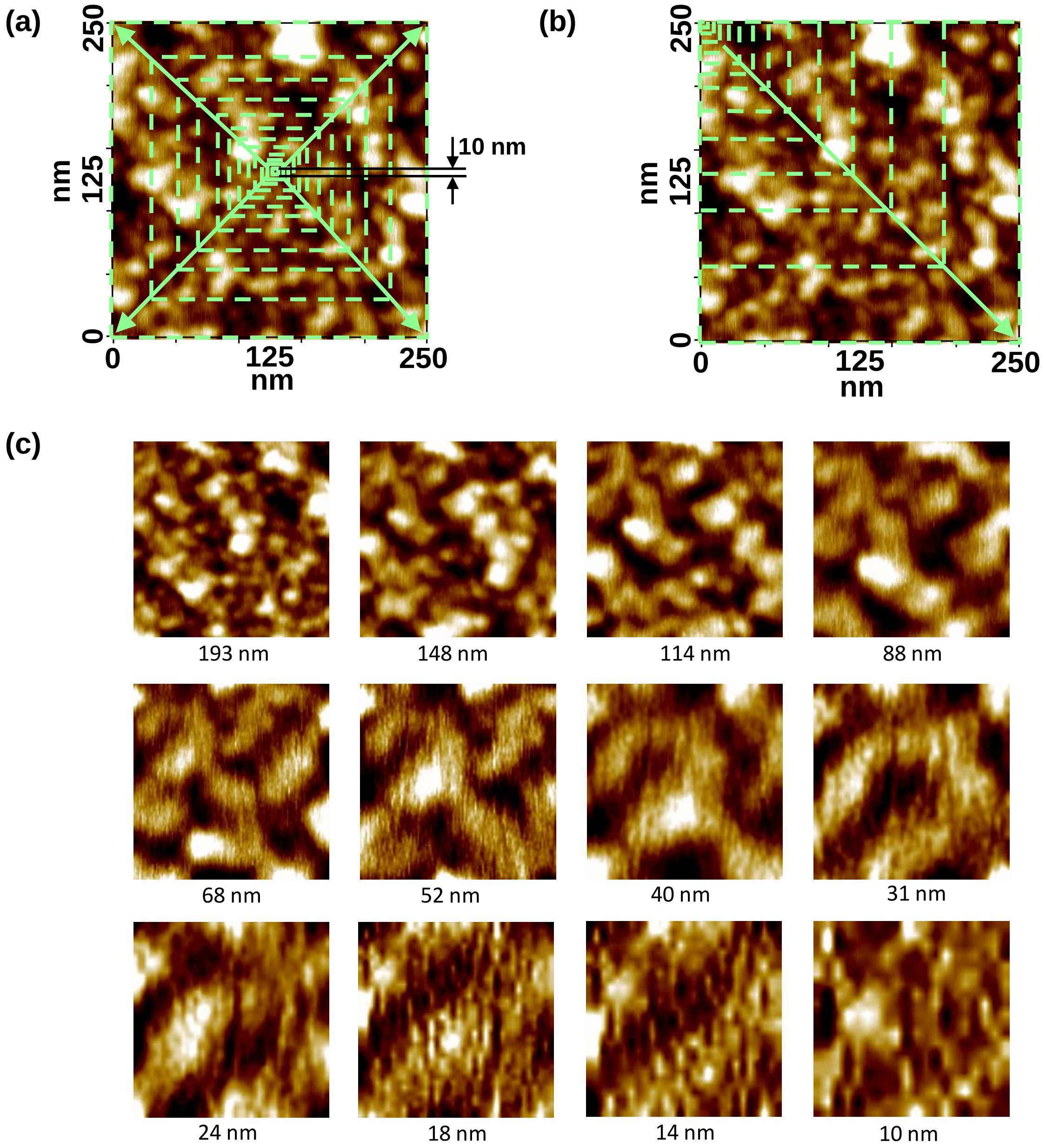

Figure 6.4 (a) In order to test for self-affinity, the AFM images were scaled down towards the centre of the image to a minimum lateral length of ~10 nm. (b) To improve accuracy and account for roughness variations with the sample orientation each AFM image was also scaled down and analysed from each of the four corners. (c) The 12 areas resulting from the scaling of image (b) with a scaling factor ~1.3 starting from the top-left corner. The image corresponds to a 1.3% uniaxially strained sample.

6.4 Results and discussion

In order to analyse the surface roughness at the nanoscale, the AFM images were filtered using a low-pass wavelength filter (high-pass in the frequency domain) with different cut-off wavelengths. A low-pass wavelength filter eliminates the long wavelength undulations above the cut-off wavelength. In this work, the notation low-pass wavelength filter will be used instead high-pass frequency filter to better describe the impact of the filter on the surface roughness undulations and more especially on the correlation length.

There are some side effects as a consequence of filtering the AFM images such as a reduction in the RMS roughness with decreasing cut-off wavelength. Thus, first, it is necessary to evaluate the filter response and the signal-to-noise ratio at each cut-off wavelength.

6.4.1 Filter response evaluation: Signal-to-noise ratio

Figure 6.5 shows the height-profile taken across the middle of a 250 × 250 nm^2 area of a 2.0 % strained sample before and after applying a 50, 30, 20, and 10 nm low-pass cut-off wavelength filter. As shown in the left column of Figure 6.5, the low-pass filter suppresses most of the long wavelength undulations above the cut-off wavelength (red line). However, the short wavelength undulations are still visible (right column of Figure 6.5). The rectangular areas highlight the filtering effect showing that the small features, before and after filtering, are still discernible. Below 10 nm however, the noise level (dashed line) is similar to that of the filtered signal. This is understood considering that a low-pass wavelength filter (high-pass in the frequency domain) will accentuate the noise and at low cut-off wavelengths will predominate over the real surface roughness features. In order to compare the filter response (signal) to the noise background a useful figure of merit is the signal-to-noise ratio (SNR) defined as:

$$SNR = \frac{P_{signal}}{P_{noise}} = \frac{RMS_{signal}^2}{RMS_{noise}^2} \tag{6.10}$$

Here, P_{signal} and P_{noise} are the power of the signal and noise respectively.

The signal-to-noise ratio is frequently expressed in decibels (dB):

$$SNR_{dB} = 10\log_{10}\frac{P_{signal}}{P_{noise}} \tag{6.11}$$

As shown in Figure 6.5, filter cut-off wavelengths ~10 nm result in a SNR_{dB} ~ *0 dB.* Therefore, for the uniaxially strained samples, cut-off wavelengths below 20 nm are not considered since the signal-to-noise ratio is too low. This results in a minimum *SNR* ~2. In case of the biaxially strained samples values of SNR_{dB} ~ *0 dB* were obtained for cut-off wavelengths ~30 nm. Thus, for the biaxial samples, only cut-off wavelengths of 50 nm are considered. Above 50 nm, the effect of the filter on the short wavelength undulations is negligible since the cut-off wavelength approaches that of the scan size. Cut-off wavelengths above 50 nm are not considered.

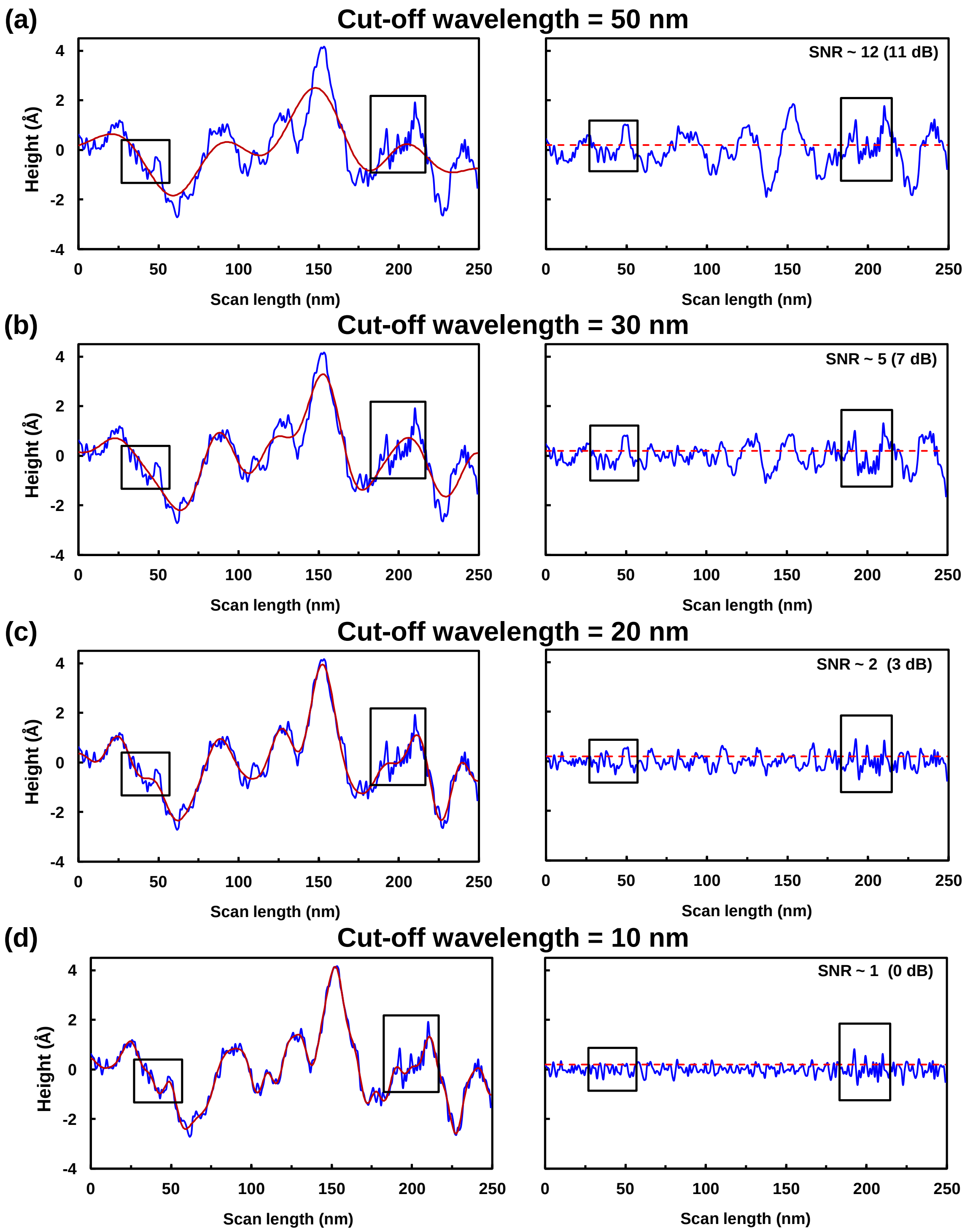

Figure 6.5 Effect of the filter on the surface roughness of a 2.0% uniaxially strained sample. Left column: height profile before applying the filter. Right column: height profile after applying a low-pass filter with (a) 50, (b) 30, (c) 20 and (d) 10 nm cut-off wavelength. The filter eliminates the long wavelength undulations above the cut-off wavelength (red line in the unfiltered images). For filter cut-off wavelengths above 10 nm, the small features and low wavelength undulations are still discernible (rectangular areas) and the SNR >1. Below 10 nm, the noise level (dashed line) is comparable with the signal (SNR ~1).

6.4.1.1 Effect of filtering on the surface undulations wavelength

Figure 6.6 shows the 2D and 3D views of an AFM scanned area (250 × 250 nm^2) in a 0.2% strained wire before and after applying the 50, 30 and 20 nm low-pass wavelength filter. The effect of the cut-off wavelength used for the image filtration is noticeable at the edges of the 3D images where a reduction in the wavelength of the surface undulations with decreasing cut-off wavelength is observed. This is more clearly observed in a height-profile plot across the sample. Figure 6.7 shows the height profile across the middle of the sample. Taking as a reference a peak position A in the height-profile, the distance towards the nearest peak (above the mean of the surface undulations) reduces with decreasing filter cut-off wavelength. There is also an increase in the number of peaks above the mean of the surface undulations as the cut-off wavelength decreases. This increase in the number of peaks confirms the reduction in wavelength undulations as the filter cut-off wavelength decreases, which is required for the nanoscale analysis of the surface roughness.

6.4.1.2 Effect of filtering on the surface RMS roughness

Filtering the surface height profile causes the RMS roughness to reduce with decreasing filter cut-off wavelength. This is because the number of frequency components eliminated by a low-pass filter increases with decreasing cut-off wavelength. Figure 6.6 shows that the RMS roughness of a 250 × 250 nm^2 area reduces from 2.62 Å (before filtering the image) down to 0.48 Å (after applying a 20 nm cut-off wavelength filtering). The reduction in RMS roughness is also reflected in the peak-to-valley values of the height profile (Figure 6.7). The peak-to-valley values reduce from 10.2 Å for the non-filtered images to 1.8 Å for the 20 nm cut-off wavelength filtered images.

(a) Non-filtered

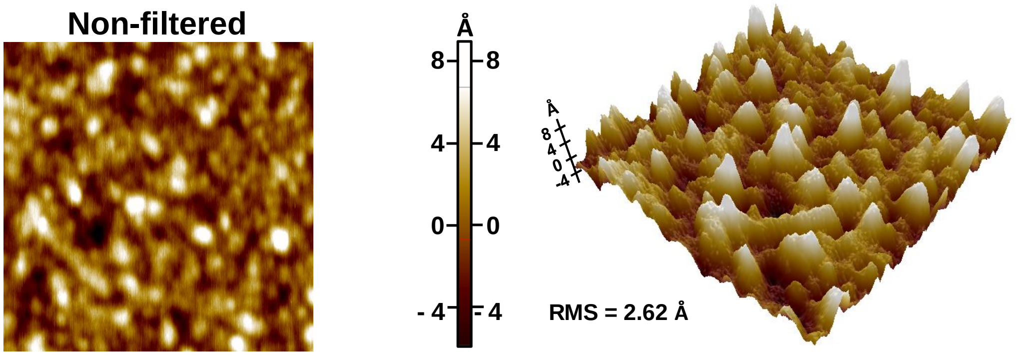

(b) Cut-off wavelength = 50 nm

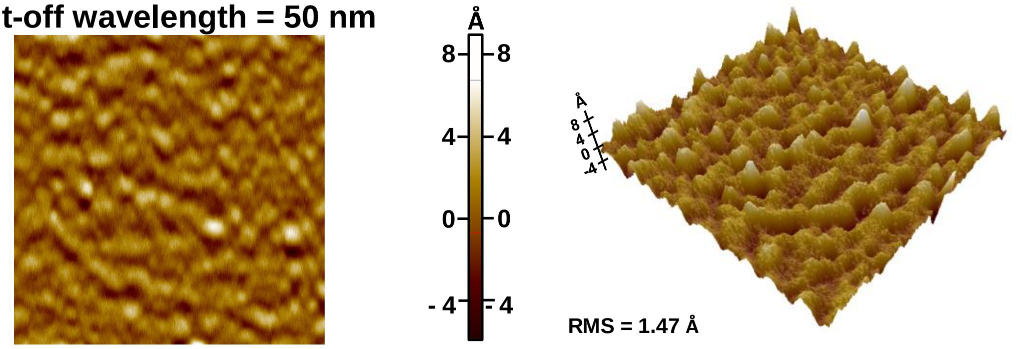

(c) Cut-off wavelength = 30 nm

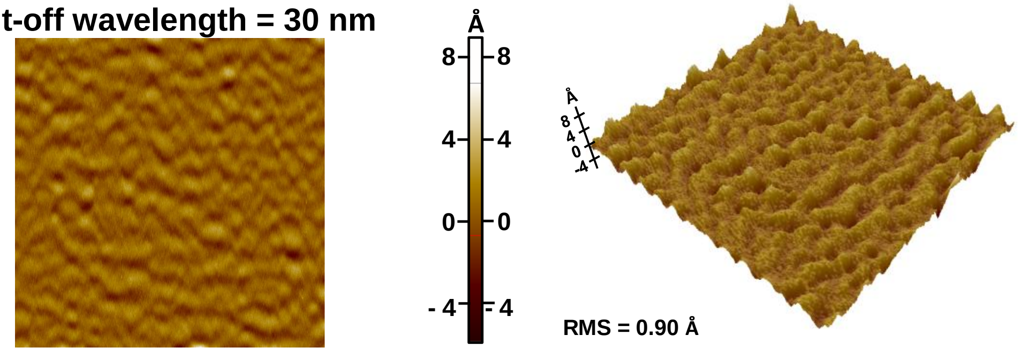

(d) Cut-off wavelength = 20 nm

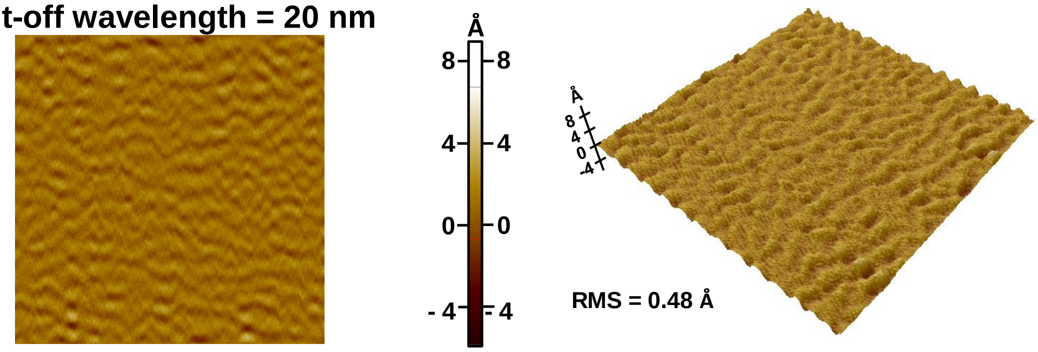

Figure 6.6 AFM images (2D and 3D views) of a 250 × 250 nm^2 area in a 0.2% uniaxially strained sample. Before filtering (a) and after applying a low-pass wavelength filter with a cut-off wavelength of (b) 50 nm, (c) 30 nm and (d) 20 nm. There is a reduction in RMS roughness with decreasing filter cut-off wavelength. Also, a reduction in the wavelength of the surface undulations with decreasing cut-off wavelength can be observed at the edges of the 3D images.

(a) Non-filtered

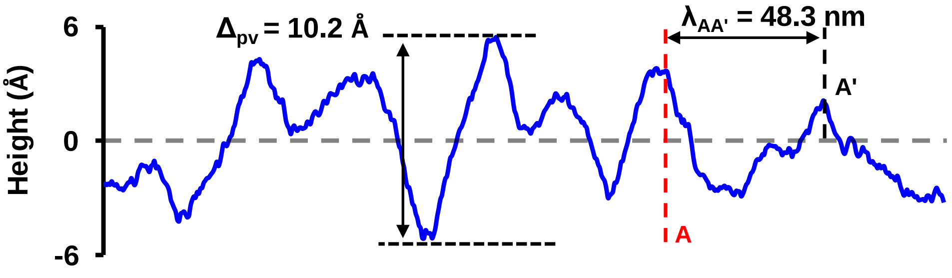

(b) Cut-off wavelength = 50 nm

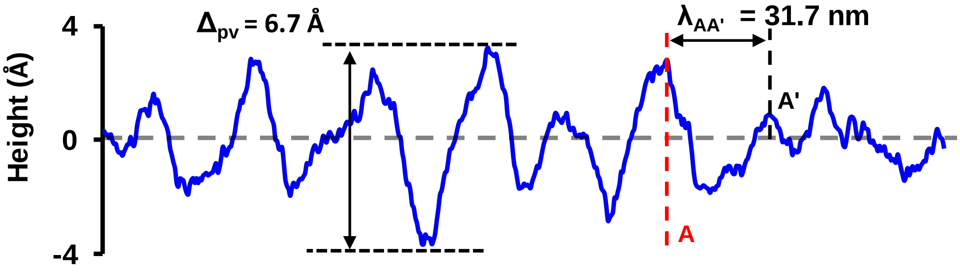

(c) Cut-off wavelength = 30 nm

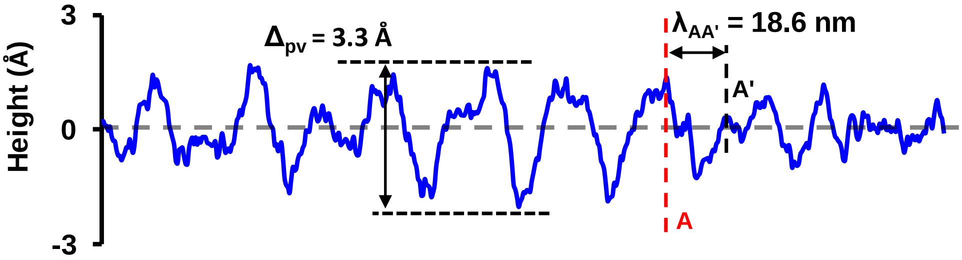

(d) Cut-off wavelength = 20 nm

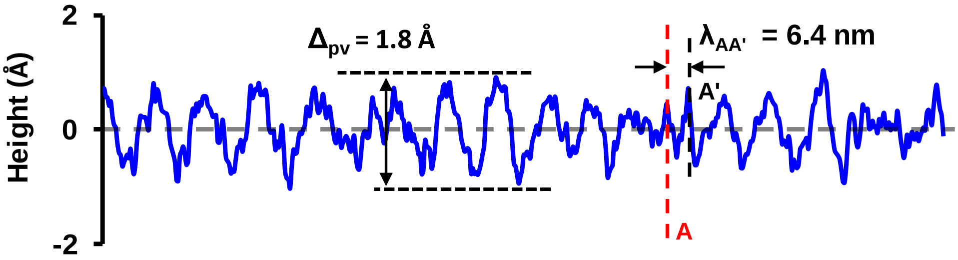

Figure 6.7 Height-profile of the AFM images shown in Figure 6.6 across the middle of the sample (0.2% uniaxially strained). Before filtering (a) and after applying a low-pass wavelength filter with a cut-off wavelength of (b) 50 nm, (c) 30 nm and (d) 20 nm. Similar to the RMS roughness value, there is a reduction in the peak-to-valley height (Δpv) with decreasing filter cut-off wavelength.

6.4.2 RMS roughness scale-dependency.

The analysis of the RMS roughness variation with the filter cut-off wavelength performed in section 6.4.1.2 was performed in a 250 × 250 nm^2 area. For a self-affine surface however, the RMS roughness varies with the size of the area. Thus, it is important to examine the dependency of the RMS roughness with the scan-size (or scan-length). As mentioned in section 6.3.1, each scanned image was progressively scaled down to a minimum scan-length of ~10 nm. This resulted in 12 areas of different size (Figure 6.4c).

6.4.2.1 Uniaxial strain

Figure 6.8 shows the RMS roughness variation for a 2.0% uniaxially strained sample with the scan-length and with the filter cut-off wavelength. RMS values of each data point correspond to the average of all the areas with equal size of each sample i.e. 15 (section 6.3.1). At areas smaller than ~100 × 100 nm^2 the RMS roughness exhibits scale dependency with the scan-length. This confirms that the surface is self-affine and the surface roughness parameters including the RMS roughness, correlation length and Hurst exponent, have to be determined considering the scan-size dependency.

Error bars in Figure 6.8 show the deviation from the mean (standard deviation) in RMS roughness observed in the 15 analysed areas of equal size. As expected, due to the decrease in RMS roughness with decreasing filter cut-off wavelength, the variation (error bars) in RMS roughness between the 15 analysed areas also decreases. The maximum variation in RMS roughness for the sample in Figure 6.8 is ~0.5 Å. This corresponds to a 150 × 150 nm^2 area with no filtration. For all the samples the maximum RMS roughness variation was ~0.8 Å corresponding to a 0.2% strained sample and no filtration.

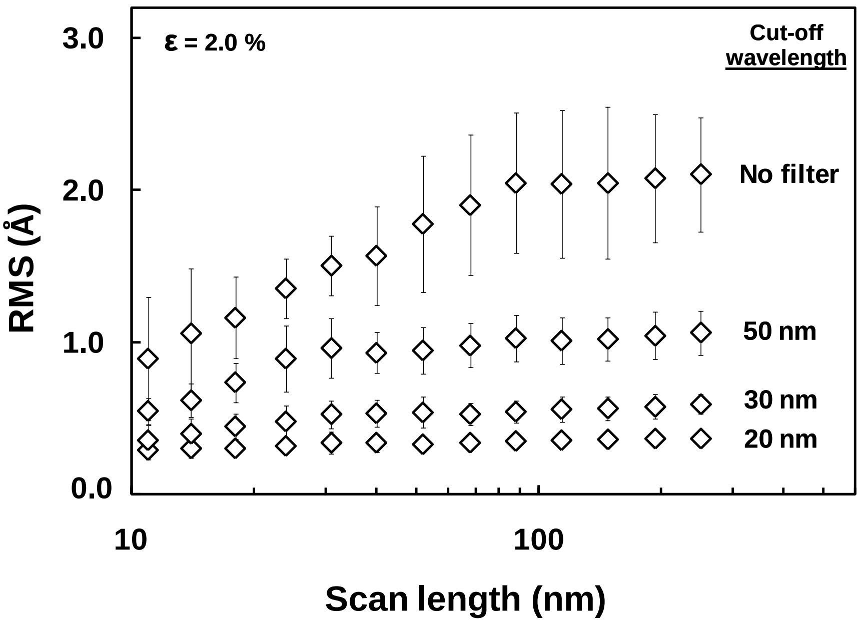

Figure 6.8 RMS roughness values in a 2.0% uniaxially strained sample with the scan-length and with the filter cut-off wavelength. Error bars represent the deviations from the mean (standard deviation) in RMS roughness observed in all the analysed areas with equal scan-length.

6.4.2.2 Biaxial strain

The variation of the RMS roughness with the scan-length and with the filter cut-off wavelength for a 1.3% biaxially strained sample is shown in Figure 6.9. Similar to the uniaxially strained samples, the RMS roughness exhibits scale dependency with the scan-size at scan-lengths ~50 − 100 nm. However, the precise point for the RMS roughness scale-dependency is not clear. This will be discussed in section 6.4.2.3.1.

The maximum variation in RMS roughness for the biaxially strained sample in Figure 6.9 is ~0.17 Å. This also corresponds to the maximum variation in RMS roughness encountered within all the samples. This variation relates to a 31 × 31 nm^2 area with no filtration.

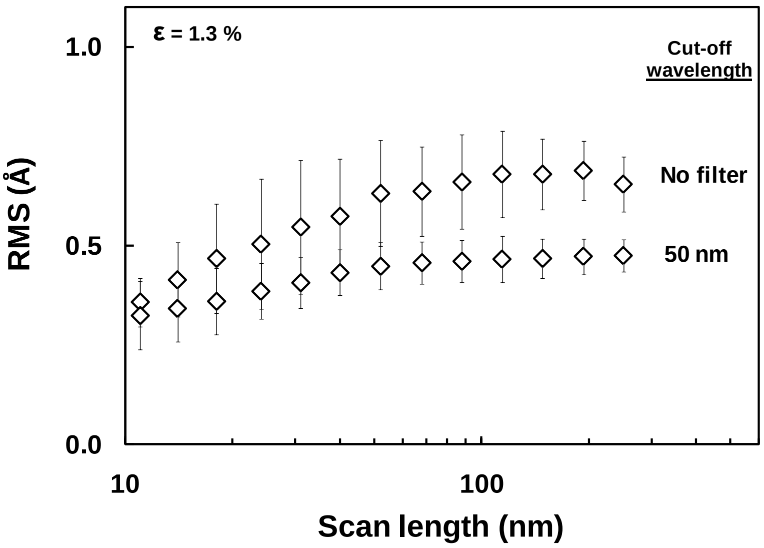

Figure 6.9 RMS roughness variation in a 1.3% biaxially strained sample with the scan-length and with the filter cut-off wavelength. Error bars represent the deviations from the mean (standard deviation) in RMS roughness observed in all the analysed areas with equal scan-length.

6.4.2.3 Determination of roughness parameters: Fitting procedure.

In order to determine the roughness parameters, the experimental values of the RMS roughness extracted from the AFM images were fitted using Equation 6.9. The experimental data were fitted by a weighted least-square (chi-squared) non-linear regression in Matlab 7.10 (R2010a) using the curve fitting tool with a custom equation in the form of Equation 6.9. In a least-squares non-linear regression fitting, the experimental data are fitted by successive approximations and the target is to minimise the error between the fitting curve and the experimental data. The input variables were the true interface width w_0, the correlation length ξ, and the Hurst exponent α (Equation 6.9). All the input variables were initiated at 0. The correlation-length was restricted to vary between 0 and the maximum scan-length i.e. 250 nm for the unfiltered images, and between 0 and the filter cut-off wavelength for the filtered images. The Hurst exponent was restricted to vary between 0 and 1. The goodness-of-fit was assessed by the reduced chi-squared and the adjusted R-squared or $\tilde{R}^2$ (more appropriate for non-linear regressions) figures-of-merit and the uncertainty in the fitted parameters i.e. RMS, correlation length and Hurst exponent was computed with 95% confidence bounds. Figure 6.10a shows the fitting (for a 2.0% strained sample before filtration) and the values obtained for the interface width, correlation length and Hurst exponent.

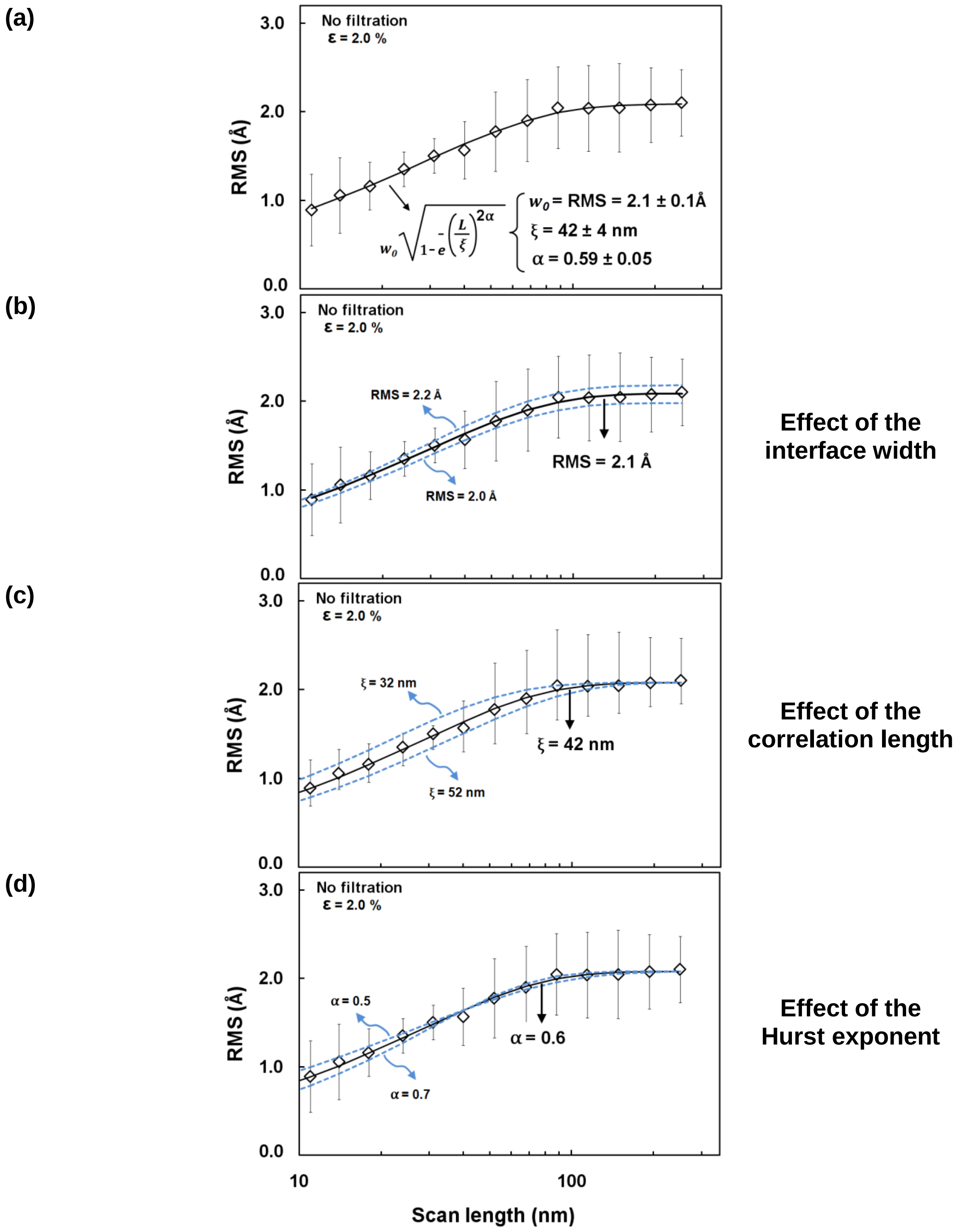

Figure 6.10 Fitting of the experimental data by a weighted least-squares non-linear regression and effect of the different parameters. (a) Optimum fitting. The result of the fitting procedure is given by the interface width w_0 (or RMS roughness), the correlation length ξ and the Hurst exponent α. (b) Effect of the interface width on the fitting. (c) Effect of the correlation length on the fitting. (c) Effect of the Hurst exponent of the fitting.

The impact of the different input variables on the fitting is also shown in Figure 6.10b-d. The effect of the interface width (Figure 6.10b) is related to the lifting of the curve with little change on the curvature and the slope. In contrast, the correlation length (Figure 6.10c) has a major effect on the curvature and the Hurst exponent (Figure 6.10d) on the slope of the curve.

6.4.2.3.1 Self-affine and saturation regions

All the graphs studied in this work exhibit the characteristic asymptotic behaviour described by Equation 6.9 for a real self-affine surface (Figure 6.11): there is a saturation region characterised by a plateau where the RMS roughness is constant, and a self-affine region where the RMS roughness scale with the lateral scan-length. There is also a slight bending of the self-affine region near the minimum scan-length. This bending effect at the end of the self-affine region is due to the shortage of data at small scan areas.

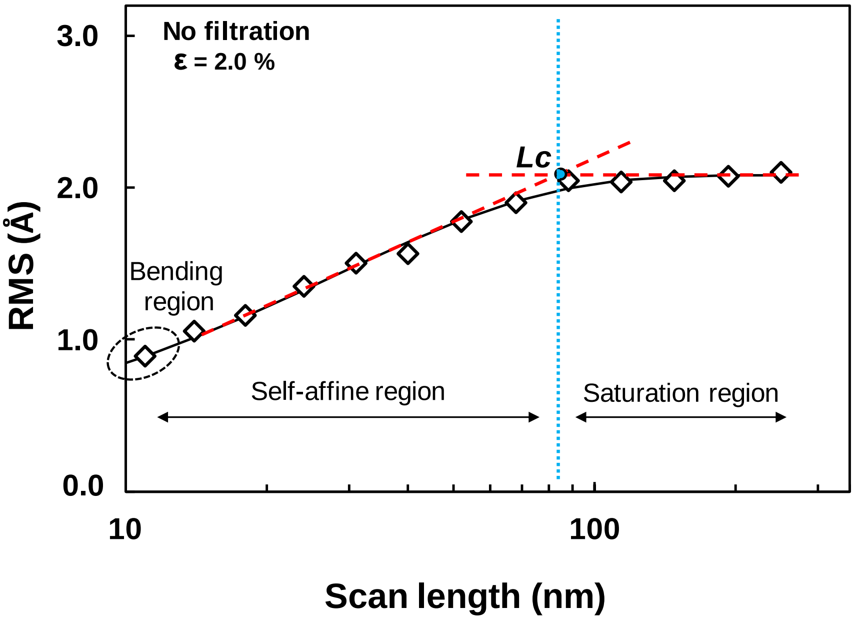

Figure 6.11 Self-affine and saturation region. L_c is defined as the intersection between the asymptotic lines of the saturation and self-affine regions. At small scan-lengths, there is a slight bending due to the shortage of data of the area.

Due to the asymptotic behaviour, there is no precise boundary between the saturation and the self-affine region. In order to compare the behaviour of the two regions with strain, the intersection L_c between the asymptotic lines of the saturation and self-affine regions (dashed lines in Figure 6.11) have been used as a reference. The asymptotic line of the saturation region (plateau) was modelled with a horizontal line crossing the RMS roughness at L = 250 nm. The self-affine region was modelled with a straight line tangent at the inflexion point between the end of the self-affine region and the beginning of the bending zone. In most cases however, the straight line defining the self-affine region started at the minimum scan-length L = 10 nm.

6.4.3 Impact of uniaxial strain on the surface roughness

Figures 6.12 to 6.19 show the AFM images and height profiles for each value of strain i.e. 0.2%, 0.6%, 1.3%, 2.0% and 2.3%. Only one area of 250 × 250 nm^2 for each strain level and filter cut-off wavelength is presented. There is a reduction of RMS roughness and peak-to-valley heights with increasing strain in most images. In some cases however, (e.g. Figure 6.12b and Figure 6.12c, or Figure 6.12d and Figure 6.12e) due to the small differences in RMS roughness between samples with similar values of strain, the trend in RMS with strain is not clear. This shows that wrong conclusions may be obtained if the analysis is limited to only one scan-size.

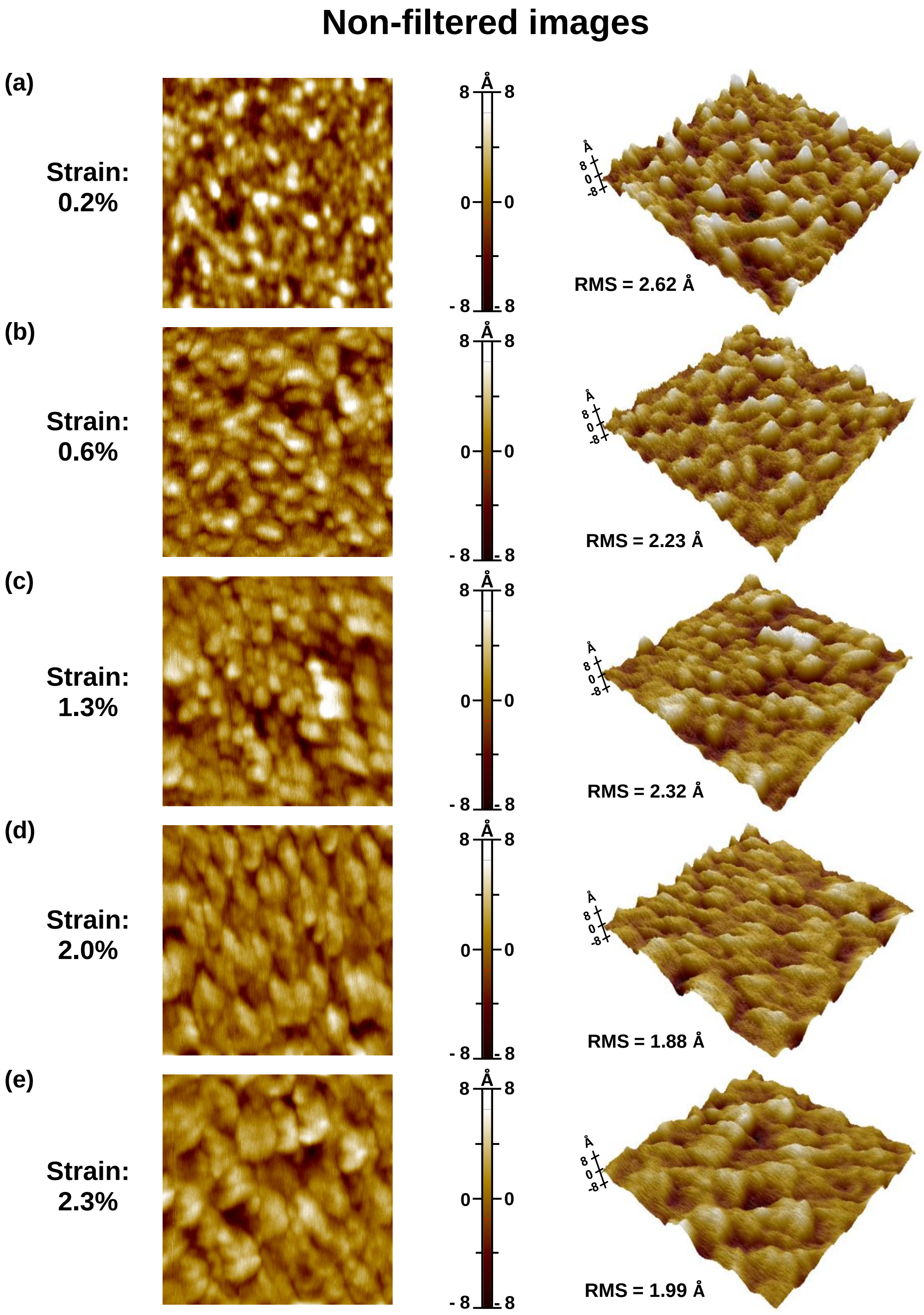

Figure 6.12 AFM images (2D and 3D views) of a 250 × 250 nm^2 area of uniaxially tensile sample beams with no filtration and strain values of (a) 0.2%, (b) 0.6%, (c) 1.3%, (d) 2.0% and (e) 2.3%.

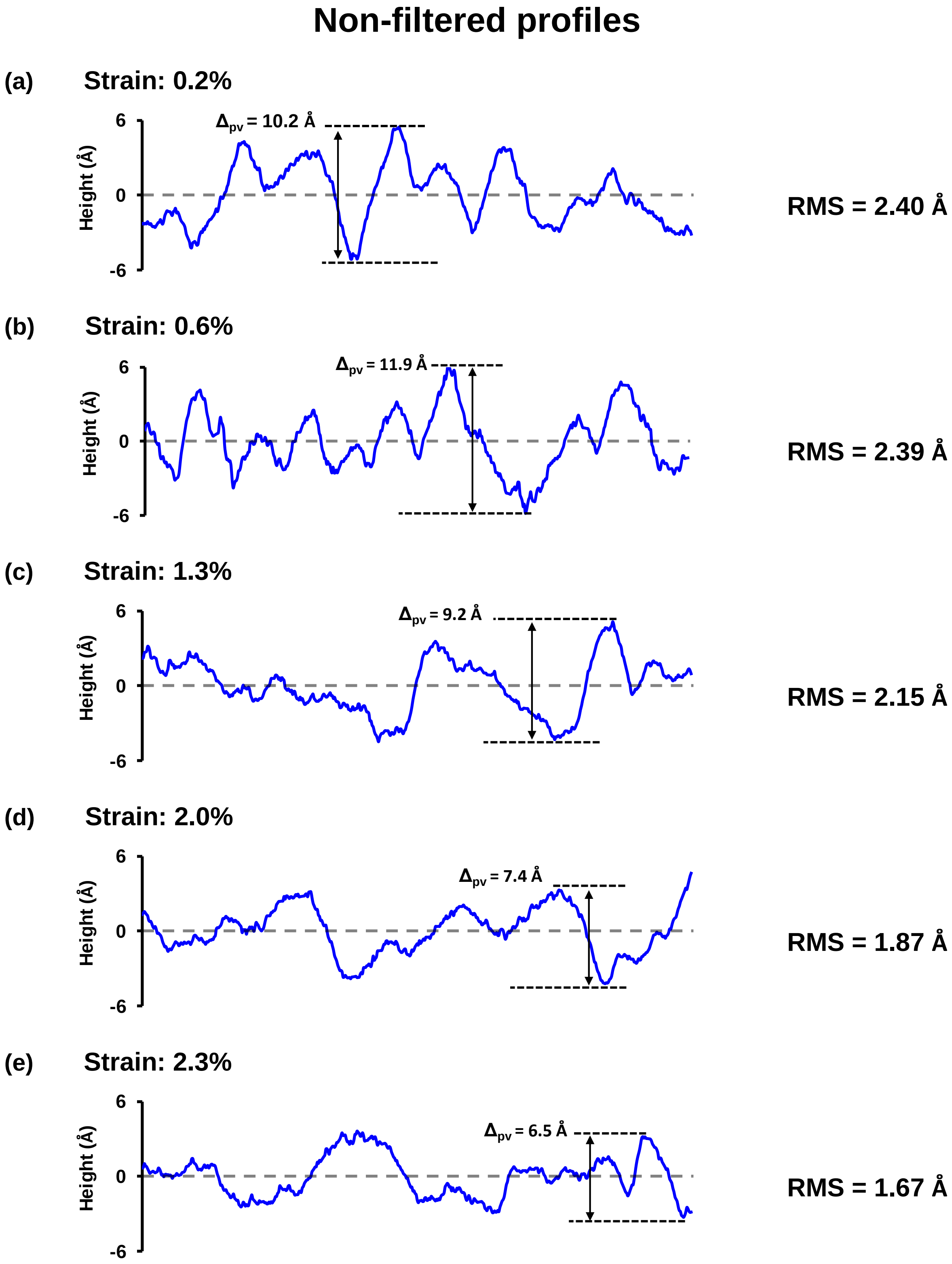

Figure 6.13 Height-profile of the non-filtered AFM images shown in Figure 6.12, across the middle of the sample beam with strain values of (a) 0.2%, (b) 0.6%, (c) 1.3%, (d) 2.0% and (e) 2.3%.

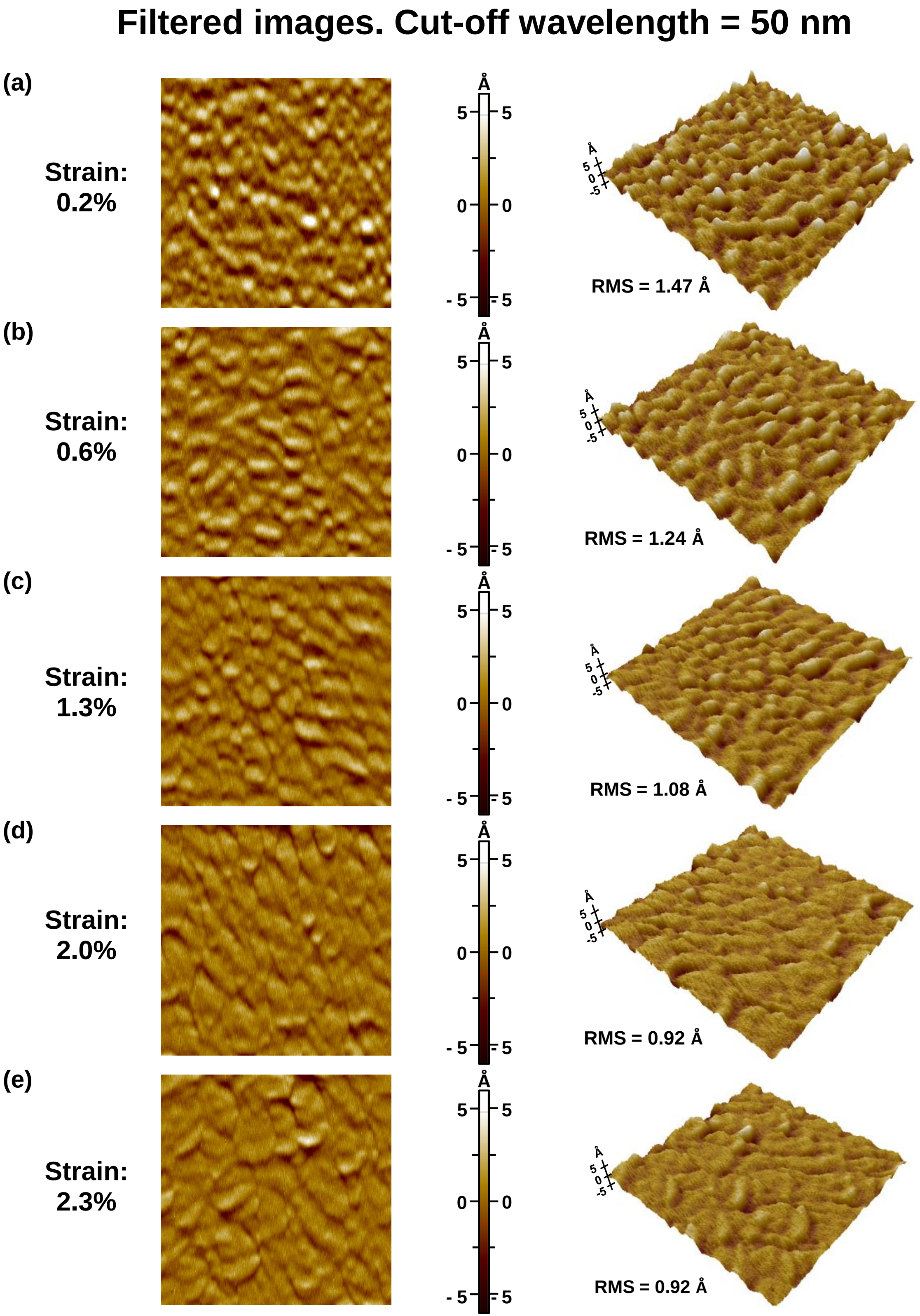

Figure 6.14 AFM images (2D and 3D views) of a 250 × 250 nm^2 area of uniaxially tensile sample beams after applying a 50 nm low-pass wavelength filter and strain values of (a) 0.2%, (b) 0.6%, (c) 1.3%, (d) 2.0% and (e) 2.3%.

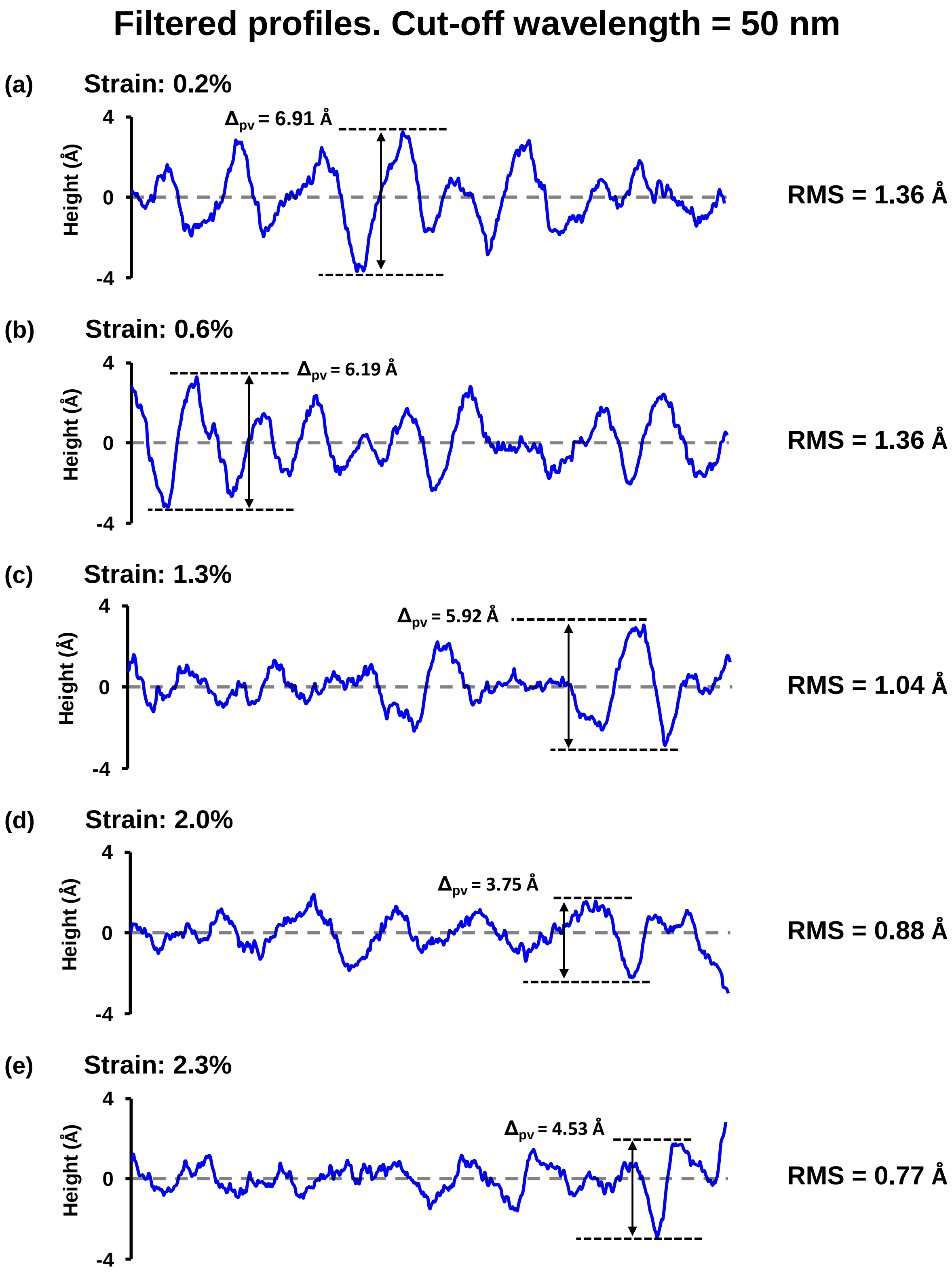

Figure 6.15 Height-profile of the filtered (cut-off wavelength = 50 nm) AFM images shown in Figure 6.14, across the middle of the sample beam with strain values of (a) 0.2%, (b) 0.6%, (c) 1.3%, (d) 2.0% and (e) 2.3%.

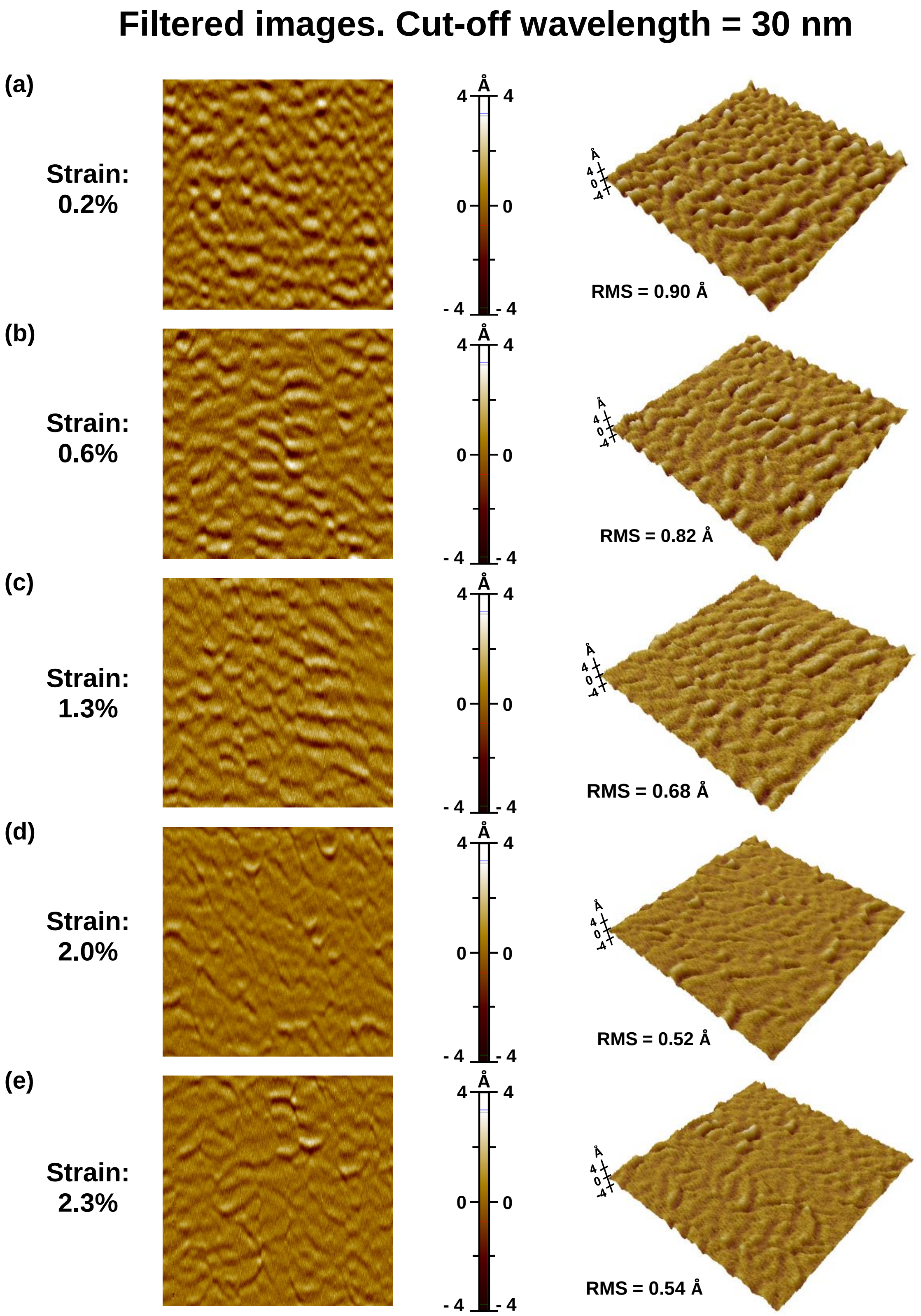

Figure 6.16 AFM images (2D and 3D views) of a 250 × 250 nm^2 area of uniaxially tensile sample beams after applying a 30 nm low-pass wavelength filter and strain values of (a) 0.2%, (b) 0.6%, (c) 1.3%, (d) 2.0% and (e) 2.3%.

Filtered profiles. Cut-off wavelength = 30 nm

(a) Strain: 0.2%

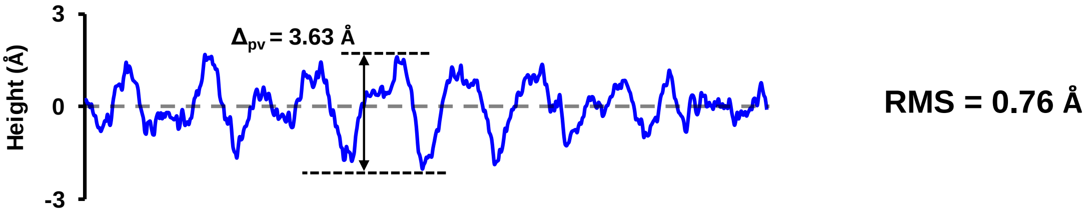

(b) Strain: 0.6%

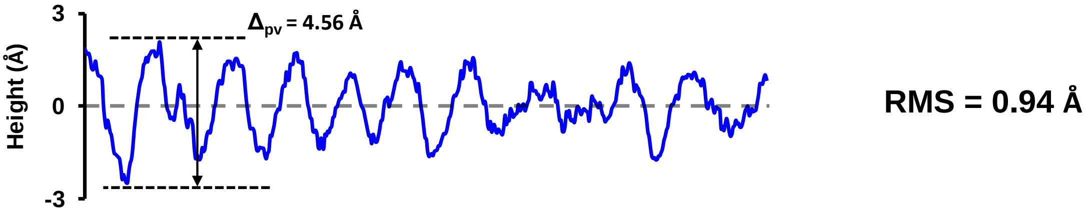

(c) Strain: 1.3%

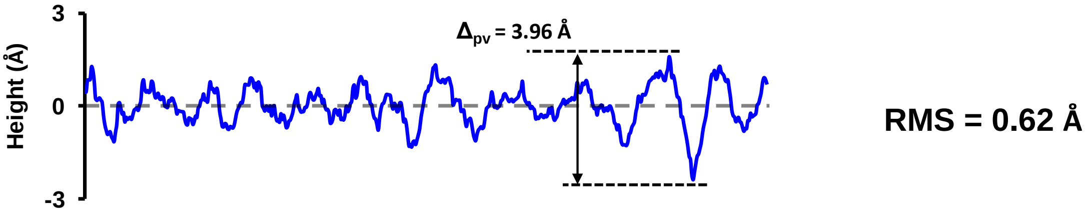

(d) Strain: 2.0%

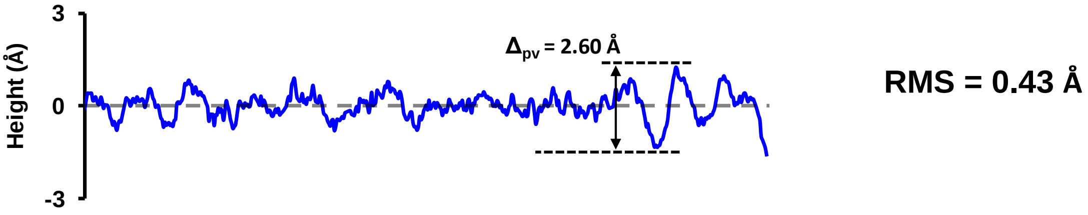

(e) Strain: 2.3%

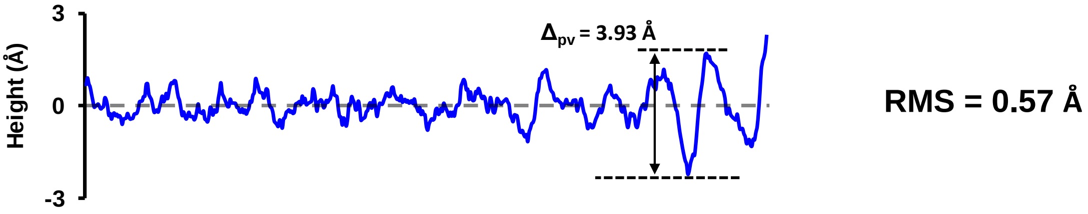

Figure 6.17 Height-profile of the filtered (cut-off wavelength = 30 nm) AFM images shown in Figure 6.16, across the middle of the sample beam with strain values of (a) 0.2%, (b) 0.6%, (c) 1.3%, (d) 2.0% and (e) 2.3%.

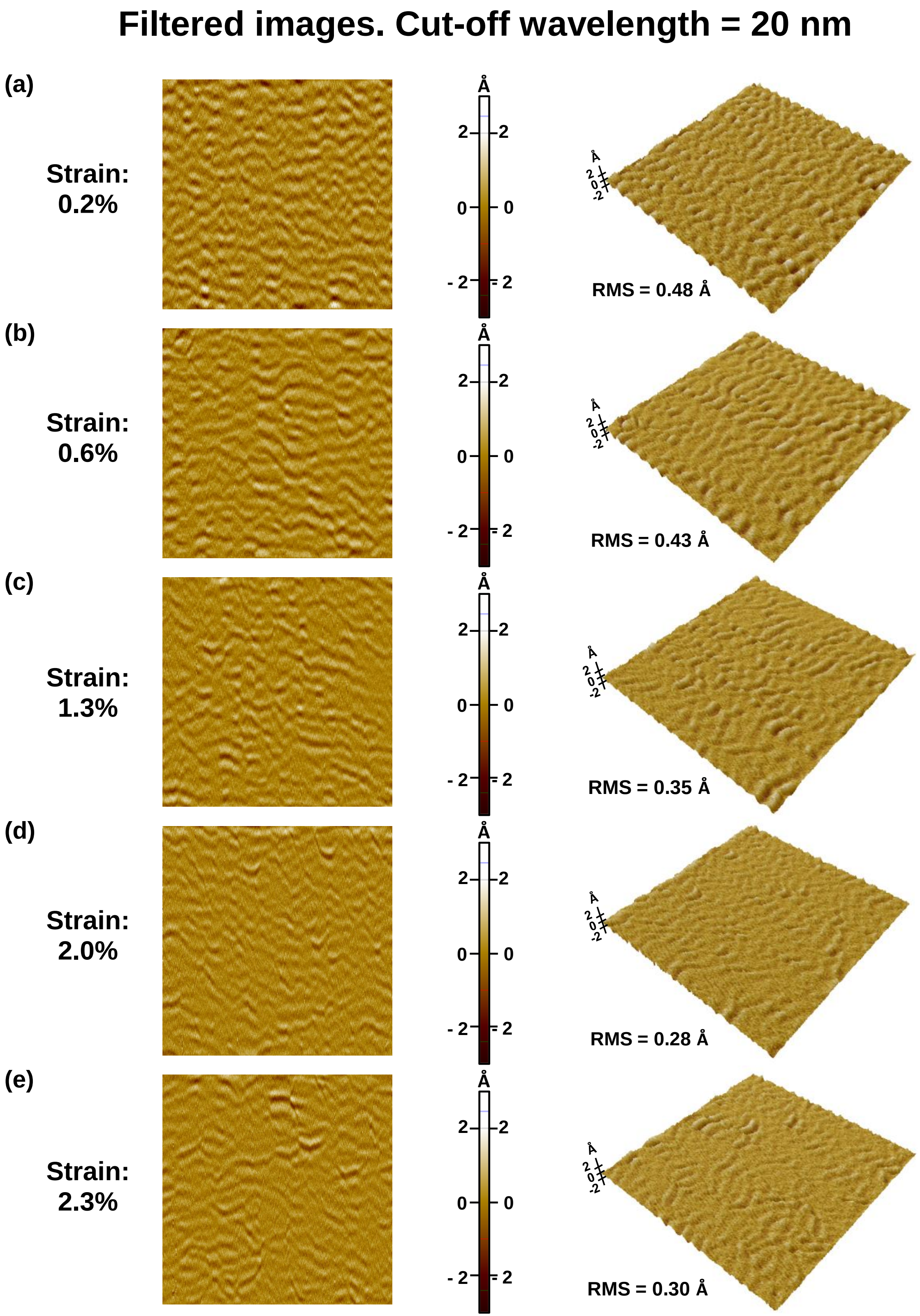

Figure 6.18 AFM images (2D and 3D views) of a 250 × 250 nm^2 area of uniaxially tensile sample beams after applying a 20 nm low-pass wavelength filter and strain values of (a) 0.2%, (b) 0.6%, (c) 1.3%, (d) 2.0% and (e) 2.3%.

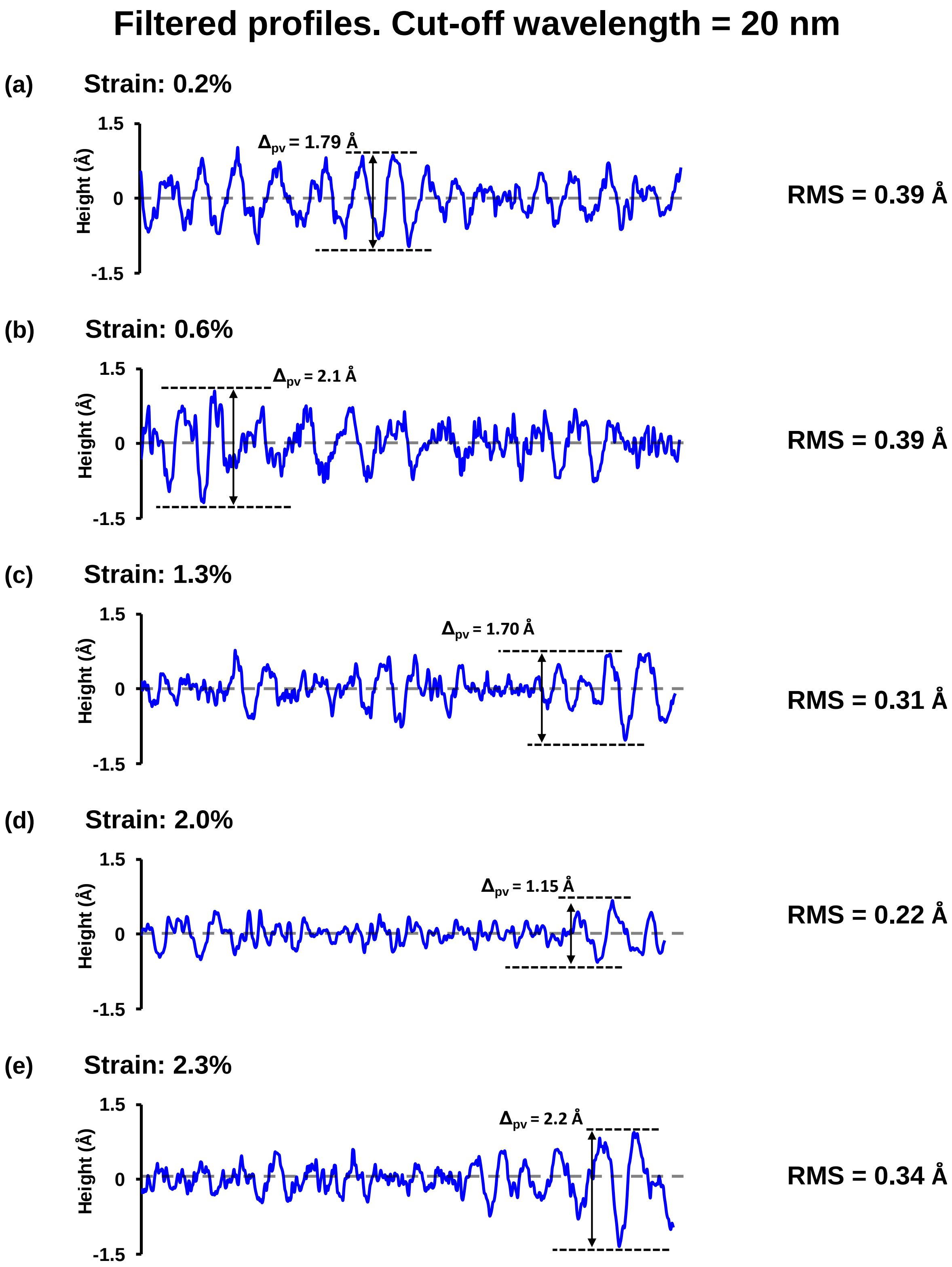

Figure 6.19 Height-profile of the filtered (cut-off wavelength = 20 nm) AFM images shown in Figure 6.18, across the middle of the sample beam with strain values of (a) 0.2%, (b) 0.6%, (c) 1.3%, (d) 2.0% and (e) 2.3%.

To get more reliable information and account for the self-affine behaviour of the RMS roughness, the data for each scan-size is fitted using the same fitting procedure described in section 6.4.2.3. Figures 6.20a - 6.20e show the weighted least-squares non-linear regression fitting of the experimental data of the unfiltered images for all the scan-sizes and strain values. Error bars correspond to the standard deviation (deviation from the mean) of the experimental data at each scan-size. The reduced chi-squared for the fits shown in Figures 6.20a - 6.20e varies between $0.01 < \tilde{\chi}^2 < 0.04$ and the adjusted R-squared between $0.978 < \tilde{R}^2 < 0.997$. The uncertainty in the fitted parameters (with 95% confidence bounds) i.e. RMS, correlation length and Hurst exponent is also shown in the legend of each figure. These results will be summarised in sections 6.4.3.1 - 6.4.3.3. Figure 6.20f shows all the fitted lines and the distance (or scan-length) corresponding to the intersection point L_c between the saturation and self-affine region. L_c increases with increasing strain from ~50 to ~110 nm. This increase suggests that the surface features might be expanding horizontally with increasing tensile strain.

Figures 6.21 - 6.23 show the non-linear regression fitting of the experimental data of the filtered images and the uncertainty in the adjusted parameters. The reduced-chi squared for the fittings shown in figures 6.21 - 6.23 varies between $0.01 < \tilde{\chi}^2 < 0.26$ and the adjusted R^2 varies between $0.700 < \tilde{R}^2 < 0.987$. The values of $\tilde{\chi}^2 < 1$ and $\tilde{R}^2 \simeq 1$ validate the model used in Equation 6.9 to fit the experimental data and confirm the goodness-of-fit. The values of $\tilde{\chi}^2 \ll 1$ suggest however, that the uncertainties in RMS roughness determination from the experiments are significantly large. This indicates that both the technique and the instrument used to measure the RMS roughness are approaching the limits to accurately resolve the small values of RMS roughness of the samples (0.35 Å < w_0 < 2.36 Å).

All the filtered images show an increase in Lc with increasing strain (Figures 6.21f, 6.22f and 6.23f). The maximum increase of L_c with strain (from ~20 to ~60 nm) is for the 20 nm cut-off wavelength filtered images (Figure 6.23f). Interestingly, for the 0.2% strained samples, L_c also decreases with increasing the level of filtration. Thus, whereas for the unfiltered images, L_c is ~50 nm, after applying a 20 nm cut-off wavelength filtration, L_c reduces to 20 nm. This can be understood considering that the scaling behaviour of the self-affine region only holds within a certain range of lengths (the height values cannot keep increasing or decreasing indefinitely, section 6.2). Thus, the effect of reducing the RMS roughness (due to the filter) can be considered as a shift of the self-affine and saturation regions.

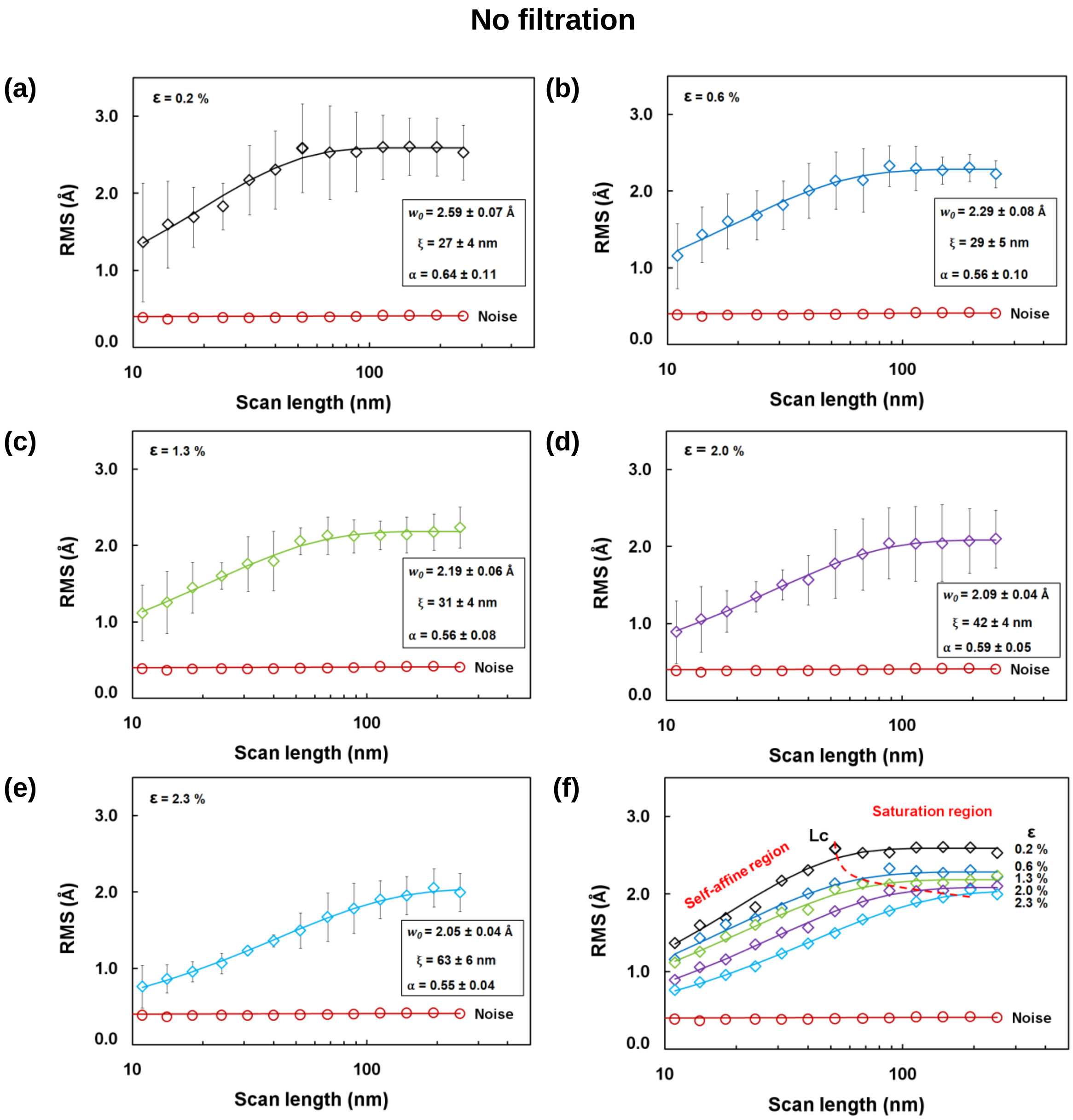

Figure 6.20 Non-linear regression fitting of the experimental RMS roughness values with scan-length in the wires before applying the low-pass wavelength filter for uniaxial strain values of a) 0.2%, b) 0.8%, c) 1.3%, d) 2.0% and e) 2.3% and f) for all the strain values in the range 0.2-2.3%. The legends show the uncertainties (with 95% confidence bounds) in the fitted parameters i.e. RMS, correlation length and Hurst exponent. The reduced chi-squared and adjusted *R*-squared for these fittings vary between $0.01 < \tilde{\chi}^2 < 0.04$ and $0.978 < \tilde{R}^2 < 0.997$. The red dashed line in f) shows the variation of *Lc* with strain.

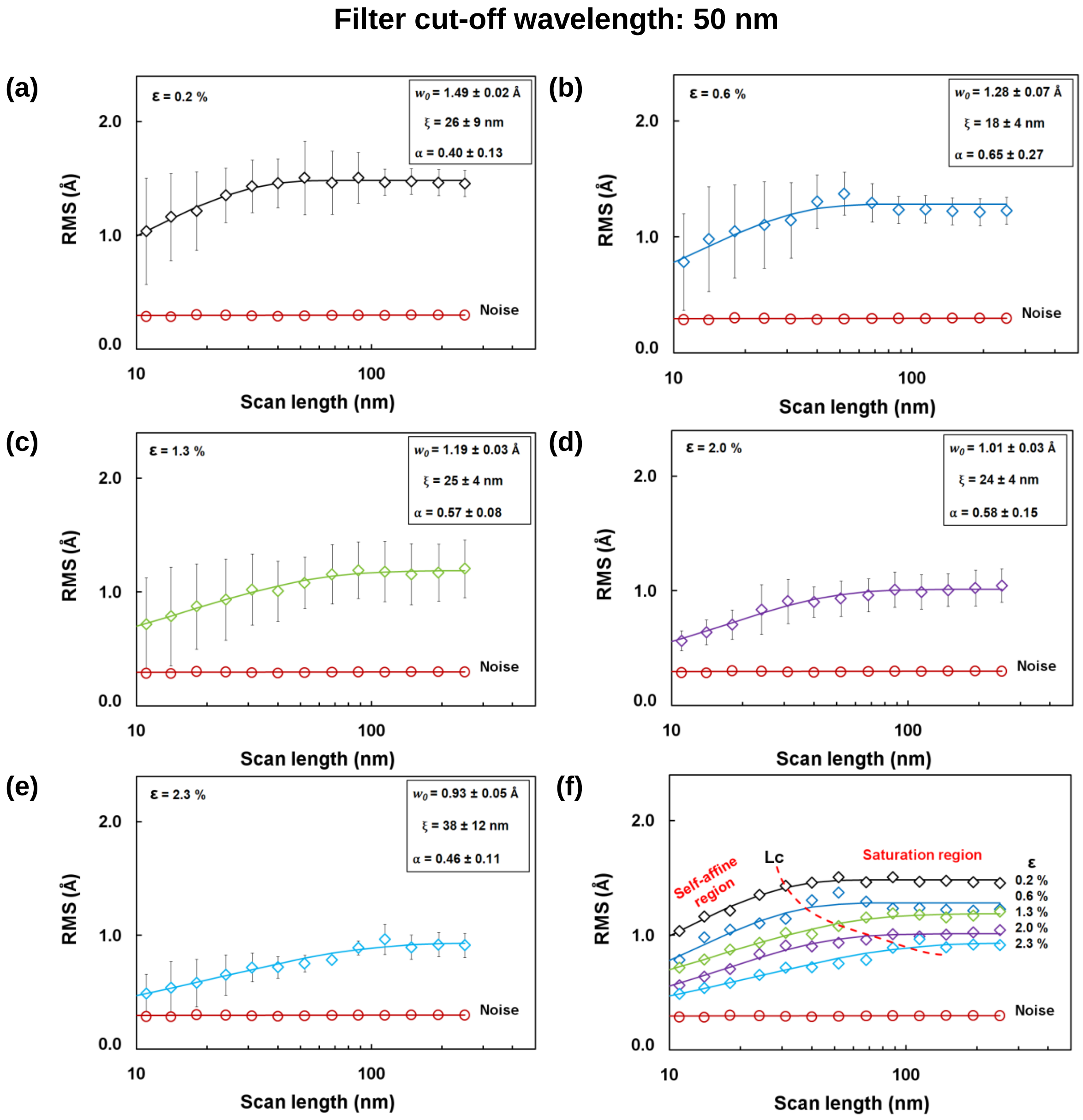

Figure 6.21 Non-linear regression fitting of the experimental RMS roughness values with scan-length in the wires after applying a 50 nm cut-off wavelength filter for uniaxial strain values of a) 0.2%, b) 0.8%, c) 1.3%, d) 2.0% and e) 2.3% and f) for all the strain values in the range 0.2-2.3%. The legends show the uncertainties (with 95% confidence bounds) in the fitted parameters i.e. RMS, correlation length and Hurst exponent. The reduced chi-squared and adjusted *R*-squared for these fittings vary between $0.01 < \tilde{\chi}^2 < 0.16$ and $0.888 < \tilde{R}^2 < 0.984$. The red dashed line in f) shows the variation of *Lc* with strain.

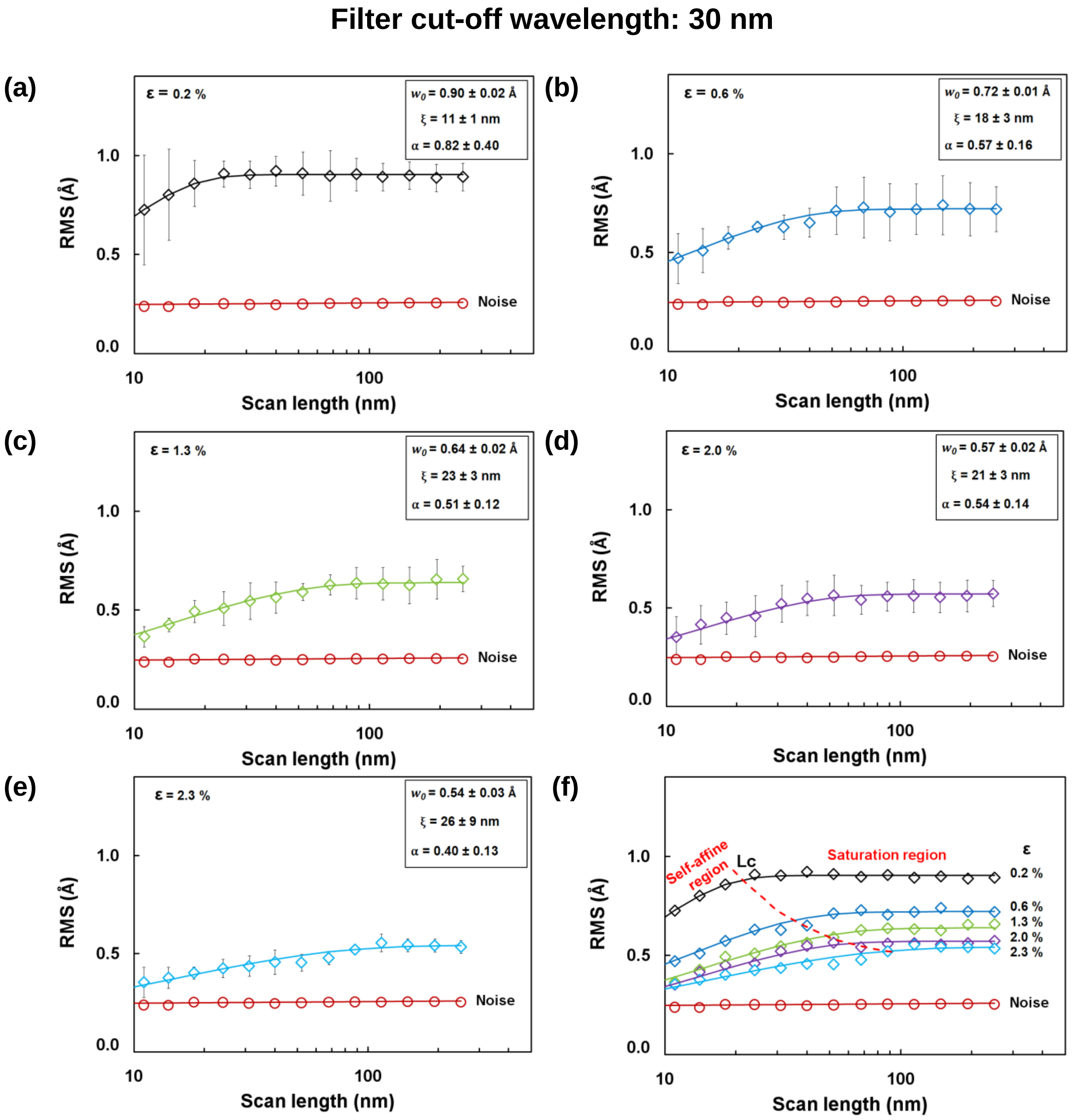

Figure 6.22 Non-linear regression fitting of the experimental RMS roughness values with scan-length in the wires after applying a 30 nm cut-off wavelength filter for uniaxial strain values of a) 0.2%, b) 0.8%, c) 1.3%, d) 2.0% and e) 2.3% and f) for all the strain values in the range 0.2-2.3%. The legends show the uncertainties (with 95% confidence bounds) in the fitted parameters i.e. RMS, correlation length and Hurst exponent. The reduced chi-squared and adjusted *R*-squared for these fittings vary between $0.02 < \tilde{\chi}^2 < 0.26$ and $0.919 < \tilde{R}^2 < 0.987$. The red dashed line in f) shows the variation of *Lc* with strain.

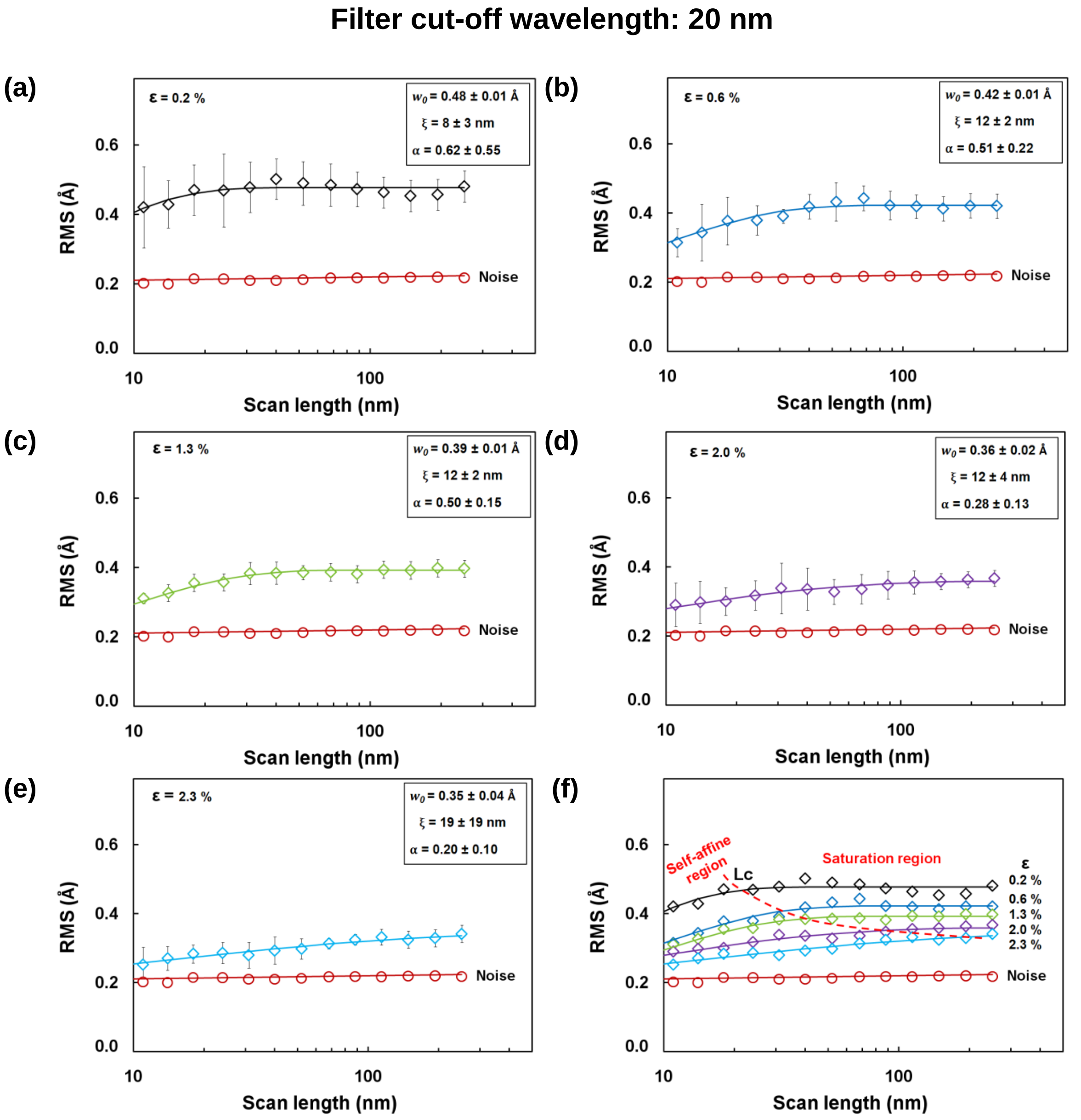

Figure 6.23 Non-linear regression fitting of the experimental RMS roughness values with scan-length in the wires after applying a 20 nm cut-off wavelength filter for uniaxial strain values of a) 0.2%, b) 0.8%, c) 1.3%, d) 2.0% and e) 2.3% and f) for all the strain values in the range 0.2-2.3%. The legends show the uncertainties (with 95% confidence bounds) in the fitted parameters i.e. RMS, correlation length and Hurst exponent. The reduced chi-squared and adjusted *R*-squared for these fittings vary between $0.05 < \tilde{\chi}^2 < 0.12$ and $0.700 < \tilde{R}^2 < 0.934$. The red dashed line in f) shows the variation of *Lc* with strain.

6.4.3.1 Effect of uniaxial strain on the RMS roughness

The weighted least-squares non-linear fitting shown in Figures 6.20 - 6.23, shows a decrease of the RMS roughness with increasing applied strain for all the filtered and non-filtered images. This confirms the reduction of RMS roughness observed (section 6.4.3) in most of the AFM images and height profiles (Figures 6.12 to 6.19). Also the RMS roughness reduction suggests a relation between morphology changes in the horizontal and vertical directions. Figure 6.24 summarises the RMS roughness extracted from the least-squares non-linear fitting shown in Figures 6.20 - 6.23 for the filtered and non-filtered images with strain. Error bars in RMS for each data point are smaller than 0.1 Å and they are not visible.

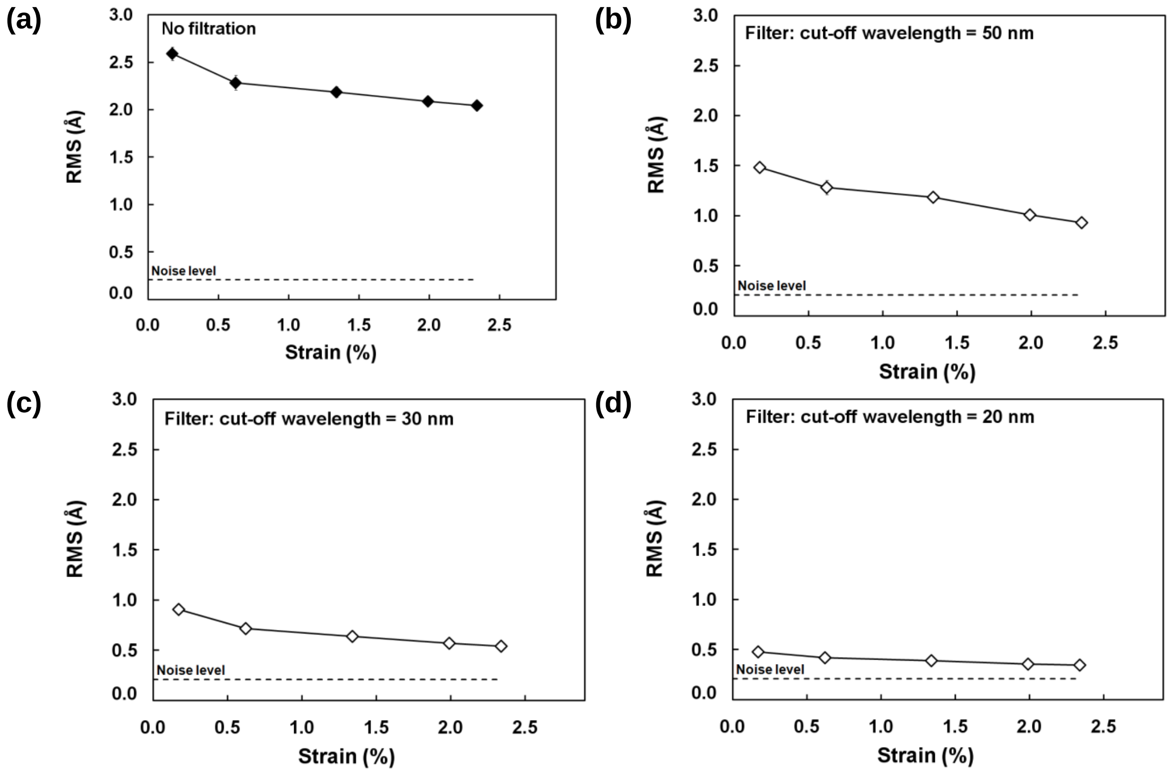

Figure 6.24 RMS roughness variation with strain as determined from the fitting of the experimental data in Figures 6.20 - 6.23 in the wires a) before applying the low-pass wavelength filter and after applying a low-pass wavelength filter with cut-off wavelengths of b) 50 nm, c) 30 nm and d) 20 nm.

There is a progressive decrease in RMS roughness with increasing strain at all the wavelength regimes (filter cut-off wavelength). The maximum RMS roughness variation with strain in the range 0.2 − 2.3% is ~0.6 Å for the non-filtered images. In percentage however, the maximum decrease in RMS roughness for the same range of strain is ~40% for the 30 nm cut-off wavelength filtration.

6.4.3.2 Effect of uniaxial strain on the correlation length

The correlation length variation with strain and with the cut-off wavelength of the filter determined from the fitting procedure (section 6.4.2.3) in Figures 6.20 - 6.23 is shown in Figure 6.25.

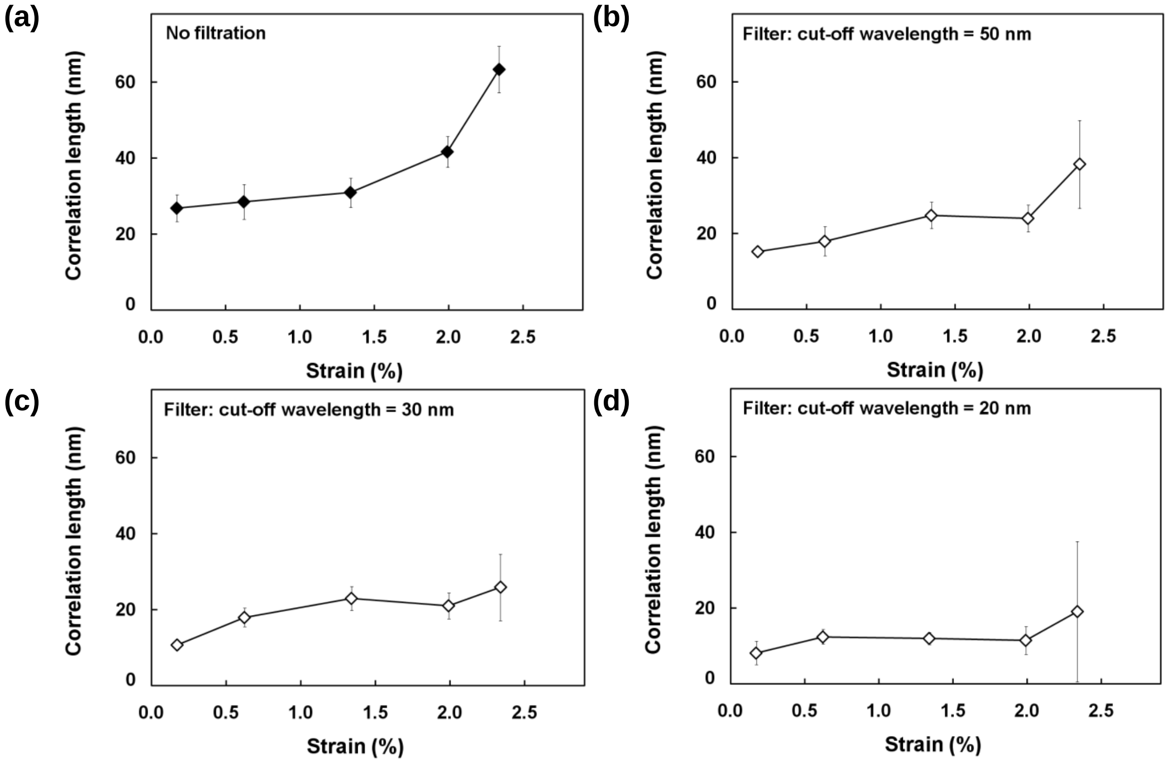

Figure 6.25 Correlation length variation with strain as determined from the fitting of the experimental data in Figures 6.20 - 6.23 in the wires a) before applying the low-pass wavelength filter and after applying a low-pass wavelength filter with cut-off wavelengths of b) 50 nm, c) 30 nm and d) 20 nm.

There is an increase in correlation length with increasing strain for the non-filtered and the 50 and 30 nm cut-off wavelength filtered images (for the 20 nm cut-off wavelength filtered images, the increase is less clear). This increase in correlation length also agrees with the previous hypothesis of the surface features expanding horizontally (section 6.4.3) while shrinking in the vertical direction (as observed in section 6.4.3.1 with the RMS roughness reduction with increasing strain) with increasing strain. The maximum variation in correlation length values with strain is ~37 nm for the non-filtered images. In percentage, the maximum increase is ~150% for the 50 nm cut-off wavelength filtration. The increase in correlation length is generally more pronounced at high values of strain ($\varepsilon > 1.3\%$) and is especially significant for the non-filtered images. For the non-filtered images, the increase in correlation length is ~15% in the range 0.2 – 1.3% of strain compared with ~100% increase in the range 1.3 – 2.3% of strain. This agrees with the observations in a previous work [66] where large variations in correlation length were found to be initiated at strain values higher than 1.7%. This also suggests that a threshold value of strain may exist from which the impact on the surface undulations in the horizontal direction will be more significant. Like the RMS roughness variation with the filter cut-off wavelength, (section 6.4.1.2), the correlation length also decreases with decreasing filter cut-off wavelength since a low-pass wavelength filter supress the wavelengths above the cut-off wavelength.

6.4.3.3 Effect of uniaxial strain on the Hurst exponent

The Hurst exponent variation with strain and with the cut-off wavelength of the filter determined from the fitting procedure (section 6.4.2.3) in Figures 6.20 - 6.23 is shown in Figure 6.26. For the non-filtered images, the Hurst exponent is constant ~0.6 in the range of strain 0.2 – 2.3 %. This indicates that the surface roughness can be reasonably well represented by the exponential model ($\alpha = 0.5$) in Equation 6.9. For the filtered images however, the Hurst exponent significantly changes. For a cut-off wavelength of 30 nm and 0.2% of applied strain, the Hurst exponent is ~0.8. These high values of Hurst exponent indicate that the surface roughness is better described by the Gaussian model ($\alpha = 1$) in Equation 6.9. Contrastingly, at high levels of strain (2.3 %) and low filter cut-off wavelengths (20 nm) the Hurst exponent decreases to ~0.2. At this regime of wavelengths and strain values, neither the exponential nor the Gaussian models can successfully describe the surface roughness. The large variations in Hurst exponent from $\alpha = 0.8$ to 0.2 indicate that the Hurst exponent might be highly dependent on the strain and the surface undulations wavelength regime. However, as shown in Figure 6.26, the uncertainties in

Hurst exponent (error bars) especially at low values of strain are significant. These large uncertainties indicate that the Hurst exponent may also be highly sensitive to additional factors including the technique used for its determination. This will be further discussed in section 6.4.6.1.

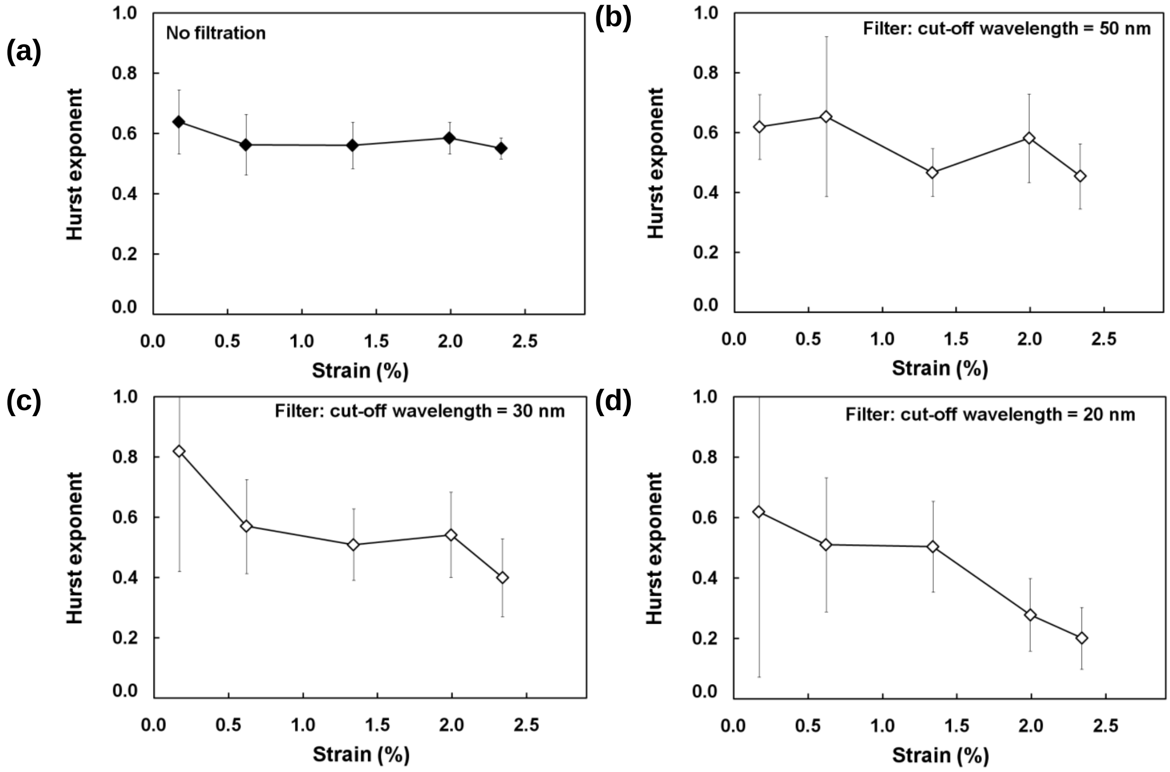

Figure 6.26 Hurst exponent variation with strain as determined from the fitting of the experimental data in Figures 6.20 - 6.23 in the wires a) before applying the low-pass wavelength filter and after applying a low-pass wavelength filter with cut-off wavelengths of b) 50 nm, c) 30 nm and d) 20 nm

6.4.4 Impact of biaxial strain on the surface roughness

Figures 6.27 to 6.30 show the AFM images of 250 × 250 nm^2 areas and the height profiles taken across the middle of the area for the unstrained and strained SOI films (0.8% and 1.3%). Only one area of 250 × 250 nm^2 for each strain level and filter cut-off wavelength is presented.

The RMS roughness values of the areas shown in the AFM images exhibit a decreasing trend with increasing strain. The difference between the maximum and minimum RMS roughness is ~0.2 Å for the unfiltered images and 0.1 Å for the 50 nm cut-off wavelength filtered images. In contrast, the peak-to-valley values in the height profiles for the 50 nm cut-off wavelength filtered images increase with increasing strain. The small differences in RMS roughness determined from the 250 × 250 nm^2 areas and the opposite trend obtained from the peak-to-valley values in the height profiles confirm that the extraction of the roughness parameters from a single scan area is highly unreliable [174, 181].

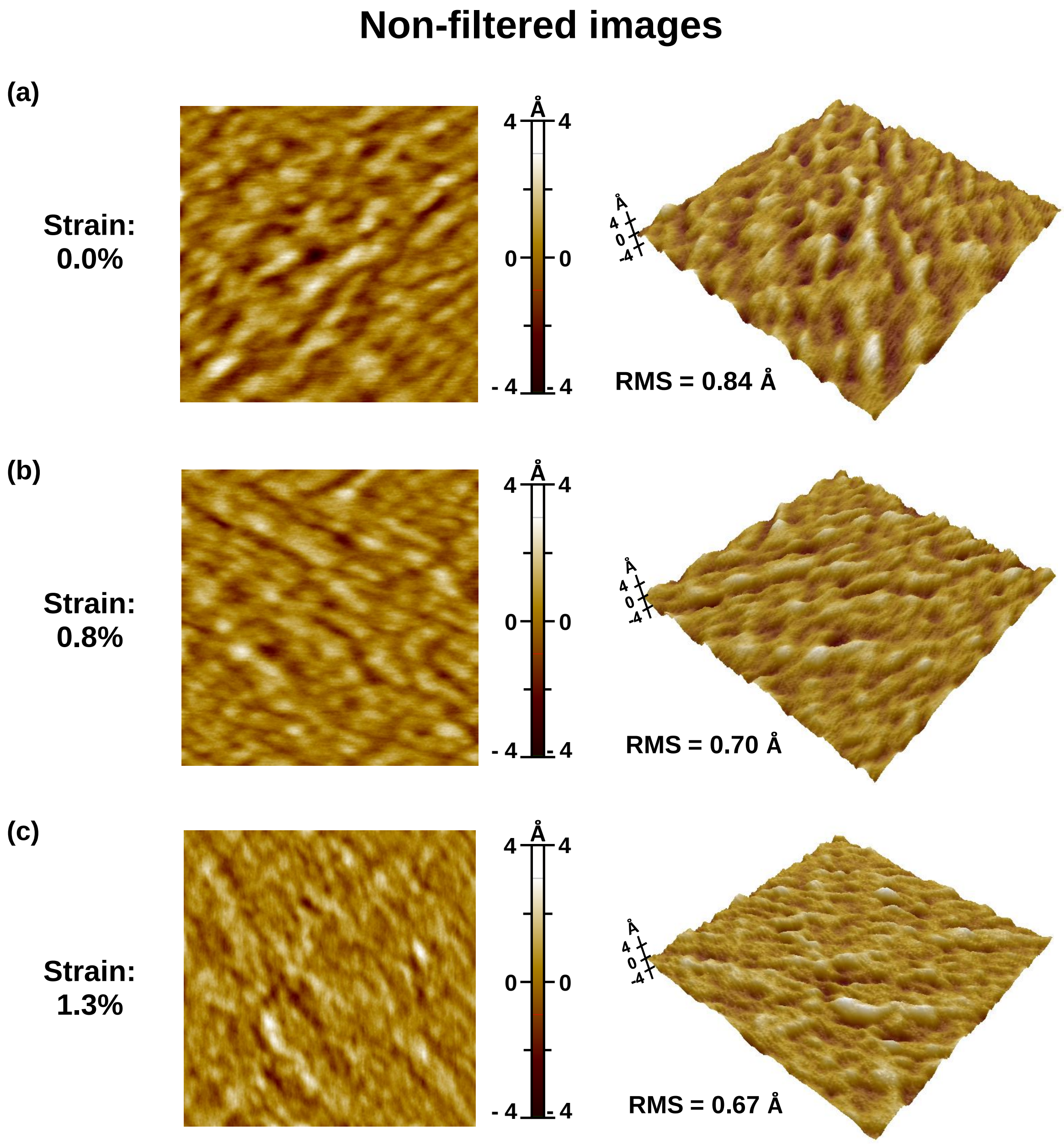

Figure 6.27 AFM images (2D and 3D views) of a 250 × 250 nm^2 area of biaxially tensile films with no filtration and strain values of (a) 0.0%, (b) 0.8% and (c) 1.3%.

Non-filtered profiles

(a) Strain: 0.0%

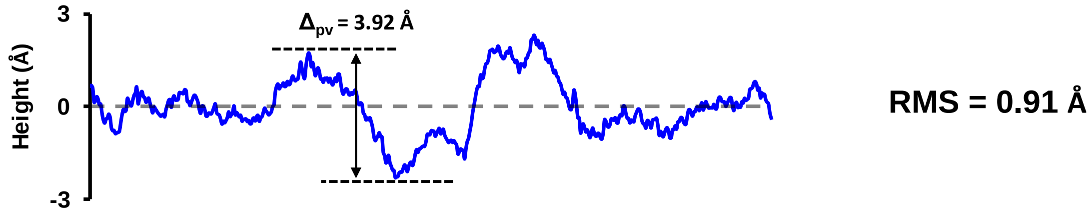

(b) Strain: 0.8%

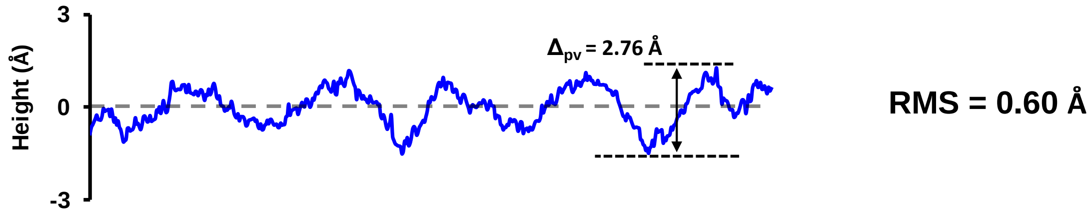

(c) Strain: 1.3%

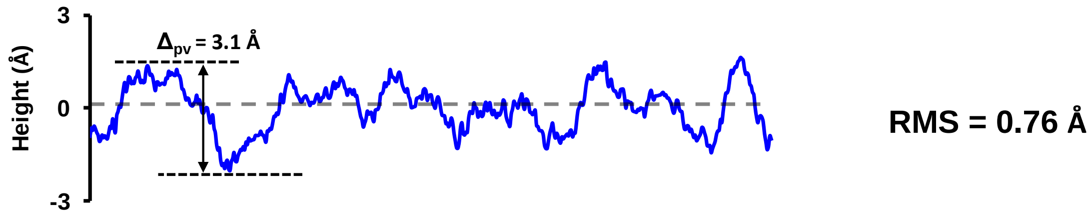

Figure 6.28 Height-profile of the non-filtered AFM images shown in Figure 6.27, across the middle of the sample with strain values of (a) 0.0%, (b) 0.8% and (c) 1.3%.

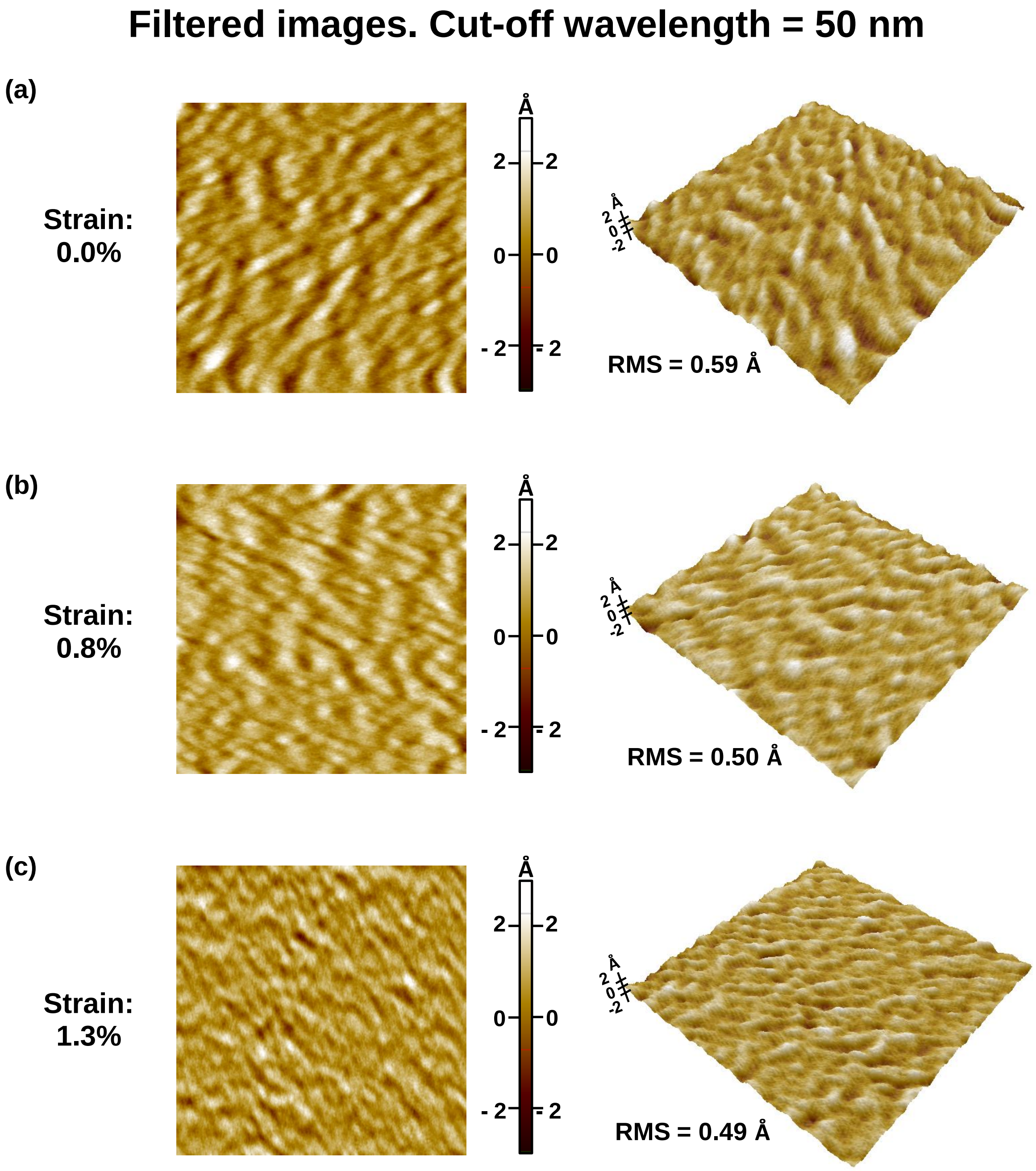

Figure 6.29 AFM images (2D and 3D views) of a 250 × 250 nm^2 area of biaxially tensile films after applying a 50 nm low-pass wavelength filter and strain values of (a) 0.0%, (b) 0.8% and (c) 1.3%.

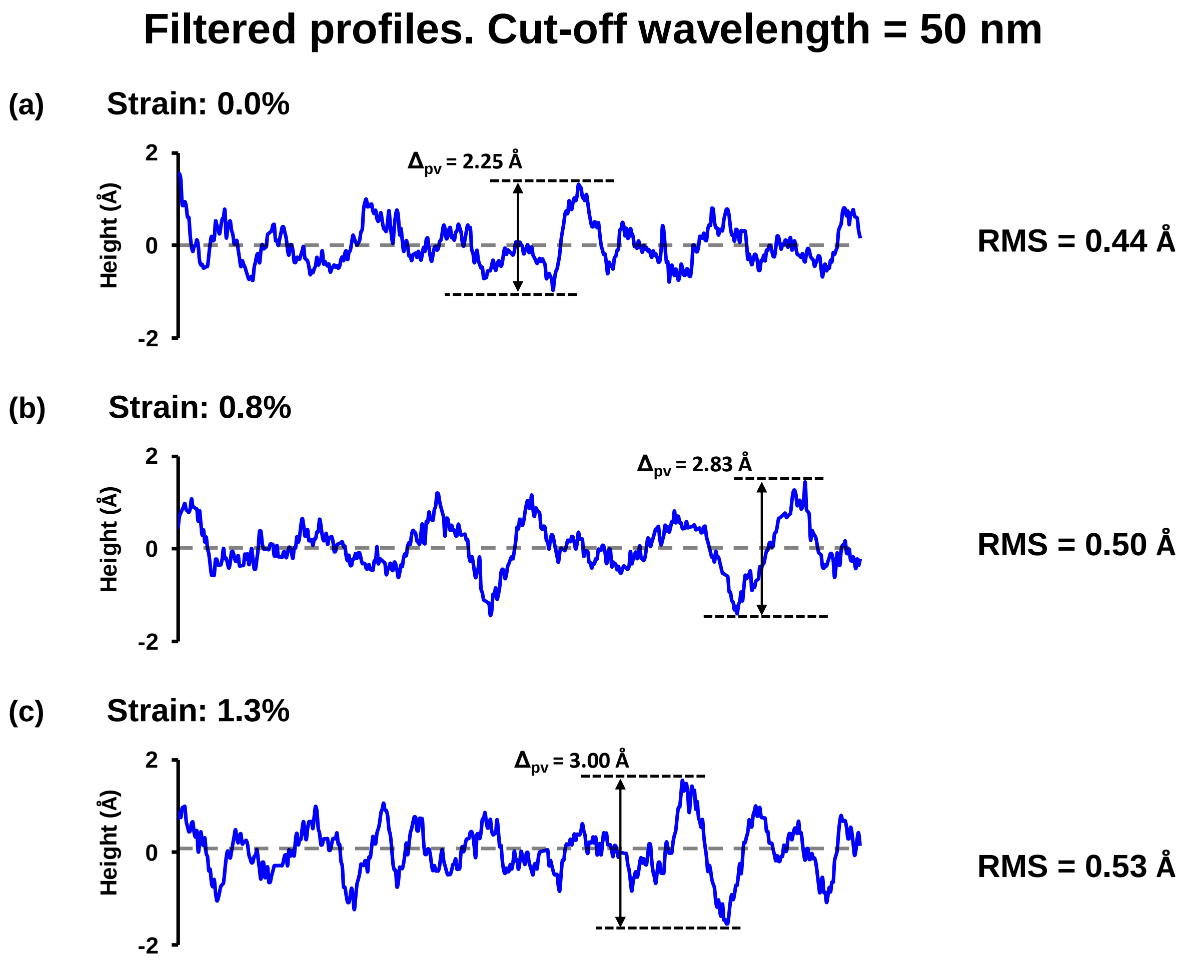

Figure 6.30 Height-profile of the filtered (cut-off wavelength = 50 nm) AFM images shown in Figure 6.29, across the middle of the sample with strain values of (a) 0.0%, (b) 0.8% and (c) 1.3%.

In order to account for the self-affinity of the biaxially strained samples deduced in section 6.4.2.2, the experimental data was fitted using the same procedure described in section 6.4.2.3 for the uniaxially strained samples. Figures 6.31 and 6.32 show the fitting of the experimental data corresponding to the RMS roughness of the surface with the scan-length in the SOI and sSOI films before and after applying a 50 nm cut-off wavelength low-pass filter. Error bars correspond to the standard deviation of the experimental data at each scan-size. The reduced chi-squared and adjusted R-squared (goodness-of-fit) for the fittings shown in Figures 6.31 and 6.32 are $0.01 < \tilde{\chi}^2 < 0.10$ and $0.974 < \tilde{R}^2 < 0.995$. The values of $\tilde{\chi}^2 < 1$ and $\tilde{R}^2 \simeq 1$ validate the model used in Equation 6.9 to fit the experimental data and confirm the goodness-of-fit.

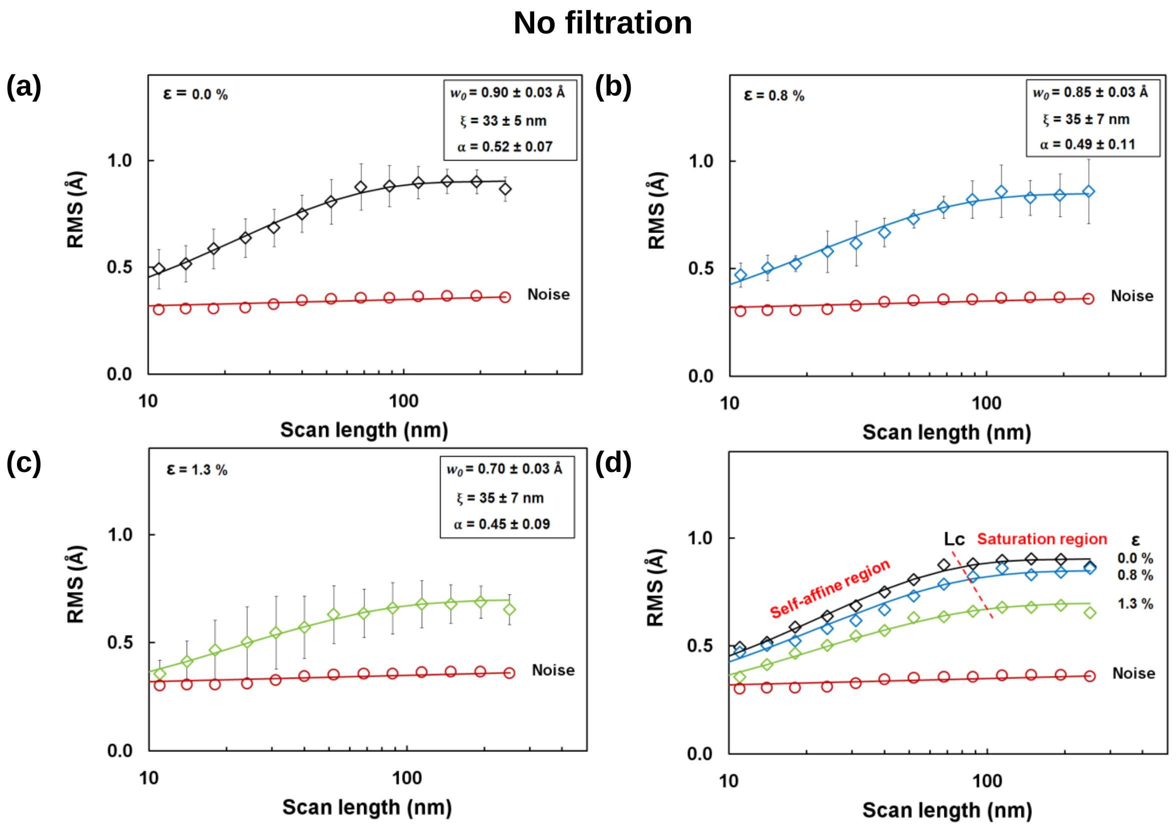

Figure 6.31 Non-linear regression fitting of the experimental RMS roughness values with scan-length in a) unstressed SOI, b) 0.8% sSOI and c) 1.3% sSOI films, and d) all the results for the unstressed SOI, 0.8% and 1.3% sSOI films before applying the low-pass wavelength filter. The legends show the uncertainties (with 95% confidence bounds) in the fitted parameters i.e. RMS, correlation length and Hurst exponent. The reduced chi-squared and adjusted *R*-squared for these fittings vary between $0.03 < \tilde{\chi}^2 < 0.10$ and $0.974 < \tilde{R}^2 < 0.986$. The red dashed line in d) shows the variation of *Lc* with strain.

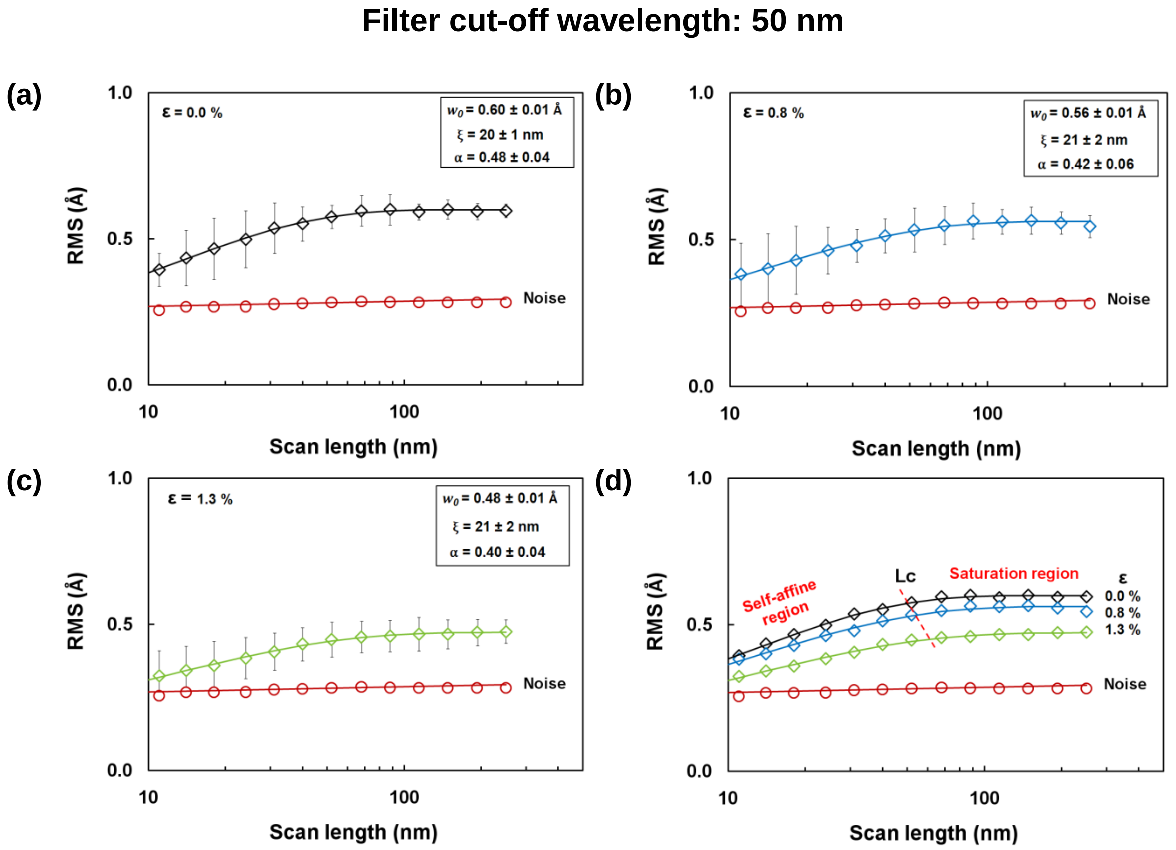

Figure 6.32 Non-linear regression fitting of the experimental RMS roughness values with scan-length in a) unstressed SOI, b) 0.8% sSOI and c) 1.3% sSOI films, and d) all the results for the unstressed SOI, 0.8% and 1.3% sSOI films before applying the low-pass wavelength filter. The legends show the uncertainties (with 95% confidence bounds) in the fitted parameters i.e. RMS, correlation length and Hurst exponent. The reduced chi-squared and adjusted *R*-squared for these fittings vary between 0.01 < $\tilde{\chi}^2$ < 0.02 and 0.990 < $\tilde{R}^2$ < 0.995. The red dashed line in d) shows the variation of *Lc* with strain.

Both SOI and sSOI films show the self-affine and saturation regions. Using the previous definition of L_c as the intersection of the asymptotes corresponding to the self-affine and saturation regions, L_c is shown to vary from ~80 to 85 nm in the range of strain 0 – 1.3%. This represents a ~5% increase. This increase is slightly lower than that obtained for the uniaxially strained samples (~12%) before applying the low pas filter for a similar range of strain (0.2 – 1.3%). Similar increase of L_c with increasing strain was found for the filtered images (Figure 6.32). The smaller increase of L_c with strain compared with the uniaxially strained samples, suggests that the sSOI films surface features may experience less lateral expansion with strain than the uniaxially strained samples for the same range of strain.

6.4.4.1 Effect of biaxial strain on the RMS roughness: Uniaxial vs. biaxial strain

Figure 6.33 shows the RMS roughness variation with strain for the non-filtered and filtered images shown in Figures 6.31 and 6.32.

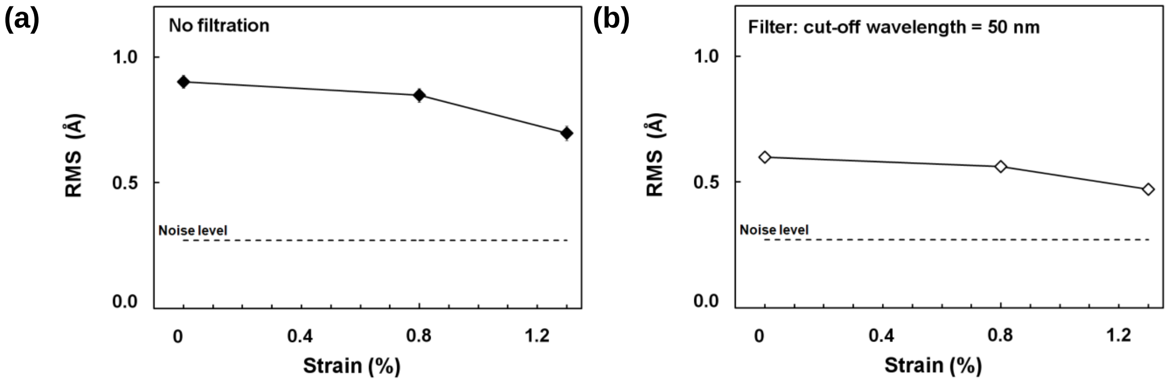

Figure 6.33 RMS roughness variation with strain as determined from the fitting of the experimental data in Figures 6.31 and 6.32 in the unstrained and biaxially strained films a) before applying the low-pass wavelength filter and b) after applying a low-pass wavelength filter with cut-off wavelengths of 50 nm.

There is a small reduction of RMS roughness (from ~0.9 to 0.7 Å for the non-filtered images and from ~0.6 to 0.5 Å for the filtered images) with increasing strain in the range 0 – 1.3%. The RMS roughness (absolute values) for the biaxial samples are ~65 – 70% smaller compared with those of the uniaxial samples for a similar range of strain (0.2 – 1.3%). In percentage however, the RMS roughness variation in the range of strain (0.2 – 1.3%) for the biaxial samples (~25 – 21% for the non-filtered and filtered images respectively) is comparable with that obtained for the uniaxial samples (~16 – 20%). Figure 6.34 shows a comparison between the RMS roughness of the uniaxial samples with that of the biaxial samples.

The higher RMS roughness of the uniaxial samples compared with that of the biaxial samples may be explained by the different fabrication processes (etching and annealing, section 4.2.1) undergone by the uniaxial samples. These processes are known to increase the RMS roughness of an initial smooth surface [182]. In case of the biaxial samples, only a mild cleaning was performed with no alteration of the silicon surface (section 6.3).

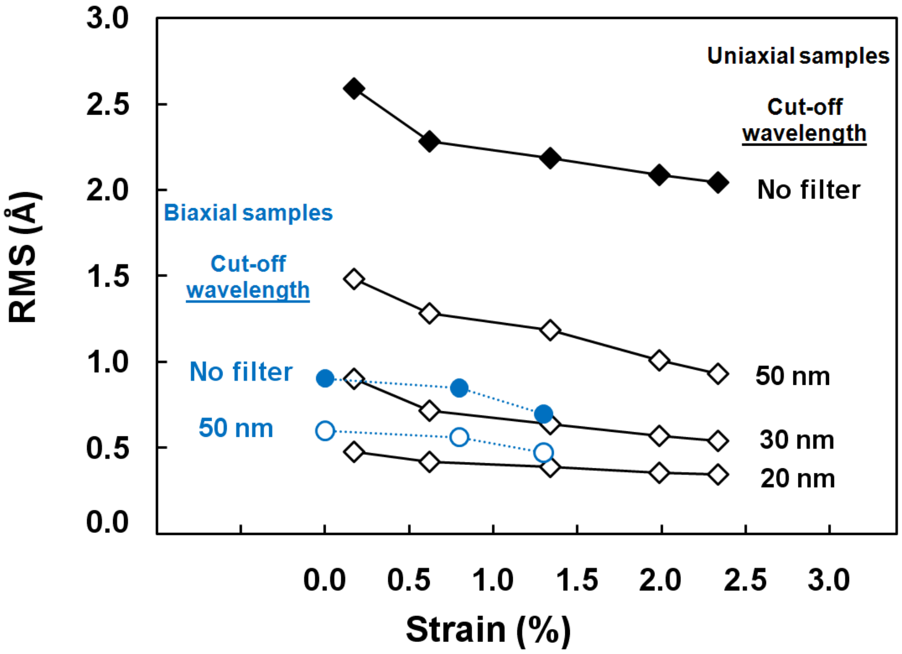

Figure 6.34 Comparison of the RMS roughness variation extracted from non-linear fitting performed in sections 6.4.3 and 6.4.4 between the uniaxial and biaxial samples.

6.4.4.2 Effect of biaxial strain on the correlation length: Uniaxial vs. biaxial strain

The variation of correlation length with strain determined from the fitting procedure for the non-filtered and filtered images (Figures 6.31 and 6.32) is shown in Figure 6.35.

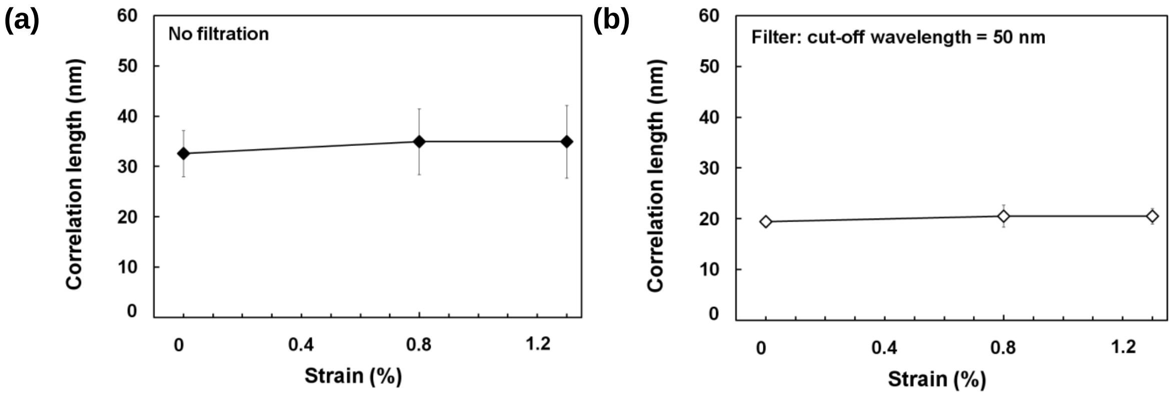

Figure 6.35 Correlation length variation with strain as determined from the fitting of the experimental data in Figures 6.31 and 6.32 in the unstrained and biaxially strained films a) before applying the low-pass wavelength filter and b) after applying a low-pass wavelength filter with cut-off wavelengths of 50 nm.

For the filtered and non-filtered images the correlation length is constant in the range 0 – 1.3%. In contrast, for a similar range of strain (0.2 – 1.3%) the uniaxially strained samples experienced an increase of ~15% (unfiltered images) and ~63% (50 nm cut-off wavelength filtered images). Figure 6.36 shows the comparison in correlation length variation with strain between the uniaxial and biaxial samples. The results indicate that biaxial strain may have a smaller impact on the correlation length than that of uniaxial strain for a similar range of strain. However, it is still possible that major changes in the topography may occur at values of strain higher than 1.3% as observed with the uniaxially strained samples (section 6.4.3.2). Thus, characterisation of samples with high values of biaxial strain (> 1.3%) would be useful.

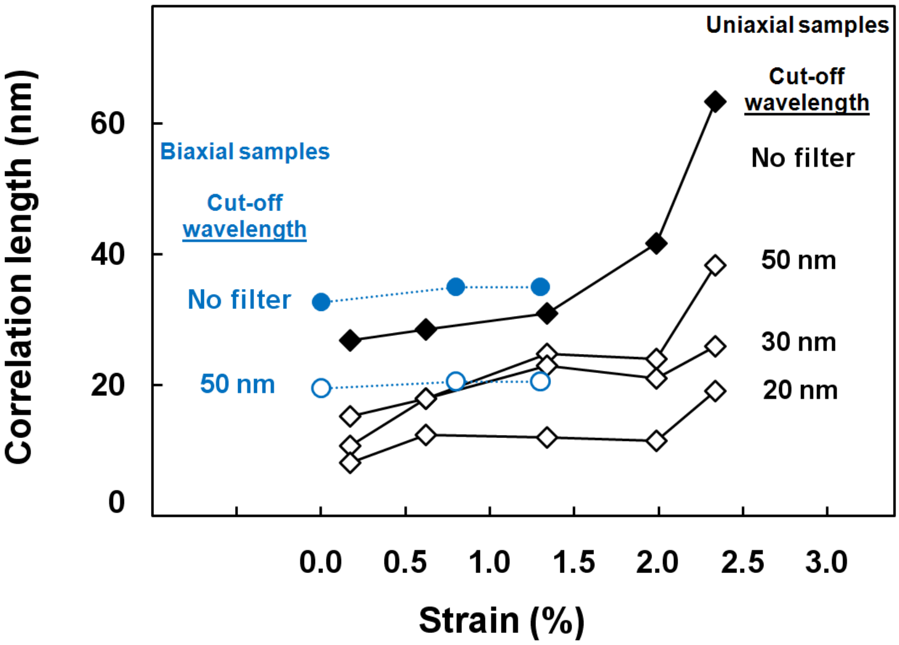

Figure 6.36 Comparison of the correlation length variation extracted from the least-squares non-linear fitting performed in sections 6.4.3 and 6.4.4 between the uniaxial and biaxial samples.

Fabrication factors may have also affected the correlation length. Conventional fabrication processes in commercial SOI and sSOI wafers usually involve some final polishing [183]. This polishing process may mask changes in the surface roughness correlation length due to the strain, and the effects of strain on the correlation length would not be noticeable. This would not be the case of the uniaxial samples where the tensile strain is induced in the beams after the final release process (step 9 in Figure 4.2).

Therefore, the induced strain can alter the roughness of the silicon surface and the changes in correlation length would be noticeable. This will be considered in section 7.3.

6.4.4.3 Effect of biaxial strain on the Hurst exponent: Uniaxial vs. biaxial strain

The Hurst exponent variation with strain of the SOI and sSOI samples is shown in Figure 6.37. The Hurst exponent is fairly constant ~0.5 for the filtered and non-filtered images in the range 0 – 1.3% of strain.

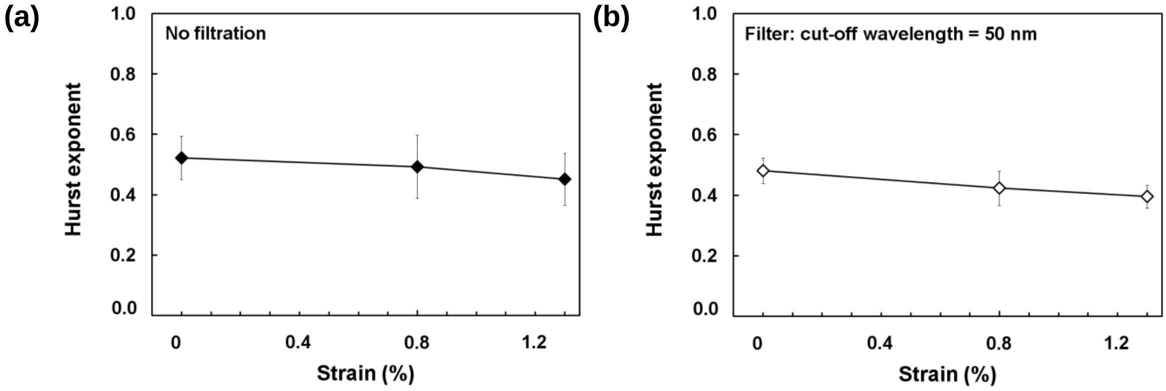

Figure 6.37 Hurst exponent variation with strain as determined from the fitting of the experimental data in Figures 6.31 and 6.32 in the unstrained and biaxially strained films a) before applying the low-pass wavelength filter and b) after applying a low-pass wavelength filter with cut-off wavelengths of 50 nm.

The Hurst exponent values ~0.5 indicate that the roughness surface distribution of the SOI and sSOI films is well represented by the exponential model. In contrast, the Hurst exponent of the uniaxially strained samples (Figure 6.38) significantly varies with strain and with the wavelength regime. This indicates that it is not possible to use a unique model (Gaussian or exponential) to fit the surface roughness distribution of the uniaxial strained samples.

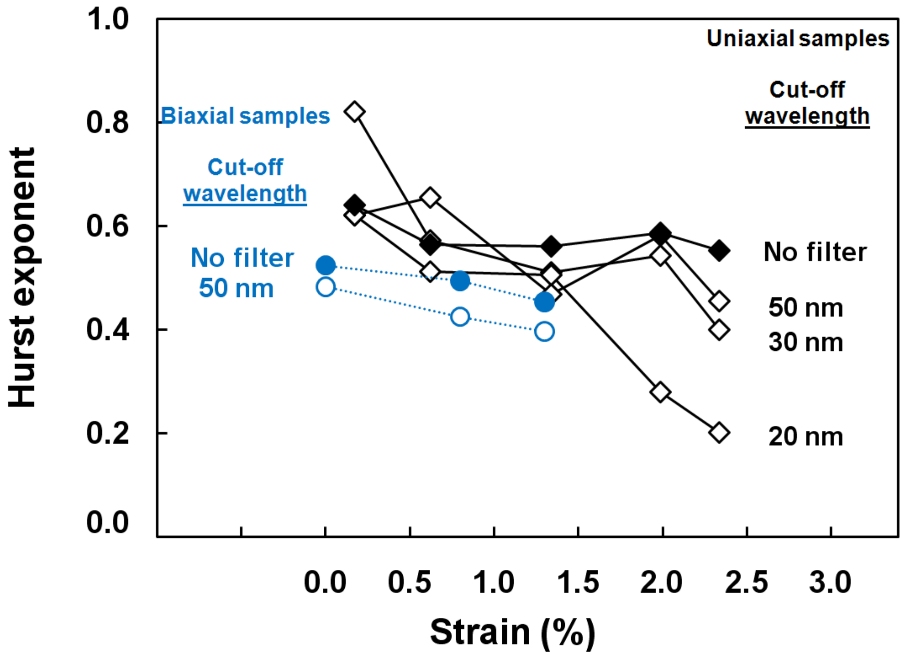

Figure 6.38 Comparison of the Hurst exponent variation extracted from the least-squares non-linear fitting performed in sections 6.4.3 and 6.4.4 between the uniaxial and biaxial samples.

The large variations of the Hurst exponent with uniaxial strain may also be connected to the variations in correlation length and RMS roughness with strain. As shown in Figure 6.39 it is possible that the impact of strain on the highest frequency undulations (jaggedness) of the surface profile may be smaller (or even negligible) compared with the impact of strain on the low frequency undulations of the surface profile. Therefore, an increase of the correlation length would be mainly ascribable to an increase of the low frequency undulations (long wavelengths) with little contribution from the high frequency undulations (short wavelengths). The jaggedness of the surface at high values of strain (Figure 6.39a) would then appear enhanced (Hurst exponent would decrease) compared with the jaggedness of the surface at low values of strain (Figure 6.39b). Unfortunately, there is no precise definition to describe the jaggedness of a surface and the interpretation of a surface as jagged or smooth is highly subjective [173]. A rigorous analysis in the frequency domain of the variation of the frequency components of the surface profile with strain is highly recommended. This will be discussed in section 7.3.

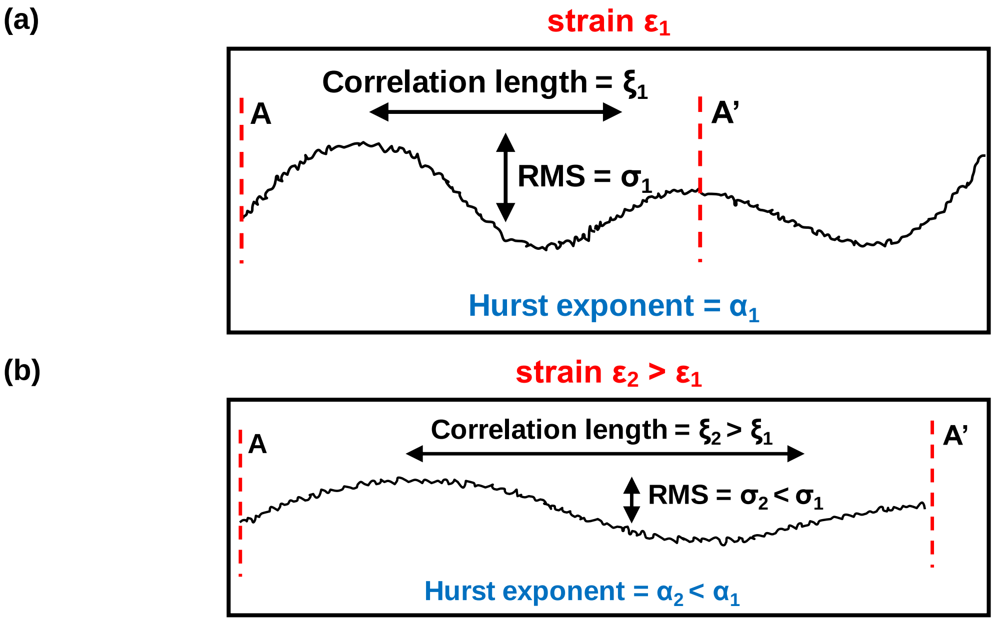

Figure 6.39 Schematic of the impact of strain on the Hurst exponent. Strain ε_1 in sample (a) is smaller than that of sample (b) ε_2. A larger impact of strain on the long wavelength undulations with respect to the low wavelength undulations would result in an increase of the gap between the high and low frequency components of the surface profile. As a consequence, the Hurst exponent in a sample with an applied strain ε_2 would appear smaller (more jagged) than that of the same sample with an applied strain ε_1.

6.4.5 Impact of the filter cut-off wavelength on the surface roughness

The impact of the filter cut-off wavelength on the RMS roughness and wavelength undulations was analysed in section 6.4.1 to evaluate the filter response. The analysis was performed only for a 250 × 250 nm^2 scan-size and for one level of strain (2.0%). In this section, the impact of the filter cut-off wavelength on the RMS roughness, correlation length and Hurst exponent is analysed for all levels of strain (0 – 2.3%) and using the results obtained from the self-affine analysis (section 6.4.2.3). Figures 6.40-6.42 show the variation in RMS roughness, correlation length and Hurst exponent with the filter cut-off wavelength. The non-filtered images have also been included within the analysis with an arbitrary cut-off wavelength of 250 nm (equivalent to the maximum scan-length). The results have been plotted using a logarithmic horizontal scale to better represent the non-linear spacing between the different cut-off wavelengths.

6.4.5.1 Effect of the filter cut-off wavelength on the RMS roughness

Figure 6.40 shows the impact of the filter cut-off wavelength on the RMS roughness. There is a reduction of RMS roughness with decreasing filter cut-off wavelength for all levels of strain. This reduction is mainly ascribed to a larger filtration of surface wavelength undulation components with decreasing filter cut-off wavelength (section 6.4.1.2).

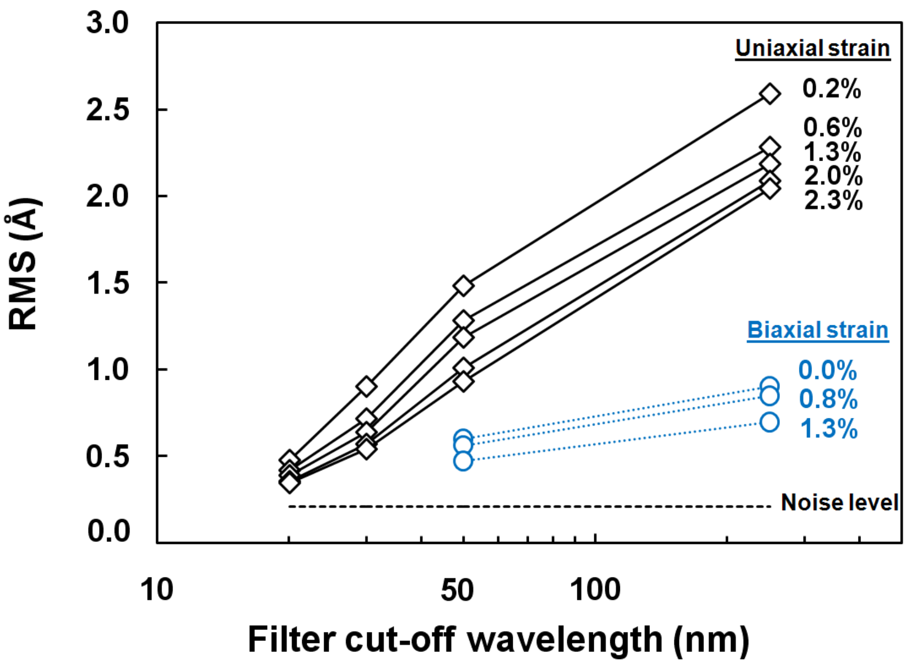

Figure 6.40 Comparison of RMS roughness variation with the filter cut-off wavelength between the uniaxial and biaxial samples.

From the slope of the curves, the reduction is more pronounced in case of the uniaxially strained samples. This effect however, may be related to the different fabrication processes undergone by the uniaxial and biaxial samples mentioned in section 6.4.3.

6.4.5.2 Effect of the filter cut-off wavelength on the correlation length

Figure 6.41 shows the variation of the correlation length with the filter cut-off wavelength. As expected from the reduction in roughness wavelength undulations with decreasing filter cut-off wavelength observed in section 6.4.1.1, the reduction in roughness wavelength causes also a reduction in correlation length with decreasing filter cut-off wavelength. From the slope of the curves, there are no significant differences between the impact of the filter cut-off wavelength on the uniaxial and biaxial samples.

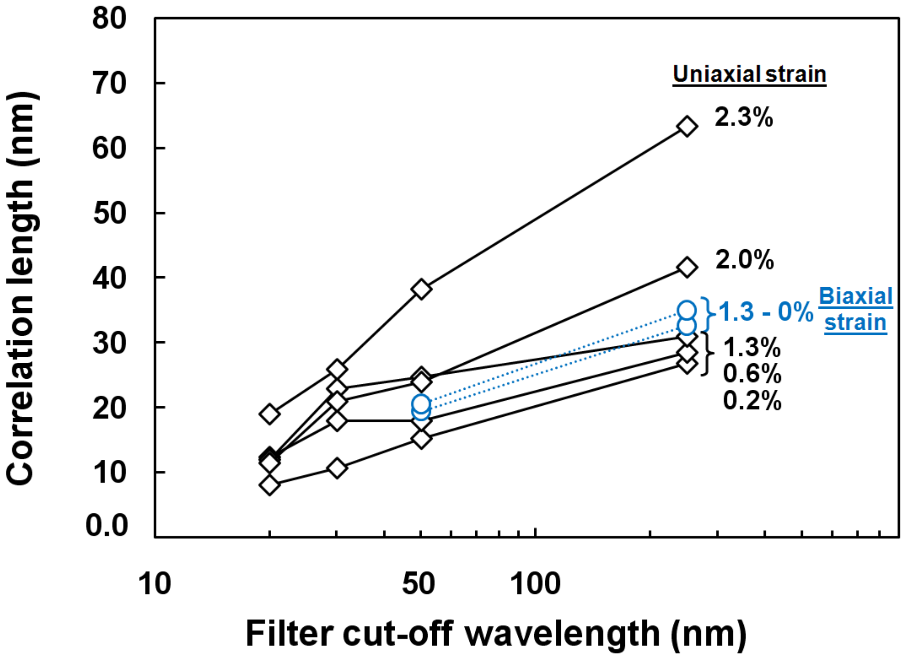

Figure 6.41 Comparison of correlation length variation with the filter cut-off wavelength between the uniaxial and biaxial samples.

6.4.5.3 Effect of the filter cut-off wavelength on the Hurst exponent

Figure 6.42 shows the impact of the filter cut-off wavelength on the Hurst exponent. There is a significant change in Hurst exponent with decreasing filter cut-off wavelength. The effect of the filter cut-off wavelength on the Hurst exponent is to increase the splitting of the Hurst exponent with decreasing filter cut-off wavelength. This phenomenon is more clearly observed with the uniaxial samples (red arrows in Figure 6.42). Thus, for a 30 nm cut-off wavelength, the Hurst exponent varies between ~0.4 – 0.8 whereas for the non-filtered images, the Hurst exponent is fairly constant ~0.6. For the 20 nm filter cut-off wavelength, in addition to the splitting, the Hurst exponent experiences also a reduction in values compared with those of the 30 nm filter cut-off wavelength. This may be related to the low signal-to-noise ratio (SNR) determined in section 6.4.1 for the 20 nm cut-off wavelength. Due to the low SNR of the 20 nm cut-off wavelength, the high frequency components of the background noise would make a major impact i.e. reduction on the Hurst exponent values. For the biaxial samples, the Hurst exponent values experience less splitting and are smaller than those of the uniaxial samples for the same range of filter cut-off wavelengths.

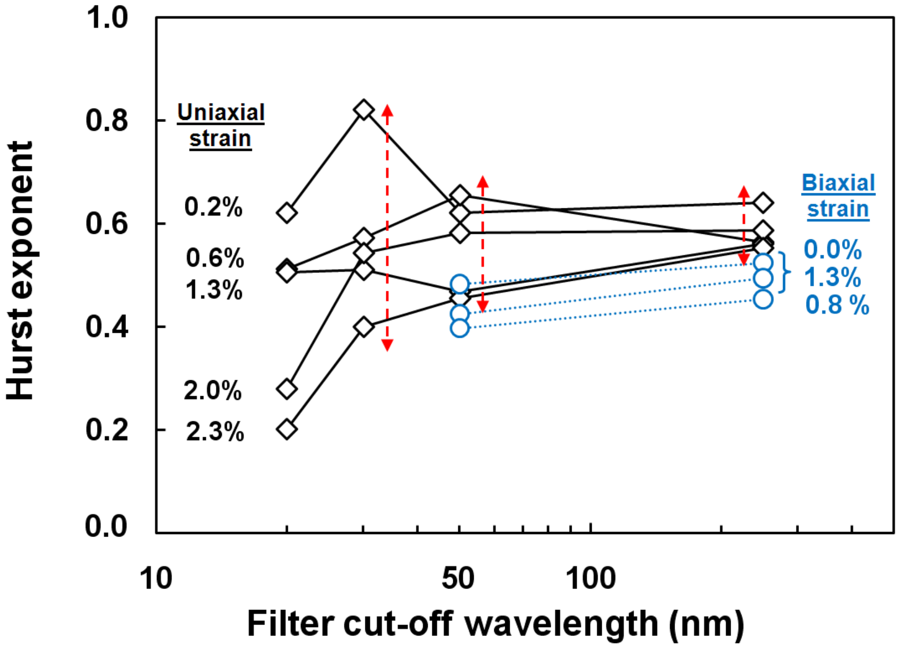

Figure 6.42 Comparison of Hurst exponent variation with the filter cut-off wavelength between the uniaxial and biaxial samples. There is a splitting of the Hurst exponent with decreasing filter cut-off wavelength for the uniaxially strained samples (red dashed arrows).

6.4.6 Surface roughness scattering mobility

The surface roughness scattering mobility μ_{SR} is usually determined from the inverse relation with the power spectral density $S(\boldsymbol{q_s})$ [65, 168]

$$\mu_{SR} \propto \frac{1}{S(\boldsymbol{q_s})} \tag{6.12}$$

Here, $\boldsymbol{q_s}$ is the wave vector in the reciprocal space. Traditionally, data from mobility experiments have been fitted with the Gaussian and exponential models of the autocorrelation function or the power spectral density (PSD) (Fourier transform of the autocorrelation function), using the RMS roughness and correlation length values as fitting parameters [62, 65, 169]. However, neither of these models can successfully fit the experimental mobility data determined for both holes and electrons with the same RMS roughness and correlation length values [43]. Therefore, in order to successfully fit the experimental data from electrons and holes mobility using the same correlation length and

RMS roughness values, alternative expressions have been suggested [170, 171]. For the autocorrelation function, Isihara *et al.* [170] proposed the functional form:

$$R(l) = w^2 e^{-\left(\frac{l}{\xi}\right)^n}, \tag{6.13}$$

where l, w and ξ, are the lag distance, interface width and correlation length parameters. Here, n is an exponential parameter used to determine the functional form of $R(l)$. For $n = 1$, Equation 6.13 reduces to the exponential form and for $n = 2$ Equation 6.13 reduces to the Gaussian form. Comparing Equations 6.8 and 6.13, the exponential parameter n and the Hurst exponent α can be related by $n = 2\alpha$. This relation suggests that the exponential parameter n used within the autocorrelation function and PSD models [170] and [171] is highly connected to the jaggedness of the surface and consequently with the high frequency components of the surface profile. This would partly explain the findings in [168] where in order to explain the dependency of electrons and holes mobility at high electric fields with the surface roughness, it was concluded that higher frequency components ($q_s \approx 10^7$ cm^{-1}) in the surface roughness spectra compared with those obtained by AFM were required.

For a self-affine surface, the PSD has been modelled as [68]:

$$S(\boldsymbol{q_s}) = \frac{4\pi\alpha w^2 \xi^2}{(1 + \boldsymbol{q_s}^2 \xi^2)^{1+\alpha}} \tag{6.14}$$

From the inverse relation between μ_{SR} and the PSD (Equation 6.12), μ_{SR} is proportional to w^{-2}. However, μ_{SR} depends also on the correlation length ξ and Hurst exponent α. Therefore, whereas for $\alpha = 0.5$, $\mu_{SR} \propto \xi$, for $\alpha = 1$, $\mu_{SR} \propto \xi^2$. Also, the relation between the surface roughness scattering mobility μ_{SR} and the correlation length ξ highly depends on the electron density at the inversion layer. This relation is further complicated when screening effects of electrons in the inversion layer are considered e.g. dielectric screening effect [65]. Thus, in order to determine the surface roughness mobility, it is important to understand the different factors affecting the roughness parameters which enter the PSD. Next section summarises and discusses the main factors affecting the surface roughness parameters determined in this work.

6.4.6.1 Discussion about the factors affecting the surface roughness parameters

The roughness parameters are highly dependent on the statistical functions used to fit the experimental data (Equation 6.9 in this work), order of the flattening process used to correct for AFM artefacts and sample tilt (section 3.3.3) and length of the available data [62, 65]. Stommer *et al.* [174] analysed the changes in morphology due to wet chemical etching of the (100) silicon surface using the multiple scan technique and Equation 6.9 to fit the experimental data. They found large variations in the correlation length (from 18.2 nm to 145 nm) and in the Hurst exponent (from 0.4 to 0.95) depending on the scan technique used (single or multiple scan). It was concluded from this work [174] that the flattening process used to correct the tilt of the sample, favoured the accumulation of the height data in the self-affine region. This could lead to wrong results when using the single scan technique to determine the roughness parameters. They also concluded that a finite scan-size cuts off those wavelength undulations longer than the scan-length and as a consequence the correlation length is underestimated. In contrast, the use of the multiple scan technique and Equation 6.9 (to fit the experimental data) yield more reliable results. This is because Equation 6.9 takes into account the self-affine behaviour and is less prone to the shortage of data since it relies only on RMS roughness measurements to determine the roughness parameters.

From the AFM measurements, the RMS roughness, correlation length and Hurst exponent have shown to vary with strain (sections 6.4.3 and 6.4.4) and with the wavelength regime (filter cut-off wavelength) (section 6.4.5). The variation with the wavelength regime, especially for the uniaxial samples, confirms that the roughness parameters are highly dependent on the fabrication process and treatments undergone by the sample [174]. The dependency of the roughness parameters, and especially the changes in Hurst exponent with the wavelength regime determined in this work and in [174], may be related to the different agreement of the exponential parameter n (section 6.4.6) found in [170] for different silicon interfaces.

These results show that numerous factors including the strain, wavelength regime, fabrication process, technique used for the determination of the parameters and image processing affect the roughness parameters.

6.5 Summary and conclusions

The chapter has investigated the impact of strain on the SiO_2/Si interface roughness at the nanoscale under uniaxial and biaxial strain of wires and thin films in the range 0 − 2.3% by atomic force microscopy (AFM). The analysis of roughness at the nanoscale has been possible by filtering the AFM images with a low-pass wavelength filter and three cut-off wavelengths: 50, 30 and 20 nm. The root mean square (RMS) roughness variation of the surface roughness with strain has been investigated using the technique of multiple scan analysis. The results have confirmed that the SiO_2/Si interface is self-affine and significantly changes with the applied strain.

The RMS roughness has shown to decrease with increasing uniaxial and biaxial strain (~40% decrease for the uniaxially strained samples filtered with a 30 nm cut-off wavelength low-pass filter in the range 0.2 − 2.3% of strain, and ~20% decrease for the biaxially strained samples filtered with a 50 nm cut-off wavelength low-pass filter in the range 0 − 1.3% of strain). In addition to the RMS roughness, the self-affine analysis has allowed us to determine the correlation length and Hurst exponent.

The correlation length has shown to increase with increasing uniaxial strain. The increase was more pronounced in the range 1.3 – 2.3% of strain. For the non-filtered images, the increase was ~100% in the range 1.3 – 2.3% of strain compared with only ~15% increase in the range 0.2 – 1.3%. This suggests that a threshold value of strain ~1.3% may exist from which the impact on the surface features is more significant. In contrast, the correlation length change for the biaxially strained samples varies only ~7 and 6% for the non-filtered and filtered images respectively (the correlation length for the uniaxially strained samples filtered with a 50 nm cut-off wavelength and within similar range of strain increased ~63%).

The Hurst exponent showed also to vary with uniaxial strain. Thus for a 30 nm filter cut-off wavelength, the Hurst exponent of a 0.2% uniaxially strained sample is ~0.8 (close to the Gaussian model $\alpha = 1$) whereas that of a 2.3% uniaxially strained sample is ~0.4 (close to the exponential model $\alpha = 0.5$). This is in contrast to the Hurst exponent variation with biaxial strain. For the biaxially strained samples, the Hurst exponent showed to be constant ~0.5 for all the strain values and wavelength regimes (exponential model $\alpha = 0.5$).

The roughness parameters dependency with the wavelength regime (filter cut-off wavelength) was also analysed. The RMS roughness and correlation length exhibited a decrease with decreasing filter cut-off wavelength regardless of the type of strain (uniaxial or biaxial). The reduction though, is mainly ascribed to the effect of the low-pass filter on the surface roughness undulations. The change in RMS roughness with decreasing filter cut-off wavelength was more pronounced in the uniaxial samples (~46% reduction between the non-filtered images and the 50 nm cut-off wavelength filtered images with 1.3% of strain) than in the biaxial samples (~32% reduction for the same wavelength range and strain). The Hurst exponent showed also high dependency with the wavelength regime (~64% decrease for the 2.3% uniaxially strained samples between the non-filtered and 20 nm cut-off wavelength filtered images). The large dependency of the Hurst exponent and the different variation in RMS roughness with the wavelength regime between the uniaxial and biaxial samples (which had undergone different processes), indicated that the roughness parameters might be highly sensitive on the fabrication process and treatments undergone by a sample.

The Hurst exponent was also shown to be related to the exponent parameter *n* used in some models of the PSD and autocorrelation functions for the surface roughness scattering limited-mobility. The dependency of the Hurst exponent with the wavelength regime and the relation with the exponent parameter *n* might be the reason behind the different values found for the exponential parameter *n* for different silicon interfaces [170].

To summarise, the results have shown that numerous factors affect the roughness parameters including the strain, fabrication process, technique used for the determination of the parameters and image processing. The results also indicate that the models used for the analysis of the carrier transport at high electric fields with strain have to include the RMS roughness, correlation length and Hurst exponent as fitting parameters. The determination and analysis of these parameters by AFM has to consider the self-affine behaviour of the SiO_2/Si interface.

Chapter 7. Summary, conclusions and future work

7.1 Summary

In this work strain in silicon nanostructures has been experimentally and theoretically (by analytical calculations and FE simulations) investigated for strain values ranging from 0 to 3.6%. The structures were tested using an on-chip technique especially adapted for measuring the material properties of micro- and nanometre-thick films under large values of tensile strain. The fabrication method used with this technique allows multiple geometries (and thus strain values) to be processed simultaneously on the same wafer while being studied independently. A total of 1440 structures were investigated. The structures were fabricated with widths ranging 1 to 10 μm and lengths ranging 3 to 1,300 μm. The thickness was 200 nm for all the structures.

The large number of samples and different geometries enabled, in chapter 4, the investigation of the size dependency of the Young's modulus, fracture strain, thermal conductivity and the role of the surface in the size dependent physics. Owing to the specific design of the nanostructures, strain was characterised using SEM and Raman spectroscopy (using 458 nm and 364 nm laser radiations), and theoretically with analytical calculations and finite element simulations.

Despite Raman spectroscopy being a technique widely used to characterise strain, to date there was no strain-shift coefficient (to convert Raman shifts to strain) validated for structures at the nanometric regime. This was investigated in chapter 5. It was mentioned that several values for the strain-shift coefficient could be found in the literature, all for bulk silicon and low values of strain. Moreover, the discrepancies between the reported phonon deformation potentials (PDPs), used to calculate the strain-shift coefficient for bulk silicon, are large and not well understood. The large number of samples investigated and the determination of strain by three independent techniques (SEM, analytical calculations and finite element simulations), enabled an accurate determination of the strain-shift coefficient for nanometric structures under large values of strain along the <110> direction. The utilised technique allowed also the extraction of the transversal strain-shift coefficient in backscattering geometry which in general is not characterised in experiments with this geometry. The comparison of the two strain-shift coefficients with those extracted from the reported PDPs provided a better knowledge of the origin of the discrepancies between the reported PDPs.

Motivated by the accurate determination of strain in the nanostructures and by the agreement obtained with the different techniques, a thorough analysis of the impact of strain on the surface roughness of silicon in nanostructures and thin films was conducted in chapter 6. The role of the surface roughness on the mobility enhancement in strained channel MOSFETs has been largely studied. However to date, all these studies did not consider the self-affine behaviour of the SiO_2/Si interface. The study of the surface-roughness was performed by AFM and using a multiple scan analysis technique particularly suitable to study the self-affine behaviour of a rough surface. The technique allowed the investigation of the scaling behaviour of the SiO_2/Si interface roughness with uniaxial and biaxial strain in wires and thin films. Section 7.2 summarises the main conclusions from the work.

7.2 Conclusions

In chapter 4, the on-chip tensile testing technique was validated as a method to produce accurate strain levels in beams over a large range of sample lengths. The discrepancies in strain between experiment and analytical calculations were ~0.05% using Raman spectroscopy and ~0.04% using SEM. These small discrepancies confirmed that accurate conversions of Raman measurements to strain are possible for large ranges of strain (0 − 3%).

The dependency of Young’s modulus and fracture strain on beam size was also studied. The Young’s modulus of 200 nm-thick samples was extracted from the slope of the stress-strain curve based on the SEM measurements of the samples cursor displacements. It was found a Young’s modulus $E_{<110>} = 161 \pm 6$ GPa which is equal to that of bulk silicon ($E_{<110>} = 169$ GPa) within the experimental error. This result was the same as that obtained previously with dynamic resonance methods for the same thickness $E_{<110>} = 160$ GPa. The large discrepancies in Young’s modulus previously reported for structures with similar thickness and the large errors in stress determination determined by the cursor displacement technique, indicated that the Young's modulus determination highly depends on the measurement technique. Internal and external factors including surface stress, native oxide, loading conditions were also considered. This was studied by analysing the discrepancies in strain obtained from the Raman measurements using the UV and visible radiation (the visible radiation probed the bulk whereas the UV radiation provided information from the near surface). Only minor discrepancies in strain determination, lower than 0.2%, were found between the two radiations. However, since some minor sample heating in the Raman UV measurements was found and based on the results of the surface effects in the Young's modulus from previous works, it was concluded that the surface stress, native oxide and loading conditions could have also affected the determination of the Young's modulus.

The fracture strain was investigated by visual inspection of the last unbroken sample within forty arrays of thirty samples. Strain values up to 3.6% were identified. The fracture strain was found to increase with decreasing beam width. The increase in fracture strain was shown to be most likely related to a decrease in the defect size for smaller widths. The fracture strain value was found to be in good agreement with previous experiments in silicon nanowires with similar dimensions.

The variation of thermal conductivity with tensile strain was also investigated using the discrepancy between Raman UV and visible measurements as a measure of heat evacuation. For the data acquisition, both the UV and visible laser powers were kept constant. Thus, any significant change in UV-visible discrepancy could indicate a change in heat evacuation related to the thermal conductivity. Within the range of strain studied (0 – 3%), and limited by the scatter in the data, no change in UV-visible discrepancy, hence variation in thermal conductivity with strain, was found. Thus, it was concluded that other factors such as a less effective heat evacuation in samples with smaller dimensions could have dominated the results. In order to confirm these results alternative techniques to characterise the thermal conductivity should be investigated as proposed in section 7.3.

In chapter 5, the strain-shift coefficient for the longitudinal optical mode (LO) of the structures (and stress values up to 4.5 GPa) was determined. The determined value, $b_3 = -343$, is in close agreement with that obtained using the PDPs of Anastassakis *et al.* in

1970 [78], $b_3 = -337$, and Chandrasekhar *et al.* in 1978 [79], $b_3 = -339$, but significantly differ from that of Anastassakis *et al.* in 1990 [80], $b_3 = -389$. These are the most widely used PDPs to date for silicon. The analysis of these results and those of previous works indicated that the effects of stress relaxation near the surface either do not affect or equally affect the strain-shift coefficient for laser radiations within the range 364 – 647 nm. Thus, it was concluded that the strain-shift coefficient determined in this work, along with the PDPs in [78] and [79], are the most suitable to determine strain in silicon nanostructures using the shift of the LO peak with either visible or UV Raman spectroscopy in backscattering geometry from a (001) surface.

The TO1 strain-shift coefficient in backscattering geometry from a (001) surface was also characterised. A value $b_1 = -485$ was determined. In contrast with the LO strain-shift coefficient, the TO1 value has a closer agreement with the strain-shift coefficient obtained using the 1990 PDPs [80], $b_1 = -486$. After eliminating factors including temperature and potential changes in crystal structure during sample fabrication, it was concluded that the strong dependence of the Raman frequency on the incident light polarisation on the (110) and (111) planes and the different scattering geometries could explain the significant discrepancies between the different sets of PDPs reported to date [78-80]. Thus, that the PDPs from 1990 [80] are more accurate to characterise the TO1 mode in silicon nanostructures in backscattering from a (001) plane than the PDPs of 1970 [78] and 1978 [79].

In chapter 6, the SiO_2/Si interface roughness was investigated by AFM for uniaxial strain values in the range 0.2 – 2.3% and biaxial strain values in the range 0 – 1.3%. In order to analyse the surface roughness at the nanoscale, the AFM images were filtered with a low-pass wavelength filter and three cut-off wavelengths: 50, 30 and 20 nm. The results confirmed that the SiO_2/Si interface is self-affine and that significantly changes with the applied strain. The RMS roughness values showed to decrease with increasing strain with both uniaxial and biaxial strains (40% reduction for the uniaxially strained samples with the 30 nm wavelength regime in the range 0.2 – 1.3% of strain, and 20% reduction for the biaxially strained samples with the 50 nm wavelength regime in the range 0 – 1.3% of strain). The correlation length showed to significantly increase with increasing uniaxial strain. The increase was more pronounced in the range 1.3 – 2.3 % of strain (~100%

increase in the 1.3 – 2.3 % range of strain compared with only ~15% increase in the range 0.2 – 1.3% for the unfiltered images). This suggested that a threshold value of strain ~1.3 % may exist from which the impact on the surface features is more significant. However, in order to confirm these conclusions, the analysis of samples with higher values of biaxial strain (> 1.3%) is strongly recommended. This will be explained in section 7.3.

The Hurst exponent, which is related to the jaggedness of a self-affine surface, was also shown to significantly vary with uniaxial strain and with the wavelength regime. At 30 nm wavelength regime (filter cut-off wavelength), the Hurst exponent α was found to be ~0.8 (close to the Gaussian model $\alpha = 1$) for a 0.2% strained sample whereas it reduced to ~0.4 (close to the exponential model $\alpha = 0.5$) for a 2.3% strained sample. In contrast, the Hurst exponent for the biaxailly strained samples was constant ~0.5 with strain in the range 0 – 1.3% and for all wavelength regimes These values of Hurst exponent are in excellent agreement with the exponential model ($\alpha = 0.5$).

Also in chapter 6, it was shown that the Hurst exponent is highly related to the exponent parameter *n* used in some models of the power spectral density (PSD) and the autocorrelation functions used to study the surface roughness scattering limited-mobility. The results showed that numerous factors affect the roughness parameters including the strain, fabrication process, technique used for the determination of the parameters and image processing. The results also indicated that the models used for the analysis of the carrier transport at high electric fields with strain have to include the RMS roughness, correlation length and Hurst exponent as fitting parameters. The determination and analysis of these parameters by AFM has to consider the self-affine behaviour of the SiO_2/Si interface.

7.3 Future work

The analysis of the mechanical properties in the 200 nm thick structures investigated in this work, revealed a slight decrease in Young's modulus, compared with the Young's modulus of bulk silicon, and an increase in fracture strain with decreasing size (chapter 4). Experimentally, several groups have found a size-dependency in Young's modulus although the onset of the Young's modulus size-dependency varied. Theoretical analysis and simulations predict changes in Young’s modulus for dimensions below 10 nm. The fracture strain mechanisms are also complex and not well understood. From all these considerations, it is clear that new experiments with structures with dimensions below 200 nm are required to better understand the size-dependency in the mechanical properties. Using the on-chip tensile testing technique presented in this work, new structures have already been fabricated with thickness down to 40 nm. Preliminary results using dynamic resonance-based methods are presented in Figure 7.1. There is a significant reduction in Young’s modulus with the thickness of the samples. However, as stated in section 4.6.1, the accuracy in Young’s modulus determination largely depends on the characterisation technique. Thus, new experiments and different techniques are recommended in order to confirm these results.

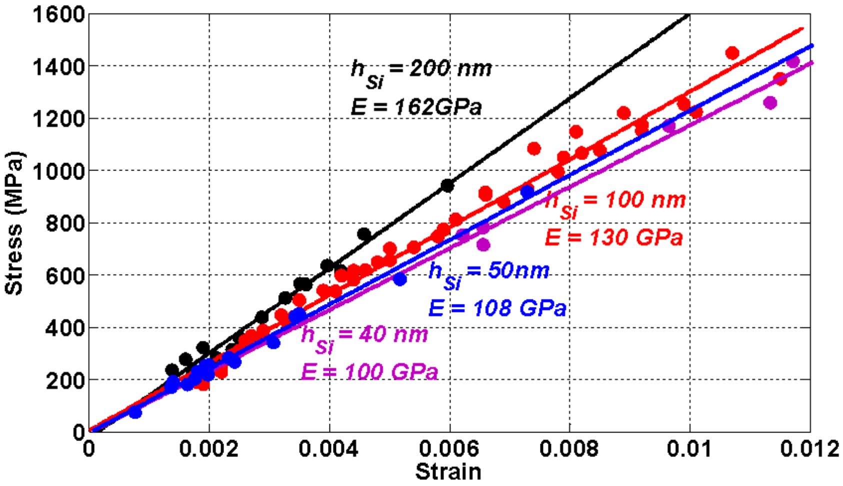

Figure 7.1 Young’s modulus in silicon nanostructures of 200, 100, 50 and 40 nm. *(Measurements by Umesh Bhaskar and Samer Houri, Université catholique de Louvain, Belgium)*

Also, as discussed in chapter 5, the strain-shift coefficient used for the characterisation of strain by Raman spectroscopy may change with structures well down to the nanometric regime. Thus, following the same approach presented in chapter 5, these new structures will offer the possibility of investigating the size-dependency of the strain-shift coefficient.

The size-dependency of the thermal conductivity was also investigated in chapter 4 by Raman spectroscopy. The thermal conductivity analysis was performed using the discrepancy between the UV and the visible Raman shift as a measure of heat evacuation.

However, it was concluded that the scattered in the data and the small dimensions of the structures (which lead to a less effective heat evacuation), may have dominated the results. Thus, alternative techniques capable of detecting small thermal changes are necessary. Scanning thermal microscopy (SThM) is an AFM-based technique in which a thermal tip is used to detect local changes in temperature. Figure 7.2 shows a thermal tip manufactured by Park Systems.

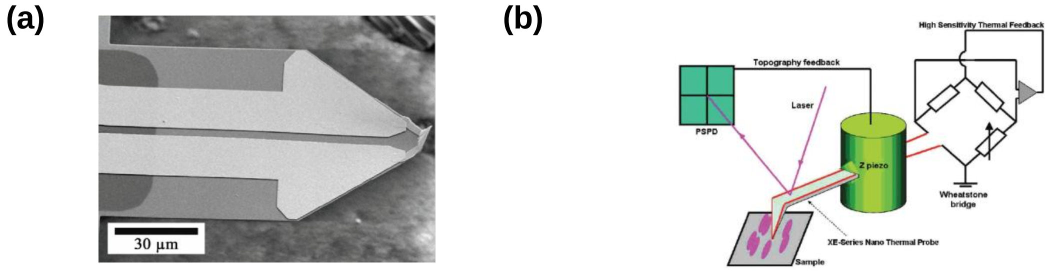

Figure 7.2 (a) SEM image of a nanothermal tip manufactured by Park Systems. (b) Schematic of the temperature contrast mode (TCM) configuration used in SThM. [184]

The SThM tip serves as a resistance thermometer and changes its resistance according to the temperature at the contact point with the surface of the sample. Two modes are possible: the temperature contrast mode (TCM) and the conductive contrast mode (CCM). In TCM, the tip is connected to a Wheatstone bridge and by means of an adjustable resistor, is calibrated to have a zero potential difference between the output terminals (Figure 7.2b). Any change in temperature at the tip will result in a non-zero potential difference at the output terminals. In CCM, the tip is used as a heater and the temperature is constantly monitored through a feedback loop. In this mode, the energy required to maintain the reference temperature represents the local thermal conductivity. When the tip is in contact with a material any temperature flow will result in the electronic controller readjusting the tip temperature. A simple calibration method can be implemented for measurements of the thermal conductivity at the sample.

Raman spectroscopy can also be used to measure the temperature at the sample by using the Stokes/anti-Stokes ratio. As explained in section 3.2, the anti-Stokes scattering requires the annihilation of a phonon in the excited state. This, results in the anti-Stokes component being proportional to the population of the excited state and thus temperature dependent. In contrast, the Stokes component requires the creation of a phonon from ground state. Thus, the Stokes component is temperature independent. The Stokes/anti-Stokes ratio is given by [185]:

$$\frac{I_S}{I_{AS}} = Ae^{\frac{\hbar\omega_0}{k_B \mathrm{T}}} \tag{7.1}$$

Here, I_S and I_{AS} are the Stokes and anti-Stokes intensities, A is a constant which depends on several factors including the temperature, laser wavelength, lattice stress and electron-hole pair populations, $\hbar$ is the Planck's reduced constant, k_B is the Boltzmann's constant, ω_0 is the Raman frequency, and T the absolute temperature. Typically, A is determined by the Stokes-anti-Stokes intensity ratio I_S/I_{AS} at room temperature and with a low laser power to eliminate laser sample-heating. However, an accurate determination of this constant is of vital importance since a minor change it may induce large errors in the temperature determination [186, 187].

In chapter 6, the impact of strain on the SiO_2/Si interface roughness was characterised by AFM. It was shown that biaxially strained samples experienced smaller changes in correlation length and Hurst exponent than the uniaxially strained samples for similar values of strain. It was suggested that a threshold value ~1.3% of strain may exist from which the impact on the surface features is more significant. However, the analysis of the biaxial samples was performed for strain values in the range $0 - 1.3\%$. Thus, in order to confirm the existence of a threshold value, it is necessary to perform an analysis in samples with biaxial strain values higher than 1.3%. Following the same approach as for the uniaxial samples, on-chip biaxially strained samples have already been fabricated for this purpose. Figure 7.3 shows the SEM image of a biaxially strained sample fabricated with the same technique as that described in section 4.2.

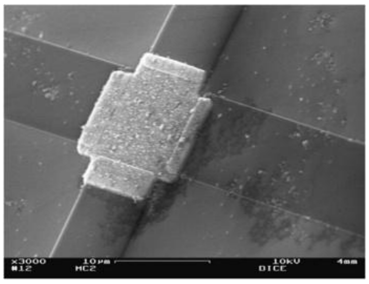

Figure 7.3 SEM image of an on-chip biaxially strained sample. The fabrication process and the working principle are similar to those of the uniaxal samples (section 4.2). *(Sample fabricated at the Université catholique de Louvain, Belgium).*

In section 6.4.6.1, the factors affecting the roughness parameters were discussed. It was mentioned that the differences in the fabrication process undergone by the uniaxial and biaxial samples may have played a major role in the variation of the roughness parameters determined for the uniaxial and biaxial strain. Specifically, it was indicated that the polishing process typically performed in the commercial SOI and sSOI samples may have masked the possible changes in surface roughness otherwise ascribable to strain. In order to elucidate the effects of the fabrication factors on the surface roughness, some arrays of patterned nanowires with different dimensions were fabricated alongside the SOI and sSOI biaxial samples. SEM and AFM images of the patterned nanowires were already shown in Figures 3.13 and 3.14. Owing to the specific dimensions (~ 15 nm thick, ~ 40 − 200 nm wide and ~ 2 μm long), it is expected that these patterned nanowires will undergo high degrees of uniaxial strain. This would allow a comparison between the impact of biaxial and uniaxial strain in samples with the same process and an evaluation of the impact on the surface roughness due to the polishing effectuated on the SOI and sSOI wafers. Likewise, fabrication and characterisation of free-standing samples under biaxial strain as those shown in Figure 7.3 would allow characterising the impact of large values of biaxial strain and a comparison of the results with those determined in chapter 6 for uniaxially strained samples with the same fabrication process.

Finally, in section 6.4.4.3, it was shown that the impact of uniaxial strain on the Hurst exponent was larger than that of biaxial strain. It was mentioned that the impact of strain on the highest frequency undulations (jaggedness) of the surface profile could be smaller (or even negligible) compared with the impact of strain on the low frequency undulations of the surface profile. The jaggedness of the surface at high values of strain would then appear enhanced (Hurst exponent would decrease) compared with the jaggedness of the surface at low values of strain. In order to better understand the impact of strain on the Hurst exponent (and on the other roughness parameters), it is highly recommended an analysis in the frequency domain of the surface roughness. This analysis and the comparison with the results obtained in this work in the space domain would also help to better understand the impact of the different factors affecting the roughness parameters (section 6.4.6.1). The analysis methods could also be used to improve the understanding of carrier transport measurements and modelling in other advanced material systems.

References

[1] J. Bardeen and W. Shockley, "Deformation potentials and mobilities in non-polar crystals," *Physical Review,* vol. 80, pp. 72-80, 1950.

[2] C. S. Smith, "Piezoresistance effect in germanium and silicon," *Physical Review,* vol. 94, pp. 42-49, 1954.

[3] A. A. Barlian, W. T. Park, J. R. Mallon Jr, A. J. Rastegar, and B. L. Pruitt, "Review: Semiconductor piezoresistance for microsystems," *Proceedings of the IEEE,* vol. 97, pp. 513-552, 2009.

[4] B. Olbrechts, B. Rue, T. Pardoen, D. Flandre, and J. P. Raskin, "A Novel Approach for Active Pressure Sensors in Thin Film SOI Technology," *Procedia Engineering,* vol. 25, pp. 43-46, 2011.

[5] B. L. Pruitt and T. W. Kenny, "Piezoresistive cantilevers and measurement system for characterizing low force electrical contacts," *Sensors and Actuators, A: Physical,* vol. 104, pp. 68-77, 2003.

[6] S. X. P. Su, H. S. Yang, and A. M. Agogino, "A resonant accelerometer with two-stage microleverage mechanisms fabricated by SOI-MEMS technology," *IEEE Sensors Journal,* vol. 5, pp. 1214-1222, 2005.

[7] Y. D. Kim, C. S. Lee, and S. J. Kwon, "Novel 3D force sensor using ultra-thin silicon strain gauge bonded on metal membrane," presented at the Actuators and Microsystems Conference 2009, Denver, CO, USA, 2009.

[8] M. M. Atalla and D. Kahng, "A new 'Hot electron' triode structure with semiconductor-metal emitter," *IRE Transactions on Electron Devices,* vol. 9, pp. 507-508, 1962.

[9] J. J. Liou and F. Schwierz, "RF MOSFET: recent advances, current status and future trends," *Solid-State Electronics,* vol. 47, pp. 1881-1895, 2003.

[10] D. J. Frank, R. H. Dennard, E. Nowak, P. M. Solomon, Y. Taur, and H. S. P. Wong, "Device scaling limits of Si MOSFETs and their application dependencies," *Proceedings of the IEEE,* vol. 89, pp. 259-287, 2001.

[11] M. Chu, Y. K. Sun, U. Aghoram, and S. E. Thompson, "Strain: A Solution for Higher Carrier Mobility in Nanoscale MOSFETs," *Annual Review of Materials Research,* vol. 39, pp. 203-229, 2009.

[12] M. L. Lee, E. A. Fitzgerald, M. T. Bulsara, M. T. Currie, and A. Lochtefeld, "Strained Si, SiGe, and Ge channels for high-mobility metal-oxide-semiconductor field-effect transistors," *Journal of Applied Physics,* vol. 97, p. 011101, 2005.

[13] V. Chan, K. Rim, M. Ieong, S. Yang, R. Malik, Y. W. Teh*, et al.*, "Strain for CMOS performance improvement," in *Custom Integrated Circuits Conference, 2005. Proceedings of the IEEE 2005*, 2005, pp. 662-669.

[14] B. Tian, Y. Zhao, Z. Jiang, and B. Hu, "The design and analysis of beam-membrane structure sensors for micro-pressure measurement," *Review of Scientific Instruments,* vol. 83, p. 045003, 2012.

[15] L. Lou, S. Zhang, W. T. Park, J. M. Tsai, D. L. Kwong, and C. Lee, "Optimization of NEMS pressure sensors with a multilayered diaphragm using silicon nanowires as piezoresistive sensing elements," *Journal of Micromechanics and Microengineering,* vol. 22, pp. 1-15, 2012.

[16] C. H. Wu, C. A. Zorman, and M. Mehregany, "Fabrication and testing of bulk micromachined silicon carbide piezoresistive pressure sensors for high temperature applications," *IEEE Sensors Journal,* vol. 6, pp. 316-323, 2006.

[17] Y. Cui, Q. Wei, H. Park, and C. M. Lieber, "Nanowire nanosensors for highly sensitive and selective detection of biological and chemical species," *Science,* vol. 293, pp. 1289-1292, 2001.

[18] V. Passi, F. Ravaux, E. Dubois, S. Clavaguera, A. Carella, C. Celle*, et al.*, "High Gain and Fast Detection of Warfare Agents Using Back-Gated Silicon-Nanowired MOSFETs," *IEEE Electron Device Letters,* vol. 32, pp. 976-978, 2011.

[19] X. T. Zhou, J. Q. Hu, C. P. Li, D. D. D. Ma, C. S. Lee, and S. T. Lee, "Silicon nanowires as chemical sensors," *Chemical Physics Letters,* vol. 369, pp. 220-224, 2003.

[20] R. Degraeve, G. Groeseneken, I. De Wolf, and H. E. Macs, "The effect of externally imposed mechanical stress on the hot-carrier-induced degradation of deep-sub micron nMOSFET's," *IEEE Transactions on Electron Devices,* vol. 44, pp. 943-950, 1997.

[21] S. M. Hu, "Stress-related problems in silicon technology," *Journal of Applied Physics,* vol. 70, pp. R53-R80, 1991.

[22] R. Hull, *Properties of Crystalline Silicon*. Institution of Engineering and Technology, 1959.

[23] X. Han, K. Zheng, Y. Zhang, X. Zhang, Z. Zhang, and Z. L. Wang, "Low-temperature in situ large-strain plasticity of silicon nanowires," *Advanced Materials,* vol. 19, pp. 2112-2118, 2007.

[24] X. Li, T. Ono, Y. Wang, and M. Esashi, "Ultrathin single-crystalline-silicon cantilever resonators: Fabrication technology and significant specimen size effect on Young's modulus," *Applied Physics Letters,* vol. 83, pp. 3081-3083, 2003.

[25] H. Sadeghian, H. Goosen, A. Bossche, B. Thijsse, and F. Van Keulen, "On the size-dependent elasticity of silicon nanocantilevers: Impact of defects," *Journal of Physics D: Applied Physics,* vol. 44, p. 072001, 2011.

[26] L. B. Freund and S. Suresh, *Thin film materials: stress, defect formation, and surface evolution*. New York: Cambridge University Press, 2003.

[27] H. Ibach, "The role of surface stress in reconstruction, epitaxial growth and stabilization of mesoscopic structures," *Surface Science Reports,* vol. 29, pp. 195-263, 1997.

[28] S. M. Sze, *Semiconductor devices: physics and technology*. 2nd ed.: John Wiley & Sons, 2002.

[29] H. Sadeghian, J. F. L. Goosen, A. Bossche, B. J. Thijsse, and F. van Keulen, "Surface reconstruction and elastic behavior of silicon nanobeams: The impact of applied deformation," *Thin Solid Films,* vol. 518, pp. 3273-3275, 2010.

[30] I. Ponomareva, D. Srivastava, and M. Menon, "Thermal conductivity in thin silicon nanowires: Phonon confinement effect," *Nano Letters,* vol. 7, pp. 1155-1159, 2007.

[31] S. H. Park, J. S. Kim, J. H. Park, J. S. Lee, Y. K. Choi, and O. M. Kwon, "Molecular dynamics study on size-dependent elastic properties of silicon nanocantilevers," *Thin Solid Films,* vol. 492, pp. 285-289, 2005.

[32] H. Sadeghian, C. K. Yang, J. F. L. Goosen, E. Van Der Drift, A. Bossche, P. J. French, *et al.,* "Characterizing size-dependent effective elastic modulus of silicon nanocantilevers using electrostatic pull-in instability," *Applied Physics Letters,* vol. 94, p. 221903, 2009.

[33] C. L. Hsin, W. Mai, Y. Gu, Y. Gao, C. T. Huang, Y. Liu, *et al.*, "Elastic properties and buckling of silicon nanowires," *Advanced Materials,* vol. 20, pp. 3919-3923, 2008.

[34] Y. S. Sohn, J. Park, G. Yoon, J. Song, S. W. Jee, J. H. Lee, *et al.*, "Mechanical Properties of Silicon Nanowires," *Nanoscale Research Letters,* vol. 5, pp. 211-216, 2010.

[35] M. J. Gordon, T. Baron, F. Dhalluin, P. Gentile, and P. Ferret, "Size effects in mechanical deformation and fracture of cantilevered silicon nanowires," *Nano Letters*, vol. 9, pp. 525-529, 2009.

[36] C. J. Glassbrenner and G. A. Slack, "Thermal conductivity of silicon and germanium from 3°K to the melting point," *Physical Review,* vol. 134, pp. A1058-A1069, 1964.

[37] E. S. Toberer, L. L. Baranowski, and C. Dames, "Advances in thermal conductivity," *Annual Review of Materials Research,* vol. 42, pp. 179-209, 2012.

[38] X. Li, K. Maute, M. L. Dunn, and R. Yang, "Strain effects on the thermal conductivity of nanostructures," *Physical Review B - Condensed Matter and Materials Physics*, vol. 81, p. 245318, 2010.

[39] T. M. Gibbons, B. Kang, S. K. Estreicher, and C. Carbogno, "Thermal conductivity of Si nanostructures containing defects: Methodology, isotope effects, and phonon trapping," *Physical Review B - Condensed Matter and Materials Physics,* vol. 84, p. 035317, 2011.

[40] M. Liangruksa and I. K. Puri, "Lattice thermal conductivity of a silicon nanowire under surface stress," *Journal of Applied Physics*, vol. 109, p. 113501, 2011.

[41] B. Ghyselen, J. M. Hartmann, T. Ernst, C. Aulnette, B. Osternaud, Y. Bogumilowicz, *et al.*, "Engineering strained silicon on insulator wafers with the Smart Cut™ technology," *Solid-State Electronics*, vol. 48, pp. 1285-1296, 2004.

[42] S. E. Thompson, M. Armstrong, C. Auth, S. Cea, R. Chau, G. Glass, *et al.*, "A logic nanotechnology featuring strained-silicon," *IEEE Electron Device Letters*, vol. 25, pp. 191-193, 2004.

[43] Y. Zhao, H. Matsumoto, T. Sato, S. Koyama, M. Takenaka, and S. Takagi, "A novel characterization scheme of Si/SiO2 interface roughness for surface roughness scattering-limited mobilities of electrons and holes in unstrained- and strained-Si MOSFETs," *IEEE Transactions on Electron Devices*, vol. 57, pp. 2057-2066, 2010.

[44] Y. Song, H. Zhou, Q. Xu, J. Luo, H. Yin, J. Yan, *et al.*, "Mobility enhancement technology for scaling of CMOS devices: Overview and status," *Journal of Electronic Materials*, vol. 40, pp. 1584-1612, 2011.

[45] S. E. Thompson, G. Sun, Y. S. Choi, and T. Nishida, "Uniaxial-process-induced Strained-Si: Extending the CMOS roadmap," *IEEE Transactions on Electron Devices*, vol. 53, pp. 1010-1020, 2006.

[46] T. Satô, Y. Takeishi, H. Hara, and Y. Okamoto, "Mobility anisotropy of electrons in inversion layers on oxidized silicon surfaces," *Physical Review B,* vol. 4, pp. 1950-1960, 1971.

[47] S. Takagi, A. Toriumi, M. Iwase, and H. Tango, "On the universality of inversion layer mobility in Si MOSFET's: Part II-effects of surface orientation," *IEEE Transactions on Electron Devices,* vol. 41, pp. 2363-2368, 1994.

[48] M. Yang, V. W. C. Chan, K. K. Chan, L. Shi, D. M. Fried, J. H. Stathis, *et al.*, "Hybrid-orientation technology (HOT): Opportunities and challenges," *IEEE Transactions on Electron Devices,* vol. 53, pp. 965-978, 2006.

[49] S. M. Pandey, J. Liu, Z. S. Hooi, S. Flachowsky, T. Herrmann, W. Tao, *et al.*, "Mechanism of stress memorization technique (SMT) and method to maximize its effect," *IEEE Electron Device Letters,* vol. 32, pp. 467-469, 2011.

[50] K. W. Ang, K. J. Chui, C. H. Tung, N. Balasubramanian, G. S. Samudra, and Y. C. Yeo, "Performance enhancement in uniaxial strained silicon-on-insulator N-MOSFETs featuring silicon-carbon source/drain regions," *IEEE Transactions on Electron Devices,* vol. 54, pp. 2910-2917, 2007.

[51] S. Pidin, T. Mori, K. Inoue, S. Fukuta, N. Itoh, E. Mutoh, *et al.*, "A novel strain enhanced CMOS architecture using selectively deposited high tensile and high compressive silicon nitride films," in *Electron Devices Meeting, 2004. IEDM Technical Digest. IEEE International,* pp. 213-216, 2004.

[52] M. Horstmann, A. Wei, T. Kammler, J. Höntschel, H. Bierstedt, T. Feudel, *et al.*, "Integration and optimization of embedded-SiGe, compressive and tensile stressed liner films, and stress memorization in advanced SOI CMOS technologies," in *Electron Devices Meeting, 2005. IEDM Technical Digest. IEEE International*, Washington, DC, USA, pp. 233-236, 2005.

[53] S. Takagi, A. Toriumi, M. Iwase, and H. Tango, "On the universality of inversion layer mobility in Si MOSFET's: Part I-effects of substrate impurity concentration," *IEEE Transactions on Electron Devices,* vol. 41, pp. 2357-2362, 1994.

[54] Y. Sun, S. E. Thompson, and T. Nishida, *Strain effect in semiconductors : theory and device applications*. London: Springer, 2010.

[55] O. Zitouni, K. Boujdaria, and H. Bouchriha, "Band parameters for GaAs and Si in the 24-kp model," *Semiconductor Science and Technology,* vol. 20, pp. 908-911, 2005.

[56] N. Mohta and S. E. Thompson, "Mobility enhancement," *IEEE Circuits and Devices Magazine,* vol. 21, pp. 18-23, 2005.

[57] B. G. Streetman and S. K. Banerjee, *Solid state electronic devices*. 6th ed.: Prentice Hall, 2006.

[58] M. V. Fischetti, F. Gamiz, and W. Hansch, "On the enhanced electron mobility in strained-silicon inversion layers," *Journal of Applied Physics,* vol. 92, pp. 7320-7324, 2002.

[59] Y. Zhao, M. Takenaka, and S. Takagi, "On surface roughness scattering-limited mobilities of electrons and holes in biaxially tensile-strained Si MOSFETs," *IEEE Electron Device Letters,* vol. 30, pp. 987-989, 2009.

[60] Z. Y. Cheng, M. T. Currie, C. W. Leitz, G. Taraschi, E. A. Fitzgerald, J. L. Hoyt, *et al.*, "Electron mobility enhancement in strained-Si n-MOSFETs fabricated on SiGe-on-insulator (SGOI) substrates," *IEEE Electron Device Letters,* vol. 22, pp. 321-323, 2001.

[61] K. Rim, J. L. Hoyt, and J. F. Gibbons, "Fabrication and analysis of deep submicron strained-Si N-MOSFET's," *IEEE Transactions on Electron Devices,* vol. 47, pp. 1406-1415, 2000.

[62] S. M. Goodnick, D. K. Ferry, C. W. Wilmsen, Z. Liliental, D. Fathy, and O. L. Krivanek, "Surface roughness at the Si(100)-SiO2 interface," *Physical Review B,* vol. 32, pp. 8171-8186, 1985.

[63] F. Gámiz, J. B. Roldán, J. A. López-Villanueva, P. Cartujo-Cassinello, and J. E. Carceller, "Surface roughness at the Si-SiO2 interfaces in fully depleted silicon-on-insulator inversion layers," *Journal of Applied Physics,* vol. 86, pp. 6854-6863, 1999.

[64] S. Jin, M. V. Fischetti, and T. W. Tang, "Modeling of surface-roughness scattering in ultrathin-body SOI MOSFETs," *IEEE Transactions on Electron Devices*, vol. 54, pp. 2191-2203, 2007.

[65] O. Bonno, S. Barraud, D. Mariolle, and F. Andrieu, "Effect of strain on the electron effective mobility in biaxially strained silicon inversion layers: An experimental and theoretical analysis via atomic force microscopy measurements and Kubo-Greenwood mobility calculations," *Journal of Applied Physics*, vol. 103, p. 063715, 2008.

[66] E. Escobedo-Cousin, S. H. Olsen, T. Pardoen, U. Bhaskar, and J. P. Raskin, "Experimental observations of surface roughness in uniaxially loaded strained Si microelectromechanical systems-based structures," *Applied Physics Letters*, vol. 99, p. 241906, 2011.

[67] M. Pelliccione and T.-M. Lu, *Evolution of Thin-film Morphology: Modeling and Simulations*. Dordrecht: Springer, 2007.

[68] Y. P. Zhao, G. C. Wang, T.-M. Lu, M. De Graef, and T. Lucatorto, *Characterization of Amorphous and Crystalline Rough Surface: principles and applications*. Elsevier Science, 2000.

[69] T. Yoshinobu, A. Iwamoto, K. Sudoh, and H. Iwasaki, "Scaling of Si/SiO2 interface roughness," *Journal of Vacuum Science and Technology B: Microelectronics and Nanometer Structures*, vol. 13, pp. 1630-1634, 1995.

[70] B. B. Mandelbrot, *The fractal geometry of nature*. Updated and augment ed.: W.H. Freeman, 1982.

[71] A. Goedecke, *Transient Effects in Friction: Fractal Asperity Creep*. Springer Vienna, 2013.

[72] G. Binnig, H. Rohrer, C. Gerber, and E. Weibel, "Surface Studies by Scanning Tunneling Microscopy," *Physical Review Letters*, vol. 49, pp. 57-61, 1982.

[73] G. Binnig, C. F. Quate, and C. Gerber, "Atomic force microscope," *Physical Review Letters*, vol. 56, pp. 930-933, 1986.

[74] T. Namazu and S. Inoue, "Characterization of single crystal silicon and electroplated nickel films by uniaxial tensile test with in situ X-ray diffraction measurement," *Fatigue and Fracture of Engineering Materials and Structures*, vol. 30, pp. 13-20, 2007.

[75] A. Armigliato, R. Balboni, S. Balboni, S. Frabboni, A. Tixier, G. P. Carnevale, *et al.*, "TEM/CBED determination of strain in silicon-based submicrometric electronic devices," *Micron*, vol. 31, pp. 203-209, 2000.

[76] A. Toda, N. Ikarashi, and H. Ono, "Local lattice strain measurements in semiconductor devices by using convergent-beam electron diffraction," *Journal of Crystal Growth*, vol. 210, pp. 341-345, 2000.

[77] P. Zhang, A. A. Istratov, E. R. Weber, C. Kisielowski, H. He, C. Nelson, *et al.*, "Direct strain measurement in a 65 nm node strained silicon transistor by convergent-beam electron diffraction," *Applied Physics Letters*, vol. 89, p. 161907, 2006.

[78] E. Anastassakis, A. Pinczuk, E. Burstein, F. H. Pollak, and M. Cardona, "Effect of static uniaxial stress on the Raman spectrum of silicon," *Solid State Communications*, vol. 8, pp. 133-138, 1970.

[79] M. Chandrasekhar, J. B. Renucci, and M. Cardona, "Effects of interband excitations on Raman phonons in heavily doped n-Si," *Physical Review B*, vol. 17, pp. 1623-1633, 1978.

[80] E. Anastassakis, A. Cantarero, and M. Cardona, "Piezo-Raman measurements and anharmonic parameters in silicon and diamond," *Physical Review B*, vol. 41, pp. 7529-7535, 1990.

[81] D. J. Lockwood and J. M. Baribeau, "Strain-shift coefficients for phonons in Si1-xGex epilayers on silicon," *Physical Review B*, vol. 45, pp. 8565-8571, 1992.

[82] W. Kang, J. H. Han, and M. T. A. Saif, "A novel method for in situ uniaxial tests at the micro/nanoscalepart II: Experiment," *Journal of Microelectromechanical Systems,* vol. 19, pp. 1322-1330, 2010.

[83] M. S. Steighner, L. P. Snedeker, B. L. Boyce, K. Gall, D. C. Miller, and C. L. Muhlstein, "Dependence on diameter and growth direction of apparent strain to failure of Si nanowires," *Journal of Applied Physics,* vol. 109, p. 033503, 2011.

[84] Y. Zhang, X. Liu, C. Ru, Y. L. Zhang, L. Dong, and Y. Sun, "Piezoresistivity characterization of synthetic silicon nanowires using a MEMS Device," *Journal of Microelectromechanical Systems,* vol. 20, pp. 959-967, 2011.

[85] J. F. Nye, *Physical properties of crystals : their representation by tensors and matrices*. 1st published in pbk. with corrections ed. Oxford Oxfordshire: Clarendon Press, 1985.

[86] I. Fridtjov, *Continuum mechanics*. Berlin: Springer Berlin Heidelberg 2008.

[87] J. J. Hall, "Electronic effects in the elastic constants of n-type silicon," *Physical Review,* vol. 161, pp. 756-761, 1967.

[88] J. Turley and G. Sines, "The anisotropy of Young's modulus, shear modulus and Poisson's ratio in cubic materials," *Journal of Physics D: Applied Physics,* vol. 4, pp. 264-271, 1971.

[89] G. E. Dieter, *Mechanical metallurgy*. London, New York McGraw-Hill, 1988.

[90] T. M. Tritt, *Thermal conductivity. Theory, properties and applications*. New York: Kluwer Academic/Plenum Publishers, 2004.

[91] S. Makovejev, J. P. Raskin, M. K. Md Arshad, D. Flandre, S. Olsen, F. Andrieu, *et al.*, "Impact of self-heating and substrate effects on small-signal output conductance in UTBB SOI MOSFETs," *Solid-State Electronics,* vol. 71, pp. 93-100, 2012.

[92] R. Agaiby, Y. Yang, S. H. Olsen, A. G. O'Neill, G. Eneman, P. Verheyen, *et al.*, "Quantifying self-heating effects with scaling in globally strained Si MOSFETs," *Solid-State Electronics*, vol. 51, pp. 1473-1478, 2007.

[93] T. H. Maiman, "Stimulated optical radiation in Ruby," *Nature*, vol. 187, pp. 493-494, 1960.

[94] P. Y. Yu and M. Cardona, *Fundamentals of Semiconductors*. Springer Berlin Heidelberg, 2010.

[95] I. De Wolf, "Micro-Raman spectroscopy to study local mechanical stress in silicon integrated circuits," *Semiconductor Science and Technology,* vol. 11, pp. 139-154, 1996.

[96] R. Loudon, "The Raman effect in crystals," *Advances in Physics,* vol. 50, pp. 813-864, 2001.

[97] *LabRAM HR System. User manual*. Horiba Jobin Yvon: Horiba Scientific, 2010.

[98] I. De Wolf, "Raman spectroscopy analysis of mechanical stress near Cu-TSVs," *AIP Conference Proceedings,* vol. 1378, pp. 138-149, 2011.

[99] P. Markiewicz and M. C. Goh, "Simulation of atomic force microscope tip–sample/sample–tip reconstruction," *Journal of Vacuum Science & Technology B,* vol. 13, pp. 1115-1118, 1995.

[100] K. L. Westra, A. W. Mitchell, and D. J. Thomson, "Tip artifacts in atomic force microscope imaging of thin film surfaces," *Journal of Applied Physics,* vol. 74, pp. 3608-3610, 1993.

[101] G. Y. Jing, H. L. Duan, X. M. Sun, Z. S. Zhang, J. Xu, Y. D. Li, *et al.*, "Surface effects on elastic properties of silver nanowires: Contact atomic-force microscopy," *Physical Review B - Condensed Matter and Materials Physics,* vol. 73, p. 235409, 2006.

[102] S. Sundararajan and B. Bhushan, "Development of AFM-based techniques to measure mechanical properties of nanoscale structures," *Sensors and Actuators, A: Physical,* vol. 101, pp. 338-351, 2002.

[103] V. T. Srikar, A. K. Swan, M. S. Ünlü, B. B. Goldberg, and S. M. Spearing, "Micro-Raman measurements of bending stresses in micromachined silicon flexures," *Journal of Microelectromechanical Systems,* vol. 12, pp. 779-787, 2003.

[104] S. S. Walavalkar, A. P. Homyk, M. D. Henry, and A. Scherer, "Controllable deformation of silicon nanowires with strain up to 24%," *Journal of Applied Physics,* vol. 107, p. 124314, 2010.

[105] H. D. Espinosa, Y. Zhu, and N. Moldovan, "Design and operation of a MEMS-based material testing system for nanomechanical characterization," *Journal of Microelectromechanical Systems,* vol. 16, pp. 1219-1231, 2007.

[106] M. A. Haque and M. T. A. Saif, "In-situ tensile testing of nano-scale specimens in SEM and TEM," *Experimental Mechanics,* vol. 42, pp. 123-128, 2002.

[107] S. Lu, Z. Guo, W. Ding, and R. S. Ruoff, "Analysis of a microelectromechanical system testing stage for tensile loading of nanostructures," *Review of Scientific Instruments,* vol. 77, p. 056103, 2006.

[108] S. Gravier, M. Coulombier, A. Safi, N. Andre, A. Boe, J. P. Raskin*, et al.*, "New On-Chip Nanomechanical Testing Laboratory - Applications to Aluminum and Polysilicon Thin Films," *Journal of Microelectromechanical Systems,* vol. 18, pp. 555-569, 2009.

[109] R. F. Bunshah, *Handbook of Deposition Technologies for Films and Coatings - Science, Technology and Applications*. 2nd ed.: William Andrew Publishing/Noyes, 1994.

[110] V. Passi, U. Sodervall, B. Nilsson, G. Petersson, M. Hagberg, C. Krzeminski*, et al.*, "Anisotropic vapor HF etching of silicon dioxide for Si microstructure release," *Microelectronic Engineering,* vol. 95, pp. 83-89, 2012.

[111] M. A. Hopcroft, W. D. Nix, and T. W. Kenny, "What is the Young's modulus of silicon?," *Journal of Microelectromechanical Systems,* vol. 19, pp. 229-238, 2010.

[112] *Ansys 13.0, ANSYS Inc.,* Southpointe, 275 Technology Drive, Canonsburg, PA 15317, USA.

[113] J. J. Wortman and R. A. Evans, "Young's modulus, shear modulus, and poisson's ratio in silicon and germanium," *Journal of Applied Physics,* vol. 36, pp. 153-156, 1965.

[114] K. F. Dombrowski, I. De Wolf, and B. Dietrich, "Stress measurements using ultraviolet micro-raman spectroscopy," *Applied Physics Letters,* vol. 75, pp. 2450-2451, 1999.

[115] I. De Wolf, "Stress measurements in si microelectronics devices using Raman spectroscopy," *Journal of Raman Spectroscopy,* vol. 30, pp. 877-883, 1999.

[116] C. Georgi, M. Hecker, and E. Zschech, "Effects of laser-induced heating on Raman stress measurements of silicon and silicon-germanium structures," *Journal of Applied Physics,* vol. 101, p. 123104, 2007.

[117] V. V. Kozhushko, A. M. Lomonosov, and P. Hess, "Intrinsic strength of silicon crystals in pure-and combined-mode fracture without precrack," *Physical Review Letters,* vol. 98, p. 195505, 2007.

[118] T. Ando, M. Shikida, and K. Sato, "Tensile-mode fatigue testing of silicon films as structural materials for MEMS," *Sensors and Actuators, A: Physical,* vol. 93, pp. 70-75, 2001.

[119] D. Roundy and M. L. Cohen, "Ideal strength of diamond, Si, and Ge," *Physical Review B - Condensed Matter and Materials Physics,* vol. 64, pp. 2121031-2121033, 2001.

[120] Y. Umeno, A. Kushima, T. Kitamura, P. Gumbsch, and J. Li, "Ab initio study of the surface properties and ideal strength of (100) silicon thin films," *Physical Review B - Condensed Matter and Materials Physics,* vol. 72, p. 165431, 2005.

[121] C. Tuma and A. Curioni, "Large scale computer simulations of strain distribution and electron effective masses in silicon 〈100〉 nanowires," *Applied Physics Letters,* vol. 96, p. 193106, 2010.

[122] D. Shiri, Y. Kong, A. Buin, and M. P. Anantram, "Strain induced change of bandgap and effective mass in silicon nanowires," *Applied Physics Letters,* vol. 93, p. 073114, 2008.

[123] Y. Zhu, F. Xu, G. Qin, W. Y. Fung, and W. Lu, "Mechanical properties of vapor - Liquid - Solid synthesized silicon nanowires," *Nano Letters,* vol. 9, pp. 3934-3939, 2009.

[124] U. Bhaskar, V. Passi, S. Houri, E. Escobedo-Cousin, S. H. Olsen, T. Pardoen*, et al.*, "On-chip tensile testing of nanoscale silicon free-standing beams," *Journal of Materials Research,* vol. 27, pp. 571-579, 2012.

[125] Q. H. Jin, T. Li, Y. L. Wang, X. L. Gao, and F. F. Xu, "Confirmation on the size-dependence of Young's modulus of single crystal silicon from the TEM tensile tests," presented at the IEEE SENSORS 2010 Conference, Kona, HI, USA, 2010.

[126] A. Heidelberg, L. T. Ngo, B. Wu, M. A. Phillips, S. Sharma, T. I. Kamins*, et al.*, "A generalized description of the elastic properties of nanowires," *Nano Letters,* vol. 6, pp. 1101-1106, 2006.

[127] B. Lee and R. E. Rudd, "First-principles calculation of mechanical properties of Si001 nanowires and comparison to nanomechanical theory," *Physical Review B - Condensed Matter and Materials Physics,* vol. 75, p. 195328, 2007.

[128] P. W. Leu, A. Svizhenko, and K. Cho, "Ab initio calculations of the mechanical and electronic properties of strained Si nanowires," *Physical Review B - Condensed Matter and Materials Physics,* vol. 77, p. 235305, 2008.

[129] H. Sadeghiant, C. K. Yang, K. B. Gavan, J. F. L. Goosen, E. W. J. M. Van Der Drift, H. S. J. Van Der Zant*, et al.*, "Effects of surface stress on nanocantilevers," *e-Journal of Surface Science and Nanotechnology,* vol. 7, pp. 161-166, 2009.

[130] H. Yao, G. Yun, N. Bai, and J. Li, "Surface elasticity effect on the size-dependent elastic property of nanowires," *Journal of Applied Physics,* vol. 111, p. 083506, 2012.

[131] H. Sadeghian, C. K. Yang, J. F. L. Goosen, A. Bossche, U. Staufer, P. J. French, *et al.*, "Effects of size and defects on the elasticity of silicon nanocantilevers," *Journal of Micromechanics and Microengineering,* vol. 20, p. 064012, 2010.

[132] C. C. Röhlig, M. Niebelschütz, K. Brueckner, K. Tonisch, O. Ambacher, and V. Cimalla, "Elastic properties of nanowires," *Physica Status Solidi (B) Basic Research,* vol. 247, pp. 2557-2570, 2010.

[133] J. Wang, Q. A. Huang, and H. Yu, "Effect of native oxides on the elasticity of a silicon nano-scale beam," *Solid State Communications,* vol. 145, pp. 351-354, 2008.

[134] D. M. Tang, C. L. Ren, M. S. Wang, X. Wei, N. Kawamoto, C. Liu, *et al.*, "Mechanical properties of Si nanowires as revealed by in situ transmission electron microscopy and molecular dynamics simulations," *Nano Letters,* vol. 12, pp. 1898-1904, 2012.

[135] H. A. Wu, G. R. Liu, and J. S. Wang, "Atomistic and continuum simulation on extension behaviour of single crystal with nano-holes," *Modelling and Simulation in Materials Science and Engineering,* vol. 12, pp. 225-233, 2004.

[136] A. M. Lomonosov and P. Hess, "Impulsive fracture of silicon by elastic surface pulses with shocks," *Physical Review Letters,* vol. 89, pp. 955011-955014, 2002.

[137] S. J. Zhou, P. S. Lomdahl, R. Thomson, and B. L. Holian, "Dynamic crack processes via molecular dynamics," *Physical Review Letters,* vol. 76, pp. 2318-2321, 1996.

[138] G. Lehmann, A. M. Lomonosov, P. Hess, and P. Gumbsch, "Impulsive fracture of fused quartz and silicon crystals by nonlinear surface acoustic waves," *Journal of Applied Physics,* vol. 94, pp. 2907-2914, 2003.

[139] E. D. Reedy, B. L. Boyce, J. W. Foulk, R. V. Field, M. P. De Boer, and S. S. Hazra, "Predicting fracture in micrometer-scale polycrystalline silicon mems structures," *Journal of Microelectromechanical Systems,* vol. 20, pp. 922-932, 2011.

[140] T. Tsuchiya, O. Tabata, J. Sakata, and Y. Taga, "Specimen size effect on tensile strength of surface-micromachined polycrystalline silicon thin films," *Journal of Microelectromechanical Systems,* vol. 7, pp. 106-113, 1998.

[141] B. L. Boyce, J. M. Grazier, T. E. Buchheit, and M. J. Shaw, "Strength Distributions in Polycrystalline Silicon MEMS," *Journal of Microelectromechanical Systems,* vol. 16, pp. 179-190, 2007.

[142] O. Borrero-López, M. Hoffman, A. Bendavid, and P. J. Martin, "Reverse size effect in the fracture strength of brittle thin films," *Scripta Materialia,* vol. 60, pp. 937-940, 2009.

[143] W. N. Sharpe Jr, O. Jadaan, G. M. Beheim, G. D. Quinn, and N. N. Nemeth, "Fracture strength of silicon carbide microspecimens," *Journal of Microelectromechanical Systems,* vol. 14, pp. 903-913, 2005.

[144] G. E. Dieter, *Mechanical metallurgy*. SI metric ed. adapted by David Bacon. New York: McGraw-Hill, 1988.

[145] J. Zang and F. Liu, "Theory of bending of Si nanocantilevers induced by molecular adsorption: A modified Stoney formula for the calibration of nanomechanochemical sensors," *Nanotechnology,* vol. 18, p. 064012, 2007.

[146] R. C. Cammarata and K. Sieradzki, "Surface and interface stresses," *Annual Review of Materials Science,* vol. 24, pp. 215-234, 1994.

[147] H. Ni, X. Li, and H. Gao, "Elastic modulus of amorphous SiO 2 nanowires," *Applied Physics Letters,* vol. 88, pp. 1-3, 2006.

[148] R. G. Ross, P. Andersson, B. Sundqvist, and G. Backstrom, "Thermal conductivity of solids and liquids under pressure," *Reports on Progress in Physics,* vol. 47, pp. 1347-1402, 1984.

[149] I. Rosenblum, J. Adler, S. Brandon, and A. Hoffman, "Molecular-dynamics simulation of thermal stress at the (100) diamond/substrate interface: Effect of film continuity," *Physical Review B - Condensed Matter and Materials Physics,* vol. 62, pp. 2920-2936, 2000.

[150] M. Gan and V. Tomar, "Correlating microscale thermal conductivity of heavily-doped silicon with simultaneous measurements of stress," *Journal of Engineering Materials and Technology, Transactions of the ASME,* vol. 133, p. 041013, 2011.

[151] J. Anaya, A. Torres, A. Martín-Martín, O. Martínez, A. C. Prieto, J. Jiménez*, et al.*, "Raman spectroscopy study of group IV semiconductor nanowires," presented at the VI Encuentro Franco-Español de Quimica y Fisica del Estado Solido - VI Rencontre Franco-Espagnole sur la Chimie et la Physique de l'Etat Solide, Tarragona, Spain, 2010.

[152] C. Y. Peng, C. F. Huang, Y. C. Fu, Y. H. Yang, C. Y. Lai, S. T. Chang*, et al.*, "Comprehensive study of the Raman shifts of strained silicon and germanium," *Journal of Applied Physics,* vol. 105, p. 083537, 2009.

[153] S. Nakashima, T. Mitani, M. Ninomiya, and K. Matsumoto, "Raman investigation of strain in Si/SiGe heterostructures: Precise determination of the strain-shift coefficient of Si bands," *Journal of Applied Physics*, vol. 99, p. 053512, 2006.

[154] I. De Wolf, H. E. Maes, and S. K. Jones, "Stress measurements in silicon devices through Raman spectroscopy: Bridging the gap between theory and experiment," *Journal of Applied Physics,* vol. 79, pp. 7148-7156, 1996.

[155] S. J. Harris, A. E. O'Neill, W. Yang, P. Gustafson, J. Boileau, W. H. Weber*, et al.*, "Measurement of the state of stress in silicon with micro-Raman spectroscopy," *Journal of Applied Physics,* vol. 96, pp. 7195-7201, 2004.

[156] T. Miyatake and G. Pezzotti, "Validating Raman spectroscopic calibrations of phonon deformation potentials in silicon single crystals: A comparison between ball-on-ring and micro-indentation methods," *Journal of Applied Physics,* vol. 110, p. 093511, 2011.

[157] V. Poborchii, T. Tada, and T. Kanayama, "Observation of the forbidden doublet optical phonon in Raman spectra of strained Si for stress analysis," *Applied Physics Letters*, vol. 97, p. 041915, 2010.

[158] K. Arimoto, D. Furukawa, J. Yamanaka, K. Nakagawa, K. Sawano, S. Koh*, et al.*, "Changes in elastic deformation of strained Si by microfabrication," *Materials Science in Semiconductor Processing,* vol. 8, pp. 181-185, 2005.

[159] V. Poborchii, T. Tada, K. Usuda, and T. Kanayama, "Polarized Raman microscopy of anisotropic stress relaxation in strained-Si-on-insulator stripes," *Applied Physics Letters*, vol. 99, p. 191911, 2011.

[160] S. Ganesan, A. A. Maradudin, and J. Oitmaa, "A lattice theory of morphic effects in crystals of the diamond structure," *Annals of Physics,* vol. 56, pp. 556-594, 1970.

[161] J. Jie, W. Zhang, K. Peng, G. Yuan, C. S. Lee, and S. T. Lee, "Surface-dominated transport properties of silicon nanowires," *Advanced Functional Materials,* vol. 18, pp. 3251-3257, 2008.

[162] H. Pan and Y. P. Feng, "Semiconductor nanowires and nanotubes: Effects of size and surface-to-volume ratio," *ACS Nano,* vol. 2, pp. 2410-2414, 2008.

[163] D. Kosemura and A. Ogura, "Transverse-optical phonons excited in Si using a high-numerical-aperture lens," *Applied Physics Letters,* vol. 96, p. 212106, 2010.

[164] I. De Wolf, C. Jian, and W. M. Van Spengen, "The investigation of microsystems using Raman spectroscopy," *Optics and Lasers in Engineering,* vol. 36, pp. 213-223, 2001.

[165] V. Poborchii, T. Tada, and T. Kanayama, "Study of stress in a shallow-trench-isolated Si structure using polarized confocal near-UV Raman microscopy of its cross section," *Applied Physics Letters,* vol. 91, p. 241902, 2007.

[166] A. Pirovano, A. L. Lacaita, G. Zandler, and R. Oberhuber, "Explaining the dependences of the hole and electron mobilities in Si inversion layers," *IEEE Transactions on Electron Devices,* vol. 47, pp. 718-724, 2000.

[167] L. L. Minjoo, A. F. Eugene, T. B. Mayank, T. C. Matthew, and L. Anthony, "Strained Si, SiGe, and Ge channels for high-mobility metal-oxide-semiconductor field-effect transistors," *Journal of Applied Physics*, vol. 97, p. 011101, 2005.

[168] A. Pirovano, A. L. Lacaita, G. Ghidini, and G. Tallarida, "On the correlation between surface roughness and inversion layer mobility in Si-MOSFET's," *IEEE Electron Device Letters,* vol. 21, pp. 34-36, 2000.

[169] G. Mazzoni, A. L. Lacaita, L. M. Perron, and A. Pirovano, "On surface roughness-limited mobility in highly doped n-MOSFET's," *IEEE Transactions on Electron Devices,* vol. 46, pp. 1423-1428, 1999.

[170] T. Ishihara, K. Matsuzawa, M. Takayanagi, and S. I. Takagi, "Comprehensive understanding of electron and hole mobility limited by surface roughness scattering in pure oxides and oxynitrides based on correlation function of surface roughness," *Japanese Journal of Applied Physics, Part 1: Regular Papers and Short Notes and Review Papers,* vol. 41, pp. 2353-2358, 2002.

[171] A. Pirovano, A. L. Lacaita, G. Zandler, and R. Oberhuber, "Explaining the dependences of electron and hole mobilities in Si MOSFET's inversion layer," in *Electron Devices Meeting, 1999. IEDM '99. Technical Digest. International,* pp. 527-530, 1999.

[172] E. Escobedo-Cousin, S. H. Olsen, T. Pardoen, U. Bhaskar, and J. P. Raskin, "Experimental observations of surface roughness in uniaxially loaded strained Si microelectromechanical systems-based structures," *Applied Physics Letters,* vol. 99, 2011.

[173] S. K. Sinha, E. B. Sirota, S. Garoff, and H. B. Stanley, "X-ray and neutron scattering from rough surfaces," *Physical Review B,* vol. 38, pp. 2297-2311, 1988.

[174] R. Stommer, A. R. Martin, T. Geue, H. Goebel, W. Hub, and U. Pietsch, "Comparative studies of fractal parameters of Si(100) surfaces measured by X-ray scattering and atomic force microscopy," *Adv. X-Ray Anal.,* vol. 41, pp. 101-110, 1999.

[175] T. Vicsek, M. Cserző, and V. K. Horváth, "Self-affine growth of bacterial colonies," *Physica A: Statistical Mechanics and its Applications,* vol. 167, pp. 315-321, 1990.

[176] J. C. Arnault, A. Knoll, E. Smigiel, and A. Cornet, "Roughness fractal approach of oxidized surfaces by AFM and diffuse X-ray reflectometry measurements," *Applied Surface Science,* vol. 171, pp. 189-196, 2001.

[177] X. H. Liu, J. Chen, M. Chen, and X. Wang, "Investigation of interface in silicon-on-insulator by fractal analysis," *Applied Surface Science,* vol. 187, pp. 187-191, 2002.

[178] T. Vicsek, *Fractal growth phenomena*. 2nd ed.: World Scientific, 1992.

[179] J. B. Da Silva Jr, E. A. De Vasconcelos, B. E. C. A. Dos Santos, J. A. K. Freire, V. N. Freire, G. A. Farias*, et al.*, "Statistical analysis of topographic images of nanoporous silicon and model surfaces," *Microelectronics Journal,* vol. 36, pp. 1011-1015, 2005.

[180] Z. J. Liu, N. Jiang, Y. G. Shen, and Y. W. Mai, "Atomic force microscopy study of surface roughening of sputter-deposited TiN thin films," *Journal of Applied Physics,* vol. 92, pp. 3559-3563, 2002.

[181] P. C. Y. Wong, Y. N. Kwon, and C. S. Criddle, "Use of atomic force microscopy and fractal geometry to characterize the roughness of nano-, micro-, and ultrafiltration membranes," *Journal of Membrane Science,* vol. 340, pp. 117-132, 2009.

[182] L. Lai and E. A. Irene, "Limiting Si/SiO2 interface roughness resulting from thermal oxidation," *Journal of Applied Physics,* vol. 86, pp. 1729-1735, 1999.

[183] W. Schwarzenbach, N. Daval, S. Kerdilès, G. Chabanne, C. Figuet, S. Guerroudj*, et al.*, "Strained silicon on insulator substrates for fully depleted application," presented at the IEEE International Conference on Integrated Circuit Design and Technology, Austin, TX, USA, 2012.

[184] "Scanning Thermal Microscopy (SThM)," *Park Systems,* (online): http://www.parkafm.com/AFM_guide/download.php?code=advanced&filename=Scanning-Thermal-Microscopy-(SThM)_20130412.pdf, Last access: 21-12-2013.

[185] B. McCarthy, Y. Zhao, R. Grover, and D. Sarid, "Enhanced Raman scattering for temperature measurement of a laser-heated atomic force microscope tip," *Applied Physics Letters,* vol. 86, pp. 1-3, 2005.

[186] G. E. Jellison Jr, D. H. Lowndes, and R. F. Wood, "Importance of temperature-dependent optical properties for Raman-temperature measurements for silicon," *Physical Review B,* vol. 28, pp. 3272-3276, 1983.

[187] M. Balkanski, R. F. Wallis, and E. Haro, "Anharmonic effects in light scattering due to optical phonons in silicon," *Physical Review B,* vol. 28, pp. 1928-1934, 1983.